UNIVERSITY OF OKLAHOMA

GRADUATE COLLEGE

INVESTIGATIONS OF SECONDARY METABOLITES FROM FUNGI: ISOLATION, STRUCTURE ELUCIDATION, AND COMPUTATIONAL STUDIES

A DISSERTATION

SUBMITTED TO THE GRADUATE FACULTY

in partial fulfillment of the requirements for the

Degree of

DOCTOR OF PHILOSOPHY

By

ADAM C. CARTER
Norman, Oklahoma
2018

Downloaded from SHAREOK. Persistent Handle URL: https://hdl.handle.net/11244/316324

INVESTIGATIONS OF SECONDARY METABOLITES FROM FUNGI: ISOLATION, STRUCTURE ELUCIDATION, AND COMPUTATIONAL STUDIES

A DISSERTATION APPROVED FOR THE
DEPARTMENT OF CHEMISTRY AND BIOCHEMISTRY

BY

Dr. Robert H. Cichewicz, Chair

Dr. Mark A. Nanny

Dr. Daniel T. Glatzhofer

Dr. Charles V. Rice

Dr. Indrajeet Sharma

© Copyright by ADAM C. CARTER 2018
All Rights Reserved.

Acknowledgements

Many thanks are owed to the many individuals who have supported and assisted me in this undertaking. First, I would like to thank my advisor, Dr. Robert Cichewicz. His constant support, enthusiasm, and desire to challenge me have helped me tremendously in my doctoral studies. I have learned a tremendous amount working under his supervision, and will carry this knowledge and experience with me in all of my future scientific endeavors. I would also like to take the time to thank Dr. Daniel Glatzhofer, Dr. Mark Nanny, Dr. Charles Rice, and Dr. Indrajeet Sharma for the time and support they have given as my committee members to ensure my success in my research and studies. Additionally, I would like to thank Dr. Steven Foster and Dr. Susan Nimmo for their expertise and assistance in collecting data that was essential for my graduate research. I would also like to extend tremendous gratitude towards past and current members of the Natural Products Discovery Group. From this group of individuals, I was not only able to glean a tremendous amount of knowledge, but I could also turn to them when I encountered troubles of all kinds.

Finally, I would like to acknowledge my family and friends for their endless support and encouraging words through the high points and the low points of my time in graduate school. Last, but certainly not least, I would like to give the most thanks to my loving wife, Heather. She was always there to offer a kind word, encouragement, and support whenever I needed it the most. She is the reason I was able to persevere through even the most difficult challenges of my studies, and I truly believe that without her this would not be possible.

Table of Contents

Acknowledgements iv

List of Tables x

List of Schemes xi

List of Figures xii

Abstract xvi

Chapter 1: An Introduction to Fungal and Bacterial Natural Products 1

1.1 Natural Products from Terrestrial Sources 1

1.2 Natural Products in Modern Pharmaceuticals 5

1.3 Fungi as a Source of Natural Products 6

1.4 Biosynthesis of Fungal Natural Products 8

1.5 Endosymbionts as a Source of Natural Products 12

1.6 Prospects for Natural Product Discovery and Future Opportunities 15

Chapter 2: Chapter Overviews 17

2.1 Overview of Graduate Research, Development and Accomplishments 17

2.2 Chapter 3. Creation of a High-Throughput, High-Content Screening Assay for the Human Parasite *Trichomonas vaginalis* 18

2.3 Chapter 4. Natural-Product-Inspired Compounds as Countermeasures Against the Liver Carcinogen Aflatoxin B_1 19

2.4 Chapter 5. *In Situ* Ring Contraction and Transformation of the Rhizoxin Macrocycle through an Abiotic Pathway 19

Chapter 3: Creation of a High-Throughput, High-Content Screening Assay for the Human Parasite *Trichomonas vaginalis* 21

3.1 Introduction 21

3.2 Results and Discussion 23

3.2.1 Development of an Assay for Detecting *T. vaginalis* Inhibitors 23

3.2.2 Testing Purified Natural Products 26

3.2.3 Testing Fungal Natural Product Extracts 29

3.2.4 Bioassay-Guided Purification of Natural Products from a *F. solani* Isolate 30

3.2.5 Structure-Activity Relationship Study of Quinones 31

3.2.6 Bioassay-Guided Purification of Natural Products from a *Humicola grisea* Isolate 33

3.2.7 Reduction of Xanthoquinodin A1 34

3.2.8 Counter-Screen with *Lactobacillus acidophilus*. 35

3.2.9 Conclusions and Discussion 36

3.3 Materials and Methods 37

3.3.1 General Experimental Procedures 37

3.3.2 Culture of Organisms 37

3.3.3 *Trichomonas vaginalis* Assays 38

3.3.4 Mammalian Cell Cytotoxicity Assays 40

3.3.5 *Lactobacillus acidophilus* Viability Assays 40

3.3.6 Fungal Procurement and Culture Conditions 41

3.3.7 Isolation of Quinone-Containing Natural Products 1-3 41

3.3.8 Further Screening of Purchased and Synthesized Quinones 42

3.3.9 Synthesis of Naphthopurpurin (4) 42

3.3.10 Synthesis of 2-methoxynaphthazarin (5) 43

3.3.11 Synthesis of 1,4-dihydro-5,8-dihydroxy-2-methyl-9,10-anthracenedione (6) 43
3.3.12 Synthesis of 1,4-dihydro-2-methyl-9,10-anthracenedione (7) 44
3.3.13 Isolation of Xanthoquinodin A1 (42) 44
3.3.14 Borohydride Reduction of Compound 42 45
Chapter 4: Natural-Product-Inspired Compounds as Countermeasures Against the Liver Carcinogen Aflatoxin B_1 47
4.1 Introduction 47
4.2 Results and Discussion 49
4.2.1 Assay Development and Optimization 49
4.2.2 Testing Two Putative AfB_1 Protective Compounds: Oltipraz and *N*-Acetylcysteine 51
4.2.3 Screening of Natural Product Extracts 52
4.2.4 Purification of Compounds 1-3 from *A. alternata* 54
4.2.5 Assessing the Protective Properties of Compounds 4-12 56
4.2.6 Testing a HepG2 Spheroid Model for Assessing AfB_1 Protection 61
4.2.7 Conclusions 64
4.3 Materials and Methods 64
4.3.1 General Experimental Procedures and Chemicals Used 64
4.3.2 Aflatoxin Protection Assay 65
4.3.3 Screening Natural Product Extracts 67
4.3.4 Purification of Compounds 1-3 67
4.3.5 Synthesis of 4-hydroxy-3-methoxybenzophenone (8) 69

4.3.6 Synthesis of 4-hydroxy-3-methoxybenzhydrol (9) 70
4.3.7 Synthesis of 1-hydroxy-3-methoxyxanthone (10) 71
4.3.8 Synthesis of 2-hydroxy-4-methoxy-*N*-(3-pyridinylmethyl)benzamide (12) 72
Chapter 5: *In Situ* Ring Contraction and Transformation of the Rhizoxin Macrocycle through an Abiotic Pathway 73
5.1 Introduction 73
5.2 Results and Discussion 76
5.2.1 Isolation and Structure Elucidation of Rhizoxins 1-6 76
5.2.2 Biological Evaluation of Rhizoxins 1-6 87
5.2.3 Computational and Degradation Studies of the Formation of 2 88
5.2.4 Conclusions 93
5.3 Materials and Methods 93
5.3.1 General Experimental Procedures 93
5.3.2 Fungal Isolate Procurement and Identification 94
5.3.3 Extraction and Purification of Rhizoxin Analogs 94
5.3.4 DFT NMR Calculations 96
5.3.5 Biological Evaluations 97
5.3.6 Chemical Transformation Studies 98
5.3.7 DFT Calculations for Formation of 2 99
References 100
Appendix A: Supporting Data for Chapter 3 113
Appendix Table of Contents 113
Appendix B: Supporting Data for Chapter 4 127

Appendix Table of Contents 127

Appendix C: Supporting Data for Chapter 5 133

Appendix Table of Contents 133

List of Tables

Table 4.1. Maximum protection afforded by pure compounds 1-12 from AfB_1 toxicity in HepG2 monolayers, expressed as relative live cell area ± 1 S.D. with respect to no AfB_1 controls. As AfB_1 exposure alone typically resulted in relative live cell areas of approximately 30%, we considered values >50% to be "protective". 61

Table 5.1. ^1H NMR [∂, mult. (J in Hz)] spectroscopic data (500 MHz, CD_3OD) for rhizoxin analogs 2-6 78

Table 5.2. ^{13}C NMR spectroscopic data (125 MHz, CD_3OD) for rhizoxin analogs 2-6 .. 79

List of Schemes

Scheme 3.1. Chemical structure of natural product 42 obtained from a *Humicola grisea* isolate and its reduction through the use of sodium borohydride to yield the secondary alcohol 43. 34

Scheme 4.1. Synthesis of compounds 8 and 9 from vanillin 57

Scheme 4.2. Synthesis of compound 10 from 2,4,6-trihydroxybenzoic acid 58

Scheme 4.3. One-pot synthesis of compound 12 60

Scheme 5.1. Proposed pathway for the formation of rhizoxin 2 from 1 under mildly acidic conditions 91

List of Figures

Figure 1.1. Natural products isolated from plants in the early 1800s 2

Figure 1.2. Examples of clinically relevant natural products isolated from microbial sources..... 3

Figure 1.3. Examples of notable natural products synthesized during the 20th century and first synthesis 4

Figure 1.4. Examples of polyketide natural products of fungal origin 9

Figure 1.5. Examples of nonribosomal peptide natural products of fungal origin 10

Figure 1.6. Examples of terpenoid natural products of fungal origin..... 11

Figure 1.7. Examples of indole alkaloid natural products of fungal origin 12

Figure 1.8. Examples of bioactive natural products of endosymbiotic origin (the host organism and the microbial endosymbiont source are listed in parenthesis)..... 14

Figure 3.1. A comparison of the traditionally used resazurin fluorescence assay (red squares) and our newly developed imaging-based assay (green triangles). Using two fields per well, we determined the limit of detection of the Operetta to be 1,000 trichomonads per well. This limit of detection arises as a result of whether a trichomonad appears in an image field. The resazurin assay was unable to detect less than 10,000 trichomonads per well. 24

Figure 3.2. (Left) Sample field from the Operetta of a fixed and stained (0.5% glutaraldehyde, 2.5 μM propidium iodide, and 2.5 μM acridine orange) population of healthy and growing *T. vaginalis* after 17 hours incubation. One dead trichomonad (red) can be seen. (Right) Sample screening image from the Operetta showing partial inhibition due to a fungal extract after 17 hours incubation. 26

Figure 3.3. Nine pure natural products evaluated for SI_{3T3} values in initial pure compound screening against *T. vaginalis*. Compound sources were diverse and are shown under the compound names. LC_{50} values were determined in *T. vaginalis* and 3T3 mammalian cells to obtain the SI_{3T3} values shown. Notably, 2-bromoascididemin exhibited a SI_{3T3} value of 14.0, which was much higher than any of the other compounds tested..... 28

Figure 3.4. Selectivity indices of 71 fungal crude extract library hits with activity exceeding that of 25 μM metronidazole. All hits indicated with arrows were later found to be strains of the species *Fusarium solani.* The isolate corresponding to plate 55 well F11 (internal strain designation Tree 400 EW+PNGP-3) was grown in large scale to yield active compounds 1-2. 30

Figure 3.5. Structures of isolated secondary metabolites 1-3 from *Fusarium solani.* LC_{50} values for each compound against *T. vaginalis* and Ect1 mammalian cells are also listed, as well as their calculated SI_{Ect1} values. 31

Figure 3.6. Structures and biological activity of synthetic and commercially available quinone-containing compounds with SI_{Ect1} values calculated to be greater than 1. LC_{50} values for each compound in *T. vaginalis* and Ect1 cells are listed. 32

Figure 3.7. Bioactivity of compounds 1, 5, and metronidazole against *T. vaginalis* in atmospheres of varying oxygen levels. Numbers shown are calculated from two fields in each well, three replicate wells per condition. Notably, potency of 1 and 5 decreases as oxygen level decreases, while metronidazole maintains approximately the same level of potency under all conditions tested. 33

Figure 3.8. Comparison of anti-trichomoniasis activity of 42 and 43 under anaerobic conditions. Numbers shown are calculated from two fields in each well, three replicate wells per concentration tested. Error bars are equal to 1 S.D. (n=3). 35

Figure 4.1. Oxidative toxification of aflatoxin B_1 to form aflatoxin B_1-8,9-epoxide 48

Figure 4.2. Effect of oltipraz and *N*-acetylcysteine on AfB_1 toxicity in HepG2 cells. Error bars represent one standard deviation, calculated from a total of two replicate measurements of live cell area. 52

Figure 4.3. Top bioactive samples (hits) from screening fungal and bacterial extracts using HepG2 monolayers. Plate 58 well B1 (source of compound 1-3) preserved cell morphologies reasonably well to appear similar to the no AfB_1 control. For comparison, the cells in plate 59 well E6, exhibited increased cell area, but lacked the morphological similarities of 58B1. 54

Figure 4.4. Structures of secondary metabolites 1-3 from *Alternaria alternata* 55

Figure 4.5. Structures of additional compounds (4-12) tested. 59

Figure 4.6. Relative live cell areas of HepG2 spheroids resulting from the application of selected compounds at a concentration of 10 μM and exposure to AfB_1. Compounds were considered “protective” if they achieved >50% relative live cell areas. Error bars are expressed as ± 1 S.D., n=3. 62

Figure 4.7. Protection from aflatoxin in HepG2 spheroids by compounds 1 and 10. In live spheroids, calcein AM is converted to calcein, which fluoresces green, after hydrolysis by intracellular esterases. Pure blue spheroids are dead and only fluoresce due to Hoechst staining of DNA. 63

Figure 5.1. Structures of isolated natural products 1-6 76

Figure 5.2. Key COSY and HMBC correlations for 2..... 80

Figure 5.3. ^{13}C calculation results of two plausible stereoisomers at the mPW1PW91/6-311G(d,p)-IEFPCM (methanol)//mPW1PW91/6-31G(d)-IEFPCM (methanol) level. Includes relative errors of selected carbon nuclei (top) and corrected mean absolute deviations (CMAD) and R^2 values (bottom) for calculated vs. experimental ^{13}C and ^{1}H NMR chemical shift values of (a-e) 2-6 and (f) rhizoxin (1)..... 82

Figure 5.4. Antiproliferative and cytotoxic activity of rhizoxin in a panel of pediatric cancer cell lines. (a) Concentration-response curves for antiproliferative and cytotoxic activity of rhizoxin using the SRB assay. (b) Percent cytotoxicity of rhizoxin at 40 nM in a panel of cell lines. Using a one-way ANOVA with Tukey's post hoc test for multiple comparisons, we observe no significant difference among cell lines in the Ewing's and non-Ewing's groups. However, each comparison between a cell line in the Ewing's group and a cell line in the non-Ewing's group is significant with $p \leq 0.035$. Results are represented as the mean ± SEM. (n=3)..... 88

Figure 5.5. Degradation of compound 1 incubated in acidified aqueous methanol for one day. Peak heights are expressed as a percentage relative to the peak height of compound 1 ± 1 S.D. (n=3). Peak heights were taken at a wavelength of 310 nm..... 90

Figure 5.6. DFT calculations for the acid-catalyzed formation of 2 from 1. Reaction pathway was calculated at M06-2X/6-311++G(d,p)-IEFPCM (water)//M06-2X/6-31G(d)-IEFPCM (water) level. All energies are given in kcal/mol. 92

Abstract

Natural products have served as therapeutic agents in the treatment of many human health ailments for thousands of years. In order to find new therapeutic agents for future human health problems, those in the field of natural product drug discovery will need to take advantage of technological advances in screening capabilities such as high-content imaging-based assays for the identification of promising lead compounds, as well as computational calculations to aid in natural product structure determination and chemical reactivity studies. The research reported in this dissertation demonstrates the applications of these methodological approaches in three applications.

Trichomonas vaginalis is a sexually transmitted parasite that infects at least 170 million people worldwide and current treatments are limited to a single therapeutic agent, metronidazole. As a result, there is a need for new drug leads to treat this as well as other anaerobic parasites. To address this need, a high-throughput imaging-based assay was developed to screen a fungal crude extract library for inhibition of *T. vaginalis* and Ect1/E6E7 human cervical cells. This information was used to determine selectivity indices (SIs), and bioassay-guided fractionation led to the purification of promising leads that inhibit *T. vaginalis* while remaining safe to human cells. We found that the quinone-containing compounds fusarubin (SI=30) and xanthoquinodin A1 (SI=20) were promising leads, but as quinones are known to have indiscriminate activities, further protocols were developed to probe the potential liabilities of these compounds. Manipulation of oxygen levels led to a loss of potency in fusarubin, while xanthoquinodin A1 inhibited *Lactobacillus acidophilus*, a beneficial bacterium found in the vaginal tract. As such, we determined that while quinones show antitrichomonal

activities, these compounds should be approached with caution when considering them as leads.

Aflatoxin B_1 (AfB_1) is a mycotoxin with tremendous health impacts as it is widely considered one of the most potent liver carcinogens known to humankind, and billions of people worldwide are exposed to it through their diets. While efforts have been made to find small molecules capable of protecting the liver from AfB_1, there has been little success. In order to address this problem, we developed a high-throughput and high-content screening assay to identify and test natural products that are capable of protecting HepG2 liver cells, grown as monolayers and spheroids, against AfB_1 toxicity. The use of spheroids proved to be excellent for the production of *in vivo* sensitivity of HepG2 cells under *in vitro* conditions, and led to the identification of two promising compounds, alternariol-9-methyl ether (purified from an *Alternaria alternata* isolate) and 1-hydroxy-3-methoxyxanthone, as potential future starting points for the development of new AfB_1-protective agents.

Finally, Ewing sarcoma, while rare, is a debilitating disease affecting primarily children, teens, and young adults. Through a screening of fungal extracts, we identified a *Rhizopus microsporus* isolate containing the endosymbiotic partner *Burkholderia rhizoxinica* that produced an extract showing potent and selective inhibition of Ewing sarcoma cell lines. Bioassay-guided fractionation led to the purification of the known antimitotic agent rhizoxin and five new analogs. The structures of these analogs were determined through the use of NMR data analysis, and configurations of new stereocenters were established through the use of ROESY spectra in conjunction with computational calculations of chemical shifts and $^3J_{HH}$ coupling data. While rhizoxin was

determined to have selectivity for a subset of Ewing sarcoma cell lines, the new analogs were found to be inactive. However, one analog stood out chemically as it contained a 15-membered macrolactone that was previously not reported for this class of compounds. Using a combination of degradation experiments and computational calculations, we determined that this compound likely arose through an acid-catalyzed Meinwald rearrangement of rhizoxin as a result of the mildly acidic environment created by *R. microsporus* and its bacterial endosymbiont.

Chapter 1: An Introduction to Fungal and Bacterial Natural Products

1.1 Natural Products from Terrestrial Sources

Dating as far back as 2600 BC, chemical components from plant sources were utilized for medicinal purposes in the form of traditional medicines. Many civilizations used these plants as medicines including the Mesopotamians, Egyptians, Chinese, Indians, Tibetans, Greek, Mayan, and Aztecs, and some of these sources, including *Papaver somniferum* (opium poppy), *Commiphora* species (myrrhs), and *Glycyrrhiza glabra* (licorice), are still commonly used today.[1] In addition to plant sources, fungi were used in Chinese traditional medicine including *Calvatia craniiformis* (brain puffball), *Ganoderma lucidum* (Lingzhi mushroom), *Ophiocordyceps sinensis* (caterpillar fungus), and *Pulveroboletus ravenelii* (Ravenel's bolete).[2-3] These terrestrial fungi were used to treat a variety of ailments including coughs, colds, inflammation, parasitic infections, and bleeding.[2]

Beginning in the early 1800s, chemists began purifying organic compounds from medicinal plants, resulting in the birth of the scientific field of pharmacognosy, which is a field of study concerned with natural product molecules and their medicinal uses. In 1816, Friedrich Wilhelm Adam Sertürner purified and described morphine from *P. somniferum*.[4] Following this discovery, other secondary metabolites were isolated including strychnine in 1818,[5] colchicine and quinine in 1820,[6-7] and salicin in 1828 (Figure 1.1).[8] These compounds came to be known as natural products or secondary metabolites, which by definition, are organic compounds produced by organisms that do not play direct roles in growth, development or reproduction. Instead, secondary

metabolites are generally thought to play roles in protection, competition, and other interactions with organisms in their environment.

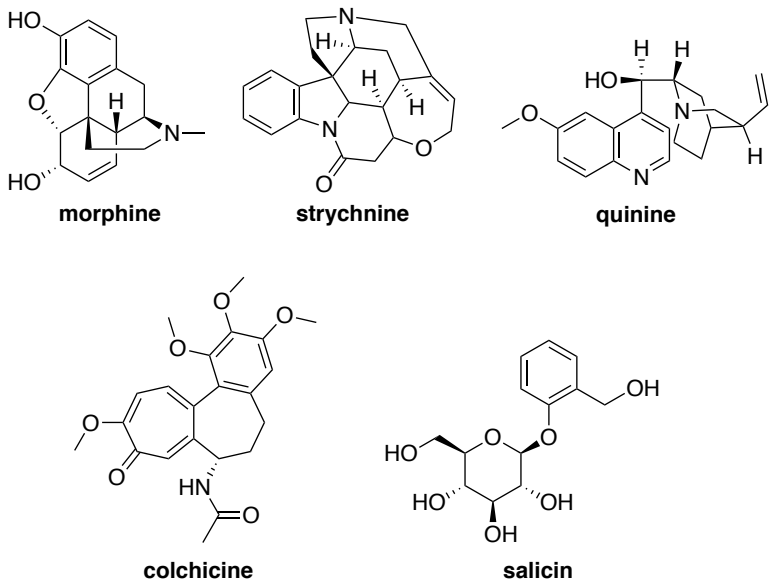

Figure 1.1. Natural products isolated from plants in the early 1800s

As time progressed, microbial sources of secondary metabolites received increased attention. As a result, an increasing number of compounds of medicinal value were discovered from these microbes. These discoveries include many clinically important microbial natural products such as streptomycin from *Streptomyces griseus* in 1943,[9] chlortetracycline from *Streptomyces aureofaciens* in 1945,[10] chloramphenicol from *Streptomyces venezulae* in 1947,[11] erythromycin from *Streptomyces erythraea* in 1952,[12] vancomycin from *Amycolatopsis orientalis* in 1953,[13] and rifamycins from *Streptomyces mediterranei* in 1959.[14] In addition to the discovery of a vast assortment of antibacterial agents, the examination of microbial source organisms yielded many other therapeutics of note including immunosuppressive compounds (e.g., cyclosporins and rapamycin), cholesterol-lowering agents (e.g., the statins), anti-parasitics (e.g.,

ivermectins), and chemotherapeutic agents (e.g., actinomycins and mitomycins) (Figure 1.2).

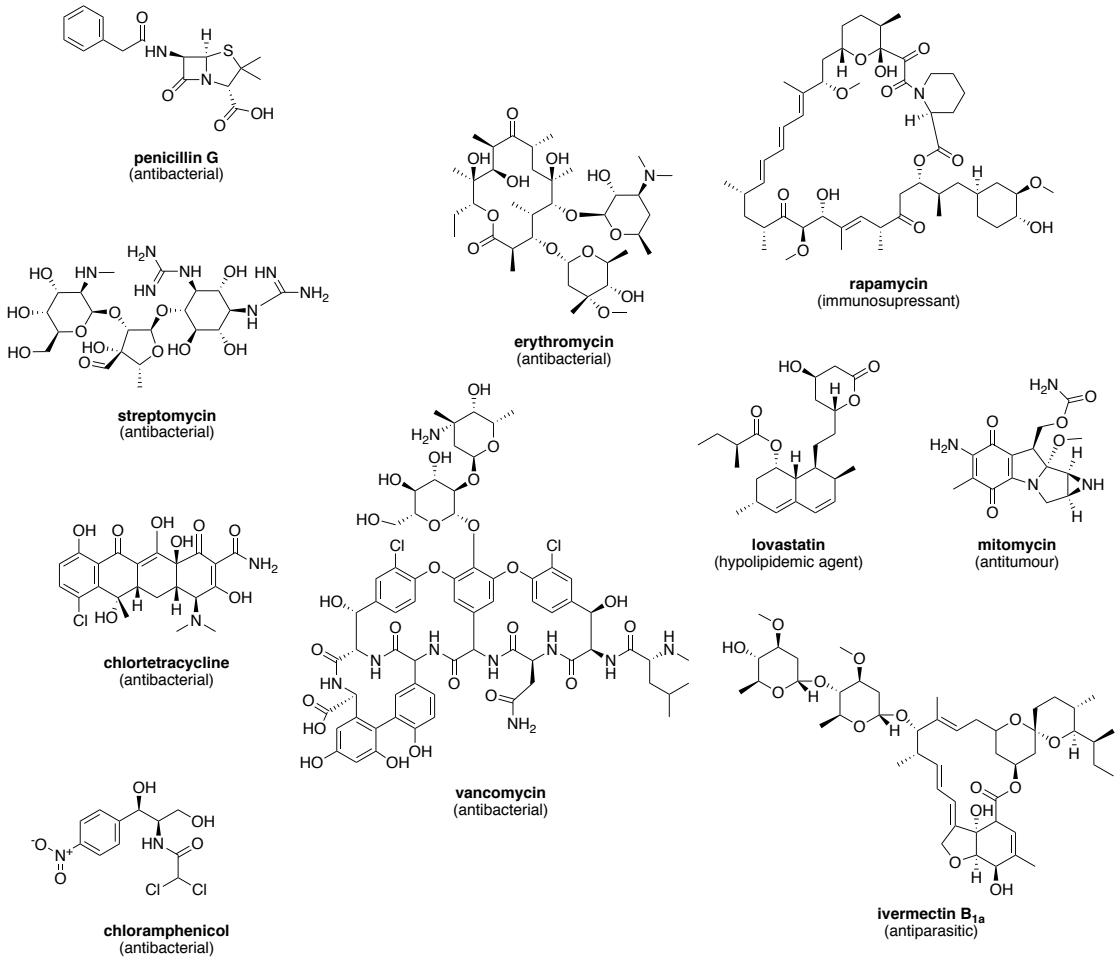

Figure 1.2. Examples of clinically relevant natural products isolated from microbial sources

In addition to the discovery of new chemical entities with therapeutic properties, the field of natural product drug discovery has also served to develop the field of organic synthesis. In fact, many consider Friedrich Wöhler's synthesis of urea from cyanic acid and ammonia in 1828 to be the beginning of modern organic chemistry.[15] This was followed by other syntheses of organic compounds such as Hermann Kolbe's synthesis of

acetic acid from carbon disulfide in 1845[16] and Charles Frédéric Gerhardt's synthesis of acetylsalicylic acid in 1853.[17] These early syntheses of the 19th century paved the way for many of the well-known chemists of the 20th and 21st centuries such as Robert Burns Woodward, who synthesized natural products such as quinine,[18] cholesterol,[19] strychnine,[20] and cephalosporin;[21] E.J. Corey, who synthesized ginkgolide A[22] and ecteinascidin 743;[23] and K.C. Nicolaou, who synthesized paclitaxel,[24] brevetoxin B,[25] amphotericin B,[26] and vancomycin[27] (Figure 1.3). In order to synthetically build the complex scaffolds of these molecules, organic chemists have had to develop new chemical reactions that have increased what can be accomplished through modern organic synthesis and have increased our understanding of organic structures and their biological functions.

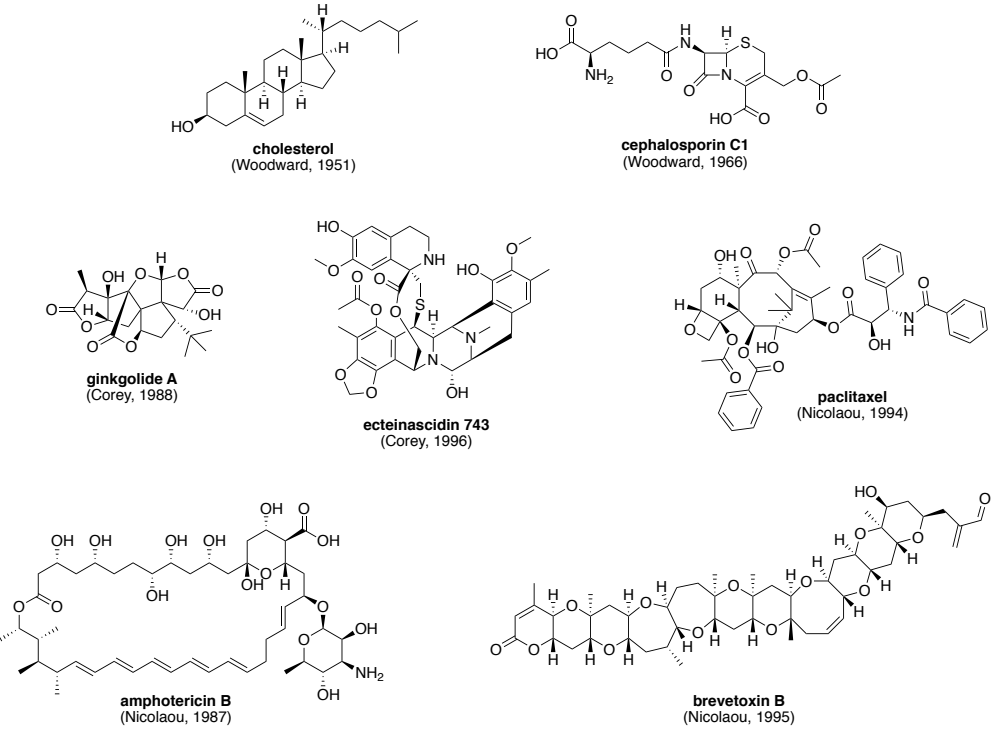

Figure 1.3. Examples of notable natural products synthesized during the 20th century and first synthesis

1.2 Natural Products in Modern Pharmaceuticals

In modern times, natural products make up a significant portion of clinically approved pharmaceuticals. It is estimated that approximately 50% of the drugs approved in the United States between 1981 and 2014 are natural products, natural product derivatives, natural product mimics, or synthetic compounds with natural product-derived pharmacophores.[28] Moreover, natural products and natural product inspired compounds have typically made up 10-50% of small molecule drugs approved each year, with this figure typically being around 20%.[28] As these naturally occurring compounds still make up such a large portion of drug approvals each year, natural products should remain a prominent focus in the development of new therapeutic agents. Despite the prominence of natural products in the modern pharmacopoeia, many pharmaceutical companies have focused more attention on developing synthesis-driven drug discovery programs. The primary driving force behind this shift in focus was the development of automated high throughput screening (HTS) programs, allowing for the testing of large libraries of pure compounds for bioactivity.[29] This in turn led to a demand for the development of large chemical libraries, which could not feasibly be met with the isolation of natural products. Additionally, issues regarding the patentability of natural products makes them less attractive as drug candidates.[30] Therefore, pharmaceutical companies began using techniques such as combinatorial chemistry to meet the demand instead.[31]

Despite this shift in focus, new and successful pharmaceuticals continue to come from natural sources or be inspired by compounds from nature. Such pharmaceuticals include successful anticancer drugs such as paclitaxel, vinblastine, and topotecan; lipid-lowering medications such as atorvastatin; and antifungals such as amphotericin B. In all,

between 1981 and 2014, 58% of antibacterial and 32% of anticancer new chemical entities were natural products or derived from natural products.[28]

1.3 Fungi as a Source of Natural Products

Microbes have historically been a prolific source of natural product-based drugs. As of 2002, it was estimated that microbes were responsible for the production of approximately 22,500 bioactive secondary metabolites, with about 38% of those being produced by fungi. These bioactive secondary metabolites include 30% of the approximately 16,500 secondary metabolites produced by microbes that were known at that time to have antibiotic activities.[32] As such, fungi are an important and prolific group of organisms with regards to the discovery of bioactive secondary metabolites.

One of the most famous discoveries of a natural product from a fungus was that of penicillin by Alexander Fleming in 1929.[33] This discovery has helped to save many millions of lives over the years and won Fleming, along with Howard Florey and Ernst Chain, the Nobel Prize in Physiology or Medicine in 1945.[34] It also paved the way for the discovery of other classes of β-lactam antibiotics such as the cephalosporins, norcardicins, carbapenems, and monobactams.[1] In addition to penicillin, another notable natural product that originated from fungi includes cyclosporine, an immunosuppressant used in the treatment of rheumatoid arthritis,[35] psoriasis,[36] Crohn's disease,[37] as well as to prevent rejection in organ transplants.[38] Fungi are also responsible for the class of drugs known as the statins, which are used to treat cardiovascular disease,[39] and naturally occurring statins have served as the inspiration for blockbuster drugs such as atorvastatin.[40]

Recent advances in DNA sequencing and synthetic biology are currently providing new opportunities in the field of fungal natural product discovery. With these advances in DNA sequencing, it has been estimated that there could be as many as approximately 5.1 million fungal species on earth based on environmental DNA sequencing data. Of these, only 70,000, or 1.4%, have been described, leaving many fungi that have yet to be explored as potential sources for bioactive natural products and drugs.[41] However, many fungi cannot be cultured under laboratory conditions, and many more have cryptic or silent biosynthetic gene clusters that are only expressed under yet-to-be-determined growth conditions. For example, mining of the published genome from the fungus *Aspergillus nidulans* reveals a total of 53 putative biosynthetic gene clusters, but not all of the encoded secondary metabolites are produced under laboratory culture conditions.[42] Accordingly, much work has been done recently in the heterologous expression of fungal biosynthetic pathways. One such development in this area that has occurred recently is that of the HEx (Heterologous Expression) platform developed by Harvey *et al.* in which fungal biosynthetic gene clusters are expressed in *Saccharomyces cerevisiae*, resulting in the production of the encoded secondary metabolites. In its first report, this technique was applied to 41 fungal biosynthetic gene clusters, resulting in the successful expression of 22, for a success rate of 58%.[39] While the compounds produced were structurally relatively simple and of low molecular weight, this technique provides a basis for future work that may enable the expression of more complex biosynthetic gene clusters that are not active under laboratory conditions or from fungi that cannot yet be cultured.

1.4 Biosynthesis of Fungal Natural Products

Fungi possess a diverse set of biosynthetic machinery that enables them to produce many classes of secondary metabolites. The range of secondary metabolites produced by fungi can be broadly divided into polyketides, nonribosomal peptides, terpenes, and indole alkaloids based on differences in the biosynthetic precursors used to make these metabolites.

The polyketides make up the largest portion of secondary metabolites produced by fungi and are generated through the action of polyketide synthases (PKSs). Polyketide synthases are composed of various domains including a ketoacyl coenzyme A (CoA) synthase, acyltransferase, and acyl carrier domains. They may also contain structure-modifying domains such as ketoreductases, dehydratases, and enoyl reductases, which allow for a greater variety of polyketide natural products to be produced. These PKS enzymes function by linking short-chain carboxylic acids such as acetyl CoA or malonyl CoA in an iterative process to form a carbon chain, which can undergo a variety of reductions by other domains of the PKS to allow for diversity in the compounds produced. The resulting carbon chain may then undergo further post-PKS modifications to yield the final secondary metabolite.[43] Examples of polyketide natural products from fungi include compounds such as lovastatin, aflatoxin B_1, xanthoquinodin A1, and asteltoxin (Figure 1.4).

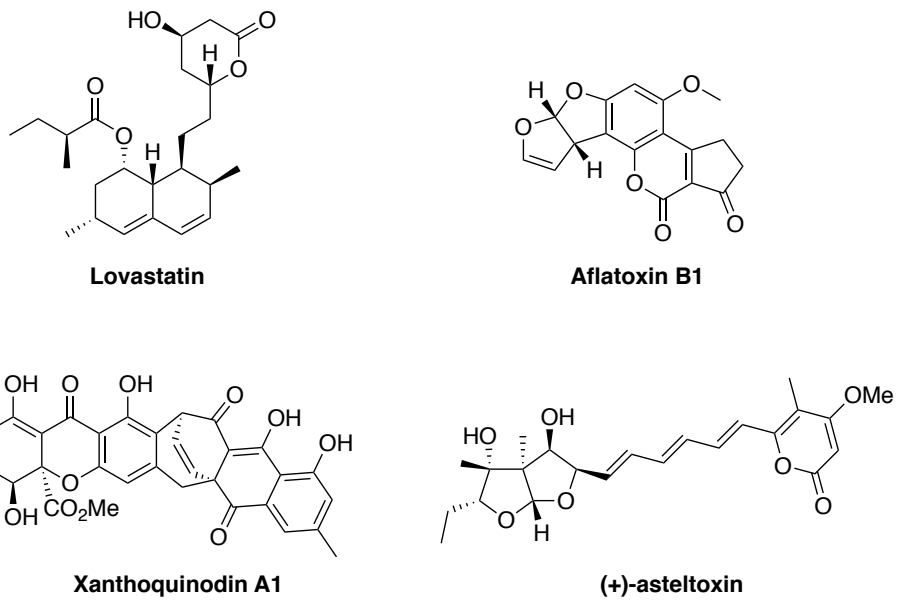

Figure 1.4. Examples of polyketide natural products of fungal origin

Another group of fungal secondary metabolites are the nonribosomal peptides, which are constructed through the actions of nonribosomal peptide synthetases (NRPSs). These enzymes are composed of distinct domains that typically include adenylation, thiolation, and condensation domains, which together make up a single module. Each module is then responsible for incorporating an additional amino acid into a growing peptide chain.[44] This is accomplished through recognition and activation of the substrate by the adenylation domain, transport of a specific amino acid by the thiolation domain, and finally, amide bond formation catalyzed by the condensation domain.[45] While less numerous than fungal polyketide natural products, their nonribosomal peptide counterparts include many molecules with useful bioactivities such as beauvericin and cyclosporin A (Figure 1.5).

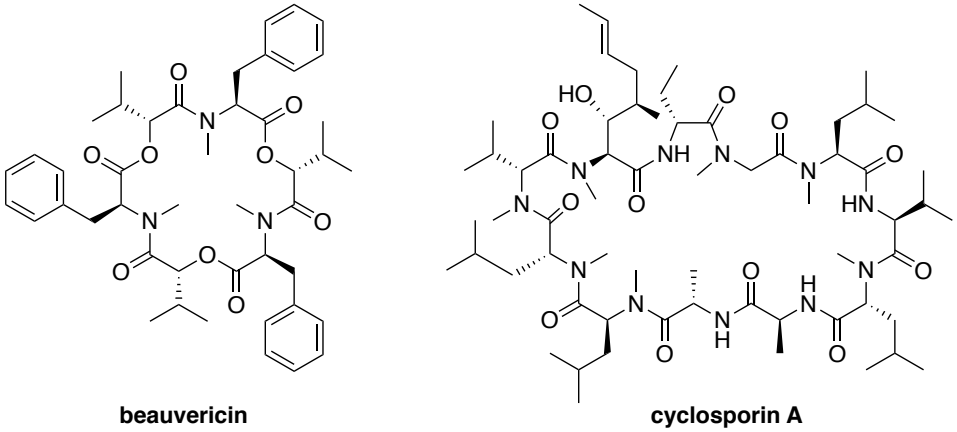

Figure 1.5. Examples of nonribosomal peptide natural products of fungal origin

A third class of natural products produced by fungi is that of the terpenoids, which are composed of isopentenyl diphosphate (IPP) and dimethylallyl diphosphate (DMAPP). One to three units of IPP may undergo condensation with DMAPP, catalyzed by isoprenyl diphosphate synthase enzymes, leading to the formation of isoprenyl diphosphate molecules that are composed of ten (geranyl diphosphate), fifteen (farnesyl diphosphate), or twenty (geranylgeranyl diphosphate) carbons. Once these intermediates have formed, they may be further modified through the actions of prenyl transferases or cyclases to form a large assortment of possible terpenoid secondary metabolites,[46] which include molecules such as paclitaxel, trichodermin, and fumagilin (Figure 1.6).

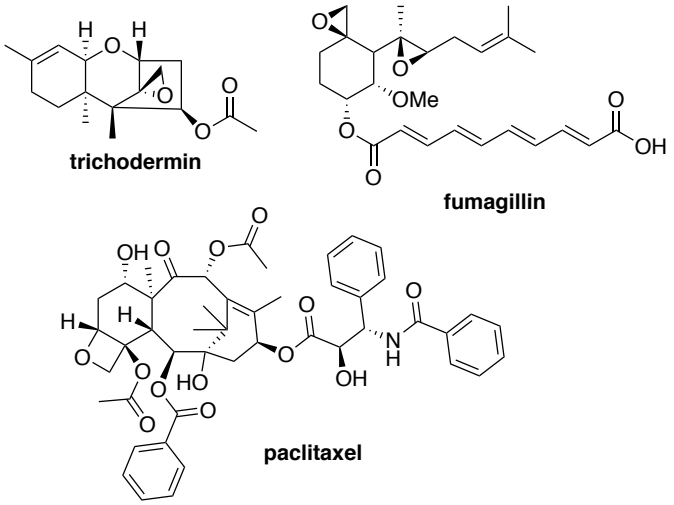

Figure 1.6. Examples of terpenoid natural products of fungal origin

A final class of secondary metabolites produced by fungi is the indole alkaloids. These compounds contain an indole or indoline moiety and are formed through a variety of pathways in fungi including decarboxylation of tryptophan to form tryptamine, prenylation of tryptophan to form 4-dimethylallyl tryptophan, activation of tryptophan by adenylation domains of NRPSs, or prenylation of indole-3-glycerol-phosphate. These different pathways are capable of leading to a variety of classes of indole alkaloids including peptide indole alkaloids and indole terpenoids.[47] Overall, there are many molecules belonging to this class of fungal secondary metabolites including lysergic acid, chaetoglobosin A, and psilocybin (Figure 1.7).

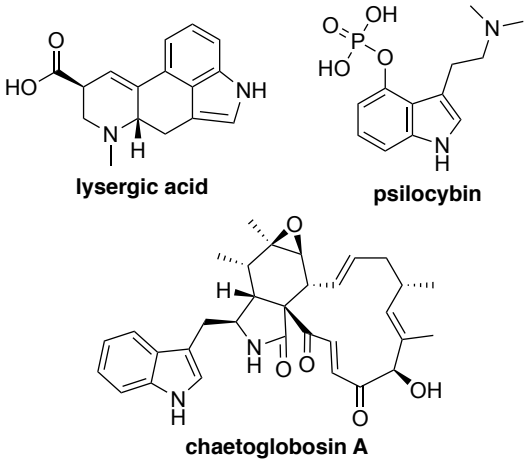

Figure 1.7. Examples of indole alkaloid natural products of fungal origin

The diversity of chemical structures that fungi are capable of producing reflects the diversity of their biosynthetic machinery. As a result of the diversity of compounds that they produce, fungi continue to be of interest to natural product chemists with the hope that there are many new compounds that have yet to be discovered.

1.5 Endosymbionts as a Source of Natural Products

An interesting phenomenon that occurs in nature is that of endosymbiosis, in which an organism lives symbiotically on or within another organism. Because of the close relationship between these organisms, there have been instances where the production of certain secondary metabolites has been attributed to the incorrect source. For example, the potent anticancer compound rhizoxin (Figure 1.8), which was initially isolated from the fungus *Rhizopus microsporus*, was thought to be produced by the fungus.[48] However, subsequent studies of the biosynthesis of this compound that sought the putative genes for its production revealed that these genes are not found in the genome of the fungus. Instead, the compound is the product of a bacterial type I PKS

gene set. Further work led to the discovery that the biosynthetic genes are part of the genome of a bacterial endosymbiont belonging to the genus *Burkholderia*. Production of rhizoxin by this bacterial endosymbiont was further proven through isolation of the bacterium and analysis of its secondary metabolite production in culture.[49-50]

Another interesting secondary metabolite with anticancer activity that is of an endosymbiotic source is ecteinascidin 743 (Figure 1.8).[51] This compound was initially isolated from a tunicate belonging to the species *Ecteinascidia turbinata.* Comparison of the structure of ecteinascidin 743 to other known secondary metabolites revealed that this compound bore many similarities to compounds belonging to the class of saframycins, which had been previously isolated from bacterial sources.[52] While the endosymbiotic microbe could not be cultured under laboratory conditions, genomic efforts were effective in determining the source of this secondary metabolite as being *Candidatus* Endoecteinascidia frumentensis.[53]

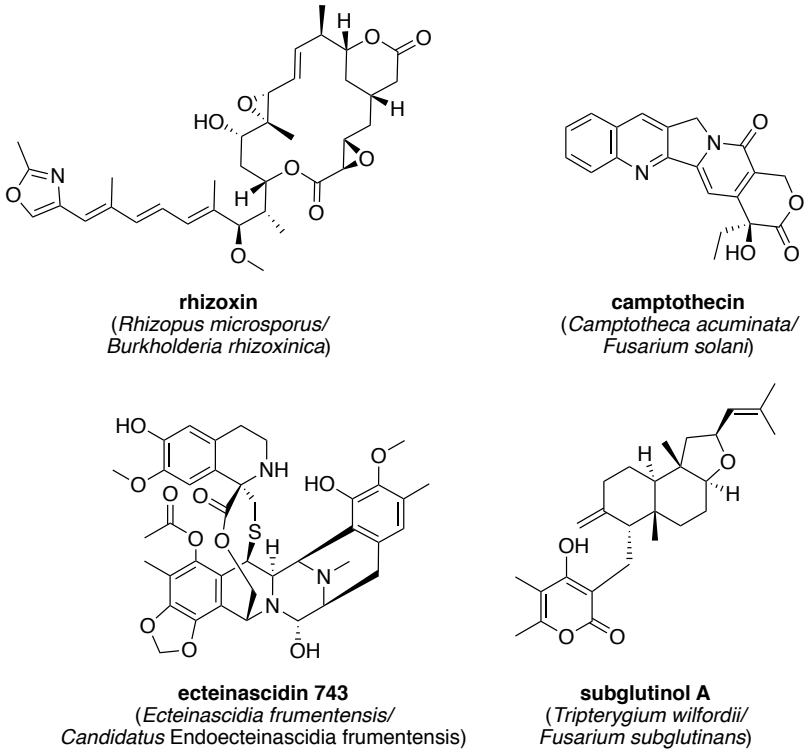

Figure 1.8. Examples of bioactive natural products of endosymbiotic origin (the host organism and the microbial endosymbiont source are listed in parenthesis)

While endosymbionts have proven to be a promising source for the discovery of novel secondary metabolites with interesting bioactivities, many suffer from an inability to be easily cultured under laboratory conditions. In some cases, this is believed to be due to the fact that these organisms are in such a close relationship with their host organism that they have diminished capacities for independent survival.[52] Many obligate endosymbionts have undergone reduction in their genomes as a result of sustained, close relationships, and as such, are unable to survive outside of their hosts.[54-55] The inability to culture many symbiotic organisms provides an obstacle to the study of these symbiotic assemblages and has led to a gap in our knowledge of the secondary metabolites that they are capable of producing. To fill this gap, efforts have gone into the genomic analysis of these organisms as well as the use of novel host cell culture tools to enable their growth

in laboratory settings.[56-57] As more effort is put into the study of these organisms, we may ultimately benefit from the discovery of new bioactive secondary metabolites from these species.

In addition to bacterial endosymbionts, many plant species contain endosymbiotic fungi, which collectively are known as endophytic fungi. Overall, it is believed that nearly every plant on earth may contain at least one species of endophytic fungus, and that this subset of fungi may comprise one million different species.[58-59] A subset of these organisms have been studied with regard to their production of bioactive secondary metabolites, which include compounds such as paclitaxel from *Taxomyces andreanae*, camptothecin from *Fusarium solani*, and subglutinol A from *Fusarium subglutinans* (Figure 1.8).[60-61] Despite the wealth of species belonging to the fungal endophytes, there is an overall lack of characterization of these endophytes, leaving a tremendous opportunity for the discovery of new fungal species within plants. As such, these endophytic fungi may present an additional area that is currently underexplored but may yield promising new secondary metabolites with interesting bioactivities.

1.6 Prospects for Natural Product Discovery and Future Opportunities

While the pharmaceutical industry has largely abandoned the pursuit of discovering new bioactive natural products to fuel their drug development efforts, the structures of these compounds continue to serve as inspiration with about 35% of clinically approved drugs being made through either semisynthetic modifications of a natural product or total synthesis of compounds with pharmacophores found in natural products.[28] Additionally, this decline in interest in natural product drug discovery led to

an overall decline in the number of clinically approved drugs.[29] Therefore, I believe that academic research groups will need to play a larger role to maintain this field and support industrial drug development.

Recent advances in DNA sequencing and synthetic biology will also play larger roles in natural product drug discovery. These technologies are proving to be useful tools in the discovery of new natural products that were previously not accessible through traditional means and are the basis for many new pharmaceutical startups.[39, 62-64] Additionally, advances in culture techniques such as the iChip technology used in the discovery of the new antibiotic teixobactin[65] may also play a prominent role in increasing the numbers of organisms that we will be able to investigate for their production of new natural products.

From the standpoint of structure elucidation, which is a vital part of natural product drug discovery, I believe that advances are being made with respect to traditional methods such as NMR spectroscopy, but also in the development of new methods that may improve the speed and accuracy with which structures of these complex molecules are determined. One such technology that is gaining attention is that of electron diffraction, which has allowed for the determination of structures from microcrystalline materials using a cryo-electron microscope.[66-67] As this technology becomes more widely used, I believe that it will be a powerful technique for determining the structures of natural products and may serve as a viable alternative to x-ray diffraction experiments when adequate crystals cannot be obtained.

Chapter 2: Chapter Overviews

2.1 Overview of Graduate Research, Development and Accomplishments

As a graduate student, my research focused very heavily on the purification and subsequent identification of fungal natural products with interesting bioactivities. As this discipline relies heavily on separations and spectroscopic techniques, I was able to master a variety of laboratory techniques including column chromatography, high-performance liquid chromatography (HPLC), mass spectrometry (MS), circular dichroism (CD) spectroscopy, vibrational circular dichroism (VCD) spectroscopy, nuclear magnetic resonance (NMR) spectroscopic experiments (1D and 2D), as well as computational calculations of CD, VCD, and NMR spectra using computational chemistry software packages. However, as our laboratory is also very cross disciplinary in nature, I was able to gain exposure and experience to other methods such as microbiology techniques, assay development, computational calculations of thermodynamic properties and reaction pathways, and organic synthesis. Therefore, I believe that my experience as a graduate student has made me very well rounded and better able to work with individuals from backgrounds differing from my own.

In addition to the technical skills gained through this experience, I have also gained many more soft skills. Time-management was a key skill in my graduate studies as I worked on a total of twenty projects, many of which were abandoned due to difficulties in pursuing the compounds that were purified for further study. Thus, being able to recognize that these projects were potentially difficult to move forward in the early stages was key. In addition to time-management, I believe that the experience of graduate school has led me to be a better communicator of my work. It has given me the

opportunity to present my research not only to the other members of my laboratory in the form of group meetings, but also to my colleagues in the department through colloquium presentations, and to other academic researchers through a poster presentation at the American Society of Pharmacognosy's annual meeting.

As science is often a collaborative exercise, bringing in expertise from an assortment of backgrounds, much of the work presented in this dissertation is a result of collaboration with others. Therefore, each chapter will begin with a statement that clearly describes the contributions of others as well as my own contributions to the work being presented.

2.2 Chapter 3. Creation of a High-Throughput, High-Content Screening Assay for the Human Parasite *Trichomonas vaginalis*

In Chapter 3, I discuss the investigation of compounds that have potential application in the treatment of *T. vaginalis* infections. In this work, a new bioassay was developed to allow for high-throughput screening of our fungal extract library in *T. vaginalis* and Ect1/E6E7 human cervical epithelial cells. Screening of our fungal extract library resulted in the identification of two fungal isolates belonging to the species of *Fusarium solani* and *Humicola grisea* that exhibited selective inhibition of the parasite *T. vaginalis*. Further studies of the resulting bioactive secondary metabolites as well as structurally related compounds that were purchased or synthesized led to the development of new insights and counter screens to effectively eliminate compounds such as quinones that are notorious pan-assay interference compounds (PAINS) with indiscriminate activities.

2.3 Chapter 4. Natural-Product-Inspired Compounds as Countermeasures Against the Liver Carcinogen Aflatoxin B_1

In Chapter 4, the investigation of compounds with potential aflatoxin B_1 (AfB_1) toxicity mitigating effects is discussed. In these studies, a new bioassay was developed to allow high-throughput screening of fungal and bacterial extract libraries for extracts that afforded protection to HepG2 human hepatocellular carcinoma cells against the toxic effects of the mycotoxin AfB_1. Screening of our fungal extract library led to the identification of a fungal isolate of the species *Alternaria alternata*, whose crude extract showed strong protection of HepG2 cells in the presence of AfB_1. Isolation of the bioactive compounds was followed by identification of other active secondary metabolites from our laboratory's pure compound repository and synthesis of structurally related compounds. To better approximate human physiological conditions, these compounds were also tested using HepG2 spheroids, which were significantly more sensitive to AfB_1 exposure. In HepG2 spheroids, we found that compounds often exhibited protective effects with much greater potency.

2.4 Chapter 5. *In Situ* Ring Contraction and Transformation of the Rhizoxin Macrocycle through an Abiotic Pathway

Finally, Chapter 5 will discuss the isolation and investigations into the formation of a rhizoxin analog with a novel scaffold. In this work, a crude extract from the symbiotic system composed of the fungus *Rhizopus microsporus* and bacterium *Burkholderia rhizoxinica* exhibited potent anticancer activity that was selective for Ewing

sarcoma cell lines when tested in a panel of pediatric cancer cell lines. Bioassay-guided fractionation led to the isolation of five analogs of the known compound rhizoxin. Structure elucidation of these analogs was accomplished through the use of NMR spectroscopy experiments in conjunction with computational calculations of NMR parameters (chemical shifts and coupling constants). While rhizoxin exhibited the potent and selective anticancer activity observed in the crude extract, the five new analogs were significantly less potent than rhizoxin.

Despite the lack of strong bioactivity, one analog was interesting from a structural standpoint as it contained a 15-membered macrolactone core that was previously unreported in this class of compounds. As a result, further work was performed to determine the mechanism through which this compound formed. While studying alternative culture conditions to increase yields of these new secondary metabolites, it was observed that formation of these compounds occurs only under mildly acidic media conditions. As a result, further investigations including degradation and computational studies were performed to identify the mechanism of formation of this compound.

Chapter 3: Creation of a High-Throughput, High-Content Screening Assay for the Human Parasite *Trichomonas vaginalis*

This chapter was adapted from a manuscript that is currently being prepared for submission in 2018. The authors of that manuscript are Jarrod King, Adam C. Carter, Wentao Dai, Jin Woo Lee, Yun-Seo Kil, Lin Du, Sara Helff, Brandt Huddle, and Robert H. Cichewicz.

The work presented within this chapter was conducted as follows: Jarrod King performed preliminary work related to assay development and conducted bioassays; Sara Helff performed isolation of fungal isolates and large-scale fermentations; Adam C. Carter performed extractions, purifications of secondary metabolites, structure elucidation, and organic synthesis of select quinones

3.1 Introduction

Trichomonas vaginalis is the most commonly encountered sexually transmitted parasite in the United States.[68] Individuals who are infected by this parasite are at an increased risk of (i) miscarriage and low preterm birth weight, (ii) HIV transmission, (iii) susceptibility to cervical cancer, and (iv) infertility.[69] Treatment of *T. vaginalis* infections typically involves the use of antiprotozoal nitroimidazoles (i.e., metronidazole and tinidazole), which are reported as having high levels of efficacy in the clinic (typically >90% of infections are cleared after a single course of treatment).[70-72] However, there are concerns that, in addition to their reported side effects (e.g. nausea and vomiting), this class of drugs may exhibit carcinogenic and mutagenic effects, which leads to concerns regarding their use during pregnancy, as well as general concern regarding these potential

effects on the general population.[73-74] Additionally, patients who receive treatment with nitroimidazoles experience high rates of recurrent and persistent infections, which have been reported to range from 5-31% in women.[72] While many of the recurrent cases of *T. vaginalis* infections can be linked to continued contact with untreated sexual partners, persistent infections have led to concerns regarding the limitations of current nitroimidazole treatment options.[75] Specifically, as many as 9.6% of clinical *T. vaginalis* isolates have been found to exhibit resistance to nitroimidazole drugs.[76-77] Together, these factors showcase the current drawbacks of nitroimidazole therapies and the potential threat that *T. vaginalis* poses to human health as drug-resistance in this parasite becomes more widespread and severe.

Despite this rising threat, little information has been published, to date, regarding endeavors to identify alternative treatment options for *T. vaginalis* infections. Some of these studies have focused only on plant extracts,[78-81] and as a result, uncover little regarding the molecules responsible for the anti-trichomoniasis activities observed. In a few cases, however, studies of plant extracts have led to the discovery of molecules showing anti-trichomoniasis activity such as berberine,[82] (-)-usnic acid,[83] emodin,[84] hamycin,[85] hederagin,[86] and mulinolic acid,[87] all of which lack the potency and selectivity observed for metronidazole. While there are numerous studies focusing on natural product based discovery in plants, there is an overall lack of investigations into other sources for molecules that exhibit activity against *T. vaginalis*.[88-89] While this perceived lack of research that pertains to the examination of natural sources for leads to fight *T. vaginalis* infections is worrisome, it does indicate the potential opportunities that exist to find new bioactive natural products that could potentially be developed into clinically

useful agents. As nature has been an exceptional source of new antiinfectious agents in the past,[28] including the chief antiparasitic compounds that are currently used in the clinic (e.g., avermectins and artemisinin),[28, 90] this expectation is very reasonable.

In addition to the shortage of published screening efforts to find secondary metabolites with anti-*Trichomonas* activities, there have been few reports regarding dependable assay methods for the discovery of new inhibitors of *T. vaginalis*. The methods that have been previously reported typically utilized either microscopic evaluation of trichomonads[91] or dyes such as resazurin and propidium iodide,[92-93] which suffer from incompatibilities with high-throughput screening or lack the sensitivity to detect low numbers of live trichomonads.[94] With this overall lack of high-throughput screening efforts to find new fungal secondary metabolites with antitrichomonal activity, our team focused on developing a new assay system that was capable of (i) identifying antitrichomonal compounds, (ii) high-throughput screening of samples, (iii) could reliably distinguish between complete and partial inhibition of *T. vaginalis*, and (iv) could be utilized in the evaluation of a variety of sample types ranging from natural product extracts to pure compounds. In this work, we report the results of this assay development program, describe a group of natural products that exhibit inhibitory activities against *T. vaginalis,* and describe efforts made to probe their selectivity.

3.2 Results and Discussion

3.2.1 Development of an Assay for Detecting *T. vaginalis* Inhibitors

Colorimetric assays using resazurin dyes are used extensively to screen for bioactive compounds that inhibit cell viability and proliferation in both aerobic and

anaerobic environments.[95] These assays function through the reduction of the resazurin dye by NADH, yielding the red, fluorescent molecule resorufin. While use of this dye has been reported for detecting *T. vaginalis* inhibitors, we found that this reagent was not as sensitive as desired for detecting live *T. vaginalis*. Under the anaerobic conditions used, we found that a population of ~10,000 trichomonads per well in a 96-well microtiter plate was necessary to consistently detect the presence of live *T. vaginalis*. As we determined that an initial population of 40,000 trichomonads per well was ideal for our screening efforts, this corresponded to an inability to distinguish between parasite-kill rates greater than ~75% (Figure 3.1). As such, we set out to develop a new assay system that was more sensitive than these previously reported resazurin-based approaches, while also maintaining an ability to be used with a variety of substances ranging from pure compounds to natural product extracts that contain fluorescent compounds.

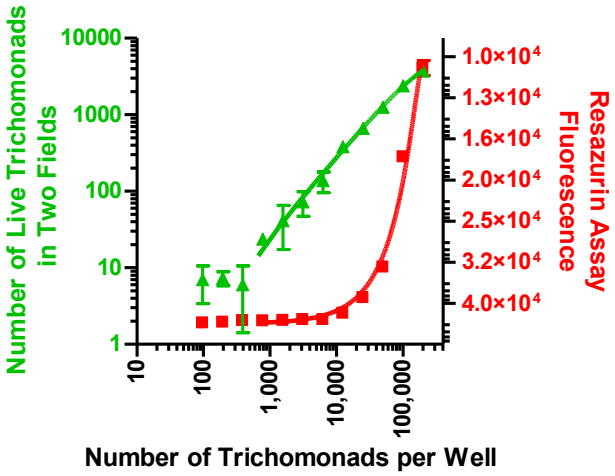

Figure 3.1. A comparison of the traditionally used resazurin fluorescence assay (red squares) and our newly developed imaging-based assay (green triangles). Using two fields per well, we determined the limit of detection of the Operetta to be 1,000 trichomonads per well. This limit of detection arises as a result of whether a trichomonad appears in an image field. The resazurin assay was unable to detect less than 10,000 trichomonads per well.

A method that we believed could be an alternative to the use of resazurin was that of high-content imaging.[96] We hypothesized that this methodology would provide a more sensitive tool to be used in the determination of live/dead-status of every trichomonad in a sample population. However, initial attempts led us to conclude that this approach was not well-suited for detecting live trichomonads as their rapid movement led to severe blurring of each cell, even when reasonably quick exposure times (10 ms) were used. To address this issue, we found that the trichomonads could be fixed through the use of glutaraldehyde, while a dual staining system of acridine orange, which is a cell-permeable DNA stain, and propidium iodide, which is a DNA stain that is not able to permeate live cells, could be used for live/dead determination (Figure 3.2). Using this methodology, in conjunction with the Operetta (PerkinElmer) high-content imaging system, we found that we could detect as few as one live or dead trichomonad per image field (Figure 3.2), and the assay was reliable with a calculated Z-factor of 0.92. In addition to this sensitivity, we found this system to be well suited for high-throughput screening of *T. vaginalis* viability, while also offering the ability to store image files (i.e., two image fields recorded per well) for manual inspection to eliminate false-positive and false-negative hits arising from the presence of UV/VIS-active secondary metabolites.

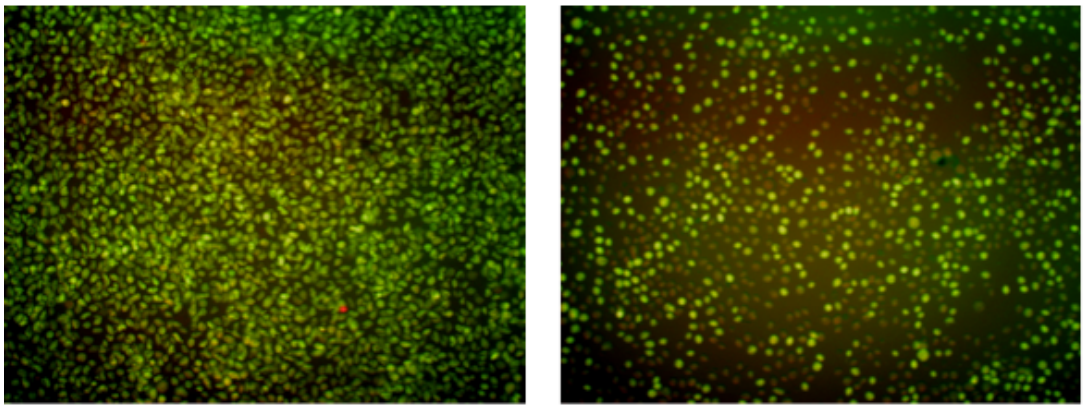

Figure 3.2. (Left) Sample field from the Operetta of a fixed and stained (0.5% glutaraldehyde, 2.5 μM propidium iodide, and 2.5 μM acridine orange) population of healthy and growing *T. vaginalis* after 17 hours incubation. One dead trichomonad (red) can be seen. (Right) Sample screening image from the Operetta showing partial inhibition due to a fungal extract after 17 hours incubation.

3.2.2 Testing Purified Natural Products

To evaluate the capabilities of the newly developed *T. vaginalis* imaging-based assay, we first tested a library of chemically diverse natural products consisting of 430 metabolites from marine organisms, plants, bacteria, and fungi. Initially, these compounds were screened at a single high-dose concentration (100 μM) to allow for the evaluation of challenging screening scenarios involving potential false-positives or false-negatives as a result of compound precipitation and UV/VIS-interference. This imaging-based assay proved to be extremely helpful, as all potential hits (i.e., compounds that provided inhibition greater than the 25 μM metronidazole control) could be inspected visually to confirm that the number of live trichomonads had been reduced. This preliminary screening led to the identification of 64 natural products that exhibited activities better than or equal to that of the metronidazole control. As this set of pure compounds largely was composed of bioactive substances that had previously exhibited cytotoxicity toward mammalian cells and/or inhibited the proliferation of

microorganisms, the large number of hits observed did not surprise us. However, these results also indicated the need for a mammalian-cell-based cytotoxicity counter screen to be used to eliminate any undesirable non-specific cellular toxins. To further narrow the list of natural products, the 64 hit compounds were screened at 25 μM, leading to a subset of 9 compounds with bioactivities comparable to 25 μM metronidazole. These nine compounds were then tested over a range of concentrations (0.25-25 μM) against both *T. vaginalis* as well as a normal mouse fibroblast NIH/3T3 cell line. From this data, the LC_{50} values for each compound with respect to the parasite and the mammalian cells were estimated. The LC_{50} values were then used to calculate a selectivity index (SI) value [SI_{3T3} = (LC_{50} for 3T3 cells)/(LC_{50} for *T. vaginalis*)] for each of the active natural products (Figure 3.3). While the SI_{3T3} values revealed that most of the natural products identified were non-selective inhibitors, one compound of note was 2-bromoascididemin, which was found to have slight selectivity (SI_{3T3} = 14) (Figure 3.3). Thus, we were encouraged that the newly developed assay was capable of testing structurally diverse natural products across a wide range of concentrations and could be used to measure each compound's ability to selectively inhibit the parasite species being targeted.

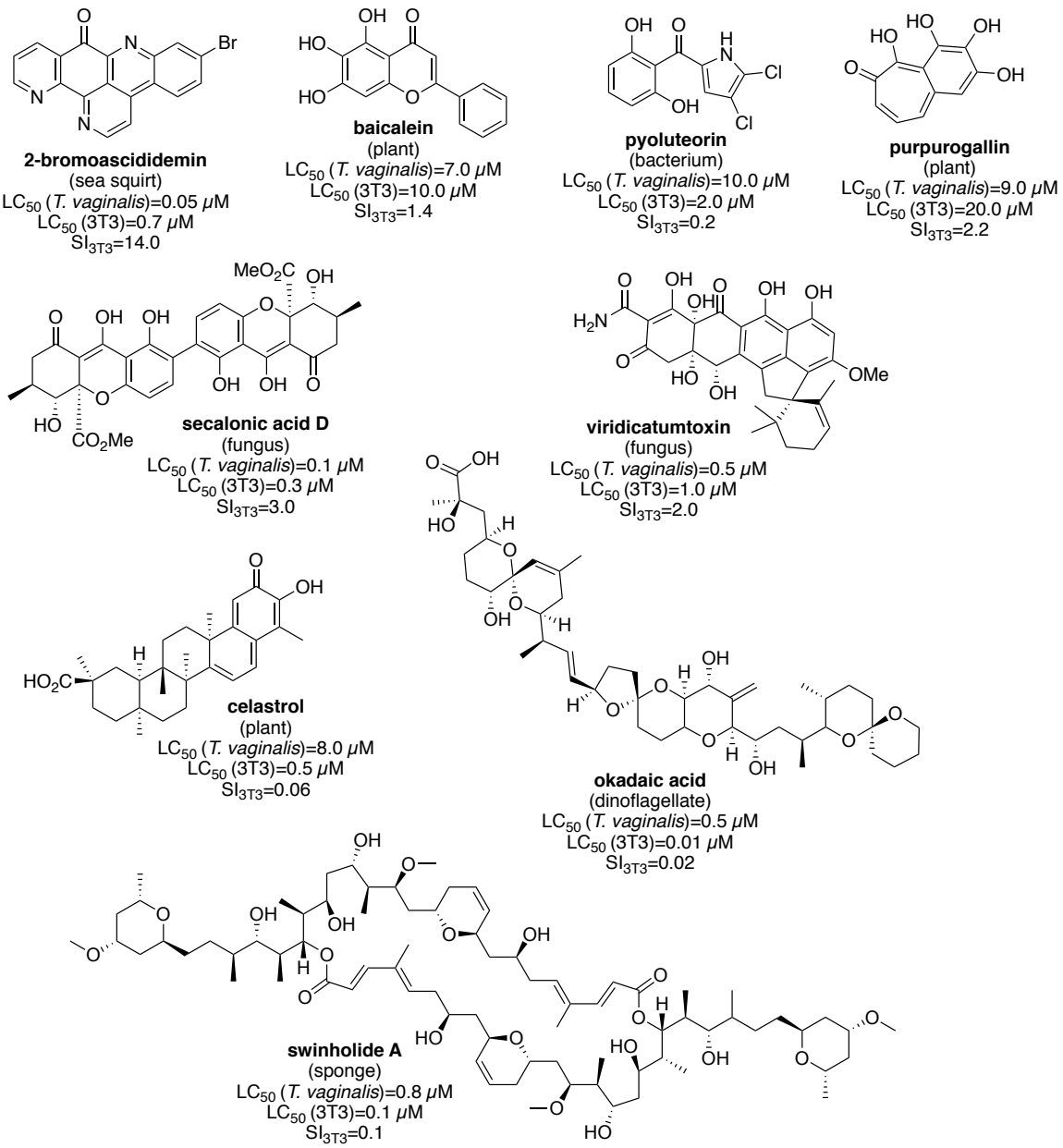

Figure 3.3. Nine pure natural products evaluated for SI_{3T3} values in initial pure compound screening against *T. vaginalis*. Compound sources were diverse and are shown under the compound names. LC_{50} values were determined in *T. vaginalis* and 3T3 mammalian cells to obtain the SI_{3T3} values shown. Notably, 2-bromoascididemin exhibited a SI_{3T3} value of 14.0, which was much higher than any of the other compounds tested.

3.2.3 Testing Fungal Natural Product Extracts

At the University of Oklahoma, the Natural Products Discovery Group has generated a library of over 50,000 fungal extracts that consist of the organic residue remaining after a fungal isolate is cultured for four weeks on Cheerios breakfast cereal, extracted with ethyl acetate, and partitioned against water. A set consisting of 1,748 of these fungal extracts were tested using our newly developed high-content imaging assay system. Initially, each extract was tested in duplicate at a concentration of 15 μg/mL, resulting in a total of 111 hits, which were defined as having equal or greater inhibition of *T. vaginalis* compared to metronidazole tested at a concentration of 25 μM. These 111 hits were then tested over a range of concentrations (0.15-15 μg/mL), resulting in a total of 71 samples that maintained potent anti-*Trichomonas* activity and showed sigmoidal dose-response curves. The LC_{50} value for each of these extracts against *T. vaginalis* was determined, along with LC_{50} values obtained for each in an Ect1/E6E7-cell-line cytotoxicity counter screen. These values were plotted as shown in Figure 3.4, enabling us to prioritize extracts with favorable SI_{Ect1} values. These extracts are those that exhibited both potent antiparasitic activity and low mammalian cytotoxicity, corresponding to points found in the upper right quadrant of Figure 3.4. Accordingly, we chose to proceed with a *Fusarium solani* isolate (plate 55 well F11; SI_{Ect1}=36) and *Humicola grisea* (plate 78 well A3; SI_{3T3}=25).

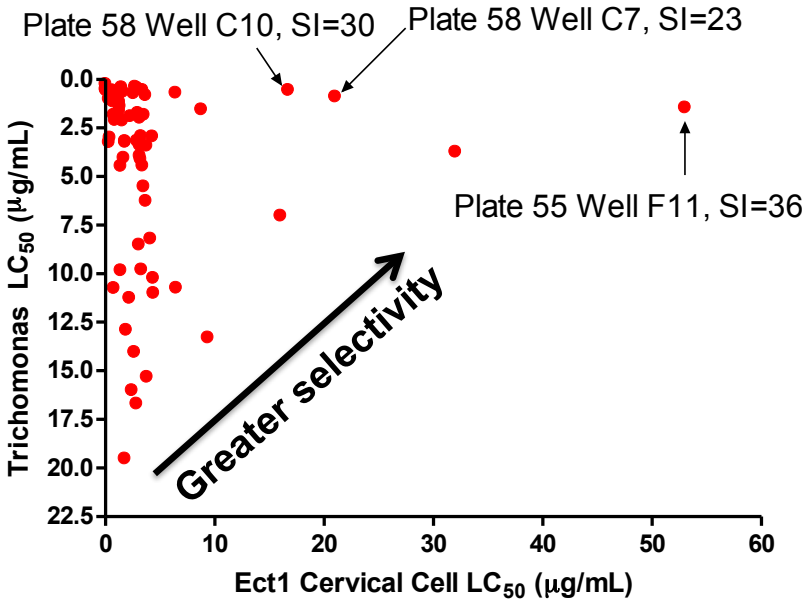

Figure 3.4. Selectivity indices of 71 fungal crude extract library hits with activity exceeding that of 25 µM metronidazole. All hits indicated with arrows were later found to be strains of the species *Fusarium solani.* The isolate corresponding to plate 55 well F11 (internal strain designation Tree 400 EW+PNGP-3) was grown in large scale to yield active compounds **1**-**2**.

3.2.4 Bioassay-Guided Purification of Natural Products from a *F. solani* Isolate

The isolate of the fungus *F. solani* that was responsible for the fungal extract showing the greatest SI_{Ect1} value was grown on Cheerios breakfast cereal supplemented with a 0.3% sucrose solution with 0.005% chloramphenicol for a total of four weeks. The *F. solani* fungal extract was subjected to bioassay-guided fractionation using silica gel vacuum liquid chromatography (VLC), HP-20SS VLC, and C_{18} HPLC, yielding three known quinone-containing natural products: fusarubin (**1**) (1.5 mg),[97] javanicin (**2**) (1.8 mg),[98] and solaniol (**3**) (3.0 mg)[99] (compounds were identified based on comparisons of experimental LC-ESIMS and NMR data to published data) (Figure 3.5).[100-101] These three metabolites exhibited a range of potencies against *T. vaginalis*, with **1** and **2** having the

greatest potencies (LC_{50} values of 2.5 μM and 1.3 μM, respectively), while **3** showed greatly reduced activity (LC_{50} of 40 μM). However, compound **1** notably also exhibited an SI_{Ect1} value of 30, which greatly exceeded the SI_{Ect1} values for **2** and **3**, which were determined to be 3.1 and 0.4, respectively. These results suggested that changes to the quinone-containing scaffolds might result in dramatic alterations in the activities of structurally similar molecules.

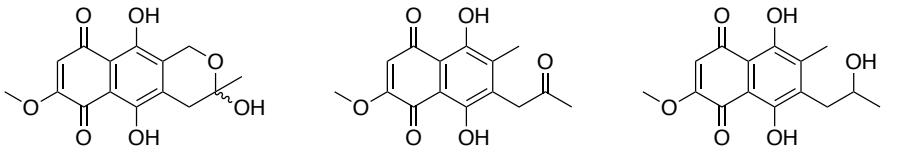

Figure 3.5. Structures of isolated secondary metabolites **1-3** from *Fusarium solani*. LC_{50} values for each compound against *T. vaginalis* and Ect1 mammalian cells are also listed, as well as their calculated SI_{Ect1} values.

3.2.5 Structure-Activity Relationship Study of Quinones

Our previous observation with quinone-containing secondary metabolites **1-3** prompted us to test an additional 38 natural and synthetic quinone-containing compounds (compounds **4-41**, Appendix A) to determine if other selective *T. vaginalis* inhibitors could easily be identified. Although many of these compounds exhibited low-to-mid-micromolar inhibition of *T. vaginalis* viability, none of the additional compounds tested showed an SI value comparable to metabolite **1** (SI_{Ect1} values ≤4.5). The most promising of these hits are summarized in Figure 3.6. Interestingly, we observed a poor SI_{Ect1} value of <0.1 for the clinically available antiparasitic drug atovaquone (**33**).[102-103] A lack of a clear relationship between the structure of the quinones tested and their activity as well as

the fact that none showed as great of an SI_{Ect1} value as **1** led us to reevaluate quinone-containing compounds as viable candidates for inhibitors of *T. vaginalis*.

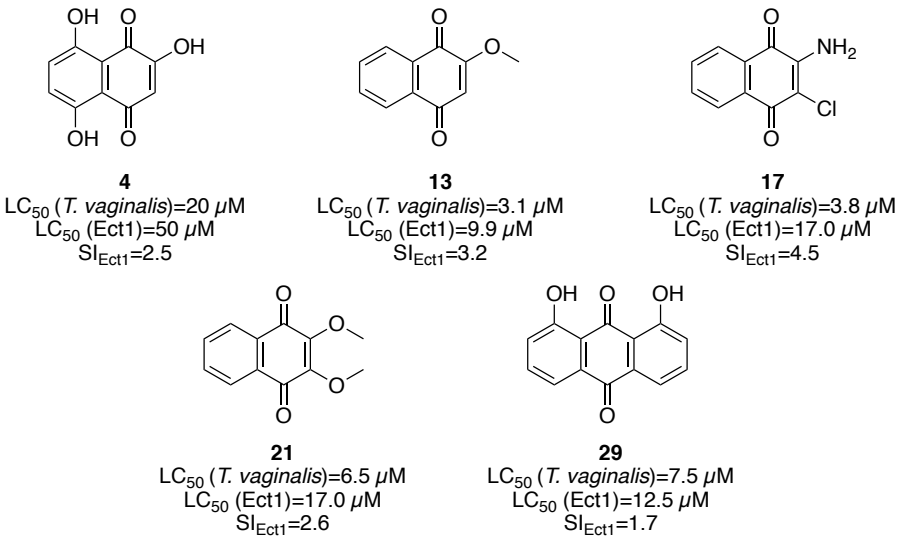

Figure 3.6. Structures and biological activity of synthetic and commercially available quinone-containing compounds with SI_{Ect1} values calculated to be greater than 1. LC_{50} values for each compound in *T. vaginalis* and Ect1 cells are listed.

As quinones have a tendency to be redox-active and act as electrophiles toward nucleophilic amino acid residues of proteins, these compounds are typically classified as having indiscriminate reactivity (i.e., PAINS).[104] As such, we next investigated the possibility of redox cycling as the mechanism of action for compound **1**. Dose-response curves were generated for 2-methoxynaphthazarin (**5**), compound **1**, and metronidazole under three different levels of oxygen (anaerobic, microaerophillic, and aerobic). Compound **5** was selected due to its structural similarity to compound **1**. In comparing the activities of **1** and **5** to metronidazole under these varying oxygen conditions, **1** lost its potency when incubated under anaerobic conditions (Figure 3.7). As *T. vaginalis* is typically encountered in low-oxygen environments, this loss of potency is detrimental,

and this compound was not pursued further. Metronidazole, on the other hand, maintained an LC_{50} that was relatively constant over the wide range of oxygen concentrations tested.

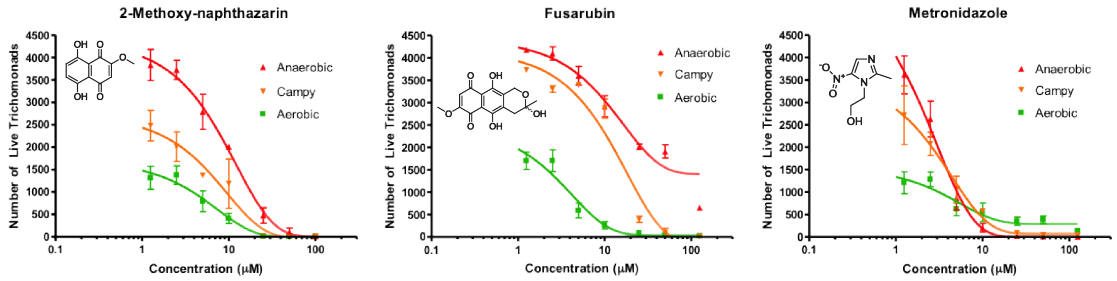

Figure 3.7. Bioactivity of compounds **1**, **5**, and metronidazole against *T. vaginalis* in atmospheres of varying oxygen levels. Numbers shown are calculated from two fields in each well, three replicate wells per condition. Notably, potency of **1** and **5** decreases as oxygen level decreases, while metronidazole maintains approximately the same level of potency under all conditions tested.

3.2.6 Bioassay-Guided Purification of Natural Products from a *Humicola grisea* Isolate

An isolate of the species *Humicola grisea* was grown on Cheerios breakfast cereal supplemented with a 0.3% sucrose solution containing 0.005% chloramphenicol for four weeks. The fungal extract was subjected to bioassay-guided purification using silica gel VLC, HP20SS VLC, and C_{18} HPLC, yielding the known xanthone-anthraquinone dimer xanthoquinodin A1 (**42**) (52.2 mg) as confirmed by comparison of its ^{1}H and ^{13}C NMR spectra, LC-ESIMS data, and specific rotation to values found in the literature.[105] Compound **42** was evaluated for *T. vaginalis* inhibitory activity and counter-screened against Ect1/E6E7 cells, yielding a favorable SI_{Ect1} value of about 20. As we had previously encountered issues with quinone-containing compounds, **42** was tested under

varying levels of oxygen as done previously for compound **1**. As a result of this testing, we found that **42**, unlike **1**, retained its potency under anaerobic conditions (average LC_{50}=3 μM), suggesting that this compound functioned in a manner that was different from the other metabolites that were prone to redox-transformations under assay conditions and spurring further interest in this compound as a potential lead for further work.

3.2.7 Reduction of Xanthoquinodin A1

To further evaluate the inhibitory activity of compound **42** on *T. vaginalis*, we set out to reduce the molecule using a sodium borohydride reduction. Compound **42** was treated with sodium borohydride in methanol and allowed to react such that one of the carbonyls present on the molecule was reduced to the corresponding secondary alcohol **43.** Following the reaction, analysis of the ^{13}C NMR spectrum revealed the loss of a carbonyl chemical shift when compared to the spectrum of **42** with a corresponding addition of a new spin at ∂_C 71.9 ppm. Follow-up HSQC and HMBC experiments [e.g., correlation from H-10' (5.04 ppm) to C-13 (30.5 ppm)] and ROESY (e.g., cross-peak observed between H-10' and H-4' (6.47 ppm)) confirmed that the C-10' carbonyl in **42** was stereospecifically reduced to an alcohol yielding a single isomer as the product **43**.

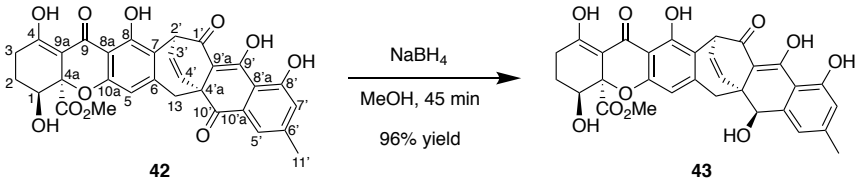

Scheme 3.1. Chemical structure of natural product **42** obtained from a *Humicola grisea* isolate and its reduction through the use of sodium borohydride to yield the secondary alcohol **43**.

Compound **43** was tested for activity against *T. vaginalis* and was found to be equally potent to compound **42** (LC_{50} of approximately 3 μM, Figure 3.8). This observation led us to conclude that the anthraquinone moiety of **42** is not essential for its *T. vaginalis* inhibition and does not appear to act through a non-specific redox pathway.

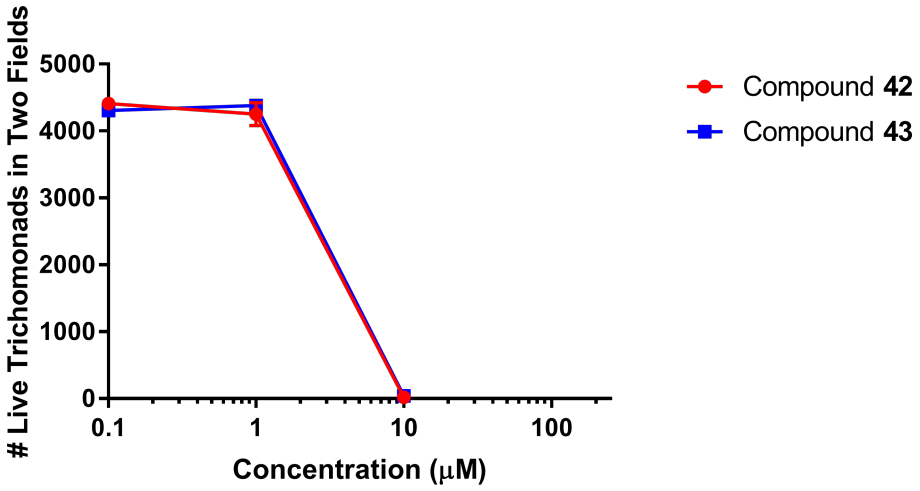

Figure 3.8. Comparison of anti-trichomoniasis activity of **42** and **43** under anaerobic conditions. Numbers shown are calculated from two fields in each well, three replicate wells per concentration tested. Error bars are equal to 1 S.D. (n=3).

3.2.8 Counter-Screen with *Lactobacillus acidophilus.*

While the antitrichomonal activity of compound **42** appeared to be encouraging, it was unclear whether this compound could adversely affect a person's native vaginal microflora, since further disrupting the microbiome can be detrimental to patient recovery after antibiotic treatment.[106] For this reason, we tested compound **42** against *Lactobacillus acidophilus* as this bacterium is representative of desirable vaginal microflora species.[107] Unfortunately, compound **42** showed nearly equal potency against *L. acidophilus* compared to *T. vaginalis*, while metronidazole showed no inhibition of the

bacterium. As a result, **42** was dropped from further testing with the hope of finding a natural product lead that would not be expected to adversely affect vaginal microflora.

3.2.9 Conclusions and Discussion

A quick and sensitive assay for *T. vaginalis* was developed and used to screen a range of substances from pure compounds to complex fungal extracts. By screening a portion of our library of fungal extracts, we were able to isolate and identify pure natural products that exhibit selective activity in *T. vaginalis* with respect to Ect1/E6E7 human cells. Compounds containing quinones were found to interfere with the *Trichomonas* assay, which is in agreement with their reputation as compounds with indiscriminate reactivity. By testing compounds belonging to this class in variable oxygen atmospheres, we were able to remove many quinone-containing compounds from further consideration. Additional screening against *L. acidophilus*, which is typically found in the female reproductive tract, allowed us to further refine the quality of lead compounds by adding an additional requirement that compounds selectively kill *T. vaginalis*, while not disrupting the bacterial flora naturally present in the reproductive tract. As quinones were a prominent class of compounds found in our initial screening efforts for this assay, appropriate caution should be taken when deciding to pursue these compounds for anti-trichomoniasis activity in the future.

3.3 Materials and Methods

3.3.1 General Experimental Procedures

Optical rotation measurements were made on an AUTOPOL® III automatic polarimeter. The LC-ESIMS analyses were performed on a Shimadzu UFLC system with a quadrupole mass spectrometer using a Phenomenex Kinetex C_{18} column (3.0 mm × 75 mm, 2.6 μm) and MeCN-H_2O (0.1% HCOOH) gradient solvent system. NMR spectra were obtained on Varian spectrometers (500 or 400 MHz for ^1H and 100 or 125 MHz for ^{13}C) using $CDCl_3$ (Cambridge Isotope Laboratories, Inc.) as solvent. Column chromatography was performed using silica gel and Diaion® HP-20SS. HPLC was performed on a Waters system equipped with a 1525 binary HPLC pump coupled to a 2998 PDA detector with a Phenomenex C_{18} column (21.2 × 250 mm or 10 × 250 mm, 5 μm particle size). Commercially available compounds tested in assays were obtained from Sigma-Aldrich, TCI, Alfa-Aesar, Santa Cruz Biotechnology, ICC, EMD, Fluka, Selleckchem, Biovision, or the National Cancer Institute.

3.3.2 Culture of Organisms

Trichomonas vaginalis Donne (PRA-98) were purchased from the American Type Culture Collection (ATCC, Bethesda, MD). They were grown in Keister's Modified TYI-S33 medium[108] with pH adjusted to 6.0 for optimal growth. Only Sigma B8381 bovine bile resulted in successful execution of assays. Trichomonads were propagated at 37°C in sealed screw cap vials. All 96-well plate assays were performed in an air incubator (21% O_2, 0.04% CO_2), candle jar (10% O_2, 5% CO_2), with BD GasPak EZ Campy sachets (6-16% O_2, 2-10% CO_2), or with EZ Anaerobe sachets (<1% O_2, >13% CO_2), depending on

the oxygen levels being tested. Ideal growth of trichomonads is achieved with added carbon dioxide as it acts to stimulate *T. vaginalis* growth.[109]

NIH/3T3 (CRL-1658) mouse fibroblast and Ect1/E6E7 (CRL-2614) human ectocervical cell lines were purchased from ATCC. NIH/3T3 cells were maintained using Dulbecco's Modified Eagle's Medium with 5% FetalClone III (Hyclone). Ect1/E6E7 cells were maintained in either keratinocyte-serum free medium (K-SFM, GIBCO-BRL 17005-042) or Roswell Park Memorial Institute (RPMI) 1640 medium supplemented with 5% FetalClone III and epidermal growth factor (EGF) (10 ng/mL, Novoprotein #C029).

Lactobacillus acidophilus (ATCC 4356) were purchased from ATCC and grown on de Man, Rogosa & Sharpe (MRS) agar and broth at 37°C under anaerobic conditions using BD GasPak EZ Anaerobe sachets.

3.3.3 *Trichomonas vaginalis* Assays

A 250 µL aliquot of *T. vaginalis* that had been cryopreserved in a 5% DMSO solution and stored in liquid N_2 was rapidly thawed at 37°C and added to a screw cap tube containing 12 mL of Modified TYI-S33 medium that had been warmed to 37°C previously. Following incubation for 24 hours, live trophozoites were counted, typically yielding greater than 30 million trophozoites per tube. A total of 100 µL of TYI-S33 medium containing 40,000 trophozoites was added to each well of a 96-well plate. Using a pin tool or pipet tip, extracts or pure compounds dissolved in dimethyl sulfoxide (DMSO) were added to appropriate wells. As controls, DMSO and 25 µM metronidazole were also tested. If testing in candle jar conditions, plates were placed into a humidified

candle jar, the candle was lit, and the lid was sealed. The jar was then placed into a 37°C incubator and allowed to incubate for 17 hours. If testing in anaerobic conditions, BD GasPak instructions were followed and plates were incubated in either the provided pouch or the BD Anaerobe Container System.

After 17 hours of incubation, plates were removed from the incubator and 100 µL of room temperature *Trichomonas* and *Giardia* assay and fixation (TGAF) solution was added to each well. TGAF solution is composed of 1% glutaraldehyde, 5 µM propidium iodide, and 5 µM acridine orange HCl salt in phosphate-buffered saline (PBS). Plates were then shaken in a plate reader for 30 seconds to break up any aggregations of trichomonads and placed in the incubator for three hours to allow enough time for proper staining and fixation. The plates were then quantitatively imaged using the PerkinElmer Operetta with the Harmony 3.5.1 software package. Quantitation was performed by differentiating live trophozoites, which were green only, from dead trophozoites, which stained green and red. The threshold for propidium iodide was set to 6500 units to allow optimal differentiation between live and dead trophozoites.

As a comparison, traditional resazurin-based assays were performed using the plate reader.[93] For these assays, known numbers of trichomonads were added to each well of a 96-well plate, followed by 10 µL of a resazurin stock (0.1 mg/mL) in PBS. The plates were then allowed to incubate for one hour at room temperature in the dark. After incubation, plates were shaken and analyzed with a fluorescence plate reader (Tecan Infinite M200) using an excitation wavelength of 556 nm and an emission wavelength of 590 nm.

3.3.4 Mammalian Cell Cytotoxicity Assays

Mammalian cell cytotoxicity assays were performed by exposing mammalian cells to DMSO solutions of extracts or pure compounds 48 hours prior to analyzing using either MTT assay[110] or calcein AM and Hoechst 33342 live cell area assay using the Operetta. For the calcein AM/Hoechst 33342 based assay, a 1:5 dilution of a 40 μM calcein AM and 160 μM Hoechst 33342 DMSO solution was prepared in PBS. Aliquots of 5 μL of the diluted solution were then added to each well of the 96-well plate and allowed to incubate for 30 minutes. After incubation, the plates were analyzed using the Operetta and Harmony software package to first detect all nuclei that had been labeled by the Hoechst 33342 dye, followed by determination of cell viability based on green fluorescence. This green fluorescence is a result of acetoxymethyl ester cleavage of calcein AM by intracellular esterases.

3.3.5 *Lactobacillus acidophilus* Viability Assays

L. acidophilus viability assays were performed by first adding a single colony of *L. acidophilus* to 10 mL of MRS broth and vortexing. A 100 μL aliquot of the resulting solution was added to each well of a 96-well plate. Compounds in DMSO were added to the wells such that a final DMSO concentration of 0.05% was achieved. An optical density at 600 nm (OD_{600}) for each well was determined to obtain a baseline value, followed by incubation of the plate for 18 hours at 37°C. After incubation, OD_{600} values for each well were obtained, followed by subtraction of the initial value to determine a change in OD_{600}.

3.3.6 Fungal Procurement and Culture Conditions

A fungal isolate with internal strain designation Tree 400 EW+PNGP-3 was obtained from a soil sample collected from beneath a tree in the Oliver Wildlife Preserve in Norman, Oklahoma. Using internal transcribed spacer (ITS) sequencing data, this isolate was identified as belonging to the species *Fusarium solani*. An additional fungal isolate with internal strain designation Mystery-9 SEA-2 was obtained from a soil sample and identified as belonging to the species *Humicola grisea* based on ITS sequence data.

3.3.7 Isolation of Quinone-Containing Natural Products 1-3

A fungal isolate *Fusarium solani* (internal designation Tree 400 EW+PNGP-3) was grown for four weeks on Cheerios breakfast cereal supplemented with a 0.3% sucrose solution with 0.005% chloramphenicol in three large mycobags (Unicorn Bags, Plano, TX). After four weeks, the fungus was homogenized and extracted using EtOAc. The resulting EtOAc extract (40.4 g) was then separated using silica gel VLC with elution steps consisting of 1:1 hexanes/DCM, DCM, 10:1 DCM/MeOH, and MeOH, resulting in the collection of four fractions, Fractions A-D. The 10:1 DCM/MeOH fraction (Fraction C, 7.8 g) was then further separated using VLC with HP-20SS resin as the stationary phase. The elution steps used consisted of a step gradient of MeOH in water (30%, 50%, 70%, 90%, 100%) and a final 1:1 DCM/MeOH wash, which yielded a total of six fractions, Fractions E-J. Bioassays were performed to assess the anti-trichomoniasis activity of the resulting fractions, indicating that the 90% MeOH fraction (Fraction H) exhibited strong anti-trichomoniasis activity. This fraction was further separated using C_{18} preparative HPLC (21.2 mm × 250 mm, 5 μm) with a MeOH/H_2O

gradient (30:70 to 100:0), followed by isocratic C_{18} semipreparative HPLC (10 mm × 250 mm, 5 μm) with 50:50 MeCN/H_2O (0.1% HCOOH). This resulted in the isolation of three known bioactive naphthoquinones: fusarubin (**1**) (1.5 mg), javanicin (**2**) (1.8 mg), and solaniol (**3**) (3.0 mg).

3.3.8 Further Screening of Purchased and Synthesized Quinones

Compounds **4**-**41** used in this study are shown in Table A.1, Appendix A. The identities of synthesized compounds were confirmed through ^{1}H NMR and comparison to spectroscopic data found in the literature.

3.3.9 Synthesis of Naphthopurpurin (4)

Naphthopurpurin (**4**) was synthesized according to a previously reported protocol.[111] Specifically, 153 mg of naphthazarin (0.80 mmol), dissolved in 45 mL of aqueous potassium hydroxide (2 M), was stirred vigorously and heated to boiling for four hours. The reaction mixture was allowed to cool to room temperature, followed by addition of glacial acetic acid to neutralize the reaction mixture. This was accompanied by a change in color of the solution from purple to red. Following neutralization, the mixture was partitioned with 40 mL of chloroform a total of four times. The aqueous phase that resulted was acidified with the addition of 5 mL of hydrochloric acid (1 M), followed by partitioning with 50 mL of ethyl acetate a total of four times. The organic phases were combined and dried *in vacuo*, yielding compound **4** (130 mg, 78% yield). ^{1}H NMR (400 MHz, $CDCl_3$) 12.74 (s, 1H), 11.47 (s, 1H), 7.34 (d, *J*=9.5 Hz, 1H), 7.21 (d, *J*=9.5 Hz, 1H), 6.37 (s, 1H)

3.3.10 Synthesis of 2-methoxynaphthazarin (5)

2-methoxynaphthazarin (**5**) was synthesized according to a previously reported protocol.[112] More specifically, 120 mg of naphthopurpurin (0.58 mmol), dissolved in 5 mL of absolute methanol, was mixed with 80 µL of hydrochloric acid (12 M) and heated to boiling for four hours. After four hours, the reaction mixture was allowed to cool to room temperature and dried *in vacuo*. The reaction mixture was then purified by silica gel VLC using hexanes, 3:1 hexanes/EtOAc, 2:1 hexanes/EtOAc, 1:1 DCM/MeOH, and MeOH as eluents in a stepwise fashion. From the 3:1 hexanes/EtOAc fraction, compound **5** was obtained (17 mg, 13% yield).

^{1}H NMR (400 MHz, $CDCl_3$) 12.63 (s, 1H), 12.16 (s, 1H), 7.27 (d, *J*=9.5 Hz, 1H), 7.20 (d, *J*=9.5 Hz, 1H), 6.16 (s, 1H), 3.93 (s, 3H)

3.3.11 Synthesis of 1,4-dihydro-5,8-dihydroxy-2-methyl-9,10-anthracenedione (6)

1,4-dihydro-5,8-dihydroxy-2-methyl-9,10-anthracenedione (**6**) was synthesized according to a previously reported protocol.[113] Specifically, 157 mg of naphthazarin (0.83 mmol), dissolved in 5 mL glacial acetic acid, was mixed with 200 µL of isoprene (2.0 mmol) and heated to 70°C for 48 hours. The resulting reaction mixture was cooled and dried *in vacuo*, followed by purification with silica gel VLC. Using 25:1 hexanes/EtOAc as an eluent, a crude mixture of products was obtained. This mixture was dissolved in 5 mL of aqueous potassium hydroxide (2 M) and stirred vigorously for 30 minutes at room temperature. The reaction mixture was then acidified using hydrochloric acid (1 M) and filtered by gravity to give compound **6** (38 mg, 18% yield) as a powder.

^{1}H NMR (400 MHz, $CDCl_3$) 12.54 (s, 1H), 7.21 (s, 2H), 5.55 (m, 1H), 3.25 (m, 2H), 3.14 (m, 2H), 1.82 (s, 3H)

3.3.12 Synthesis of 1,4-dihydro-2-methyl-9,10-anthracenedione (7)

1,4-dihydro-2-methyl-9,10-anthracenedione (**7**) was synthesized according to a previously reported protocol.[113] Specifically, 187 mg of 1,4-naphthoquinone (1.2 mmol), dissolved in 5 mL glacial acetic acid, was mixed with 200 µL of isoprene (2.0 mmol) and heated to 70°C for 48 hours. After 48 hours, 5 mL of water was added to the reaction mixture, which was cooled to 0°C. Filtration of the cooled reaction mixture yielded a crude mixture of products, which was dissolved in 5 mL of aqueous potassium hydroxide (2 M) and stirred vigorously for 15 minutes at room temperature. The reaction mixture was then acidified using hydrochloric acid (12 M) and filtered by gravity to give compound **7** (95 mg, 35% yield) as a powder.

^{1}H NMR (400 MHz, $CDCl_3$) 8.07 (m, 2H), 7.69 (m, 2H), 5.54 (m, 1H), 3.23 (m, 2H), 3.12 (m, 2H), 1.80 (s, 3H)

3.3.13 Isolation of Xanthoquinodin A1 (42)

A fungal isolate *Humicola grisea* (internal designation Mystery-9 SEA-2) was grown for four weeks on Cheerios breakfast cereal supplemented with a 0.3% sucrose solution with 0.005% chloramphenicol in three large mycobags (Unicorn Bags, Plano, TX). After four weeks, the fungus was homogenized and extracted using EtOAc. The resulting EtOAc extract (57.5 g) was then separated using silica gel VLC with elution steps consisting of 1:1 hexanes/DCM, DCM, 10:1 DCM/MeOH, and MeOH, resulting in

the collection of four fractions, Fractions A-D. The 10:1 DCM/MeOH fraction (Fraction C, 8.0 g) was then further separated using VLC with HP-20SS resin as the stationary phase. The elution steps used consisted of a step gradient of MeOH in water (30%, 50%, 70%, 90%, 100%) and a final 1:1 DCM/MeOH wash, which yielded a total of six fractions, Fractions E-J. Bioassays were performed to assess the anti-trichomoniasis activity of the resulting fractions, indicating that Fractions B, I, and J exhibited strong anti-trichomoniasis activity. Fraction I was further separated using C_{18} preparative HPLC (21.2 mm × 250 mm, 5 μm) with a MeOH/H_2O gradient (50:50 to 100:0, with 0.1% HCOOH). This resulted in the isolation of the known bioactive compound xanthoquinodin A1 (**42**) (52.2 mg).

3.3.14 Borohydride Reduction of Compound 42

In a flask, 7.6 mg of sodium borohydride (0.20 mmol), dissolved in 1 mL methanol, was added to 9.0 mg of compound **42** (0.016 mmol), dissolved in 4 mL methanol, over a five-minute interval. The reaction was allowed to proceed for 45 minutes with stirring, followed by addition of 500 μL of hydrochloric acid (1 M). The acidified mixture was allowed to stir for an additional ten minutes and dried *in vacuo* to yield compound **43** (8.8 mg, 96% yield).

^{1}H NMR (500 MHz, $CDCl_3$) 14.44 (s, 1H), 13.94 (s, 1H), 11.91 (s, 1H), 11.44 (s, 1H), 7.04 (s, 1H), 6.70 (s, 1H), 6.47 (m, 2H), 6.08 (s, 1H), 5.04 (s, 1H), 4.74 (dd, *J*=5.5, 2 Hz, 1H), 4.26 (dd, *J*=4, 2 Hz, 1H), 3.68 (s, 3H), 3.05 (d, *J*=18 Hz, 1H), 2.81 (m, 1H), 2.58 (d, *J*=18 Hz, 1H), 2.40 (s, 3H), 2.37 (m, 1H), 2.12 (m, 1H), 1.91 (m, 1H)

^{13}C NMR (125 MHz, $CDCl_3$) 188.5, 186.7, 184.6, 179.4, 171.1, 161.4, 158.5, 155.9, 148.3, 147.6, 141.8, 134.9, 131.8, 117.5 (2), 111.7, 111.3, 106.5, 104.6, 100.1, 83.8, 71.9, 66.8, 53.4, 43.6, 37.6, 30.5, 24.4, 23.0, 22.4

Note: Research reported in this chapter was supported by the National Institutes of Health (5R33AI119713).

Chapter 4: Natural-Product-Inspired Compounds as Countermeasures Against the Liver Carcinogen Aflatoxin B_1

This chapter was adapted from a manuscript that is currently being prepared for submission in 2018. The authors of that manuscript are Adam C. Carter, Jarrod King, Allison O. Mattes, Shengxin Cai, Narender Singh, and Robert H. Cichewicz.

*The work presented within this chapter was performed by the following: Jarrod King performed preliminary work related to assay development and conducted bioassays; Adam C. Carter performed extractions, purifications of secondary metabolites **1-3**, structure elucidation of **1-3**, and organic synthesis of select compounds; Shengxin Cai isolated and determined the structure of compound **4**.*

4.1 Introduction

Aflatoxins are a class of highly potent and carcinogenic natural products produced by several species of fungi including *Aspergillus flavus* and *Aspergillus parasiticus.*[114-115] Since this class of mycotoxins was discovered in the 1960s following the death of over 100,000 turkeys and other poultry in England,[114, 116] extensive research has focused on this family of toxins with a particular focus on their effects on the health of humans and animals. Of the aflatoxins that have been reported to date, aflatoxin B_1 (AfB_1) is widely believed to be one of the most carcinogenic naturally occurring chemical compounds known to man.[117] AfB_1 and related aflatoxins are thought to be a cause of elevated hepatocellular carcinoma rates observed in many parts of the world including Africa, eastern Asia, and parts of South America.[118] An estimated 4.5 billion people worldwide are exposed to aflatoxin in their diet, and it is estimated that aflatoxin is responsible for

up to 28% of all hepatocellular carcinoma cases around the world.[119] The potency and ease with which it can be obtained have also generated concern that this class of mycotoxins may be developed and used as biological warfare agents, as was the case in Iraq in the 1980s.[120] In addition to their negative impacts on human health, contamination of agricultural products with aflatoxin leads to millions of dollars in losses in the United States annually.[121] As a result, AfB_1 and its carcinogenic analogs have continued to have major impacts on human and animal health safety around the world.

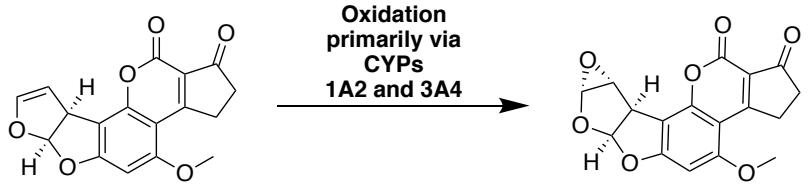

Figure 4.1. Oxidative toxification of aflatoxin B_1 to form aflatoxin B_1-8,9-epoxide

Of note is the fact that AfB_1 itself does not pose a hazard to human health, as it must first be metabolized to the active toxin 'AfB_1-8,9-epoxide' by certain isoforms of cytochrome P450 (CYP) enzymes. The most significant CYP isoforms thought to be involved in this metabolic activation of AfB_1 include the isoforms CYP3A4 and CYP1A2, which are found in the liver (Figure 4.1). However, there is still some uncertainty with regards to which CYP isoform(s) are most significant in the observed *in vivo* toxicity of this mycotoxin.[122-123] Once metabolized to the active electrophilic form, this metabolite can form covalent bonds with cellular (e.g., DNA, RNA, and proteins) targets. Of these covalent modifications, the most problematic in the context of human health are those involving the reaction between AfB_1-8,9-epoxide with DNA, which can lead to mutations and increased risk for tumor development, especially in the liver.[115]

As a result of its severe toxic effects, efforts have been taken to develop protective measures to reduce the carcinogenic properties of AfB_1, generally through (i) reduction of exposure to the mycotoxin and (ii) blocking the metabolism of AfB_1 to form the activated toxin. Of the compounds that have been reported to reduce the negative effects of AfB_1 exposure, the two most promising are chlorophyllin and oltipraz, which appear to have partial efficacy in humans who are at high risk for exposure to AfB_1 through their diet.[124-126] While these compounds have been limited in terms of their protection against AfB_1 toxicity, they do provide a precedent for the development of new and more effective agents to protect against the negative effects of AfB_1 exposure.

To address the threat posed by AfB_1 on human health, we have worked to develop a bioassay system to identify new secondary metabolites that are able to reduce the cellular toxicity of AfB_1 toward human liver-derived cells (HepG2). The HepG2 cell line has been used in the past as a representation for hepatocyte function and drug metabolism as it is known to express several CYP isoforms found in the liver, though at levels lower than those observed in intact human liver tissues.[127] In this work, we report the development and testing of our new assay system, which resulted in the identification of several molecules of natural and synthetic origin exhibiting protective effects against AfB_1 toxicity.

4.2 Results and Discussion

4.2.1 Assay Development and Optimization

To begin development of our assay system, we first identified a small number of published peer-reviewed methods that had been used previously for the identification of

compounds with *in vivo* protective activity against AfB_1 toxicity.[128-129] In finding these previous reports, we were able to identify that they exclusively utilized colorimetric assay systems to measure cellular metabolic activity (i.e., alamar blue, MTT, intracellular ATP) to assess cell viability. Using these methods, we found them to be insensitive to low levels of AfB_1 toxicity and unable to be used to evaluate the health of the cells (e.g., cell morphology). Specifically, in using microscopy to observe cells treated with AfB_1 alone as well as with putative protective agents led us to discover two problems with the methods used traditionally: (i) cells treated with low (non-toxic) concentrations of AfB_1 typically showed significant changes in their morphology that were not immediately recognizable through assessment of metabolic activity alone, and (ii) in some cases, application of putative protective compounds to AfB_1-treated cells resulted in viable cells, but their morphologies were significantly altered compared to healthy control cells (e.g., reduced cell areas, cells are angular in shape rather than rounded, isolated cell development rather than in aggregates). As a result of these observations, we realized the need for an alternative method to identify molecules capable of maintaining the viability of the cells, while also sustaining healthy morphologies in the cells. As such, we determined that high-content imaging using our Operetta (PerkinElmer) system could provide a viable alternative approach. Specifically, high-content imaging allows one to collect quantitative cell viability data and qualitative assessments of cell morphologies simultaneously.[130]

To optimize cell density for use in our high-content imaging assay system, experiments were performed to assess different cell-seeding methods on assay performance. Through these experiments, we found that 20,000 HepG2 cells per well in a

96-well microtiter plate yielded sufficient numbers of cells per field to reliably quantify their viability, but prevented overcrowding of cells such that cell morphologies could be assessed as well. Under these seeding conditions, we could observe the HepG2 cells as growing in "islands" of polygonal-shaped cells. Using the Operetta Harmony image analysis software, we automated the analysis of cell shape and area, which led to two benefits from our assay design. The first benefit was that the method allowed us to find minor changes in cell shape, and the second was that cell area could be used to estimate the cell viability. In our preliminary studies comparing this method to traditional methods (MTT and SRB assays), we found that cell viability following AfB_1 exposure was very strongly correlated to the average cell size. As a result, cell area was selected to be a new alternative metric for testing as it relates both to viability and cell health.

Finally, the dose-response relationship of AfB_1 on HepG2 cell viability (as measured by cell area) was explored with the intention of determining the LC_{50} value of the toxin following 48 hours of exposure. An LC_{50} value of 30 μM was determined for AfB_1, which was reasonably close to the values reported in other *in vitro* assay systems.[128-129] We determined that the Z-factor for this assay system was 0.82, which indicates that the system is highly likely to detect bioactive samples when used for high-throughput screening.

4.2.2 Testing Two Putative AfB_1 Protective Compounds: Oltipraz and *N*-Acetylcysteine

Previous reports that we found for two compounds, namely oltipraz and *N*-acetylcysteine, suggested that these compounds may exhibit protective properties in cells

exposed to AfB_1.[131-132] However, these reports have been disputed by later investigations,[124] which showed that oltipraz can lead to adverse effects in human patients that include gastrointestinal symptoms, phototoxicity, thermal sensitivity, and paresthesia. It has also been found that *N*-acetylcysteine can have adverse side effects that range from nausea to death.[133] When tested using our assay system, we found that neither of these compounds afforded protection against the toxic effects of AfB_1, and that oltipraz increased the toxicity of AfB_1 slightly (Figure 4.2). Interestingly, we did observe increases in HepG2 cell area when each of these compounds was administered alone, which may explain the confounding prior test results. Nevertheless, we cannot rule out the possibility that oltipraz and *N*-acetylcysteine may exhibit protective effects strictly *in vivo*, where other biological processes at the system-level are involved.

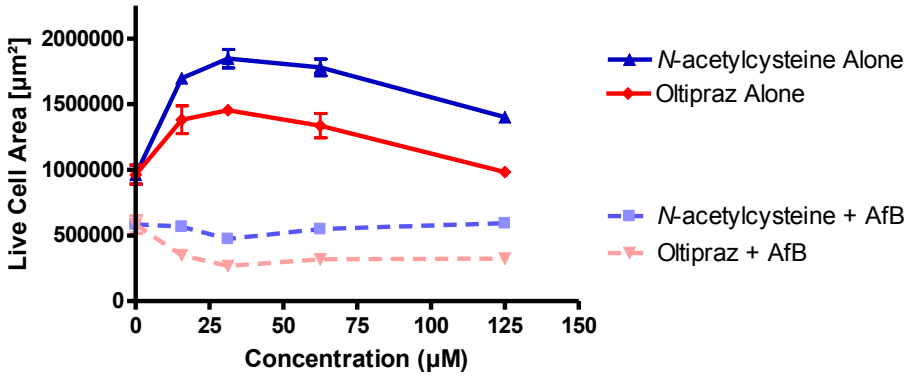

Figure 4.2. Effect of oltipraz and *N*-acetylcysteine on AfB_1 toxicity in HepG2 cells. Error bars represent one standard deviation, calculated from a total of two replicate measurements of live cell area.

4.2.3 Screening of Natural Product Extracts

An exploratory screening process was performed to test natural product extracts that were derived from both bacteria and fungi for the presence of compounds that could

afford protection against AfB_1 toxicity. In this investigative screening process, 276 bacterial extracts (tested at concentrations of 33.4 and 66.8 μg/mL) and 644 fungal extracts (tested at 16.7 μg/mL) were screened using our newly optimized assay system. While none of the bacterial extracts tested were found to be active, 21 of the fungal extracts (3.3%) were found to exhibit protective activities (protection was assessed on the basis of the live cell area relative to control cells not treated with AfB_1; compounds resulting in >50% relative live cell areas were considered "protective"). A second screening was performed to reconfirm the protective activities observed, resulting in a total of 17 extracts that showed repeatable protective activities at 16.7 μg/mL (i.e., increased live cell area and partial restoration of normal HepG2 cell morphology).

The seven fungal extracts showing the greatest improvements in HepG2 cell morphology (AfB_1-treated cells appeared to cells not exposed to AfB_1) were chosen, and the source fungal isolates were subjected to small-scale fermentation. The fungal isolates were grown for four weeks in 250 mL flasks on monolayers of Cheerios breakfast cereal, followed by extraction of the resulting cultures with ethyl acetate and subsequent partitioning with water. The resulting organic phases were retained, subjected to LC-ESIMS analysis, and tested in the assay to generate dose-response curves covering a range of concentrations from 1.25 to 50 μg/mL. Three of the seven extracts (laboratory codes 58B1, 55C11, and 59E6) displayed good dose-response protective effects, but LC-ESIMS analysis revealed that two of these samples (58B1 and 55C11) were nearly identical in their composition. As such, 58B1 and 59E6 were selected for further study (Figure 4.3). Both fungal isolates were subjected to ITS sequencing, leading to likely identifications as *Alternaria alternata* (58B1) and *Aspergillus niger* (59E6).

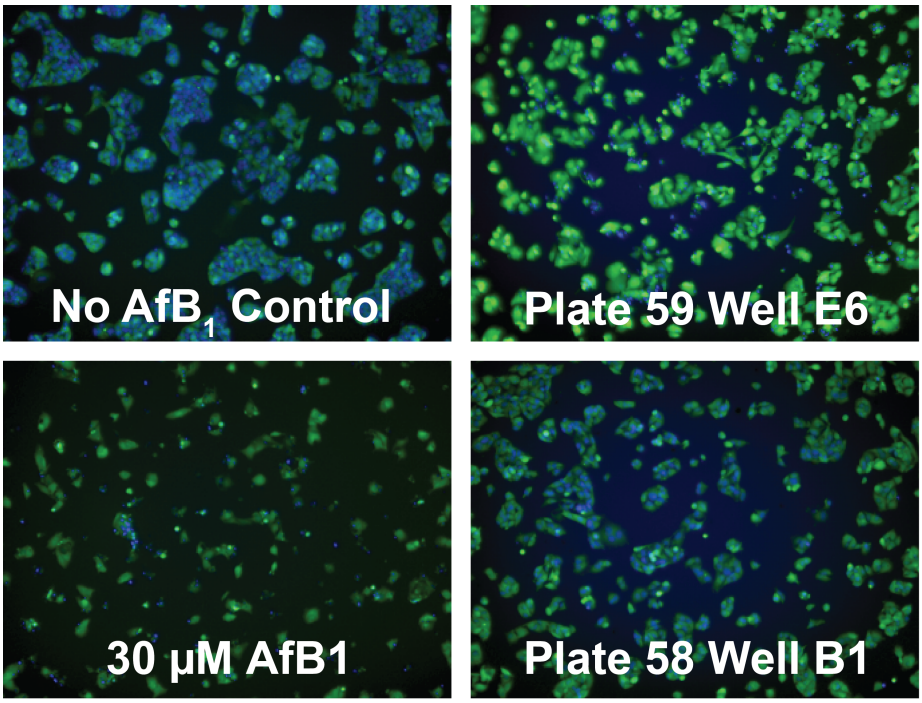

Figure 4.3. Top bioactive samples (hits) from screening fungal and bacterial extracts using HepG2 monolayers. Plate 58 well B1 (source of compound **1**-**3**) preserved cell morphologies reasonably well to appear similar to the no AfB_1 control. For comparison, the cells in plate 59 well E6, exhibited increased cell area, but lacked the morphological similarities of 58B1.

4.2.4 Purification of Compounds 1-3 from *A. alternata*

The small-scale extract produced by the *A. alternata* isolate (58B1) was subjected to HPLC over C_{18}, and the resulting fractions were collected in a deep-well 96-well plate. After removal of the solvent, the resulting residues were resuspended in DMSO and aliquots were transferred using a pin tool to new 96-well microtiter plates for bioassay testing. Our group has employed this methodology as a means of accelerating the process of identifying bioactive secondary metabolites from microbes and plants.[134] Three wells were found to exhibit protection from AfB_1 toxicity, and their contents were analyzed using LC-ESIMS. The first two active wells were composed of a mixture of two major-component molecules, while the third active well contained only one major-component

molecule. By dereplicating against our lab's internal database of fungal metabolites, we were able to immediately identify all three major-component compounds as being alternariol-9-methyl ether (**1**), altenuisol (**2**), and alternariol (**3**) (Figure 4.4). Using the supplies of these compounds that were readily available in our pure compound library, we were able to confirm that compounds **1**-**2** exhibited high levels of protection against AfB_1 toxicity, resulting in 67 and 66% maximum relative live cell areas (MRLCAs) after AfB_1 exposure. Compound **3**, on the other hand, was not found to be protective of the HepG2 cells as it only yielded a MRLCA of 15% (Table 4.1). Further testing of compounds **1** and **2** in the absence of AfB_1, showed that compound **2** was slightly cytotoxic to the HepG2 cell line, while **1** showed no adverse cytotoxic effects at the concentrations tested.

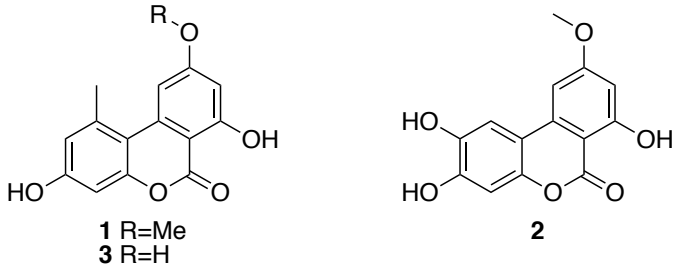

Figure 4.4. Structures of secondary metabolites **1**-**3** from *Alternaria alternata*

When comparing the structures of compounds **1** and **2** versus compound **3**, we were able to observe that the most prominent difference between these metabolites was the presence of a methoxy substituent at the 9-position of **1** and **2**. As a result of this difference and the differential protection afforded by **1**-**3**, we hypothesized that the presence of this methoxy substituent may play an important role in the protective effects observed for **1**-**2**.

4.2.5 Assessing the Protective Properties of Compounds 4-12

In addition to the methoxy substituent noted for compounds **1** and **2**, we also noted that compounds **1**-**3** were all relatively small, planar, and aromatic molecules, which are typical attributes of substrates reported as inhibitors of CYP1A2.[135] These types of compounds are believed to more easily fit in the relatively narrow binding pocket of this CYP isoform.[136] Based on this observation, we next screened a series of structurally similar molecules for protecting HepG2 cells against AfB_1-induced toxicity. As we observed weak activity for compound **3**, the *m*-methoxyphenol moiety found in **1**-**2** was also further investigated. As a result, we next looked at the known secondary metabolite monomethyl sulochrin (**4**), which is characterized as belonging to the class of benzophenones. Compound **4** showed a MRLCA of 68%, which was comparable to the activities observed in **1**-**2**. However, when testing a smaller compound, 3,5-dimethoxyphenol (**5**), we saw low activity as evidenced by the low MRLCA (37%), suggesting that compound **5** may be too small and/or that at least two rings may be needed to provide protection against AfB_1. Since benzophenones are known substrates of CYP1A2[137-138] and are easier to access through organic synthesis than the polycyclic systems observed for **1**-**3**, we decided to explore additional benzophenones with *m*-methoxyphenol rings as part of their structure. As such, oxybenzone (**6**) and benzophenone-6 (**7**) were tested using our assay system. These compounds yielded MRLCAs of 62% and 54%, respectively, suggesting that an increase in the number of *m*-methoxyphenol units in the structure of benzophenones did not necessarily lead to further increases in the protection observed. Of importance, however, was that the observation of

protection with these compounds provided evidence that benzophenones might serve as an additional scaffold for protective compounds against AfB_1 toxicity.

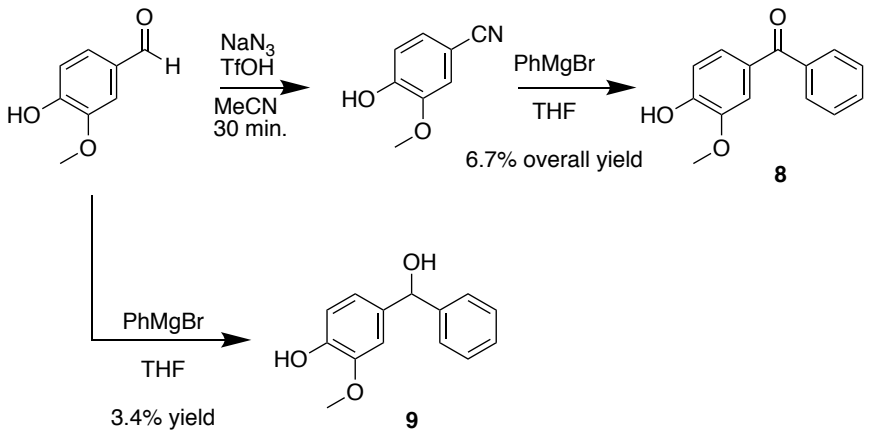

Scheme 4.1. Synthesis of compounds **8** and **9** from vanillin

Previously published work exploring other classes of compounds (e.g., flavonoids and stilbenoids) that also exhibit protective effects against AfB_1 suggest that small-molecule dependent inhibition of CYP1A2 is dependent on the placement of each molecule's pendant hydroxy and alkoxy substituents.[139-141] To assess alternative arrangements of substituents on the benzophenone's aromatic rings and the resulting effect on protective activity, we synthesized and tested the molecule 4-hydroxy-3-methoxybenzophenone (**8**) by first converting vanillin to vanillonitrile through a chemoselective Schmidt reaction using sodium azide and triflic acid,[142] followed by a Grignard reaction using phenylmagnesium bromide (Scheme 4.1). This compound resulted in a MRLCA of 60%, suggesting that *o*-methoxyphenol moieties are also tolerated for protection with the benzophenone scaffold. However, when testing 4-hydroxy-3-methoxybenzhydrol (**9**), where the ketone has been reduced to the secondary

alcohol, we observed a drop in the MRLCA to a level of 41%, suggesting that the carbonyl group contributes to the protective activity of this class of compounds.

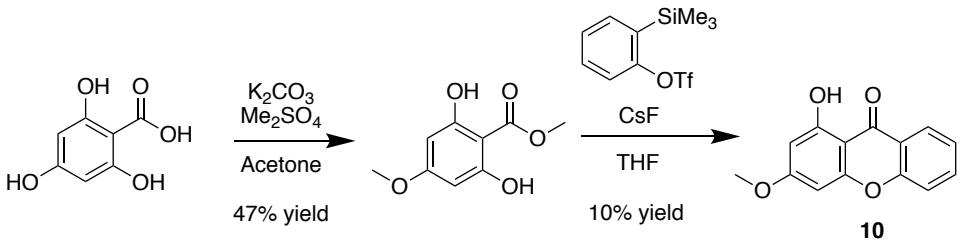

Scheme 4.2. Synthesis of compound **10** from 2,4,6-trihydroxybenzoic acid

Given the planarity of compounds **1** and **2**, we hypothesized that testing other planar aromatic scaffolds might also be of value to our studies. As a result, we recognized 1-hydroxy-3-methoxyxanthone (**10**) as an interesting xanthone to probe as it contained many structural similarities to **6**, but with the added benefit of increased planarity. Compound **10** was synthesized by first methylating 2,4,6-trihydroxybenzoic acid using dimethyl sulfate, followed by reacting the resulting methyl ester with benzyne, generated *in situ* using cesium fluoride and 2-(trimethylsilyl)phenyl triflate (Scheme 4.2). Compound **10** showed comparable MRLCA (64%) when compared to **6**; however, this compound also showed slight cytotoxicity at higher concentrations, limiting our further interest in this compound series.

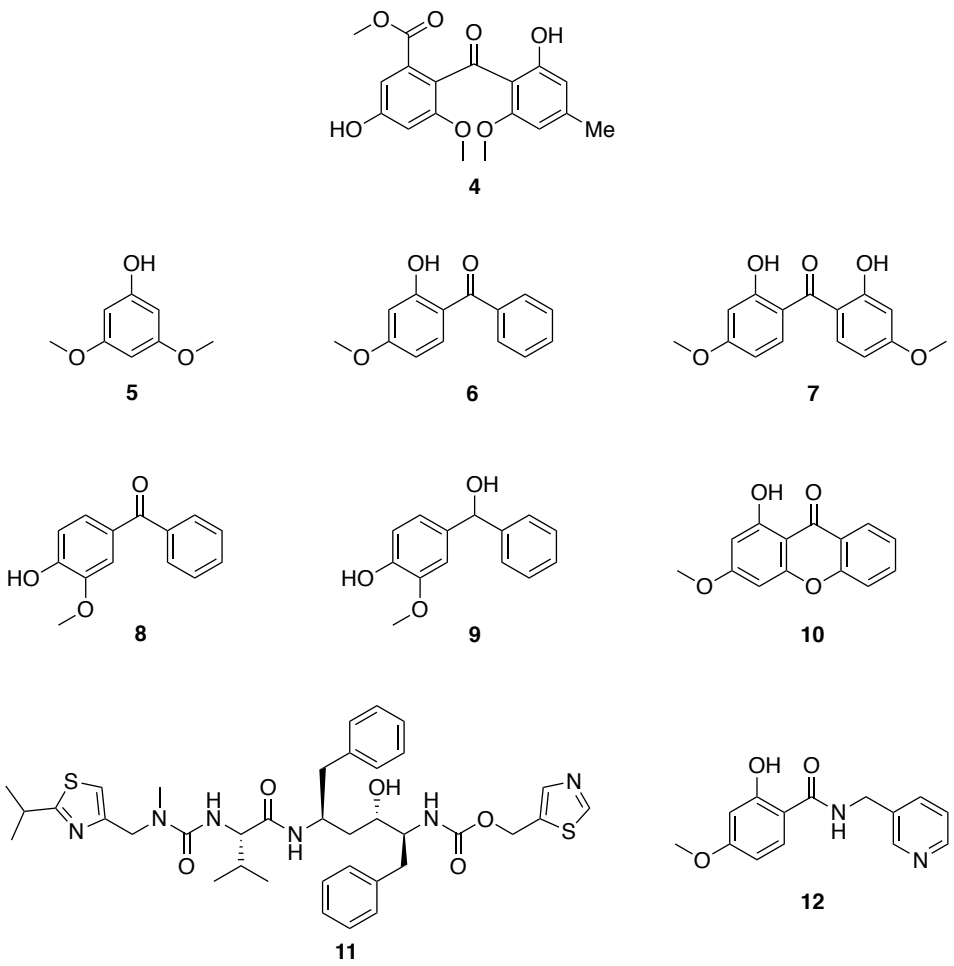

Figure 4.5. Structures of additional compounds (**4**-**12**) tested.

While reviewing published reports of CYP inhibitory small-molecules, the compound ritonavir (**11**)[143] attracted our attention as it was significantly different in structure from the aromatic systems we had investigated. In addition to this, **11** has been reported to inhibit the other major CYP isoform involved in AfB_1 activation to its toxic form, CYP3A4. However, the role of these CYP isoforms in the *in vivo* activation of AfB_1 is still disputed in the literature.[115] To test our hypothesis that **13** may protect cells from AfB_1, we tested this compound in our assay system. In doing so, we found that **13** offered a strong protection against AfB_1 toxicity (72% relative live cell area at 5 μM),

suggesting that CYP3A4 may also be contributing to the conversion of AfB_1 to its toxic form *in vitro*, as has been observed in previous studies.[122]

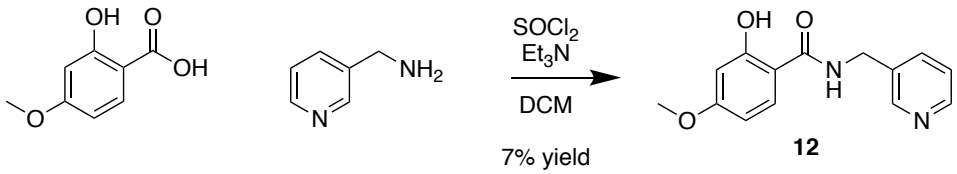

Scheme 4.3. One-pot synthesis of compound **12**

Combining this observation with other reports citing nitrogen-containing heterocycles as inhibitors of CYPs,[144-147] we next decided to see if a combination of the aromatic scaffolds investigated earlier with a nitrogen-heterocyclic moiety could confer further protection against AfB_1 toxicity. Accordingly, we next prepared the compound 2-hydroxy-4-methoxy-*N*-(3-pyridinylmethyl)benzamide (**12**) via a one-pot reaction starting with 2-hydroxy-4-methoxybenzoic acid and 3-picolylamine in the presence of thionyl chloride and triethylamine (Scheme 4.3), and tested it in our assay system. Despite the inclusion of a nitrogen heterocycle, this molecule offered little to no protection (34% MRLCA), and as a result, we did not pursue this combination further.

Table 4.1. Maximum protection afforded by pure compounds **1-12** from AfB_1 toxicity in HepG2 monolayers, expressed as relative live cell area ± 1 S.D. with respect to no AfB_1 controls. As AfB_1 exposure alone typically resulted in relative live cell areas of approximately 30%, we considered values >50% to be "protective".

Compound	Maximum Relative Live Cell Area[a] (% of No AfB Control)	Concentration Tested to Obtain Maximum Live Cell Area Observed (µM)
1	67.0 ± 1.1	50
2	65.7 ± 4.7	50
3	15.2 ± 5.8	0.5[b]
4	68.3 ± 14.5	50
5	37.0 ± 0.1	5[b]
6	61.6 ± 6.1	12.5
7	53.9 ± 1.5	50
8	60.2 ± 8.2	50
9	41.0 ± 3.4	50
10	63.9 ± 0.7	5[c]
11	72.0 ± 4.6	0.5[c]
12	33.5 ± 0.3	0.5[b]

[a]Maximum protection (greatest live cell area relative to no AfB1 control) calculated as a percentage ± 1 S.D., n=2
[b]Protection did not increase at higher concentrations tested
[c]Toxicity observed at 50µM

4.2.6 Testing a HepG2 Spheroid Model for Assessing AfB_1 Protection

Despite the fact that our assay system allowed us to detect compounds that afforded protection to HepG2 cells exposed to AfB_1, we were aware of limitations that remained in our approach. In particular, CYP expression in HepG2 monolayers is known to be lower than levels detected *in vivo*.[127, 129, 148-149] Additionally, methods to reliably and consistently upregulate the expression of CYPs *in vitro* remain difficult,[149] with our own efforts proving unreliable or only yielding minute increases in CYP activity. These lower CYP expression levels were readily seen in our assay, as well as in virtually every

published account of *in vitro* toxicity of AfB_1, as can be seen by the fact that more toxin is needed to cause cell death than the amounts needed to see toxicity *in vivo*.[148, 150]

With this limitation in mind, we were interested in reports that CYP expression is increased in HepG2 cells when they are grown in the form of spheroids rather than monolayers.[151-152] Spheroids, which are a form of 3D cell culture where cells are allowed to form aggregates without the use of a non-cellular substrate,[153] have been used in assay systems previously due to their ability to better represent *in vivo* cellular characteristics (e.g., gene expression, drug susceptibility, drug penetration, drug metabolism, morphology).[151-155] Because of this, we decided to proceed with further experiments using HepG2 spheroids in place of the HepG2 monolayers used previously.

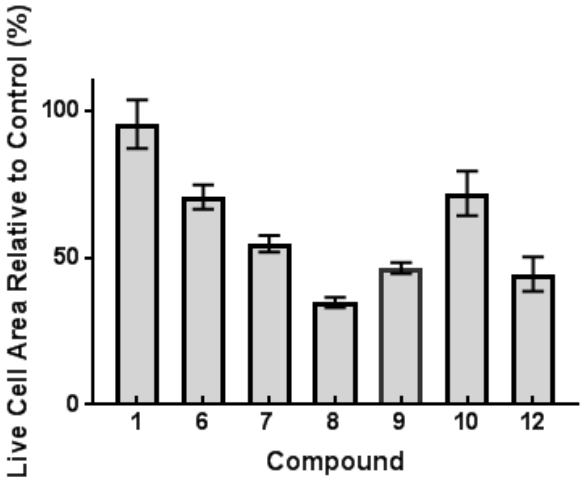

Figure 4.6. Relative live cell areas of HepG2 spheroids resulting from the application of selected compounds at a concentration of 10 μM and exposure to AfB_1. Compounds were considered "protective" if they achieved >50% relative live cell areas. Error bars are expressed as ± 1 S.D., n=3.

First, we carried out tests to determine sensitivity of these spheroids to AfB_1, and were amazed to observe a 15-fold increase in the sensitivity to AfB_1 (LC_{50} of 2 μM in spheroids versus 30 μM in monolayers). This increased sensitivity was in agreement with

reported observations that CYP1A2 is upregulated significantly in HepG2 spheroids when compared to monolayers.[151, 155] We next tested a subset of compounds previously evaluated using HepG2 monolayers to find that compounds **1**, **6**, and **10** showed protection of the HepG2 spheroids against AfB_1 toxicity. We further tested two of the top-performing compounds, **1** and **10** (Figure 4.7) at a range of concentrations (0.01 to 10 μM), which revealed that both showed strong protection (95% and 72% relative live cell areas, respectively, at 10 μM) (Figure 4.7). In addition to the live cell area, we also observed that the treated spheroids looked virtually identical to the healthy spheroid controls when inspected using the high-content imaging system.

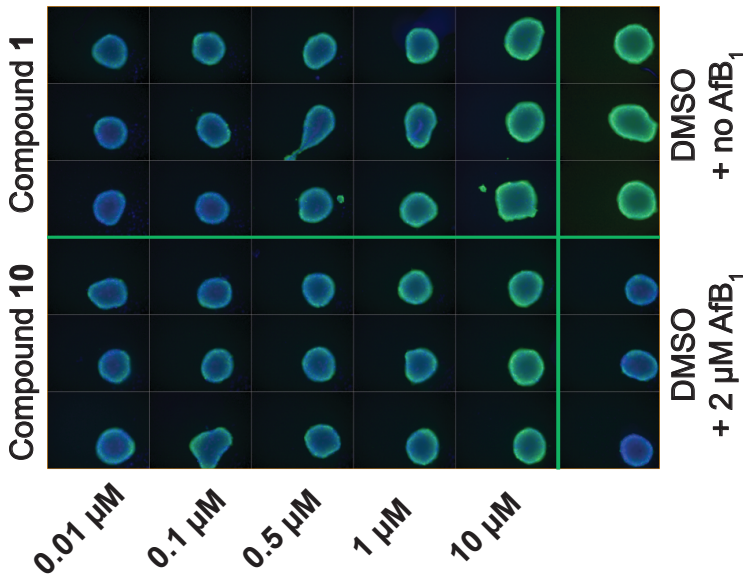

Figure 4.7. Protection from aflatoxin in HepG2 spheroids by compounds **1** and **10.** In live spheroids, calcein AM is converted to calcein, which fluoresces green, after hydrolysis by intracellular esterases. Pure blue spheroids are dead and only fluoresce due to Hoechst staining of DNA.

4.2.7 Conclusions

With this newly developed assay for screening chemoprotective qualities of fungal extracts in HepG2 cells, we were able to screen libraries of bacterial and fungal crude extracts and identify secondary metabolites responsible for the protective activities observed. We found that the images provided by the Operetta high-content imaging system allowed us to utilize the preservation of healthy cell morphology to further filter active extracts as well as pure compounds. From the structures of the natural products isolated, we were able to identify structurally similar natural products that also exhibit protective activity. Finally, we were able to find protective compounds that are easier to prepare synthetically than the structurally more complex natural products tested. While we do not know the mechanism by which these compounds confer protection to HepG2 cells, the increased sensitivity of HepG2 spheroids to AfB_1 as well as the increased protection observed in HepG2 spheroids suggests that they may be acting through inhibition of CYP1A2. This mechanism, in addition to the protective activity seen for **11**, a known CYP3A4 inhibitor, leads us to believe that the use of CYP1A2 and CYP3A4 inhibitors could be a viable route for chemoprotection in the case of exposure to AfB_1 to prevent lasting liver damage and increased risk of hepatocellular carcinoma.

4.3 Materials and Methods

4.3.1 General Experimental Procedures and Chemicals Used

NMR data was collected on Varian NMR spectrometers (400 or 500 MHz for ^{1}H and 125 or 100 MHz for ^{13}C). LC-ESIMS data was obtained on a Shimadzu LC-MS 2020 system (ESI quadrupole) coupled to a PDA detector, and equipped with a Phenomenex

Kinetex C_{18} column (3.0 mm × 75 mm, 2.6 μm). The preparative HPLC system utilized SCL-10A VP pumps and system controlled and was equipped with a Phenomenex Luna C_{18} column (21.2 mm × 250.0 mm, 5 μm), while analytical and semipreparative HPLC was performed on HPLC systems with Waters 1525 binary pumps and Waters 2998 PDA detectors. For the semipreparative and analytical systems Phenomenex Gemini C_{18} columns (4.6 mm × 250.0 mm, 5 μm; or 10.0 mm × 250.0 mm, 5 μm) were used. All solvents were of ACS grade or better. Thionyl chloride and 2-hydroxy-4-methoxybenzoic acid were purchased from Alfa Aesar; benzophenone-6 (**7**), 3-picolylamine, 2-(trimethylsilyl)phenyl trifluoromethansulfonate, and 2,4,6-trihydroxybenzoic acid were purchased from TCI America; cesium fluoride, vanillic acid, and oxybenzone (**6**) were purchased from Beantown Chemicals; oltipraz, dimethyl sulfate, vanillin, and phenylmagnesium bromide were purchased from Sigma Aldrich; sodium azide was purchased from Fluka; potassium carbonate was purchased from Fisher Scientific; ritonavir (**11**) was purchased from Selleck Chemicals; *N*-acetylcysteine was purchased from VWR; 3,5-dimethoxyphenol (**5**) was purchased from Chem Impex International.

4.3.2 Aflatoxin Protection Assay

The human hepatocellular carcinoma HepG2 (HB-8065) cell line was purchased from ATCC. Cells were maintained in Eagle's Minimum Essential Medium (EMEM, Gibco) with 5% FetalClone III (Hyclone) and penicillin/streptomycin (50 U/mL and 50 μg/mL, respectively) in a humidified incubator in 5% CO_2. Monolayer cell assays were performed by first adding approximately 20,000 cells in 100 μL of medium to each well of a 96-well plate. Cells were allowed to attach to the plate overnight, after which,

DMSO stocks of extracts, fractions or test compounds were added to the wells. Immediately following this initial addition, 100 µL of a stock solution made by adding aflatoxin B_1 (AfB_1) in DMSO to EMEM was added to each well in order to bring the total volume to 200 µL and yield a final concentration of 30 µM AfB_1. The plates were allowed to incubate for 48 hours, after which, viability was determined using a calcein AM and Hoechst 33342 live cell area assay on the PerkinElmer Operetta. To do this, a stock solution in DMSO was prepared such that calcein AM was at a concentration of 40 µM, while Hoechst 33342 was at a concentration of 160 µM. The stock solution was then diluted at a ratio of 1:5 in PBS, and 5 µL of the diluted solution was added to each well of the 96-well plate. After allowing the plate to incubate for 30 minutes, the Operetta was used to image each well of the plate. The Harmony software package was used to locate all Hoechst-labeled nuclei and assign a live/dead assessment based on the magnitude of green fluorescence (threshold of 350 units) detected for each cell. This assessment was possible due to the fact that live cells contain esterases that are capable of cleaving the acetoxymethyl (AM) ester group from calcein AM, resulting in a bright green fluorescence. DMSO controls without AfB_1 were used to determine appropriate 100% viability levels. The protection afforded by each compound tested was expressed as the live cell area of the treated cells relative to the live cell area of the DMSO controls not exposed to AfB_1, given as a percentage. A compound was considered to be "protective" if the relative live cell area was determined to be >50%. This level was chosen as 30% relative live cell area was typically observed in the AfB_1 treated controls.

Spheroid cell assays were performed in ultra-low attachment plates (Corning 7007). To each well, 1,000 cells were seeded in 100 µL of EMEM and allowed to grow

for a total of four days. This resulted in the formation of tight spheroids of cells. After the four days, DMSO stock solution of extract, fractions, or compounds being tested were added at appropriate concentrations. Additionally, 100 µL aliquots of a stock solution of AfB_1 in EMEM were added to each well such that the final volume was 200 µL, and the AfB_1 concentration was 2 µM. Spheroids were allowed to incubate for three additional days, after which, viability and live spheroid size determination was performed using the Operetta.

4.3.3 Screening Natural Product Extracts

A collection of 644 fungal extracts dissolved in DMSO at a concentration of 16.7 µg/mL was screened using a 1 µL pin tool to add these extracts to 96-well plates. In addition to these fungal extracts, 276 mammalian microbiome-derived bacterial[156] extracts were prepared at concentrations of 33.4 µg/mL and 66.8 µg/mL in DMSO. These bacterial extracts were screened by using a 2 µL pin tool to add each extract to the 96-well plates. Two fields per well were imaged for analysis using the Harmony software package. Live cell areas were compared to the no AfB_1 controls of each plate to assess protection afforded by each extract. Active extracts were considered to be those offering at least 75% relative live cell areas.

4.3.4 Purification of Compounds 1-3

A fungal isolate *Alternaria alternata* (internal designation 58B1) was identified by ITS sequence analysis (GenBank accession number MK038723). The isolate was cultured from an oral swab of a roadkill opossum.[156] The isolate was grown for four

weeks on Cheerios breakfast cereal supplemented with a 0.3% sucrose solution with 0.005% chloramphenicol in a 250 mL flask. After four weeks, the contents of the flask were extracted with EtOAc to yield a total mass of 55.2 mg. The extract was dissolved at a concentration of 100 mg/mL, after which, approximately 5 mg of material (50 µL injection volume) was separated using semi-preparative C_{18} HPLC (250 mm x 10 mm, 5 µm) with a MeOH/H_2O gradient from 10% to 100% MeOH over 30 minutes with a 10 minute MeOH wash. Fractions were collected in the wells of a 96-well plate and dried *in vacuo*. Contents of each well of the plate were tested for protective activity in HepG2 cells exposed to AfB_1, leading to the identification of three peaks observed by LC-ESIMS coinciding with bioactivity. Comparison with an internal database of fungal natural products previously isolated in our lab resulted in the identification of alternariol-9-methyl ether (**1**), altenuisol (**2**), and alternariol (**3**) as the compounds contained within the active wells. Pure samples of compounds **1**-**3** were tested in the aflatoxin protection assay, resulting in the confirmation of **1** and **2** as the active compounds.

Following this initial identification from a small-scale fermentation, the fungal isolate was grown for four weeks on Cheerios breakfast cereal that was supplemented with a 0.3% sucrose solution with 0.005% chloramphenicol in three large mycobags (Unicorn Bags, Plano, TX) prior to being homogenized and extracted with EtOAc. The resulting crude extract (28.3 g) was separated using silica gel VLC with stepwise elution using 1:1 hexanes/DCM, DCM, 10:1 DCM/MeOH, and MeOH to yield four fractions (Fractions A-D). Fraction C (7.3 g) was further separated using HP-20SS VLC and a step gradient of MeOH in water (30%, 50%, 70%, 90%, and 100%), followed by a DCM/MeOH rinse, to yield six additional fractions (Fractions E-J). Upon storage of the

fractions in MeOH at -20°C, a precipitate was observed in Fraction I and was removed by centrifugation. The precipitate was dissolved and underwent purification with semi-preparative C_{18} HPLC under isocratic conditions (60:40 MeCN/H_2O) to produce compound **1** (126 mg), whose structure was confirmed through comparison of ^{1}H and ^{13}C NMR data to the literature.[157]

4.3.5 Synthesis of 4-hydroxy-3-methoxybenzophenone (8)

1.0 g of vanillin (6.6 mmol) and 800 mg of sodium azide (12.3 mmol) were dissolved in 15 mL of acetonitrile. This mixture was allowed to stir for five minutes, after which, 2 mL of trifluoromethanesulfonic acid (22.6 mmol) was added slowly over a five-minute interval. The reaction mixture was allowed to stir for 30 minutes at room temperature. After stirring, 15 mL of acetonitrile was added and the crude reaction mixture was dried *in vacuo*. The dried material was redissolved in 80 mL of EtOAc and partitioned three times with 35 mL of water. The organic phase was dried *in vacuo* to yield 1.0 g of crude vanillonitrile. To a dry vial, 2 mL of phenylmagnesium bromide in diethyl ether (3 M, 6 mmol) was mixed with 1 mL of dry THF. The vial was cooled to 0°C in an ice bath, and 100 mg of crude vanillonitrile in 0.6 mL of dry THF was added dropwise over a five-minute interval. The reaction mixture was removed from the ice bath and allowed to stir while warming to room temperature. After reaching room temperature, the reaction was allowed to proceed for 25 hours. At this point the reaction was low yielding, so the mixture was heated to reflux for 21 hours. After refluxing, the vial was allowed to cool and quenched with 3 mL of saturated sodium bicarbonate. The mixture was then partitioned with EtOAc (three times, 10 mL each), and the organic

phase was dried *in vacuo*. The resulting material was then purified by silica gel VLC using a stepwise gradient of 10:1 hexanes/EtOAc, 1:1 DCM/hexanes, DCM, 10:1 DCM/MeOH, and MeOH. The DCM fraction was further purified by C_{18} semi-preparative HPLC using isocratic conditions of 45% acetonitrile in water to yield compound **8** (9.2 mg, 6.7% overall yield). The identity of **8** was verified through comparison of its ^{1}H and ^{13}C NMR spectra to the literature.[158]

^{1}H NMR (400 MHz, $CDCl_3$) 7.75 (dd, *J*=8, 1 Hz, 2H), 7.56 (t, *J*=7 Hz, 1H), 7.51 (d, *J*=2 Hz, 1H), 7.48 (t, *J*=7.5 Hz, 2H), 7.33 (m, 1H), 6.95 (d, *J*=8 Hz, 1H), 3.94 (s, 3H)

^{13}C NMR (100 MHz, $CDCl_3$) 195.7, 150.2, 146.7, 138.3, 131.9, 129.8 (2C), 128.2 (2C), 126.3, 113.6, 111.9, 56.1

4.3.6 Synthesis of 4-hydroxy-3-methoxybenzhydrol (9)

Compound **9** was prepared according to a protocol described previously in the literature.[159] More specifically, 290 mg of vanillin (1.9 mmol) dissolved in 1.5 mL of dry THF was added to a dry vial. The vial was cooled to 0°C, after which, 2.9 mL of phenylmagnesium bromide in diethyl ether (1.5 M, 5.7 mmol) was added to the vial dropwise over a five-minute interval with stirring. The mixture was allowed to stir for 10 minutes at 0°C, then allowed to warm to room temperature. The reaction was stirred an additional 21 hours at room temperature, then quenched with a slow addition of 2 mL of methanol. C_{18} semi-preparative HPLC was used to purify compound **9** (14.9 mg, 3.4% yield). The identity of **9** was verified through comparison of its ^{1}H and ^{13}C NMR spectra to the literature.[159]

^{1}H NMR (400 MHz, $CDCl_3$) 7.39-7.24 (m, 5H), 6.89-6.77 (m, 3H), 5.77 (s, 1H), 3.79 (s, 3H)

^{13}C NMR (100 MHz, $CDCl_3$) 146.8, 145.5, 143.9, 135.6, 128.4 (2C), 127.4, 119.8, 114.3, 109.1, 76.1, 55.8

4.3.7 Synthesis of 1-hydroxy-3-methoxyxanthone (10)

The preparation of compound **10** began by adding 160 mg of 2,4,6-trihydroxybenzoic acid (0.94 mmol) and 240 mg of potassium carbonate (1.7 mmol) to 5 mL of acetone in a glass vial. To this mixture, 0.16 mL of dimethyl sulfate (1.7 mmol) was added and allowed to stir for 19 hours at room temperature. After 19 hours, 10 mL of water was added to the reaction mixture, followed by partitioning with 10 mL of EtOAc, three times. The resulting organic phase was dried *in vacuo*, then purified using C_{18} semi-preparative HPLC with isocratic conditions (40:60 MeCN/H_2O) to yield methyl 2,6-dihydroxy-4-methoxybenzoate (88 mg, 47% yield), whose identity was verified by comparison of its ^{1}H NMR spectrum to the literature.[160]

9 mg of methyl 2,6-dihydroxy-4-methoxybenzoate (0.045 mmol), 110 mg cesium fluoride (0.73 mmol), and 25 μL of 2-(trimethylsilyl)phenyl trifluoromethanesulfonate (0.10 mmol) were added to 1 mL THF in a glass vial. The mixture was stirred and heated to reflux for 24 hours. After cooling, methanol and DCM were added and the crude mixture was dried *in vacuo*. The residue was redissolved in diethyl ether and partitioned with water three times. The organic phase was dried *in vacuo* and purified by C_{18} semi-preparative HPLC using a 10-100% gradient of MeCN in water with 0.1% formic acid

added to yield compound **10** (1.1 mg, 10% yield). The identity of **10** was confirmed through comparison of its ^{1}H NMR spectrum to the literature.[161]

^{1}H NMR (400 MHz, $CDCl_3$) 12.89 (s, 1H), 8.27 (dd, *J*=8, 2 Hz, 1H), 7.73 (dd, *J*=9, 7 Hz, 1H), 7.45 (dd, *J*=8, 1 Hz, 1H), 7.39 (dd, *J*=8, 7 Hz, 1H), 6.46 (d, *J*=2 Hz, 1H), 6.38 (d, *J*=2 Hz, 1H), 3.91 (s, 3H)

4.3.8 Synthesis of 2-hydroxy-4-methoxy-*N*-(3-pyridinylmethyl)benzamide (12)

14 mg of 2-hydroxy-4-methoxybenzoic acid (0.08 mmol), 20 µL of 3-picolylamine (0.20 mmol), 80 µL of triethylamine (0.57 mmol), and 20 µL of thionyl chloride (0.27 mmol) were added to 400 µL of DCM in a glass vial. The mixture was allowed to stir at room temperature for 23 hours, and then dried *in vacuo*. The residue was redissolved in DCM and washed three times with an equal volume of 1 M hydrochloric acid. The organic phase was dried and purified using C_{18} semi-preparative HPLC (gradient 10-100% MeCN in water with 0.1% formic acid) to yield compound **12** (1.4 mg, 7% yield). The identity of **12** was verified through comparison of its ^{1}H NMR spectrum to the literature.[162]

^{1}H NMR (400 MHz, $CDCl_3$) 12.50 (s, 1H), 8.63 (s, 1H), 8.58 (d, *J*=4 Hz, 1H), 7.72 (d, *J*=8 Hz, 1H), 7.14 (d, *J*=8 Hz, 1H), 6.82 (d, *J*=8 Hz, 1H), 6.49 (d, *J*=2.5 Hz, 1H), 6.42 (dd, *J*=9, 2.5 Hz, 1H), 4.68 (d, *J*=6 Hz, 2H), 3.83 (s, 3H)

Notes: This chapter is based upon work supported by the Army Contracting Command - Aberdeen Proving Ground - Natick Contracting Division (ACC-APG NCD) under Contract No. W911QY-17-C-0008. Any opinions, findings and conclusions or recommendations expressed in this material are those of the author(s) and do not necessarily reflect the views of the Army Contracting Command - Aberdeen Proving Ground - Natick Contracting Division (ACC-APG NCD).

Chapter 5: *In Situ* Ring Contraction and Transformation of the Rhizoxin Macrocycle through an Abiotic Pathway

This chapter was adapted from a manuscript that is currently being prepared for submission in 2018. The authors of that manuscript are Adam C. Carter, Cora L. Petersen, April L. Risinger, Karen Wendt, Sara Helff, Susan Mooberry, and Robert H. Cichewicz.

*The work presented within this chapter was performed by the following: Adam C. Carter performed extractions, purifications of secondary metabolites **1-6**, structure elucidation of **1-6**, degradation experiments, and DFT calculations; Cora L. Petersen and April L. Risinger conducted biological evaluations of all rhizoxin analogs. Karen Wendt and Sara Helff prepared fungal isolates and performed ITS and 16S sequencing analysis.*

5.1 Introduction

Ewing sarcoma is a rare form of cancer that primarily impacts children, teens, and young adults. Despite the fact that only 6-8% of bone cancers are classified as Ewing sarcomas, it still is the second most common type of bone cancer in children and young adults and is diagnosed at a rate of about 225 children per year in the United States.[163-165] Recently, advances in how Ewing sarcoma is treated have resulted in an increase in the five-year survival rate, which currently stands at ~75% for patients with localized tumors;[165] however, in the case of patients with a disseminated form of the disease, the five-year survival rate drops tremendously to about 13-30%.[165] To further complicate matters, the rate of recurrence in Ewing sarcoma patients following treatments is ~30-

40% for patients with localized tumors and ~60-80% for those with disseminated forms of the disease.[165] Today, the standard of care for Ewing sarcoma patients includes aggressive combinations of chemotherapy, surgery, and radiation treatment, which may lead to long-term health issues for these young patients.[163] Genomic studies of Ewing sarcoma patients have revealed that in about 85% of these patients, the tumors carry a mutation resulting from a cross-over event involving the *EWSR1* gene on chromosome 22 and the *FLI1* gene on chromosome 11, which has been termed the *EWSR1/FLI1* fusion gene. Efforts to understand how the *EWSR1/FLI1* fusion gene results in gains and losses of molecular functions offers hope for the development of new disease-specific therapeutics that exploit the cellular defects of these Ewing sarcoma cells.[166-167]

Strategies targeting the manipulation of microtubules have been the basis for the development of several successful cancer treatments.[168-172] The efficacy of these treatment options depends on the crucial role that microtubules play in cell division; however, recent developments in the field indicate that other mechanisms are likely involved in their anticancer efficacy.[173-174] One approach in microtubule-targeted therapies is the destabilization of the polymerized protein, which prevents the formation of the mitotic spindle and ultimately leads to mitotic arrest. An interesting microtubule depolymerizing agent of natural origin is the antimitotic natural product rhizoxin (**1**).[175] First isolated in 1984 by Iwasaki et al., **1** was proposed to be produced by fungi belonging to the species *Rhizopus microsporus,* which is responsible for rice seedling blight.[48, 176] Subsequent studies into its mechanism of action supported the theory that **1** acts as an antimitotic agent by binding to β-tubulin at the maytansine site, inhibiting microtubule polymerization.[175, 177-178] Further studies into the biosynthesis of this

compound in 2006 by the Hertweck group established that **1** is not produced by *R. microsporus*, but rather by a bacterium, *Burkholderia rhizoxinica*, that lives as an intracellular symbiont within fungal cells.[50, 179]

Compound **1** and its analogs have generated clinical interest as a result of their *in vitro* sub-nanomolar potency against several types of cancer cells.[50, 180-182] These results ultimately led to the initiation of several clinical trials in Europe during the early 1990s, focusing primarily on the treatment of breast, melanoma, non-small-cell-lung, and squamous-cell-head-and-neck cancers.[183-185] Unfortunately, these tests failed to show clinical efficacy as a result of low bioavailability and rapid clearance of the molecule from the bloodstream of patients, which ultimately resulted in the suspension of clinical trials prior to phase III.[183-187] Subsequent work has focused on improving *in vivo* bioavailability of **1** through chemical modifications,[188-189] production of new analogs through culturing the bacterial endosymbiont *B. rhizoxinica* outside of its fungal host,[49-50] and genome mining of the root-associated *Pseudomonas fluorescens* Pf-5.[181] While these efforts have successfully produced many natural and synthetic analogs of **1**, none of these resulting compounds have been successfully translated into a therapeutic agent approved for use in the clinic.[190-191]

In this work, we disclose the identification of a fungal isolate and its corresponding extract obtained from our lab's Citizen Science Soil Collection Program[192] that was found to show markedly potent inhibitory activities against a subset of Ewing sarcoma cell lines bearing the *ESWR1/FLI1* fusion gene. Chemical studies of this fungal extract led to the isolation and subsequent structure elucidation of **1** along with several previously undescribed analogs, including a novel ring-contracted compound (Figure 5.1)

This work provides detailed investigation of the chemical structures and biological activity of **1** and its analogs, as well as an exploration of the process leading to the formation of these compounds.

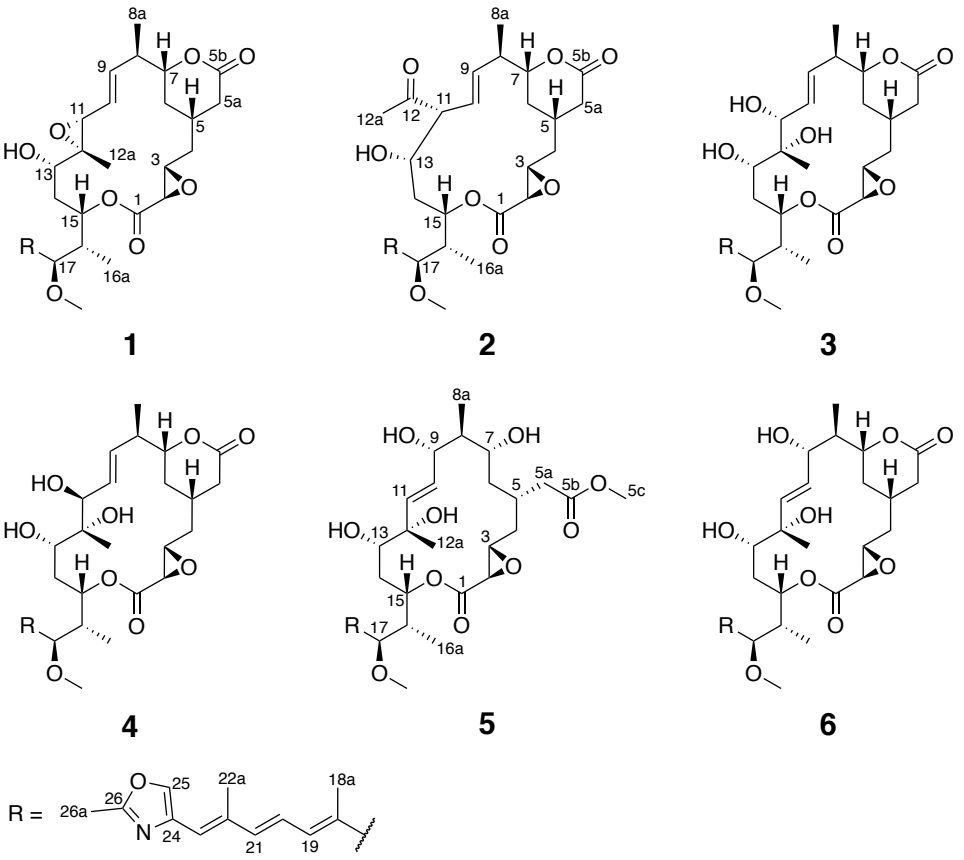

Figure 5.1. Structures of isolated natural products **1-6**

5.2 Results and Discussion

5.2.1 Isolation and Structure Elucidation of Rhizoxins 1-6

A set of fungal extracts prepared from our collection of sediment- and soil-derived fungal isolates were evaluated for antiproliferative and cytotoxic activity in a panel of pediatric (including Ewing sarcoma) and triple-negative breast cancer cell lines. This led to the identification of several fungal extracts exhibiting desirable bioactivity,

including one very potent extract (78% cytotoxicity in the A-673 Ewing sarcoma cell line at 2 μg/mL) that was produced by a fungal isolate that was identified as a likely *Rhizopus microsporus*. This isolate was obtained as a result of our Citizen Science Soil Collection Program from a soil sample originating in Tucson, Arizona.[193] A scale-up fermentation and bioassay-guided purification of the resulting crude extract led to the isolation of **1**, which was identified on the basis of ^{1}H and ^{13}C NMR spectra, as well as LC-ESIMS data matching published values.[48, 176] In addition to this active natural product, analysis of the extract by LC-ESIMS suggested the presence of several analogs of **1** (**2**-**6**), which could not be dereplicated. As a result, efforts were made to purify these analogs and determine their chemical structures.

Table 5.1. ^{1}H NMR [∂, mult. (*J* in Hz)] spectroscopic data (500 MHz, CD_3OD) for rhizoxin analogs **2-6**

	2	**3**	**4**	**5**	**6**
No.	∂_H, mult. (*J* in Hz)	∂_H, mult. (*J* in Hz)	∂_H, mult. (*J* in Hz)	∂_H, mult. (*J* in Hz)	∂_H, mult. (*J* in Hz)
2	3.35, d (1.8)	3.30, d (1.6)	3.33, d (1.6)	3.40, d (1.9)	3.47, d (1.8)
3	3.01, dt (10.3, 1.8)	3.05, dt (9.9, 1.6)	3.05, dt (9.9, 1.7)	3.10, m	3.01, dt (9.8, 2.3, 1.8)
4	2.30, m	2.19, m	2.20, m	1.61, m	2.16, m
	0.93, d (11.2)	0.99, m	0.99, m	1.61, m	0.96, m
5	2.27, m	2.22, m	2.28, m	2.23, m	2.06, m
5a	2.79, dd (17.8, 6.6)	2.70, dd (17.7, 5.4)	2.74, dd (17.6, 6.5)	2.55, dd (15.2, 5.3)	2.60, m
	2.16, dd (17.8, 9.2)	2.13, m	2.13, m	2.32, dd (15.2, 8.5)	2.12, m
5c				3.68, s	
6	2.04, m	1.99, d (13.8)	2.07, m	1.69, m	2.19, m
	1.16, m	1.14, m	1.17, m	1.31, m	1.32, m
7	3.92, td (10.7, 2.0)	4.07, ddd (11.9, 9.9, 2.5)	4.10, ddd (11.7, 9.9, 2.3)	3.77, dt (10.5, 2.0)	4.25, ddd (11.4, 7.8, 3.4)
8	2.30, m	2.34, m	2.40, m	1.37, m	1.85, m
8a	1.10, d (6.5)	1.16, d (6.5)	1.16, d (6.5)	1.04, d (6.8)	1.15, d (7.0)
9	5.30, dd (15.3, 9.9)	5.44, m	5.70, m	3.93, dd (9.0, 5.1)	4.15, ddd (5.0, 3.5, 1.2)
10	5.64, dd (15.2, 9.9)	5.48, m	5.73, m	5.91, dd (15.9, 5.6)	6.04, dd (15.5, 3.5)
11	3.56, dd (10.0, 3.8)	4.25, d (8.2)	4.04, d (2.2)	5.95, d (15.8)	5.99, dd (15.5, 1.2)
12a	2.25, s	1.07, s	1.08, s	1.24, s	1.16, s
13	3.29, dd (10.9, 3.9)	3.31, m	3.63, dd (10.3, 3.2)	3.14, d (10.7)	3.09, d (9.7)
14	1.86, dd (15.0, 10.5)	1.82, ddd (13.0, 11.7, 2.3)	1.70, m	1.72, m	1.83, m
	1.43, dd (15.0, 10.4)	1.70, ddd (14.2, 11.2, 2.0)		1.63, m	1.57, dd (14.6, 9.7)
15	5.15, dd (10.5, 4.4)	5.08, dd (11.7, 3.9)	5.11, dt (10.8, 3.9)	5.26, dd (10.6, 6.1)	5.25, dd (10.7, 5.2)
16	1.98, m	2.25, m	2.19, m	2.04, q (6.2)	2.03, m
16a	1.00, d (6.9)	1.03, d (6.9)	1.00, d (6.8)	0.95, d (6.9)	0.99, d (6.8)
17	3.41, d (7.5)	3.34, m	3.34, m	3.47, d (6.1)	3.44, d (7.0)
17-OMe	3.17, s	3.18, s	3.17, s	3.20, s	3.18, s
18a	1.79, s	1.84, s	1.81, s	1.80, s	1.80, s
19	6.20, d (11.0)	6.19, d (10.7)	6.17, d (10.8)	6.18, d (11.0)	6.19, d (11.5)
20	6.68, dd (15.2, 10.9)	6.65, dd (15.2, 10.8)	6.65, dd (15.1, 10.8)	6.67, dd (15.2, 10.9)	6.66, dd (15.1, 10.9)
21	6.42, d (15.2)	6.45, d (15.2)	6.42, d (15.2)	6.42, d (15.2)	6.41, d (15.2)
22a	2.12, s	2.09, s	2.09, s	2.11, s	2.09, s
23	6.22, s	6.24, s	6.22, s	6.23, s	6.22, s
25	7.82, s	7.82, s	7.81, s	7.82, s	7.82, s
26a	2.45, s	2.45, s	2.43, s	2.45, s	2.45, s

Table 5.2. ^{13}C NMR spectroscopic data (125 MHz, CD_3OD) for rhizoxin analogs **2-6**

	2	**3**	**4**	**5**	**6**
No.	∂_c, mult.	∂_c, mult.	∂_c, mult.	∂_c, mult.	∂_c, mult.
1	169.2, C	168.8, C	168.7, C	169.0, C	169.1, C
2	54.1, CH	53.8, CH	53.7, CH	53.2, CH	53.2, CH
3	56.3, CH	56.4, CH	56.4, CH	57.6, CH	56.6, CH
4	37.5, CH_2	37.2, CH_2	37.8, CH_2	36.9, CH_2	36.6, CH_2
5	28.8, CH	29.0, CH	28.6, CH	30.5, CH	28.5, CH
5a	35.4, CH_2	35.6, CH_2	35.5, CH_2	41.1, CH_2	36.5, CH_2
5b	172.6, C	172.1, C	172.5, C	173.4, C	172.2, C
5c				50.6, CH_3	
6	32.2, CH_2	32.3, CH_2	32.6, CH_2	40.9, CH_2	33.8, CH_2
7	82.9, CH	83.7, CH	83.5, CH	69.6, CH	83.4, CH
8	43.3, CH	44.0, CH	43.6, CH	47.3, CH	46.6, CH
8a	16.4, CH_3	18.0, CH_3	18.0, CH_3	8.6, CH_3	13.4, CH_3
9	135.8, CH	135.8, CH	131.6, CH	73.5, CH	72.5, CH
10	127.4, CH	130.3, CH	130.0, CH	136.1, CH	128.0, CH
11	62.6, CH	75.5, CH	79.8, CH	131.3, CH	134.7, CH
12	210.0, C	75.8, C	73.9, C	73.9, C	74.0, C
12a	31.4, CH_3	16.2, CH_3	20.5, CH_3	20.1, CH_3	19.9, CH_3
13	72.6, CH	69.0, CH	70.0, CH	74.7, CH	73.6, CH
14	33.9, CH_2	28.9, CH_2	28.6, CH_2	32.6, CH_2	33.4, CH_2
15	74.7, CH	73.6, CH	73.1, CH	74.2, CH	74.8, CH
16	39.8, CH	38.5, CH	38.8, CH	39.7, CH	39.5, CH
16a	10.2, CH_3	9.2, CH_3	9.1, CH_3	9.1, CH_3	9.1, CH_3
17	87.5, CH	88.3, CH	88.0, CH	86.6, CH	87.0, CH
17-OMe	55.3, CH_3	55.1, CH_3	55.1, CH_3	55.6, CH_3	55.4, CH_3
18	135.4, C	135.9, C	135.5, C	135.4, C	135.4, C
18a	11.2, CH_3	10.7, CH_3	10.9, CH_3	11.9, CH_3	11.5, CH_3
19	129.4, CH	129.3, CH	129.1, CH	127.9, CH	128.5, CH
20	124.4, CH	124.2, CH	124.3, CH	124.4, CH	124.4, CH
21	137.0, CH	137.0, CH	137.5, CH	136.6, CH	136.7, CH
22	138.1, C	137.5, C	136.9, C	137.6, C	137.6, C
22a	13.2, CH_3	13.2, CH_3	13.2, CH_3	13.3, CH_3	13.3, CH_3
23	119.5, CH	119.6, CH	119.4, CH	119.3, CH	119.3, CH
24	137.5, C	138.1, C	138.1, C	137.8, C	138.1, C
25	136.4, CH	136.3, CH	136.3, CH	136.2, CH	136.3, CH
26	161.5, C	161.5, C	161.5, C	161.5, C	161.5, C
26a	12.0, CH_3	12.0, CH_3	11.9, CH_3	12.0, CH_3	12.0, CH_3

Rhizoxin K1 (**2**) was obtained as a white, amorphous powder and was assigned the molecular formula $C_{35}H_{47}NO_9$ on the basis of HRESIMS data ($[M+H]^+$ ion at *m/z* 626.3325, calcd 626.3329). Comparison of the ^1H and ^{13}C NMR spectra to those of **1** implied that this metabolite was most likely an analog of **1**. A series of continuous COSY correlations spanning from H-6 to H-15 indicated the quaternary C-12 carbon found in **1** was missing from **2**. This observation was further reinforced by the appearance of the H-11 spin as a doublet of doublets (3.56 ppm; $^3J_{HH}$ = 10, 4 Hz) in **2**, indicating vicinal coupling of H-11 to H-10 and H-13. Additionally, a new exocyclic ketone (210.0 ppm) was determined to be attached to C-11 based on the presence of an HMBC correlation between H-11 and C-12 (Figure 5.2). The remaining fragments of **2** appear extremely similar to **1** in terms of the ^1H and ^{13}C NMR spectra (Table C.1, Appendix C), indicating that the remainder of the molecule remained unchanged from **1**. This was confirmed through the use of 1D and 2D NMR data to establish the connectivity of atoms in **2**.

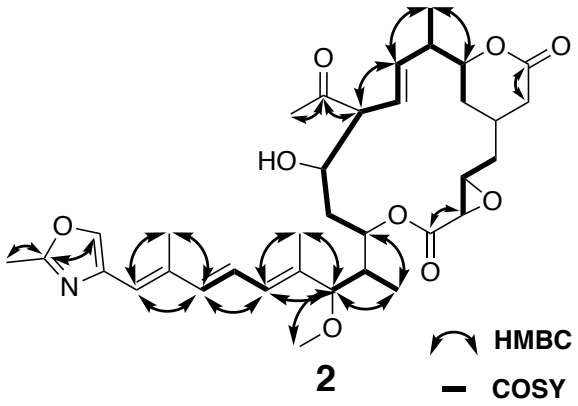

2

Figure 5.2. Key COSY and HMBC correlations for **2**

By analyzing coupling constants in the ^{1}H NMR spectrum of **2**, many similarities to those observed in **1** become readily apparent (Tables 5.1, and C.1, Appendix C) As these molecules are of the same biosynthetic origin,[50] we commenced our investigations of the relative and absolute configuration of **2** on the reasonable belief that chiral centers C-2, C-3, C-5, C-7, C-8, C-15, C-16, and C-17 were unchanged from **1**. This allowed us to focus on the assignment of configuration for the C-11 and C-13 chiral centers of the molecule. To begin, a ROESY spectrum of **2** was acquired (Figure C.7, Appendix C) and analyzed, revealing ROE cross-peaks between H-15 and H-13 (5.15 and 3.29 ppm, respectively), which supported a 13*S* assignment of configuration. Additional ROESY cross-peaks were observed between H-11 (3.56 ppm) and H-13 (3.29 ppm), which was consistent with an 11*R* assignment. However, given the novel structural motifs in **2**, we developed a second line of complementary evidence to support these assignments.

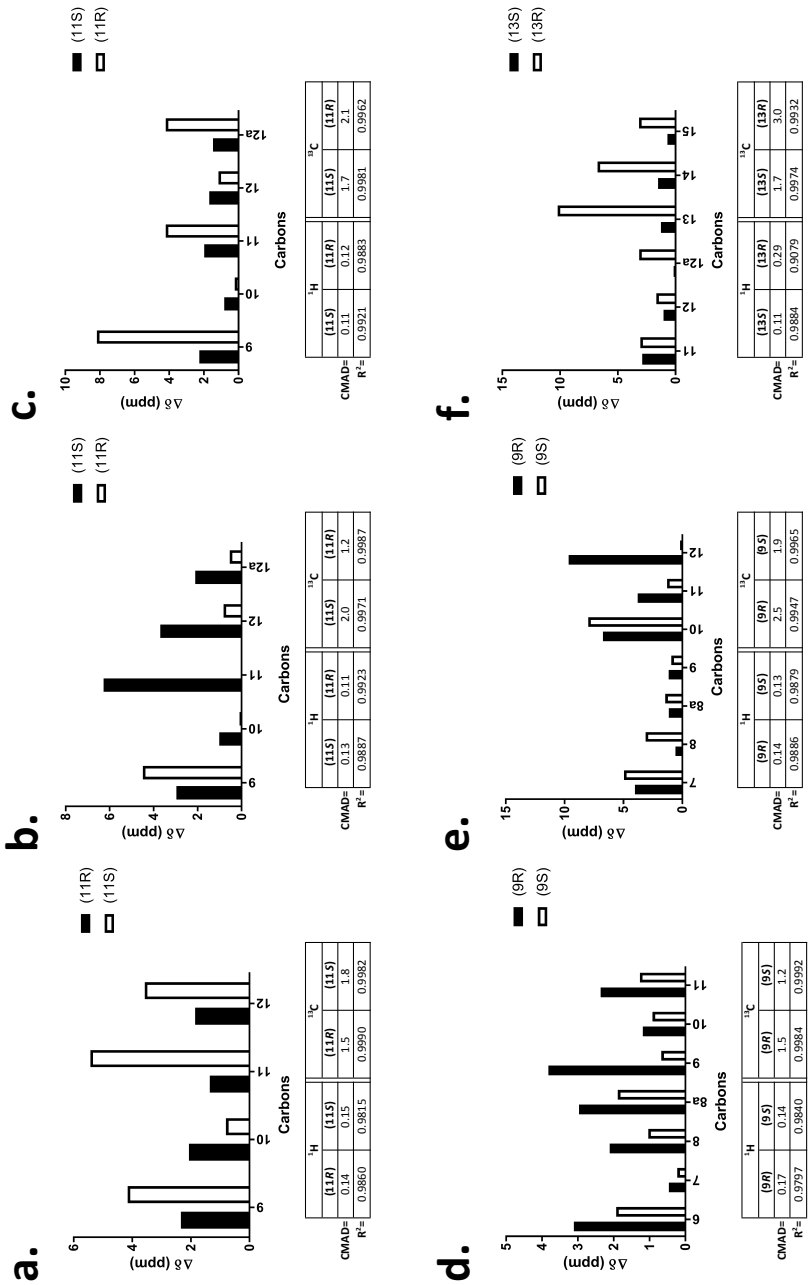

Figure 5.3. ^{13}C calculation results of two plausible stereoisomers at the mPW1PW91/6-311G(d,p)-IEFPCM (methanol)//mPW1PW91/6-31G(d)-IEFPCM (methanol) level. Includes relative errors of selected carbon nuclei (top) and corrected mean absolute deviations (CMAD) and R^2 values (bottom) for calculated vs. experimental ^{13}C and ^{1}H NMR chemical shift values of (a-e) **2**-**6** and (f) rhizoxin (**1**).

Consequently, an investigation of compound **2** was performed using gauge-independent atomic orbital (GIAO) NMR calculations at the mPW1PW91/6-311G(d,p) level of theory with Integral Equation Formalism Polarizable Continuum Model (IEFPCM) continuum dielectric solvation modeling with methanol as the solvent.[194] As we were most uncertain with the configuration at C-11, we prepared and analyzed calculated results for both the 11R and 11S diastereomers. To reduce the computational expenses of these experiments, the structure of 2 was truncated at C-19. ^{1}H and ^{13}C NMR chemical shift values and $^{3}J_{HH}$ coupling constant values were calculated for each of the two diastereomers and compared to experimentally determined values. The calculated data corresponding to the 11R diastereomers (i.e., chemical shift and coupling constants, Figure 5.3a and Tables C.14-C.15, Appendix C) showed a much stronger match with the experimental data for 2 than calculated values for the 11S diastereomer. Therefore, the structure of the new ring-contracted rhizoxin analog, rhizoxin K1, was established as shown for 2 (Figure 5.1).

Rhizoxin T1 (3) and rhizoxin T2 (4) were each obtained as white, amorphous powders and both were assigned molecular formulas of $C_{35}H_{49}NO_{10}$ on the basis of HRESIMS data ($[M+H]^+$ ions at m/z 644.3436 and 644.3435, respectively, calcd 644.3435), which corresponds to one less degree of unsaturation when compared to 1. Comparison of the ^{1}H and ^{13}C NMR spectra to those for 1 showed that the majority of the structure for 3 and 4 matched that of 1, with the exception of the region near C-12 and C-13. Both C-12 (75.5 and 75.8 ppm, respectively) and C-13 (79.8 and 73.9 ppm, respectively) appeared more deshielded in comparison to 1, which in conjunction with

the one fewer degree of unsaturation was suggestive of the 11,12-epoxide in 1 being replaced by diol moieties in 3 and 4. Further analysis of the 1D and 2D NMR data for 3 and 4 provided confirmation that both of these compounds were new diol-containing analogs of 1.[176]

Through a comparison of coupling constants observed in the ^{1}H NMR spectra of 3 and 4, we noted many similarities to those seen in 1 except a difference in those observed between H-10 and H-11. As these coupling constants varied dramatically ($^{3}J_{HH}$ = 8 Hz and 2 Hz, respectively, for 3 and 4), it was hypothesized that these two compounds were diastereomers that differed in their configurations at C-11. To further explore this hypothesis, the ROESY spectra of 3 and 4 were analyzed (Figures C.14 and C.21, Appendix C), which revealed cross-peaks between H-13 and H-15 in both molecules that were consistent with 13S configurations. Additionally, a ROESY cross-peak between H-11 (4.25 ppm) and H-13 (3.31 ppm) in 3 supported an 11R configuration; while ROESY cross-peaks between H-12a and H-13 in both 3 and 4 were consistent with 12R configurations. However, the presence of ROESY cross-peaks between H-12a and H-11 in both molecules led to uncertainty in regards to the configurations of these molecules for C-11. As such, GIAO NMR calculations were used to give further interpretive insights into the NMR data obtained for these two diasteromeric molecules.

Comparison of calculated ^{1}H and ^{13}C NMR chemical shift values for the 11R and 11S diastereomers to the experimental NMR data for 3 showed lower corrected mean absolute deviations (CMAD) in the chemical shifts and greater R^2 values, and as a result, better correlated with the 11R diastereomer (Figure 5.3b and Tables C.18-C.19, Appendix C). To support these stereochemical assignments, the experimentally

determined vicinal couplings between H-10 and H-11 for 3 and 4 were compared with calculated values. This approach gave calculated coupling constants of 9.9 Hz for the 11R diastereomer and 2.3 Hz for the 11S, which were both extremely similar to their experimentally determined values (vide supra).

Rhizoxin M3 (5) was obtained as a white, amorphous powder, and was assigned a molecular formula of $C_{36}H_{53}NO_{11}$ based on HRESIMS data ($[M+H]^+$ ion at m/z 676.3690, calcd 676.3697), which yields a total of two fewer degrees of unsaturation compared to 1. A preliminary analysis of the ^1H NMR data revealed that the resonances close in proximity to the tetrahydro-2H-pyran-2-one system varied greatly from those of 1-4. Further analysis of the ^1H and ^{13}C NMR data for this region of 5 to NMR data reported for other rhizoxin analogs revealed strong similarities in the C-5 – C-7 region of rhizoxin M2, which contains an esterified ring-opened lactone moiety.[50] The identity of this structural motif was further confirmed through an HMBC experiment, which revealed correlations between H-5c (3.68 ppm) and H-5a (2.55 and 2.32 ppm) and C-5b (173.4 ppm). Further inspection of the HMBC data showed correlations between H-8a (1.04 ppm) and C-9 (73.5 ppm), as well as between H-12a (1.24 ppm) and C-11 (131.3 ppm), suggesting the presence of the olefinic bond in **5** between C-10 and C-11.

A comparison of coupling constants in **5** versus those found for **1** and rhizoxin M2,[50] showed that the largest inconsistencies among these data sets corresponded to the region spanning H-7 to H-9. Focusing on this region, we began our determination of the configurational assignment of C-7 through the analysis of the ROESY spectrum obtained for **5** (Figure C.28, Appendix C). This analysis revealed a cross-peak between H-5 (2.23 ppm) and H-7 (3.77 ppm), which supported a 7*R* configuration. Cross-peaks were also

observed from H-8a (1.04 ppm) to H-7 (3.77 ppm) and H-9 (3.93 ppm) and from H-7 to H-9. This set of cross-peaks was suggestive of an 8*S*, 9*S* configuration for **5**. Finally, ROESY cross-peaks from H-13 (3.14 ppm) to H-12a (1.24 ppm) and H-15 (5.26 ppm) supported the assignment of 12*S*, 13*S* configurations.

With these tentative conformational assignments, we next prepared a set of calculated NMR data to evaluate the configuration assigned for C-9. GIAO NMR calculations were performed and the resulting chemical shift values for the 9*S* and 9*R* diastereomers were compared to experimentally determined chemical shifts for **5**. Comparison of these data sets revealed lower deviations in the calculated chemical shifts, lower CMAD values, and higher R^2 values for the proposed 9*S* diastereomer compared to the 9*S* diastereomer (Figure 5.3d and Tables C.20-C.21, Appendix C). Additional comparisons of the calculated vicinal coupling values between H-8 and H-9, as well as between H-9 and H-10 (8.4 Hz and 3.7 Hz, respectively, for the 9*S* diastereomer) proved the 9S diastereomer to be an excellent match with the experimentally determined coupling values. Therefore, the absolute configuration of this compound was proposed as illustrated for **5** (Figure 5.1).

Rhizoxin T3 (**6**) was obtained as a white, amorphous powder, and was found to have a molecular formula of $C_{35}H_{49}NO_{10}$ based on HRESIMS data ($[M+H]^+$ ion at *m/z* 644.3441, calcd 644.3435). This led to a calculation of one less degree of unsaturation compared to **1**. Analysis of the ^1H and ^{13}C NMR data revealed that like in compounds **1**-**4**, the tetrahydro-2*H*-pyran-2-one remained intact; however, the C-11, C-12 epoxide was missing with the olefin being shifted from C-9 to C-10 as was observed in **5**. Further analysis of data from an HMBC experiment (Figure C.27, Appendix C) provided further

evidence in support of this assignment. This structure was found to match a partial data set reported for a 11,12-deepoxy-10,11-didehydro-9,10-dihydro-9,12-dihydroxy derivative of **1**; however, no stereochemical analyses appear to have been performed for this compound.[182]

In comparing the vicinal coupling constants between H-9 (4.15 ppm) and H-10 (6.04 ppm) in **6** versus **5**, we observed considerable similarities ($^3J_{HH}$ values of 3.5 Hz and 5 Hz, respectively). This led to an initial proposal of a 9*S* configuration for **6**, but further support was desired to confirm this assignment. GIAO NMR calculations were performed and the resulting chemical shift values for the 9*S* and 9*R* diastereomers were compared to experimental chemical shift data. This analysis resulted in lower deviations in the calculated shifts versus the experimental data, lower CMAD values, and higher R^2 values for the 9*S* diastereomer (Figure 5.3e and Tables C.22-C.23, Appendix C). Additionally, the key H-9 and H-10 vicinal coupling constant was calculated as 3.9 Hz for the 9*S* diastereomer, which was found to be in strong agreement with the experimentally determined coupling value (3.5 Hz). As a result, the configuration of this compound was proposed as shown for **6** (Figure 5.1).

5.2.2 Biological Evaluation of Rhizoxins 1-6

Next, we evaluated rhizoxins **1**-**6** in terms of their biological activity by testing these compounds against a panel of pediatric cancer cell lines and evaluating their antiproliferative and cytotoxic activities. While we did not observe any cytotoxicity in the cell lines tested for compounds **2**-**6** up to a concentration of 2 μM, we did observe

notably potent cytotoxicity for compound **1** in the Ewing sarcoma cell lines that were tested.

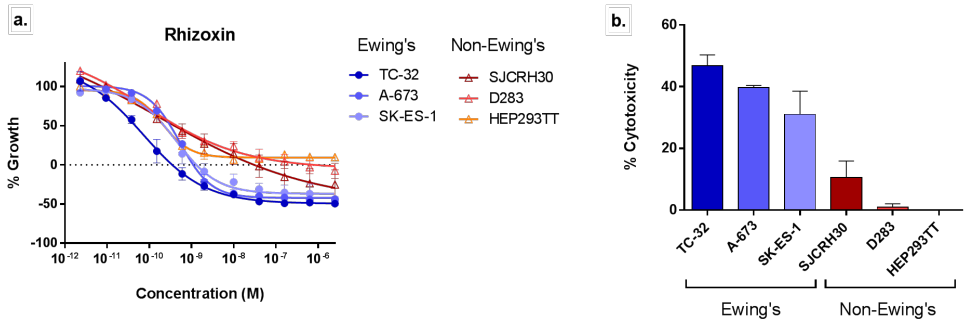

Figure 5.4. Antiproliferative and cytotoxic activity of rhizoxin in a panel of pediatric cancer cell lines. (a) Concentration-response curves for antiproliferative and cytotoxic activity of rhizoxin using the SRB assay. (b) Percent cytotoxicity of rhizoxin at 40 nM in a panel of cell lines. Using a one-way ANOVA with Tukey's post hoc test for multiple comparisons, we observe no significant difference among cell lines in the Ewing's and non-Ewing's groups. However, each comparison between a cell line in the Ewing's group and a cell line in the non-Ewing's group is significant with $p \leq 0.035$. Results are represented as the mean ± SEM. (n=3)

This compound exhibited total growth inhibition values in the sub-nanomolar range (Figure 5.4a) and showed significantly greater cytotoxicity in the Ewing sarcoma cell lines at a concentration of 40 nM, when compared to other, non-Ewing pediatric cancer cell lines such as D283 medulloblastoma, SJCRH30 rhabdomyosarcoma, and HEP293TT hepatoblastoma cell lines (Figure 5.4b). While we do observe this selective cytotoxicity for **1**, its failure to show efficacy *in vivo* during previous clinical trials[183-185] makes it less appealing, overall, as a reasonable lead for future studies.

5.2.3 Computational and Degradation Studies of the Formation of 2

Despite the lack of bioactivity observed for compound **2**, this molecule was of interest due to its novel 15-membered macrolactone core, which has not been previously

reported as a natural or synthetic analog of **1**. Wanting to study this compound further, we examined the possibility that **2** could have arisen through a rearrangement of the C-11, C-12 epoxide of **1**. In light of a recent publication by Zou et al., which revealed that some cationic epoxide rearrangements of fungal metabolites are catalyzed by enzymes produced by *Aspergillus nidulans* and *Penicillium* sp.,[195] we believed that it was possible that this rearrangement could be happening either enzymatically or chemically. To assess whether this could be occurring enzymatically, we planned to perform experiments in which **1** would be incubated with *R. microsporus* to determine if **2** formed as a result. In the process of optimizing culture conditions (Discussion C.2, Appendix C) for the production of additional quantities of **1**, we were surprised to find that we could detect compound **2** only in solid-state Cheerios and potato-dextrose broth (PDB) cultures. Additionally, we determined that **2** as well as analogs **3**-**6** began to appear only when the pH of the culture medium had significantly decreased (pH ~2-3), while the other media were unable to reach the same levels in pH due to the inclusion of buffers, leaving the pH of these media near neutral levels. These observations led us to reformulate our previous hypothesis, and to consider whether compound **2** and the other isolated rhizoxin analogs may have resulted from the acidic conditions created during the growth of the symbiotic fungus-bacterium system.

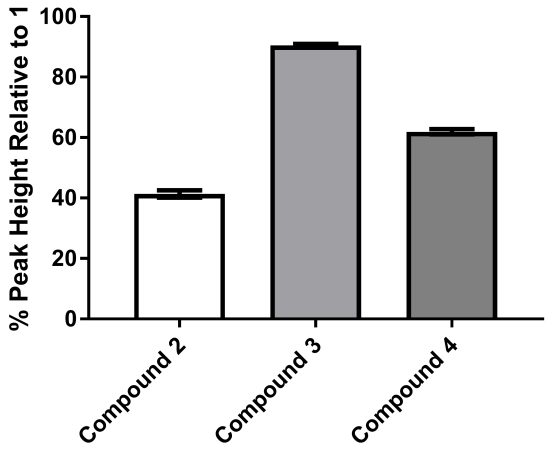

Figure 5.5. Degradation of compound **1** incubated in acidified aqueous methanol for one day. Peak heights are expressed as a percentage relative to the peak height of compound **1** ± 1 S.D. (n=3). Peak heights were taken at a wavelength of 310 nm.

With this new hypothesis, we believed that the chemical transformation to form **2** could be accomplished through either a pinacol rearrangement or a Meinwald rearrangement. Since a pinacol rearrangement would require that compounds **3** and/or **4** would serve as precursors for the formation of **2**, we set out to determine if **1**, **3**, and **4** can serve as suitable reactants to produce **2**. Compounds **1**, **3**, and **4** were incubated separately for 7 days in aqueous methanolic solutions treated with hydrochloric acid (1 mM final concentration), and the resulting reaction mixtures were sampled daily and monitored by LC-ESIMS for the formation of **2**. While we could detect **2** in as little as 24 hours when starting with **1** (Figure 5.5), we were unable to identify **2** from the samples starting with either **3** or **4**. As a result, we proposed that **2** arises from a probable Meinwald rearrangement of the C-11, C-12 epoxide of **1** under the acidic conditions produced through the culture of the fungus with its endosymbiont partner (Scheme 5.1).

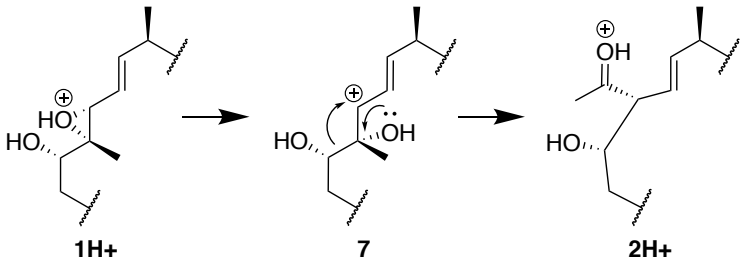

Scheme 5.1. Proposed pathway for the formation of rhizoxin **2** from **1** under mildly acidic conditions

To provide further evidence for the mechanism of this rearrangement, we used DFT calculations to approximate the energetics of the reaction steps required for this transformation to occur. Electronic and Gibbs energies were calculated for the protonated form of **1** (**1H**$^+$), the carbocation intermediate **7**, and the protonated form of **2** (**2H**$^+$), following an initial optimization at the M06-2X/6-31G(d) level of theory. Solvent effects were approximated through the use of IEFPCM solvation modeling with water as the solvent. Additional calculations of single point energies at the M06-2X/6-311++G(d,p)-IEFPCM (water) level of theory were used to correct the Gibbs free energies obtained using the 6-31G(d) basis set.[195] Following these optimization and energy calculations, transition states were determined at the M06-2X/6-31G(d)-IEFPCM (water) level of theory and were determined through intrinsic reaction coordinate calculations. Gibbs free energies were determined for each transition state, leading us to determine the approximate energy barriers to be 1.3 kcal/mol and 7.2 kcal/mol for the formation of **7** and **2H**$^+$, respectively. Based on this analysis, we also found that **2H**$^+$ is approximately 32.4 kcal/mol lower in energy than **1H**$^+$, suggesting that its formation is energetically favorable under acidic conditions (Figure 5.6).

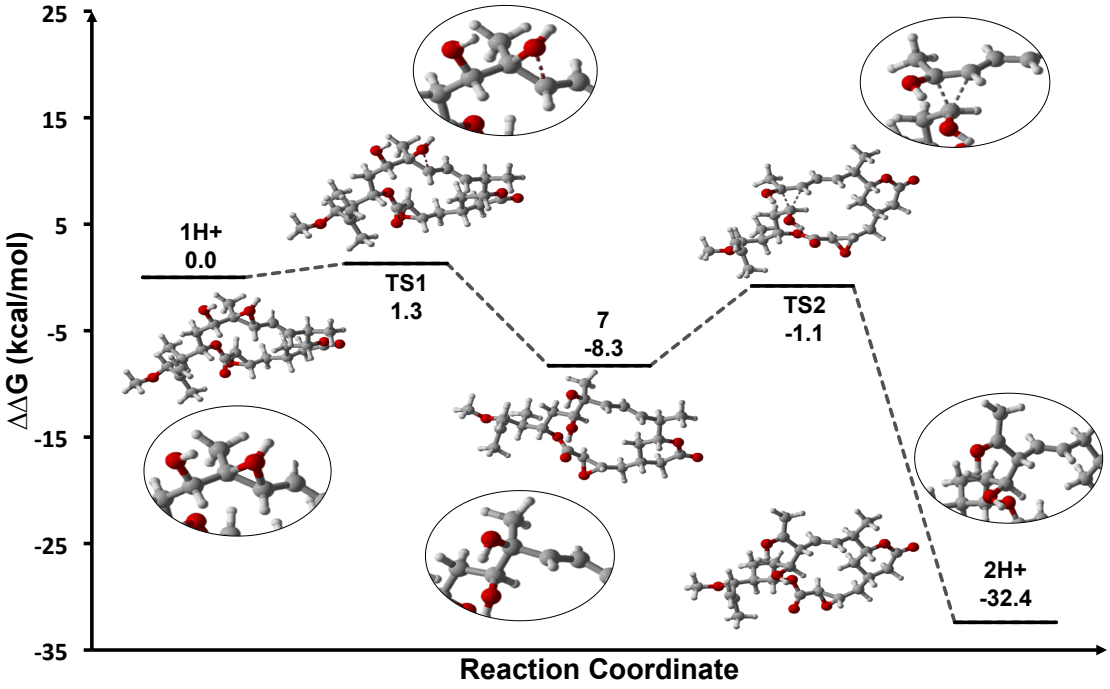

Figure 5.6. DFT calculations for the acid-catalyzed formation of **2** from **1**. Reaction pathway was calculated at M06-2X/6-311++G(d,p)-IEFPCM (water)//M06-2X/6-31G(d)-IEFPCM (water) level. All energies are given in kcal/mol.

To further address the apparent stereoselectivity in the formation of **2**, we further examined the calculated structure for allylic carbocation intermediate **7**. In order for the alkyl group to migrate to yield **2**, it would be expected to be oriented in the same plane as the empty p-orbital of the carbocation.[196-197] As such, two possible faces for migration exist. In intermediate **7**, it appeared that the *si* face of the carbocation was much more accessible for migration. To further support this observation, a scan of the energy with respect to rotation about the bond between C-11 and C-12 was carried out to examine the possibility of a *re* face migration. From this calculation, we found that the orientation favoring *si* face migration was approximately 16 kcal/mol lower in energy (Figure C.41, Appendix C), lending further support for the stereoselective formation of the 11*R* configuration in **2**.

5.2.4 Conclusions

Through the use of NMR and GIAO NMR calculations, the absolute structures of five rhizoxin analogs were determined (compounds **2**-**6**). Compound **1** was confirmed as exhibiting potent sub-nanomolar cytotoxic activity in a panel of pediatric cancer cell lines and significant cytotoxic selectivity for Ewing sarcoma cell lines in comparison to cell lines originating from other types of pediatric cancers. In contrast, compounds **2**-**6** did not show similar cytotoxic activity for any of the pediatric cancer cell lines tested or in a panel of triple negative breast cancer cell lines up to 2 μM.

Despite this lack of comparable cytotoxicity, compound **2** was of interest due to its novel skeleton when compared to other known rhizoxins. Through degradation experiments, we conclude that **2** most likely forms through an acid-catalyzed Meinwald rearrangement of rhizoxin, which is further supported by computational calculations using density functional theory. These studies found that formation of **2** from **1** is highly favorable thermodynamically under acidic conditions. Additionally, this study further emphasizes the importance and necessity of investigating the chemical and/or biochemical basis for the formation of unusual compounds and their analogs that are obtained from natural sources, and also demonstrates the power of applying DFT calculations when examining their non-enzymatic origins.

5.3 Materials and Methods

5.3.1 General Experimental Procedures

Optical rotation data was obtained using a Rudolph Research AUTOPOL III automatic polarimeter. NMR data were obtained using Varian NMR spectrometers (400

or 500 MHz for ^{1}H and 100 or 125 MHz for ^{13}C). Accurate mass (HRESIMS) data were obtained using a Waters SYNAPT G2-Si mass spectrometer. LC-ESIMS data were obtained on a Shimadzu LC-MS 2020 system (ESI quadrupole) coupled to a PDA detector, with a Phenomenex Kinetex C_{18} column (75 × 3.0 mm, 2.6 μm). The preparative HPLC system used SCL-10A VP pumps and system controller with a Phenomenex C_{18} column (250 × 21.2 mm, 5 μm), and the analytical and semi-preparative HPLC system utilized Waters 1525 binary pumps with a Waters 2998 PDA detector and a Phenomenex C_{18} column (250 × 4.6 mm, 5 μm; and 250 × 10 mm, 5 μm). All solvents were of ACS grade or better.

5.3.2 Fungal Isolate Procurement and Identification

The fungal isolate (internal designation AZ3401 RBM-3) was obtained from a soil sample collected from Tucson, Arizona. The isolate was identified as belonging to the species *Rhizopus microsporus* based on sequence analysis of the ribosomal internal transcribed spacer region and 5.8S rRNA genes (ITS1-5.8S-ITS2)[198] (GenBank accession MK037287). Additional 16S ribosomal RNA sequence analysis led to the identification of the endosymbiotic bacterium as belonging to the species *Burkholderia rhizoxinica* (GenBank accession MK041213).

5.3.3 Extraction and Purification of Rhizoxin Analogs

The isolate of *R. microsporus* was grown for a total of four weeks on Cheerios breakfast cereal that was supplemented with a 0.3% sucrose solution with 0.005% chloramphenicol added in six large mycobags (Unicorn Bags, Plano, TX). After four

weeks, the fungus was homogenized and extracted with EtOAc. The EtOAc extract (70 g) was separated using silica gel VLC with elution steps using 1:1 hexanes/DCM, DCM, 10:1 DCM/MeOH, and MeOH as eluents, yielding four fractions (Fractions A-D). Fraction C (22 g) was further separated using HP-20SS VLC and a step gradient of MeOH in water (30%, 50%, 70%, 90%, 100%) followed by a wash step of 1:1 DCM/MeOH as elution conditions, yielding six fractions (Fractions E-J). Following testing of Fractions A-J in bioassay, anticancer activity was observed for Fractions H and I. These fractions were further purified using C_{18} HPLC (250 × 21.2 mm, 5 μm) with a MeOH-H_2O gradient (50:50 to 100:0), followed by isocratic C_{18} HPLC (250 × 10 mm, 5 μm) with MeCN-H_2O (45:55) to yield rhizoxin analogs **1** (13.0 mg), **2** (3.4 mg), **3** (15.3 mg), **4** (8.1 mg), and **5** (5.7 mg), and **6** (2.9 mg).

Rhizoxin K1 (**2**)**:** white, amorphous powder; $[\alpha]^{20}_{D}$ -60.0 (*c* 0.03, MeOH); ^{1}H and ^{13}C NMR, see Tables 5.1 and 5.2; HRESIMS $[M+H]^+$ *m/z* 626.3325 (calcd for $C_{35}H_{48}NO_9$, 626.3329)

Rhizoxin T1 (**3**)**:** white, amorphous powder; $[\alpha]^{20}_{D}$ +19.6 (*c* 0.48, MeOH); ^{1}H and ^{13}C NMR, see Tables 5.1 and 5.2; HRESIMS $[M+H]^+$ *m/z* 644.3436 (calcd for $C_{35}H_{50}NO_{10}$, 644.3435)

Rhizoxin T2 (**4**)**:** white, amorphous powder; $[\alpha]^{20}_{D}$ -8.0 (*c* 0.15, MeOH); ^{1}H and ^{13}C NMR, see Tables 5.1 and 5.2; HRESIMS $[M+H]^+$ *m/z* 644.3435 (calcd for $C_{35}H_{50}NO_{10}$, 644.3435)

Rhizoxin M3 (**5**)**:** white, amorphous powder; $[\alpha]^{20}_{D}$ +38.2 (*c* 0.11, MeOH); ^{1}H and ^{13}C NMR, see Tables 5.1 and 5.2; HRESIMS $[M+H]^{+}$ *m/z* 676.3690 (calcd for $C_{36}H_{54}NO_{11}$, 676.3697)

Rhizoxin T3 (**6**)**:** white, amorphous powder; $[\alpha]^{20}_{D}$ +60.3 (*c* 0.07, MeOH); ^{1}H and ^{13}C NMR, see Tables 5.1 and 5.2; HRESIMS $[M+H]^{+}$ *m/z* 644.3441 (calcd for $C_{35}H_{50}NO_{10}$, 644.3435)

5.3.4 DFT NMR Calculations

Molecular mechanics calculations were performed using the MacroModel[199] software package within the program Maestro.[200] A Monte Carlo multiple minimum (MCMM) conformational search was performed using Merck molecular force fields (MMFFs) and structures were minimized using the truncated Newton Conjugate Gradients (TNCG) method with 500 iterations and a gradient convergence criterion of 0.05. Conformers that were within 21.0 kJ/mol of the lowest energy conformer found were stored. Each conformational search was performed with a sufficiently large number of steps to allow each conformer within 10.0 kJ/mol of the lowest energy conformer to be found an average of at least ten times. Conformers with an identical conformation of the macrolactone were eliminated using redundant conformer elimination.

Geometry optimizations, frequency calculations, and NMR calculations were done using the Gaussian 09[201] software package. All conformers remaining following redundant conformer elimination were optimized using DFT geometry optimization,

followed by a frequency calculation. These calculations were done using the mPW1PW91 functional and a 6-31G(d) basis set with Integral Equation Formalism Polarizable Continuum Model (IEFPCM) continuum dielectric solvation modeling using methanol as the solvent (ε=32.63).[194]

The calculated values of Gibbs free energy for each conformer were used to perform a Boltzmann analysis of the population of conformers. All conformers comprising ≥1% of the total population were considered for gauge-independent atomic orbitals (GIAO) method NMR chemical shift calculations at the mPW1PW91/6-311G(d,p) level of theory with IEFPCM solvation modeling using methanol as the solvent.[194] Additionally, ^{1}H-^{1}H coupling constants were calculated using the B3LYP/6-31G(d,p) level of theory.[202]

5.3.5 Biological Evaluations

The D283 (medulloblastoma), SJCRH30 (rhabdomyosarcoma), A-673 and SK-ES-1 (Ewing's sarcoma) pediatric cancer cell lines used were obtained from ATCC. The TC-32 Ewing's sarcoma cell line was obtained from the lab of Dr. Alex Bishop, and the HEP293TT hepatoblastoma cell line was obtained from the lab of Dr. Gail Tomlinson.[203] D283 cells were cultured in IMEM (Gibco) supplemented with 5% fetal bovine serum (Corning) and 50 µg/mL gentamycin (Gibco). All other cell lines were cultured in RPMI-1640 (Corning) with 5% fetal bovine serum and 0.5% gentamycin. Cells were grown using a humidified incubator at 37°C with 5% CO_2. All experiments were performed on cells within four months of being revived from liquid nitrogen.

Compounds were evaluated for cytotoxic and antiproliferative efficacy using a sulforhodamine B (SRB) assay.[204-205] Cells were initially added to tissue-culture treated 96-well plates (Falcon) at a density of 4,000-6,000 cells per well. These cells were allowed to adhere to the wells overnight. The plates were then treated with compound and allowed to incubate for 48 hours. After 48 hours, cells were fixed with 10% trichloroacetic acid (TCA). D283 medulloblastoma cells showed lower adherence, and as such, were treated with 180 μL of 20% TCA added to 200 μL media for fixation. Cell growth in the presence of the compound was calculated relative to the growth of the vehicle-treated cells. Cytotoxicity was evaluated by measuring the decrease in cell density as compared to density at the time of compound addition. Results were calculated with the GraphPad Prism 6 software package and analyzed using a one-way ANOVA with Tukey's post hoc test for multiple comparisons. Data are from three independent experiments, each of which was performed in triplicate. Compounds were dissolved in DMSO (Fisher) and stored at -20°C.

5.3.6 Chemical Transformation Studies

250 μL aliquots of 0.1 M HCl, 0.001 M HCl, or distilled water were added to glass vials, followed by an additional 200 μL of methanol. Compounds **1**, **3**, and compound **4**, were dissolved at 10 mg/mL in methanol, and 25 μL (0.25 mg) was added to each vial adjusted to a predefined pH. Samples were allowed to incubate in the dark at room temperature, and 50 μL aliquots were removed at predetermined time points (0, 1, 3, and 7 days) and mixed with 50 μL of methanol. These diluted samples were analyzed by LC-ESIMS for the presence of compound **2**. All conditions and time points were

tested and sampled in triplicate. Mean measurements were used to determine the relative quantity of **2** that was present (averaged peak heights determined at 310 nm by PDA).

5.3.7 DFT Calculations for Formation of 2

All calculations were carried out with the Gaussian 09 software package.[201] Geometry optimizations and frequency calculations were performed at the M06-2X/6-31G(d) level of theory with IEFPCM solvation with water as the solvent. Transition state calculations were carried out at the M06-2X/6-31G(d) level of theory using the Berny algorithm, followed by confirmation using intrinsic reaction coordinate calculations at the same level of theory. Single point energy calculations at the M06-2X/6-311G++(d,p) level of theory with IEFPCM solvation with water as the solvent were used to yield a correction factor for Gibbs free energies obtained at the M06-2X/6-31G(d) level of theory.[195]

Note: Research reported in this chapter was supported by the National Institutes of Health (R01GM107490).

References

1. Dias, D. A.; Urban, S.; Roessner, U., A historical overview of natural products in drug discovery. *Metabolites* **2012,** *2*, 303-336.
2. Dai, Y.; Yang, Z.; Cui, B.; Yu, C.; Zhou, L., Species diversity and utilization of medicinal mushrooms and fungi in China (Review). *Int. J. Med. Mushrooms* **2009,** *11*, 287-302.
3. Sullivan, R.; Smith, J.; Rowan, N., Medicinal mushrooms and cancer therapy: translating a traditional practice into Western medicine. *Perspect. Biol. Med.* **2006,** *49*, 159-170.
4. Schmitz, R., Friedrich Wilhelm Sertürner and the discovery of morphine. *Pharm. Hist.* **1985,** *27*, 61-74.
5. Pelletier, P.; Caventou, J., Note sur en nouvel alkalai. *Annales de Chimie et de Physique* **1818,** *8*, 323-324.
6. Pelletier, P.; Caventou, J., Suite: des recherches chimiques sur les quinquinas. *Annales de Chimie et de Physique* **1820,** *15*, 337-365.
7. Pelletier, P.; Caventou, J., Examen chimique des plusieurs végétaux de la famille des colchicées, et du principe actif qu'ils renferment. *Annales de Chimie et de Physique* **1820,** *14*, 69-81.
8. Buchner, A., Ueber das rigatallische fiebermittel und über eine in der widenrinde entdeckte alcaloidische subtanz. *Repertorium für die Pharmacie* **1828,** *29*, 405-420.
9. Schatz, A.; Bugle, E.; Waksman, S., Streptomycin, a substance exhibiting antibiotic activity against Gram-positive and Gram-negative bacteria. *Exp. Biol. Med. (London, U.K.)* **1944,** *55*, 66-69.
10. Duggar, B. M. Aureomycin and preparation of same. 1949.
11. Rebstock, M.; Crooks, H.; Controulis, J.; Bartz, Q., Chloramphenicol (chloromycetin). IV. Chemical studies. *J. Am. Chem. Soc.* **1949,** *71*, 2438-2462.
12. Garrod, L., The erythromycin group of antibiotics. *Br Med J* **1957,** *2*, 57-63.
13. Levine, D., Vancomycin: a history. *Clin. Infect. Dis.* **2006,** *42*, S5-S12.
14. Sensi, P.; Margalith, P.; Timbal, M., Rifomycin, a new antibiotic; preliminary report. *Farmaco Sci.* **1959,** *14*, 146.
15. Wöhler, F., Ueber künstliche bildung des harnstoffs. *Ann. Phys. Chem.* **1828,** *88*, 253-256.
16. Kolbe, H., Beiträge zur kenntniß der gepaarten verbindungen. *Ann. Chem. Pharm.* **1845,** *54*, 145-188.
17. Gerhardt, C., Untersuchungen über die wasserfreien organischen säuren. *Ann. Chem. Pharm.* **1853,** *87*, 149-179.
18. Woodward, R.; Doering, W., The total synthesis of quinine. *J. Am. Chem. Soc.* **1945,** *67*, 860-874.
19. Woodward, R.; Bloch, K., The cyclization of squalene in cholesterol synthesis. *J. Am. Chem. Soc.* **1953,** *75*, 2023-2024.
20. Woodward, R.; Cava, M.; Ollis, W.; Hunger, A.; Daeniker, H.; Schenker, K., The total synthesis of strychnine. *J. Am. Chem. Soc.* **1954,** *76*, 4749-4751.
21. Woodward, R.; Heusler, K.; Gosteli, J.; Naegeli, P.; Oppolzer, W.; Ramage, R.; Ranganathan, S.; Vorbrüggen, H., The total synthesis of cephalosporin C1. *J. Am. Chem. Soc.* **1966,** *88*, 852-853.

22. Corey, E.; Ghosh, A., Total synthesis of ginkgolide A. *Tetrahedron Lett.* **1988,** *29*, 3205-3206.
23. Corey, E.; Gin, D.; Kania, R., Enantioselective total synthesis of ecteinascidin 743. *J. Am. Chem. Soc.* **1996,** *118*, 9202-9203.
24. Nicolaou, K.; Yang, Z.; Liu, J.; Ueno, P.; Nantermet, R.; Guy, C.; Claiborne, C.; Renaud, J.; Couladouros, E.; Paulvannan, K.; Sorensen, E., Total synthesis of taxol. *Nature* **1994,** *367*, 630.
25. Nicolaou, K., The total synthesis of brevetoxin B: a twelve-year odyssey in organic synthesis. *Angew. Chem., Int. Ed. Engl.* **1996,** *35*, 588-607.
26. Nicolaou, K.; Daines, R.; Chakraborty, T.; Ogawa, Y., Total synthesis of amphotericin B. *J. Am. Chem. Soc.* **1987,** *109*, 2821-2822.
27. Nicolaou, K.; Mitchell, H.; Jain, N.; Winssinger, N.; Hughes, R.; Bando, T., Total synthesis of vancomycin. *Angew. Chem., Int. Ed.* **1999,** *38*, 240-244.
28. Newman, D. J.; Cragg, G. M., Natural products as sources of new drugs from 1981 to 2014. *J. Nat. Prod.* **2016,** *79*, 629-661.
29. Li, J.; Vederas, J., Drug discovery and natural products: end of an era or an endless frontier? *Science* **2009,** *325*, 161-165.
30. Kartal, M., Intellectual property protection in the natural product drug discovery, traditional herbal medicine and herbal medicinal products. *Phytother. Res.* **2007,** *21*, 113-119.
31. Baker, D.; Chu, M.; Oza, U.; Rajgarhia, V., The value of natural products to future pharmaceutical discovery. *Nat. Prod. Rep.* **2007,** *24*, 1225-1244.
32. Bérdy, J., Bioactive microbial metabolites: A personal view. *J. Antibiot.* **2005,** *58*, 1-26.
33. Fleming, A., On the antibacterial action of cultures of a *Penicillium*, with special reference to their use in the isolation of *B. influenzæ*. *Br. J. Exp. Pathol.* **1929,** *10*, 226-236.
34. Ligon, B., Penicillin: its discovery and early development. *Semin. Pediatr. Infect. Dis.* **2004,** *15*, 52-57.
35. Tugwell, P.; Bombardier, C.; Tugwell, P.; Gent, M.; Bennett, K.; Roberts, R.; Ludwin, D.; Bensen, W.; Carette, S.; Chalmers, A.; Klinkhoff, A.; Esdaile, J.; Kraag, G., Low-dose cyclosporin versus placebo in patients with rheumatoid arthritis. *Lancet* **1990,** *335*, 1051-1055.
36. Ellis, C.; Gorsulowsky, D.; Hamilton, T.; Billings, J.; Brown, M.; Headington, J.; Cooper, K.; Baadsgaard, O.; Duell, E.; Annesley, T.; Turcotte, J.; Voorhees, J., Cyclosporine improves psoriasis in a double-blind study. *JAMA, J. Am. Med. Assoc.* **1986,** *256*, 3110-3116.
37. Brynskov, J.; Freund, L.; Rasmussen, S.; Lauritsen, K.; de Muckadell, O.; Williams, N.; MacDonald, A.; Tanton, R.; Molina, F.; Campanini, M.; Bianchi, P.; Ranzi, T.; di Palo, F.; Malchow-Møller, A.; Thomsen, O.; Tage-Jensen, U.; Binder, V.; Rus, P., A placebo-controlled, double-blind, randomized trial of cyclosporine therapy in active chronic Crohn's disease. *N. Engl. J. Med.* **1989,** *321*, 845-850.
38. Cohen, D.; Loertscher, R.; Rubin, M.; Tilney, N.; Carpenter, C.; Strom, T., Cyclosporine: a new immunosuppressive agent for organ transplantation. *Ann. Intern. Med.* **1984,** *101*, 667-682.

39. Harvey, C.; Tang, M.; Schlecht, U.; Horecka, J.; Fischer, C.; Lin, H.; Li, J.; Naughton, B.; Cherry, J.; Miranda, M.; Li, Y.; Chu, A.; Hennessy, J.; Vandova, G.; Inglis, D.; Aiyar, R.; Steinmetz, L.; Davis, R.; Medema, M.; Sattely, E.; Khosla, C.; St. Onge, R.; Tang, Y.; Hillenmeyer, M., HEx: a heterlogous expression platform for the discovery of fungal natural products. *Sci. Adv.* **2018,** *4*, eaar5459.
40. Roth, B., The discovery and development of atorvastatin, a potent novel hypolipidemic agent. In *Prog. Med. Chem.*, King, F.; Oxford, A.; Reitz, A.; Dax, S., Eds. Elsevier: 2002; Vol. 40, pp 1-22.
41. Blackwell, M., The fungi: 1, 2, 3 ... 5.1 million species? *Am. J. Bot.* **2011,** *98*, 426-438.
42. Bergmann, S.; Funk, A.; Scherlach, K.; Schroeckh, V.; Shelest, E.; Horn, U.; Hertweck, C.; Brakhage, A., Activation of a silent fungal polyketide biosynthesis pathway through regulatory cross talk with a cryptic nonribosomal peptide synthetase gene cluster. *Appl. Environ. Microbiol.* **2010,** *76*, 8143-8149.
43. Keller, N.; Turner, G.; Bennett, J., Fungal secondary metabolism -- from biochemistry to genomics. *Nat. Rev. Microbiol.* **2005,** *3*, 937-947.
44. Stack, D.; Neville, C.; Doyle, S., Nonribosomal peptide synthesis in *Aspergillus fumigatus* and other fungi. *Microbiology* **2007,** *153*, 1297-1306.
45. Schwarzer, D.; Finking, R.; Marahiel, M., Nonribosomal peptides: from genes to products. *Nat. Prod. Rep.* **2003,** *20*, 275-287.
46. Schmidt-Dannert, C., Biosynthesis of terpenoid natural products in fungi. In *Biotechnology of Isoprenoids*, Schrader, J.; Bohlmann, J., Eds. Springer, Cham: 2014; Vol. 148, pp 19-61.
47. Xu, W.; Gavia, D.; Tang, Y., Biosynthesis of fungal indole alkaloids. *Nat. Prod. Rep.* **2014,** *31*, 1474-1887.
48. Iwasaki, S.; Kobayashi, H.; Furukawa, J.; Namikoshi, M.; Okuda, S.; Sato, Z.; Matsuda, I.; Noda, T., Studies on macrocyclic lactone antibiotics VII. Structure of a phytotoxin "rhizoxin" produced by *Rhizopus chinensis*. *J. Antibiot.* **1984,** *37*, 354-362.
49. Partida-Martinez, L.; Hertweck, C., Pathogenic fungus harbours endosymbiotic bacteria for toxin production. *Nature* **2005,** *437*, 884-888.
50. Scherlach, K.; Partida-Martinez, L.; Dahse, H.; Hertweck, C., Antimitotic rhizoxin derivatives from a cultured bacterial endosymbiont of the rice pathogenic fungus *Rhizopus microsporus*. *J. Am. Chem. Soc.* **2006,** *128*, 11529-11536.
51. Erba, E.; Bergamaschi, D.; Bassano, L.; Damia, G.; Ronzoni, S.; Faircloth, G.; D'Incalci, M., Ecteinascidin-743 (ET-743), a natural marine compound, with a unique mechanism of action. *Eur. J. Cancer* **2001,** *37*, 97-105.
52. Schofield, M.; Jain, S.; Porat, D.; DIck, G.; Sherman, D., Identification and analysis of the bacterial endosymbiont specialized for the production of the chemotherapeutic natural product ET-743. *Environ. Microbiol.* **2015,** *17*, 3964-3975.
53. Rath, C.; Janto, B.; Earl, J.; Ahmed, A.; Hu, F.; Hiller, L.; Dahlgren, M.; Kraft, R.; Yu, F.; Wolff, J.; Kweon, H.; Christiansen, M.; Håkansson, K.; Williams, R.; Ehrlich, G.; Sherman, D., Meta-omic characterization of the marine invertebrate microbial consortium that produces the chemotherapeutic natural product ET-743. *ACS Chem. Biol.* **2011,** *6*, 1244-1256.

54. Sabater-Muñoz, B.; Toft, C.; Alvarez-Ponce, D.; Fares, M., Chance and necessity in the genome evolution of endosymbiotic bacteria of insects. *ISME J.* **2017,** *11*, 1291-1304.
55. Manzano-Marín, A.; Latorre, A., Snapshots of a shrinking partner: genome reduction in *Serratia symbiotica*. *Sci. Rep.* **2016,** *6*, 32590.
56. Kikuchi, Y., Endosymbiotic bacteria in insects: their diversity and culturability. *Microbes Environ.* **2009,** *24*, 195-204.
57. Stewart, E., Growing unculturable bacteria. *J. Bacteriol.* **2012,** *194*, 4151-4160.
58. Strobel, G.; Daisy, B., Bioprospecting for microbial endophytes. *Microbiol. Mol. Biol. Rev.* **2003,** *67*, 491-502.
59. Deshmukh, S.; Verekar, S.; Bhave, S., Endophytic fungi: a reservoir of antibacterials. *Front. Microbiol.* **2015,** *5*, 715.
60. Guo, B.; Wang, Y.; Sun, X.; Tang, K., Bioactive natural products from endophytes: a review. *Appl. Biochem. Microbiol.* **2008,** *44*, 136-142.
61. Kusari, S.; Zühlke, S.; Spiteller, M., Effect of artificial reconstitution of the interaction between the plant *Camptotheca acuminata* and the fungal endophyte *Fusarium solani* on camptothecin biosynthesis. *J. Nat. Prod.* **2011,** *74*, 764-775.
62. Hover, B.; Kim, S.; Katz, M.; Charlop-Powers, Z.; Owen, J.; Ternei, M.; Maniko, J.; Estrela, A.; Molina, H.; Park, S.; Perlin, D.; Brady, S., Culture-independent discovery of the malacidins as calcium-dependent antibiotics with activity against multidrug-resistant Gram-positive pathogens. *Nat. Microbiol.* **2018,** *3*, 415-422.
63. Milshetyn, A.; Schneider, J. S.; Brady, S. F., Mining the metabiome: identifying novel natural products from microbial communities. *Chem. Biol.* **2014,** *21*, 1211-1223.
64. Branca, M.; Garber, K.; DeFrancesco, L., Nature Biotechnology's academic spinouts of 2017. *Nat. Biotechnol.* **2018,** *36*, 297-306.
65. Ling, L.; Schneider, T.; Peoples, A.; Spoering, A.; Engels, I.; Conlon, B.; Meuller, A.; Schäberle, T.; Hughes, D.; Epstein, S.; Jones, M.; Lazarides, L.; Steadman, V.; Cohen , D.; Felix, C.; Fetterman, K.; Millett, W.; Nitti, A.; Zullo, A.; Chen, C.; Lewis, K., A new antibiotic kills pathogens without detectable resistance. *Nature* **2015,** *517*, 455-459.
66. Gruene, T.; Wennmacher, J.; Zaubitzer, C.; Holstein, J.; Heidler, J.; Fecteau-Lefebvre, A.; De Carlo, S.; Müller, E.; Goldie, K.; Regeni, I.; Li, T.; Santiso-Quinones, G.; Steinfield, G.; Handschin, S.; van Genderen, E.; van Bokhoven, J.; Clever, G.; Pantelic, R., Rapid structure determination of microcrystalline molecular compounds using electron diffraction. *Angew. Chem., Int. Ed. Engl.* **2018**, Accepted Author Manuscript.
67. Jones, C.; Martynowycz, M.; Hattne, J.; Fulton, T.; Stoltz, B.; Rodriguez, J.; Nelson, H.; Gonen, T., The cryoEM method MicroED as a powerful tool for small molecule structure determination. *ACS Cent. Sci.* **2018,** *4*, 1587-1592.
68. Sutton, M.; Sternberg, M.; Koumans, E. H.; McQuillan, G.; Berman, S.; Markowitz, L., The prevalence of *Trichomonas vaginalis* infection among reproductive-age women in the United States, 2001-2004. *Clin. Infect. Dis.* **2007,** *45*, 1319-26.
69. Kissinger, P., *Trichomonas vaginalis*: a review of epidemiologic, clinical and treatment issues. *BMC Infect. Dis.* **2015,** *15*, 307.
70. Gabriel, G.; Robertson, E.; Thin, R. N., Single dose treatment of trichomoniasis. *J. Int. Med. Res.* **1982,** *10*, 129-30.

71. Aubert, J. M.; Sesta, H. J., Treatment of vaginal trichomoniasis. Single, 2-gram dose of metronidazole as compared with a seven-day course. *The Journal of reproductive medicine* **1982,** *27*, 743-745.
72. Howe, K.; Kissinger, P. J., Single-dose compared with multidose metronidazole for the treatment of trichomoniasis in women: a meta-analysis. *Sex. Transm. Dis.* **2017,** *44*, 29-34.
73. Bendesky, A.; Menéndez, D.; Ostrosky-Wegman, P., Is metronidazole carcinogenic? *Mutat. Res.* **2002,** *511*, 133-144.
74. Dobiás, L.; Černá, M.; Rössner, P.; Šrám, R., Genotoxicity and carciogenicity of metronidazole. *Mutat. Res.* **1994,** *317*, 177-194.
75. Centers for Disease Control and Prevention 2015 sexually transmitted diseases treatment guidelines: trichomoniasis. https://www.cdc.gov/std/tg2015/trichomoniasis.htm (accessed June 28, 2018).
76. Kirkcaldy, R. D.; Augostini, P.; Asbel, L. E.; Bernstein, K. T.; Kerani, R. P.; Mettenbrink, C. J.; Pathela, P.; Schwebke, J. R.; Secor, W. E.; Workowski, K. A.; Davis, D.; Braxton, J.; Weinstock, H. S., *Trichomonas vaginalis* antimicrobial drug resistance in 6 U.S. cities, STD Surveillance Network, 2009-2010. *Emerging Infect. Dis.* **2012,** *18*, 939-43.
77. Schwebke, J. R.; Barrientes, F. J., Prevalence of Trichomonas vaginalis isolates with resistance to metronidazole and tinidazole. *Antimicrob Agents Chemother* **2006,** *50*, 4209-10.
78. Desrivot, J.; Waikedre, J.; Cabalion, P.; Herrenknecht, C.; Bories, C.; Hocquemiller, R.; Fournet, A., Antiparasitic activity of some New Caledonian medicinal plants. *J. Ethnopharmacol.* **2007,** *112*, 7-12.
79. Calzada, F.; Yepez-Mulia, L.; Tapia-Contreras, A., Effect of Mexican medicinal plant used to treat trichomoniasis on *Trichomonas vaginalis* trophozoites. *J. Ethnopharmacol.* **2007,** *113*, 248-251.
80. Lara-Díaz, V.; Gaytán-Ramos, A.; Dávalos-Balderas, A.; Santos-Guzmán, J.; Mata-Cárdenas, B.; Vargas-Villarreal, J.; Barbosa-Quintana, A.; Sanson, M.; López-Reyes, A.; Moreno-Cuevas, J., Microbiological and toxicological effects of Perla black bean (*Phaseolus vulgaris* L.) extracts: *in vitro* and *in vivo* studies. *Basic Clin. Pharmacol. Toxicol.* **2009,** *104*, 81-86.
81. Moon, T.; Wilkinson, J.; Cavanagh, H., Antiparasitic activity of two *Lavandula* essential oils against *Giardia duodenalis*, *Trichomonas vaginalis*, and *Hexamita inflata*. *Parasitol. Res.* **2006,** *99*, 722-728.
82. Kaneda, Y.; Tanaka, T.; Saw, T., Effects of berberine, a plant alkaloid, on the growth of anaerobic protozoa in axenic culture. *Tokai J. Exp. Clin. Med.* **1990,** *15*, 417-423.
83. Wu, J.; Zhang, M.; Ding, D.; Tan, T.; Yan, B., Effect of *Cladonia alpestris* on *Trichomonas vaginalis in vitro*. *Chinese Journal of Parasitology and Parasitic Diseases* **1995,** *13*, 126-129.
84. Wang, H., Antitrichomonal action of emodin in mice. *J. Ethnopharmacol.* **1993,** *40*, 111-116.
85. Bhagwat, P.; Gokhale, B.; Sane, H.; Thirumalachar, M., Assessment of antitrichomonal activity of hamycin. *Indian J. Med. Res.* **1964,** *52*, 36-37.

86. He, W.; VanPuyvelde, L.; Maes, L.; Bosselaers, J.; DeKimpe, N., Antitrichomonas *in vitro* activity of *Cussonia holstii* Engl. *Nat. Prod. Res.* **2003,** *17*, 127-133.
87. Loyola, L.; Bórquez, J.; Morales, G.; Araya, J.; González, J.; Neira, I.; Sagua, H.; San-Martín, A., Diterpenoids from *Azorella yareta* and their trichomonicidal activities. *Phytochemistry* **2001,** *56*, 177-180.
88. Scopel, M.; dos Santos, O.; Frasson, A.; Abraham, W.; Tasca, T.; Henriques, A.; Macedo, A., Anti-*Trichomonas vaginalis* activity of marine-associated fungi from the South Brazilian Coast. *Exp. Parasitol.* **2013,** *133*, 211-216.
89. Duarte, M.; Seixas, A.; de Carvalho, M.; Tasca, T.; Macedo, A., Amaurocine: anti-*Trichomonas vaginalis* protein produced by the basidiomycete *Amauroderma camerarium*. *Exp. Parasitol.* **2016,** *161*, 6-11.
90. Kayser, O.; Kiderlen, A.; Croft, S., Natural products as antiparasitic drugs. *Parasitol. Res.* **2003,** *90*, S55-S62.
91. Meingassner, J.; Thurner, J., Strain of *Trichomonas vaginalis* resistant to metronidazole and other 5-nitroimidazoles. *Antimicrob. Agents Chemother.* **1979,** *15*, 254-257.
92. Campos Aldrete, M.; Salgado-Zamora, H.; Luna, J.; Meléndez, E.; Meráz-Ríos, M., A high-throughput colorimetric and fluorometric microassay for the evaluation of nitroimidazole derivatives anti-*Trichomonas* activity. *Toxicol. in Vitro* **2005,** *19*, 1045-1050.
93. Duarte, M.; Giordani, R.; De Carli, G.; Zuanazzi, J.; Macedo, A.; Tasca, T., A quantitative resazurin assay to determinate the viability of *Trichomonas vaginalis* and the cytotoxicity of organic solvents and surfactant agents. *Exp. Parasitol.* **2009,** *123*, 195-198.
94. Humphreys, M.; Allman, R.; Lloyd, D., Determination of the viability of *Trichomonas vaginalis* using flow cytometry. *Cytometry* **1994,** *15*, 343-348.
95. Chen, J. L.; Steele, T. W. J.; Stuckey, D. C., Modeling and application of a rapid fluorescence-based assay for biotoxicity in anaerobic digestion. *Environ. Sci. Technol.* **2015,** *49*, 13463-13471.
96. Forestier, C.; Späth, G.; Prina, E.; Dasari, S., Simultaneous multi-parametric analysis of *Leishmania* and of its hosting mammal cells: a high content imaging-based method enabling sound drug discovery process. *Microb. Pathog.* **2015,** *88*, 103-108.
97. Ruelius, H.; Gauche, A., Fusarubin, a naphthoquinone coloring matter from Fusaria. *Justus Liebigs Ann. Chem.* **1950,** *569*, 38-59.
98. Arnstein, H.; Cook, A., Production of antibiotics by fungi. Part III. Javanicin. An antibacterial pigment from *Fusarium javanicum*. *J. Chem. Soc.* **1947,** *1947*, 1021-1028.
99. Arsenault, G., Fungal metabolites. III. Quinones from *Fusarium solani* D2 purple and structure of (+)-solaniol. *Tetrahedron* **1968,** *24*, 4745-4749.
100. Kurobane, I. Z., N.; Fukuda, A, New metabolites of *Fusarium martii* related to dihydrofusarubin. *J. Antibiot.* **1985,** *39*, 205-214.
101. Hashimoto, J.; Motohashi, K.; Sakamoto, K.; Hashimoto, S.; Yamanouchi, M.; Tanaka, H.; Takahashi, T.; Takagi, M.; Shin-ya, K., Screening and evaluation of new inhibitors of hepatic glucose production. *J. Antibiot.* **2009,** *62*, 625-629.

102. Hughes, W.; Gray, V.; Gutteridge, W.; Latter, V.; Pudney, M., Efficacy of a hydroxynaphthoquinone, 566C80, in experimental *Pneumocystis carinii* pneumonitis. *Antimicrob. Agents Chemother.* **1990,** *34*, 225-228.
103. Baggish, A.; Hill, D., Antiparasitic agent atovaquone. *Antimicrob. Agents Chemother.* **2002,** *46*, 1163-1173.
104. Baell, J. B., Feeling nature's PAINS: Natural products, natural product drugs, and pan assay interference compounds (PAINS). *J. Nat. Prod.* **2016,** *79*, 616-28.
105. Tabata, N.; Tomoda, H.; Matsuzaki, K.; Omura, S., Structure and biosynthesis of xanthoquinodins, anticoccidial antibiotics. *J. Am. Chem. Soc.* **1993,** *115*, 8558-8564.
106. Sobel, J., Is there a protective role for vaginal flora? *Curr. Infect. Dis. Rep.* **1999,** *1*, 379-383.
107. Ma, B.; Forney, L.; Ravel, J., The vaginal microbiome: rethinking health and diseases. *Annu. Rev. Microbiol.* **2012,** *66*, 371-389.
108. Davids, B.; Gillin, F., Methods for *Giardia* culture, cryopreservation, encystation, and excystation *in vitro*. In *Giardia A Model Organism*, Luján, H.; Svärd, S., Eds. SpringerWienNewYork: Wien, Austria, 2011; pp 381-394.
109. Paget, T.; Lloyd, D., *Trichomonas vaginalis* requires traces of oxygen and high concentrations of carbon dioxide for optimal growth. *Mol. Biochem. Parasitol.* **1990,** *41*, 65-72.
110. Hansen, M.; Nielsen, S.; Berg, K., Re-examination and further development of a precise and rapid dye method for measuring cell growth/cell kill. *J. Immunol. Methods* **1989,** *119*, 203-210.
111. Fieser, L., The tautomerism of hydroxy quinones. *J. Am. Chem. Soc.* **1928,** *50*, 439-465.
112. Sreelatha, T.; Kandhasamy, S.; Dinesh, R.; Shruthy, S.; Shweta, S.; Mukesh, D.; Karunagaran, D.; Balaji, R.; Mathivanan, N.; Perumal, P., Synthesis and SAR study of novel anticancer and antimicrobial naphthoquinone amide derivatives. *Bioorg. Med. Chem. Lett.* **2014,** *24*, 3647-3651.
113. Burns, C.; Gill, M.; Saubern, S., Pigments of fungi. XXI. Synthesis of (±)-6-demethoxyaustrocortirubin. *Aust. J. Chem.* **1991,** *44*, 1427-1445.
114. Asao, T.; Büchi, G.; Abdel-Kader, M.; Chang, S.; Wick, E.; Wogan, G., The structures of aflatoxins B and G_1. *J. Am. Chem. Soc.* **1965,** *87*, 882-886.
115. Eaton, D.; Gallagher, E., Mechanisms of aflatoxin carcinogenesis. *Annu. Rev. Pharmacol. Toxicol.* **1994,** *34*, 135-172.
116. Monson, M.; Coulombe, R.; Reed, K., Aflatoxicosis: lessons from toxicity and responses to aflatoxin B_1 in poultry. *Agriculture* **2015,** *5*, 742-777.
117. Squire, R., Ranking animal carcinogens: a proposed regulatory approach. *Science* **1981,** *214*, 877-880.
118. Kew, M., Aflatoxins as a cause of hepatocellular carcinoma. *J. Gastrointestin. Liver Dis.* **2013,** *22*, 305-310.
119. Liu, Y.; Wu, F., Global burden of aflatoxin-induced hepatocellular carcinoma: a risk assessment. *Environ. Health Perspect.* **2010,** *118*, 818-824.
120. Bennett, J.; Klich, M., Mycotoxins. *Clin. Microbiol. Rev.* **2003,** *16*, 497-516.
121. Klich, M., *Aspergillus flavus*: the major producer of aflatoxin. *Mol. Plant Pathol.* **2007,** *8*, 713-722.

122. Gallagher, E.; Kunze, K.; Stapleton, P.; Eaton, D., The kinetics of aflatoxin B_1 oxidation by human cDNA-expressed and human liver microsomal cytochromes P450 1A2 and 3A4. *Toxicol. Appl. Pharmacol.* **1996,** *141*, 595-606.
123. Ramsdell, H.; Parkinson, A.; Eddy, A.; Eaton, D., Bioactivation of aflatoxin B_1 by human liver microsomes: role of cytochrome P450 IIIA enzymes. *Toxicol. Appl. Pharmacol.* **1991,** *106*, 436-447.
124. Sudakin, D., Dietary aflatoxin exposure and chemoprevention of cancer: a clinical review. *Clin. Toxicol.* **2003,** *41*, 195-204.
125. Kensler, T.; He, X.; Otieno, M.; Egner, P.; Jacobson, L.; Chen, B.; Wang, J.; Zhu, Y.; Zhang, B.; Wang, J.; Wu, Y.; Zhang, Q.; Qian, G.; Kuang, S.; Fang, X.; Li, Y.; Yu, L.; Prochaska, H.; Davidson, N.; Gordon, G.; Gorman, M.; Zarba, A.; Enger, C.; Muñoz, A.; Helzlsouer, K., Oltipraz chemoprevention trial in Qidong, People's Republic of China: modulation of serum aflatoxin albumin adduct biomarkers. *Cancer Epidemiol., Biomarkers Prev.* **1998,** *7*, 127-134.
126. Egner, P.; Wang, J.; Zhu, Y.; Zhang, B.; Wu, Y.; Zhang, Q.; Qian, G.; Kuang, S.; Gange, S.; Jacobson, L.; Helzlsouer, K.; Bailey, G.; Groopman, J.; Kensler, T., Chlorophyllin intervention reduces aflatoxin-DNA adducts in individuals at high risk for liver cancer. *Proc. Natl. Acad. Sci. U. S. A.* **2001,** *98*, 14601-14606.
127. Gerets, H.; Tilmant, K.; Gerin, B.; Chanteux, H.; Depelchin, B.; Dhalluin, S.; Atienzar, F., Characterization of primary human hepatocytes, HepG2 cells, and HepaRG cells at the mRNA level and CYP activity in response to inducers and their predictivity for the detection of human hepatotoxins. *Cell Biol. Toxicol.* **2012,** *28*, 69-87.
128. Chen, X.; Murdoch, R.; Shafer, D.; Ajuwon, K.; Applegate, T., Cytotoxicity of various chemicals and mycotoxins in fresh primary duck embryonic fibroblasts: a comparison to HepG2 cells. *J. Appl. Toxicol.* **2016,** *36*, 1437-1445.
129. Yokoyama, Y.; Sasaki, Y.; Terasaki, N.; Kawataki, T.; Takekawa, K.; Iwase, Y.; Shimizu, T.; Sanoh, S.; Ohta, S., Comparison of drug metabolism and its related hepatotoxic effects in HepaRG, cryopreserved human hepatocytes, and HepG2 cell cultures. *Biol. Pharm. Bull.* **2018,** *41*, 722-732.
130. Ang, M.; Pethe, K., Contribution of high-content imaging technologies to the development of anti-infective drugs. *Cytometry, Part A* **2016,** *89*, 755-760.
131. Bammler, T.; Slone, D.; Eaton, D., Effects of dietary oltipraz and ethoxyquin on aflatoxin B_1 biotransformation in non-human primates. *Toxicol. Sci.* **2000,** *54*, 30-41.
132. Valdivia, A.; Martínez, A.; Damián, F.; Quezada, T.; Ortíz, R.; Martínez, C.; Llamas, J.; Rodríguez, M.; Yamamoto, L.; Jaramillo, F.; Loarca-Piña, M.; Reyes, J., Efficacy of *N*-acetylcysteine to reduce the effects of aflatoxin B_1 intoxication in broiler chickens. *Poult. Sci.* **2001,** *80*, 727-734.
133. Sandilands, E.; Bateman, D., Adverse reactions associated with acetylcysteine. *Clin. Toxicol.* **2009,** *47*, 81-88.
134. Cai, S.; Risinger, A.; Nair, S.; Peng, J.; Anderson, T.; Du, L.; Powell, D.; Mooberry, S.; Cichewicz, R., Identification of compounds with efficacy against malarial parasites from common North American plants. *J. Nat. Prod.* **2016,** *79*, 490-498.
135. Sansen, S.; Yano, J.; Reynald, R.; Schoch, G.; Griffin, K.; Stout, C.; Johnson, E., Adaptations for the oxidation of polycyclic aromatic hydrocarbons exhibited by the structure of human P450 1A2. *J. Biol. Chem.* **2007,** *282*, 14348-14355.

136. Dutkiewicz, Z.; Mikstacka, R., Structure-based drug design for cytochrome P450 family 1 inhibitors. *Bioinorg. Chem. Appl.* **2018,** *2018*, 1-21.
137. Watanabe, Y.; Kojima, H.; Takeuchi, S.; Uramaru, N.; Sanoh, S.; Sugihara, K.; Kitamura, S.; Ohta, S., Metabolism of UV-filter benzophenone-3 by rat and human liver microsomes and its effect on endocrine-disrupting activity. *Toxicol. Appl. Pharmacol.* **2015,** *282*, 119-128.
138. Takemoto, K.; Yamazaki, H.; Nakajima, M.; Yokoi, T., Genotoxic activation of benzophenone and its two metabolites by human cytochrome P450s in SOS/*umu* assay. *Mutat. Res.* **2002,** *519*, 199-204.
139. Shimada, T.; Tanaka, K.; Takenaka, S.; Murayama, N.; Martin, M.; Foroozesh, M.; Yamazaki, H.; Guengerich, F.; Komori, M., Structure-function relationships of inhibition of human cytochromes P450 1A1, 1A2, 1B1, 2C9, and 3A4 by 33 flavonoid derivatives. *Chem. Res. Toxicol.* **2010,** *23*, 1921-1935.
140. Mikstacka, R.; Wierzchowski, M.; Dutkiewicz, Z.; Gielara-Korzańska, A.; Korzański, A.; Teubert, A.; Sobiak, S.; Baer-Dubowska, W., 3,4,2'-trimethoxy-*trans*-stilbene - a potent CYP1B1 inhibitor. *MedChemComm* **2014,** *5*, 496-501.
141. Takemura, H.; Itoh, T.; Yamamoto, K.; Sakakibara, H.; Shimoi, K., Selective inhibition of methoxyflavonoids on human CYP1B1 activity. *Bioorg. Med. Chem.* **2010,** *18*, 6310-6315.
142. Rokade, B.; Prabhu, K., Chemoselective Schmidt reaction mediated by triflic acid: selective synthesis of nitriles from aldehydes. *J. Org. Chem.* **2012,** *77*, 5364-5370.
143. Zeldin, R.; Petruschke, R., Pharmacological and therapeutic properties of ritonavir-boosted protease inhibitor therapy in HIV-infected patients. *J. Antimicrob. Chemother.* **2004,** *53*, 4-9.
144. Sevrioukova, I.; Poulos, T., Understanding the mechanism of cytochrome P450 3A4: recent advances and remaining problems. *Dalton Trans.* **2013,** *42*, 3116-3126.
145. Riley, R.; Parker, A.; Trigg, S.; Manners, C., Development of a generalized, quantitative physicochemical model of CYP3A4 inhibition for use in early drug discovery. *Pharm. Res.* **2001,** *18*, 652-655.
146. Kaur, P.; Chamberlin, A. R.; Poulos, T.; Sevrioukova, I., Structure-based inhibitor design for evaluation of a CYP3A4 pharmacophore model. *J. Med. Chem.* **2016,** *59*, 4210-4220.
147. Halpert, J., Structural basis of selective cytochrome P450 inhibition. *Annu. Rev. Pharmacol. Toxicol.* **1995,** *35*, 29-53.
148. Nakamura, K.; Aizawa, K.; Aung, K.; Yamauchi, J.; Tanoue, A., Zebularine upregulates expression of CYP genes through inhibition of DNMT1 and PKR in HepG2 cells. *Sci. Rep.* **2017,** *7*, 41093.
149. Herzog, N.; Katzenberger, N.; Martin, F.; Schmidtke, K., Generation of cytochrome P450 3A4-overexpressing HepG2 cell clones for standardization of hepatocellular testosterone 6β-hydroxylation activity. *Journal of Cellular Biotechnology* **2015,** *1*, 15-26.
150. Lauschke, V.; Hendriks, D.; Bell, C.; Anderson, T.; Ingelman-Sundberg, M., Novel 3D culture systems for studies of human liver function and assessment of the hepatotoxicity of drugs and drug candidates. *Chem. Res. Toxicol.* **2016,** *29*, 1936-1955.
151. Terashima, J.; Goto, S.; Hattori, H.; Hoshi, S.; Ushirokawa, M.; Kudo, K.; Habano, W.; Ozawa, S., CYP1A1 and CYP1A2 expression levels are differentially

regulated in three-dimensional spheroids of liver cancer cells compared to two-dimensional monolayer cultures. *Drug Metab. Pharmacokinet.* **2015,** *30*, 434-440.
152. Takahashi, Y.; Hori, Y.; Yamamoto, T.; Ohara, Y.; Tanaka, H., 3D spheroid cultures improve the metabolic gene expression profiles of HepaRG cells. *Biosci. Rep.* **2015,** *35*, e00208.
153. Fennema, E.; Rivron, N.; Rouwkema, J.; van Blitterswijk, C.; de Boer, J., Spheroid culture as a tool for creating 3D complex tissues. *Trends Biotechnol.* **2013,** *31*, 108-115.
154. Sant, S.; Johnston, P., The production of 3D tumor spheroids for cancer drug discovery. *Drug Discovery Today: Technol.* **2017,** *23*, 27-36.
155. Shah, U.-K.; Mallia, J. d. O.; Singh, N.; Chapman, K. E.; Doak, S. H.; Jenkins, G. J. S., A three-dimensional *in vitro* HepG2 cells liver spheroid model for genotoxicity studies. *Mutat. Res.* **2018,** *825*, 51-58.
156. Motley, J.; Stamps, B.; Mitchell, C.; Thompson, A.; Cross, J.; You, J.; Powell, D.; Stevenson, B.; Cichewicz, R., Opportunistic sampling of roadkill as an entry point to accessing natural products assembled by bacteria associated with non-anthropoidal mammalian microbiomes. *J. Nat. Prod.* **2017,** *80*, 598-608.
157. Lou, J.; Yu, R.; Wang, X.; Mao, Z.; Fu, L.; Liu, Y.; Zhou, L., Alternariol 9-methyl ether from the endophytic fungus *Alternaria* sp. Samif01 and its bioactivities. *Braz. J. Microbiol.* **2016,** *47*, 96-101.
158. Huang, J.; Guo, Y.; Jiang, J.; Liu, H.; Ji, Y., An eco-friendly $Co(OAc)_2$-catalyzed aerobic oxidation of 4-benzylphenols into 4-hydroxybenzophenones. *Res. Chem. Intermed.* **2015,** *41*, 7115-7124.
159. Cohrt, A.; Jensen, J.; Nielsen, T., Traceless azido linker for the solid-phase synthesis of NH-1,2,3-triazoles via Cu-catalyzed azide-alkyne cycloaddition reactions. *Org. Lett.* **2010,** *12*, 5414-5417.
160. Yuen, T.; Brimble, M., Total synthesis of 7',8'-dihydroaigialospirol. *Org. Lett.* **2012,** *14*, 5154-5157.
161. Genoux-Bastide, E.; Lorendeau, D.; Nicolle, E.; Yahiaoui, S.; Magnard, S.; Di Pietro, A.; Baubichon-Cortay, H.; Boumendjel, A., Identification of xanthones as selective killers of cancer cells overexpressing the ABC transporter MRP1. *ChemMedChem* **2011,** *6*, 1478-1484.
162. Petrlikova, E.; Waisser, K.; Palat, K.; Kunes, J.; Kaustova, J., A new group of potential antituberculotics: *N*-(2-pyridylmethyl)salicylamides and *N*-(3-pyridylmethyl)salicylamides. *Chem. Pap.* **2011,** *65*, 52-59.
163. Twardziok, M.; Kleinsimon, S.; Rolff, J.; Jäger, S.; Eggert, A.; Seifert, G.; Delebinski, C., Multiple active compounds from *Viscum album* L. synergistically converge to promote apoptosis in Ewing sarcoma. *PLoS One* **2016,** *11*, e0159749.
164. Amaral, A.; Ordóñez, J.; Otero-Motta, A.; García-Domínguez, D.; Sevillano, M.; de Álava, E., Innovative therapies in Ewing sarcoma. *Advances in Anatomic Physiology* **2014,** *21*, 44-62.
165. Stahl, M.; Ranft, A.; Paulussen, M.; Bölling, T.; Vieth, V.; Bielack, S.; Görtitz, I.; Braun-Munzinger, G.; Hardes, J.; Jürgens, H.; Dirksen, U., Risk of recurrence and survival after relapse in patients with Ewing sarcoma. *Pediatr. Blood Cancer* **2011,** *57*, 549-553.

166. Taylor, B.; Barretina, J.; Maki, R.; Antonescu, C.; Singer, S.; Ladanyi, M., Advances in sarcoma genomics and new therapeutic targets. *Nat. Rev. Cancer* **2011,** *11*, 541-557.
167. Lessnick, S.; Ladanyi, M., Molecular pathogenesis of Ewing sarcoma: new therapeutic and transcriptomal targets. *Annu. Rev. Pathol.: Mech. Dis.* **2011,** *7*, 145-159.
168. Bates, D.; Eastman, A., Microtubule destabilising agents: far more than just antimitotic anticancer drugs. *Br. J. Clin. Pharmacol.* **2017,** *83*, 255-268.
169. Mukhtar, E.; Adhami, V.; Mukhtar, H., Targeting microtubules by natural agents for cancer therapy. *Mol. Cancer Ther.* **2014,** *13*, 275-284.
170. Dumontet, C.; Jordan, M., Microtubule-binding agents: a dynamic field of cancer therapeutics. *Nat. Rev. Drug Discovery* **2011,** *9*, 790-803.
171. Risinger, A.; Giles, F.; Mooberry, S., Microtubule dynamics as a target in oncology. *Cancer Treat. Rev.* **2008,** *35*, 255-261.
172. Jordan, M.; Wilson, L., Microtubules as a target for anticancer drugs. *Nat. Rev. Cancer* **2004,** *4*, 253-265.
173. Komlodi-Pasztor, E.; Sackett, D.; Fojo, A., Inhibitors targeting mitosis: tales of how great drugs against a promising target were brought down by a flawed rationale. *Clin. Cancer Res.* **2012,** *18*, 51-63.
174. Field, J.; Kanakkanthara, A.; Miller, J., Microtubule-targeting agents are clinically successful due to both mitotic and interphase impairment of microtubule function. *Bioorg. Med. Chem.* **2014,** *22*, 5050-5059.
175. Takahashi, M.; Iwasaki, S.; Kobayashi, H.; Okuda, S.; Murai, T.; Sato, Y., Rhizoxin binding to tubulin at the maytansine-binding site. *Biochim. Biophys. Acta* **1987,** *926*, 215-223.
176. Iwasaki, S.; Namikoshi, M.; Kobayashi, H.; Furukawa, J.; Okuda, S.; Itai, A.; Kasuya, A.; Iitaka, Y.; Sato, Z., Studies on macrocyclic lactone antibiotics VIII. Absolute structures of rhizoxin and a related compound. *J. Antibiot.* **1986,** *39*, 424-429.
177. Takahashi, M.; Iwasaki, S.; Kobayashi, H.; Okuda, S., Studies on macrocyclic lactone antibiotics XI. Anti-mitotic and anti-tubulin activity of new antitumor antibiotics, rhizoxin and its homologues. *J. Antibiot.* **1987,** *40*, 66-72.
178. Prota, A.; Bargsten, K.; Diaz, J.; Marsh, M.; Cuevas, C.; Liniger, M.; Neuhaus, C.; Andreu, J.; Altmanna, K.; Steinmetz, M., A new tubulin-binding site and pharmacophore for microtubule-destabilizing anticancer drugs. *Proc. Natl. Acad. Sci. U. S. A.* **2014,** *111*, 13817-13821.
179. Scherlach, K.; Busch, B.; Lackner, G.; Paszkowski, U.; Hertweck, C., Symbiotic cooperation in the biosynthesis of a phytotoxin. *Angew. Chem., Int. Ed. Engl.* **2012,** *51*, 9615-9618.
180. Kato, Y.; Ogawa, Y.; Imada, T.; Iwasaki, S.; Shimazaki, N.; Kobayashi, T.; Komai, T., Studies on macrocyclic lactone antibiotics XIII. Anti-tubulin activity and cytotoxicity of rhizoxin derivatives: synthesis of a photoaffinity derivative. *J. Antibiot.* **1991,** *44*, 66-75.
181. Loper, J.; Henkels, M.; Shaffer, B.; Valeriote, F.; Gross, H., Isolation and identification of rhizoxin analogs from *Pseudomonas fluorescens* Pf-5 by using a genomic mining strategy. *Appl. Environ. Microbiol.* **2008,** *74*, 3085-3093.
182. Takahashi, M.; Iwasaki, S.; Kobayashi, H.; Okuda, S.; Murai, T.; Sato, Y.; Haraguchi-Hiraoka, T.; Nagano, H., Studies on macrocyclic lactone antibiotics XI. Anti-

mitotic and anti-tubulin activity of new antitumor antibiotics, rhizoxin and its homologues. *J. Antibiot.* **1987,** *40*, 66-72.
183. Hanauske, A.-R.; Catimel, G.; Aamdal, S.; ten Bokkel Huinink, W.; Paridaens, R.; Pavlidis, N.; Kaye, S.; te Velde, A.; Wanders, J.; Verweij, J., Phase II clinical trials with rhizoxin in breast cancer and melanoma. *Br. J. Cancer* **1996,** *73*, 397-399.
184. Kaplan, S.; Hanauske, A.; Pavlidis, N.; Bruntsch, U.; te Velde, A.; Wanders, J.; Heinrich, B.; Verweij, J., Single agent activity of rhizoxin in non-small-cell lung cancer: a phase II trial of the EORTC Early Clinical Trials Group. *Br. J. Cancer* **1996,** *73*, 403-405.
185. Verweij, J.; Wanders, J.; Gil, T.; Schöffski, P.; Catimel, G.; te Velde, A.; de Mulder, P., Phase II study of rhizoxin in squamous cell head and neck cancer. *Br. J. Cancer* **1996,** *73*, 400-402.
186. McLeod, H.; Murray, L.; Wanders, J.; Setanoians, A.; Graham, M.; Pavlidis, N.; Heinrich, B.; ten Bokkel Huinink, W.; Wagener, D.; Aamdal, S.; Verweij, J., Multicentre phase II pharmacological evaluation of rhizoxin. *Br. J. Cancer* **1996,** *74*, 1944-1948.
187. Bissett, D.; Graham, M.; Setanoians, A.; Chadwick, G.; Wilson, P.; Koier, I.; Henrar, R.; Schwartsmann, G.; Cassidy, J.; Kaye, S.; Kerr, D., Phase I and pharmacokinetic study of rhizoxin. *Cancer Res.* **1992,** *52*, 2894-2898.
188. Tokui, T.; Maeda, N.; Kuroiwa, C.; Sasagawa, K.; Inoue, T.; Kawai, K.; Ikeda, T.; Komai, T., Tumor selective effect of RS-1541 (palmitoyl-rhizoxin) in M5076 sarcoma and host tissues *in vivo*. *Pharm. Res.* **1995,** *12*, 370-375.
189. Kusebauch, B.; Scherlach, K.; Kirchner, H.; Dahse, H.; Hertweck, C., Antiproliferative effects of ester- and amide-functionalized rhizoxin derivatives. *ChemMedChem* **2011,** *6*, 1998-2001.
190. Hong, J.; White, J., The chemistry and biology of rhizoxins, novel antitumor macrolides from *Rhizopus chinensis*. *Tetrahedron* **2004,** *60*, 5653-5681.
191. Ottmann, C.; van der Hoorn, R.; Kaiser, M., The impact of plant-pathogen studies on medicinal drug discovery. *Chem. Soc. Rev.* **2012,** *41*, 3168-3178.
192. Du, L.; Robles, A. J.; King, J. B.; Powell, D. R.; Miller, A. N.; Mooberry, S. L.; Cichewicz, R. H., Crowdsourcing natural products discovery to access uncharted dimensions of fungal metabolite diversity. *Angew. Chem., Int. Ed.* **2014,** *53*, 804-809.
193. SHAREOK - Citizen Science Soil Collection Program - Sample ID 13401. https://shareok.org/handle/11244/29495 (accessed November 19, 2018).
194. Wu, J.; Lorenzo, P.; Zhong, S.; Ali, M.; Butts, C.; Myers, E.; Aggarwal, V., Synergy of synthesis, computation and NMR reveals correct baulamycin structures. *Nature* **2017,** *547*, 436-440.
195. Zou, Y.; Garcia-Borràs; Tang, M.; Hirayama, Y.; Li, D.; Li, L.; Watanabe, K.; Houk, K.; Tang, Y., Enzyme-catalyzed cationic epoxide rearrangements in quinolone alkaloid biosynthesis. *Nat. Chem. Biol.* **2017,** *13*, 325-332.
196. Fraile, J.; Mayoral, J.; Salvatella, L., Theoretical study on the BF_3-catalyzed Meinwald rearrangement reaction. *J. Org. Chem.* **2014,** *79*, 5993-5999.
197. Bock, C., *Ab initio* molecular orbital studies on $C_2H_5O^+$ and $C_2H_4FO^+$: oxonium ion, carbocation, protonated aldehyde, and related transition-state structures. *J. Org. Chem.* **1993,** *58*, 5816-5825.

198. Schoch, C.; Seifert, K.; Huhndorf, S.; Robert, V.; Spouge, J.; Levesque, C.; Chen, W., Nuclear ribosomal internal transcribed spacer (ITS) region as a universal DNA barcode marker for fungi. *Proc. Natl. Acad. Sci. U. S. A.* **2012,** *109*, 6241-6246.
199. *Schrödinger Release 2018-2: MacroModel*, Schrödinger, LLC: New York, NY, 2018.
200. *Schrödinger Release 2018-2: Maestro*, Schrödinger, LLC: New York, NY, 2018.
201. Frisch, M.; Trucks, G.; Schlegel, H.; Scuseria, G.; Robb, M.; Cheeseman, J.; Scalmani, G.; Barone, V.; Mennucci, B.; Petersson, G.; Nakatsuji, H.; Caricato, M.; Li, X.; Hratchian, H.; Izmaylov, A.; Bloino, J.; Zheng, G.; Sonnenberg, J.; Hada, M.; Ehara, M.; Toyota, K.; Fukuda, R.; Hasegawa, J.; Ishida, M.; Nakajima, T.; Honda, Y.; Kitao, O.; Nakai, H.; Vreven, T.; Montgomery, J., JA; Peralta, J.; Ogliaro, F.; Bearpark, M.; Heyd, J.; Brothers, E.; Kudin, K.; Staroverov, V.; Kobayashi, R.; Normand, J.; Raghavachari, K.; Rendell, A.; Burant, J.; Iyengar, S.; Tomasi, J.; Cossi, M.; Rega, N.; Millam, J.; Klene, M.; Knox, J.; Cross, J.; Bakken, V.; Adamo, C.; Jaramillo, J.; Gomperts, R.; Stratmann, R.; Yazyev, O.; Austin, A.; Cammi, R.; Pomelli, C.; Ochterski, J.; Martin, R.; Morokuma, K.; Zakrzewski, V.; Voth, G.; Salvador, P.; Dannenberg, J.; Dapprich, S.; Daniels, A.; Farkas, Ö.; Foresman, J.; Ortiz, J.; Cioslowski, J.; Fox, D. *Gaussian 09, revision B.01*, Gaussian, Inc.: Wallingford, CT, 2010.
202. Bally, T.; Rablen, P., Quantum-chemical simulation of ^{1}H NMR spectra. 2. Comparison of DFT-based procedures for computing proton-proton coupling constants in organic molecules. *J. Org. Chem.* **2011,** *76*, 4818-4830.
203. Chen, T.; Rakheja, D.; Hung, J.; Hornsby, P.; Tabaczewski, P.; Malogolowkin, M.; Feusner, J.; Miskevich, F.; Schultz, R.; Tomlinson, G., Establishment and characterization of a cancer cell line derived from an aggressive childhood liver tumor. *Pediatr. Blood Cancer* **2009,** *53*, 1040-1047.
204. Skehan, P.; Storeng, R.; Scudiero, D.; Monks, A.; McMahon, J.; Vistica, D.; Warren, J.; Bokesch, H.; Kenney, S.; Boyd, M., New colorimetric cytotoxicity assay for anticancer-drug screening. *J. Natl. Cancer Inst.* **1990,** *82*, 1107-1112.
205. Vichai, V.; Kirtikara, K., Sulforhodamine B colorimetric assay for cytotoxicity screening. *Nat. Protoc.* **2006,** *1*, 1112-1116.
206. Iwasaki, S.; Namikoshi, M.; Kobayashi, H.; Furukawa, J.; Okuda, S., Studies on macrocyclic lactone antibiotics. IX: Novel macrolides from the fungus *Rhizopus chinensis*: precursors of rhizoxin. *Chem. Pharm. Bull.* **1986,** *34*, 1387-1390.

Appendix A: Supporting Data for Chapter 3

Appendix Table of Contents

Table A.1. Structures and therapeutic indices for quinones and related structures 114

Figure A.1. ^{1}H NMR spectrum of fusarubin (**1**) 120

Figure A.2. ^{1}H NMR spectrum of javanicin (**2**)..... 120

Figure A.3. ^{1}H NMR spectrum of solaniol (**3**)..... 121

Figure A.4. ^{1}H NMR spectrum of naphthopurpurin (**4**)..... 121

Figure A.5. ^{1}H NMR spectrum of 2-methoxynaphthazarin (**5**) 122

Figure A.6. ^{1}H NMR spectrum of 1,4-dihydro-5,8-dihydroxy-2-methyl-9,10-anthracenedione (**6**)..... 122

Figure A.7. ^{1}H NMR spectrum of 1,4-dihydro-2-methyl-9,10-anthracenedione (**7**)... 123

Figure A.8. ^{1}H NMR spectrum of reduced xanthoquinodin A1 (**43**)..... 123

Figure A.9. ^{13}C NMR spectrim of reduced xanthoquinodin A1 (**43**) 124

Figure A.10. COSY spectrum of reduced xanthoquinodin A1 (**43**) 124

Figure A.11. HSQC spectrum of reduced xanthoquinodin A1 (**43**) 125

Figure A.12. HMBC spectrum of reduced xanthoquinodin A1 (**43**) 125

Figure A.13. 1D ROESY spectrum (500 MHz, $CDCl_3$) irradiated at 5.04 ppm for reduced xanthoquinodin A1 (**43**). 126

Table A.1. Structures and therapeutic indices for quinones and related structures. *Trichomonas* LC_{50} values were obtained in a candle jar.

Cpd. No.	Structure	Ect1 IC_{50} (μM)	*T. vaginalis* IC_{50} (μM)	SI_{Ect1}
1	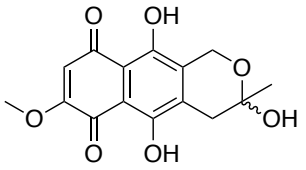	75	2.5	30
2	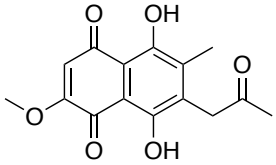	4.0	1.3	3.1
3	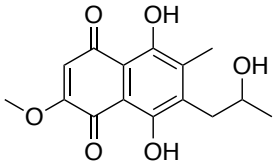	15	40	0.4
4	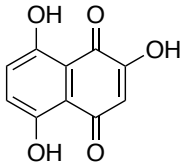	50	20	2.5
5	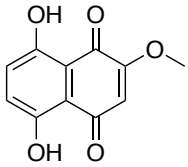	0.9	2.0	0.5
6	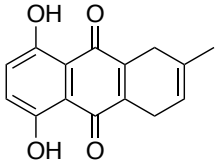	3.0	15	0.2
7	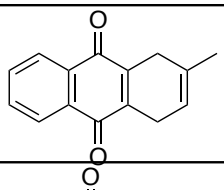	N.D.	>50	N.D.
8	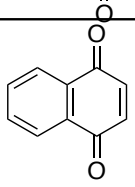	4.3	20.9	0.2

9	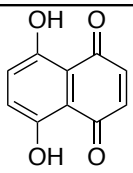	N.D.	>50	N.D.
10	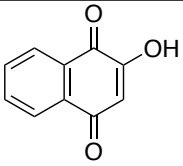	N.D.	>50	N.D.
11	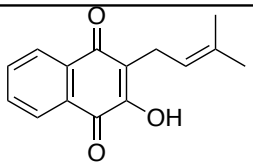	N.D.	>50	N.D.
12	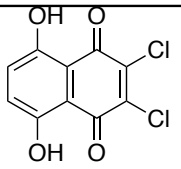	N.D.	>50	N.D.
13	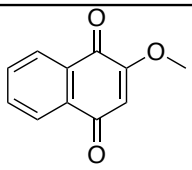	9.9	3.1	3.2
14	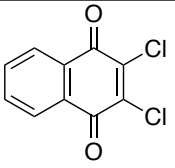	N.D.	>50	N.D.
15	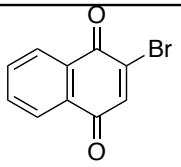	N.D.	>50	N.D.
16	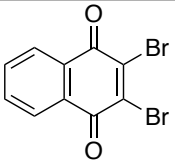	N.D.	>50	N.D.
17	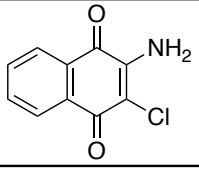	17.0	3.8	4.5

18	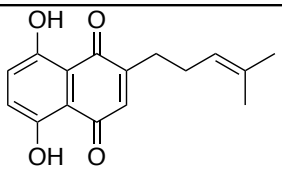	1.0	5.1	0.2
19	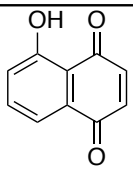	5.4	28.9	0.4
20	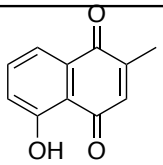	N.D.	>50	N.D.
21	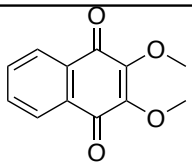	17.0	6.5	2.6
22	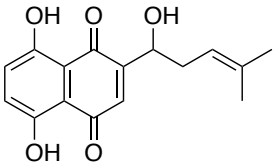	1.0	8.7	0.1
23	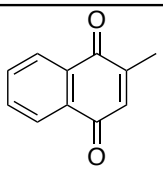	N.D.	>50	N.D.
24	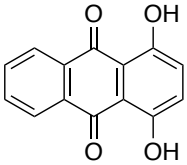	N.D.	>50	N.D.
25	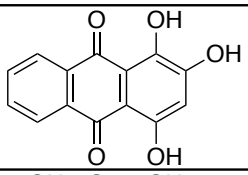	N.D.	>50	N.D.
26	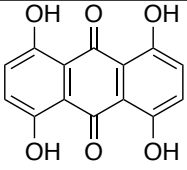	N.D.	>50	N.D.

27	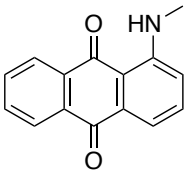	N.D.	>50	N.D.
28	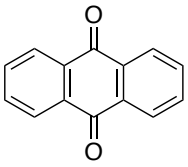	N.D.	>50	N.D.
29	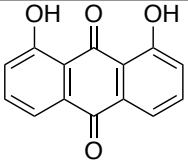	12.5	7.5	1.7
30	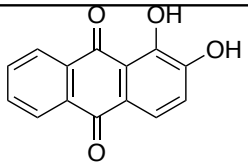	N.D.	>50	N.D.
31	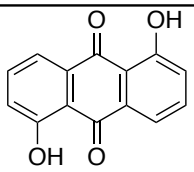	N.D.	>50	N.D.
32	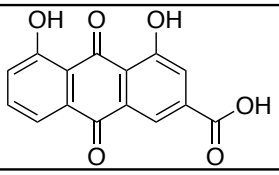	1.9	5	0.4
33	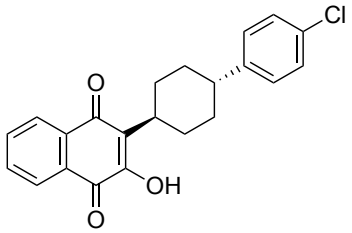	<4	>50	<0.1
34	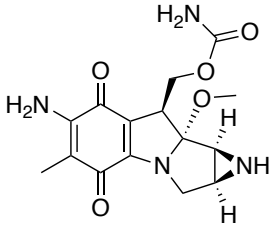	<1	7.5	<0.1

35	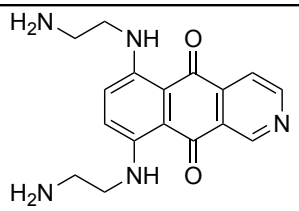	N.D.	>50	N.D.
36	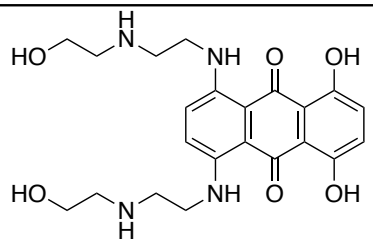	4.6	12.7	0.4
37	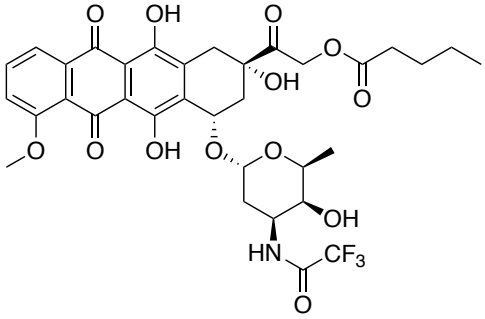	<1	>10	<0.1
38	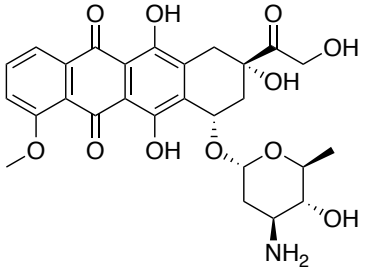	<1	>10	<0.1
39	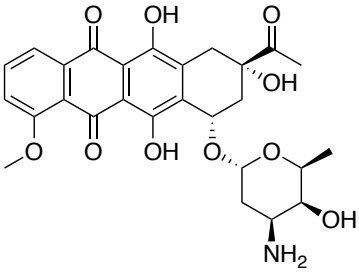	<1	>10	<0.1
40	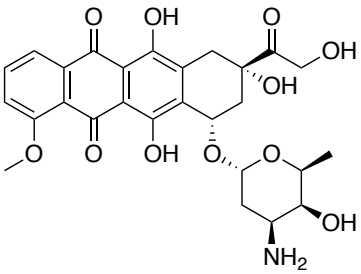	<1	>10	<0.1

41	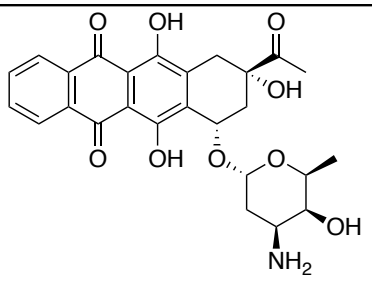	<1	>10	<0.1
42	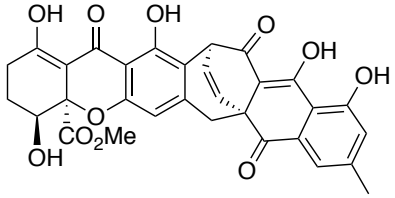	20.0	1.0	20.0
43	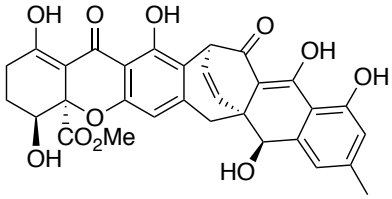	N.D.	1.0	N.D.

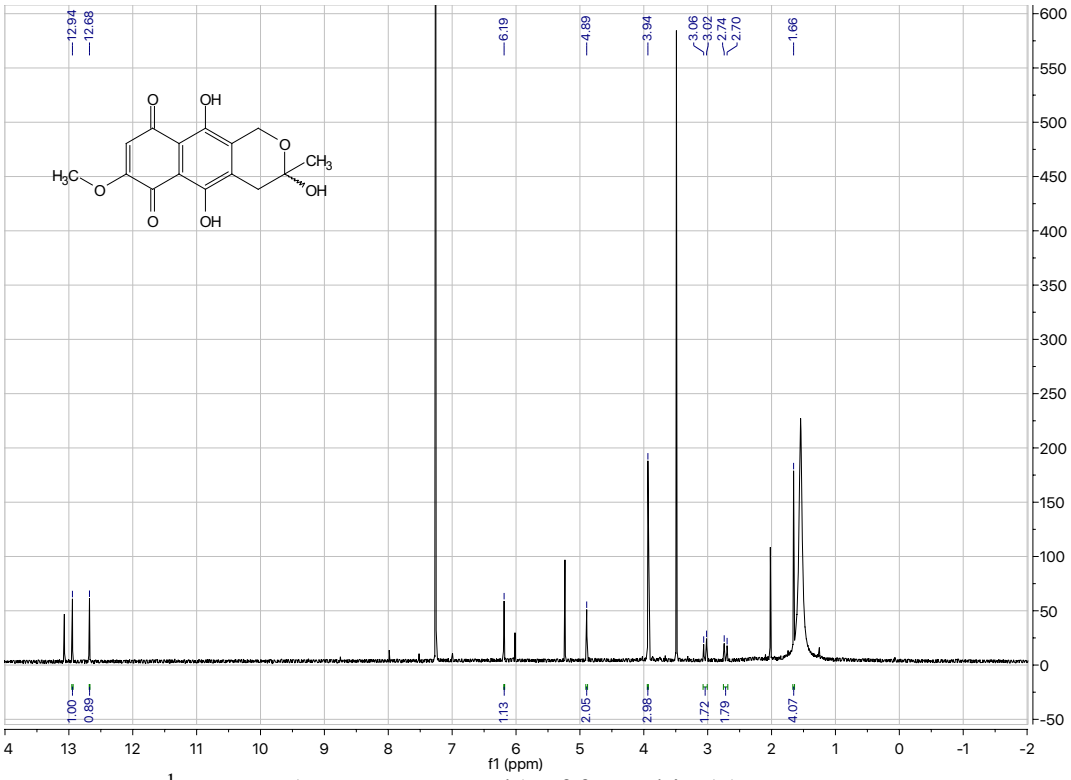

Figure A.1. ^{1}H NMR (400 MHz, $CDCl_3$) of fusarubin (**1**)

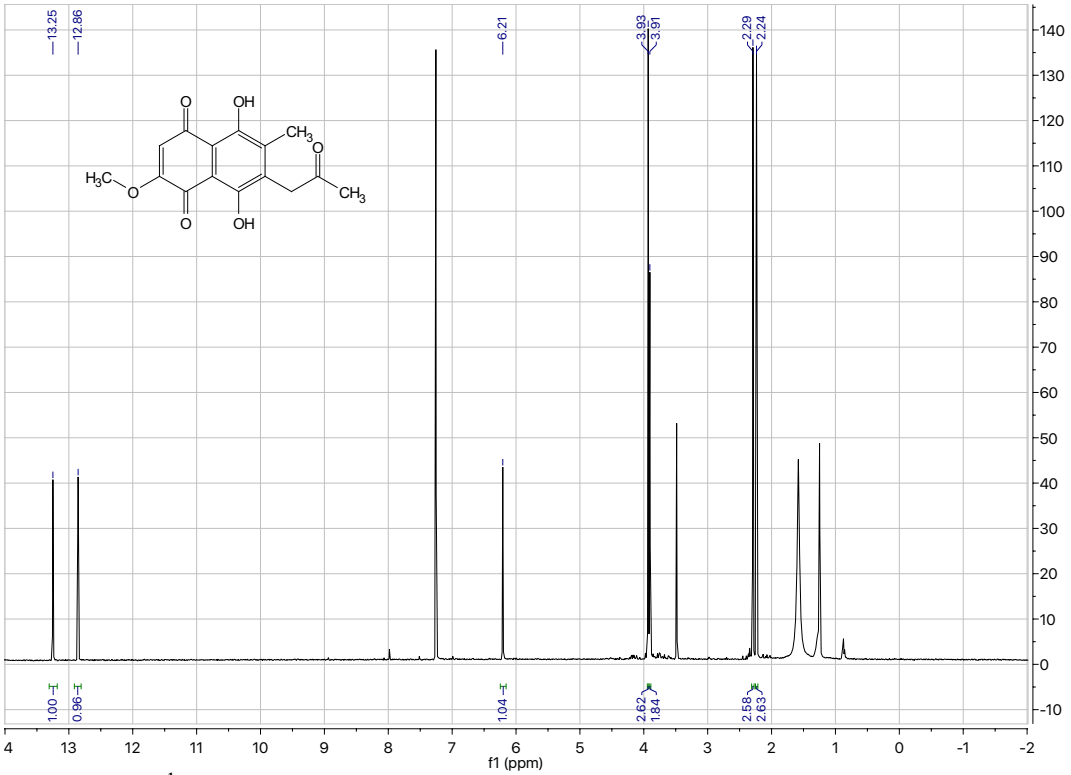

Figure A.2. ^{1}H NMR (400 MHz, $CDCl_3$) spectrum of javanicin (**2**)

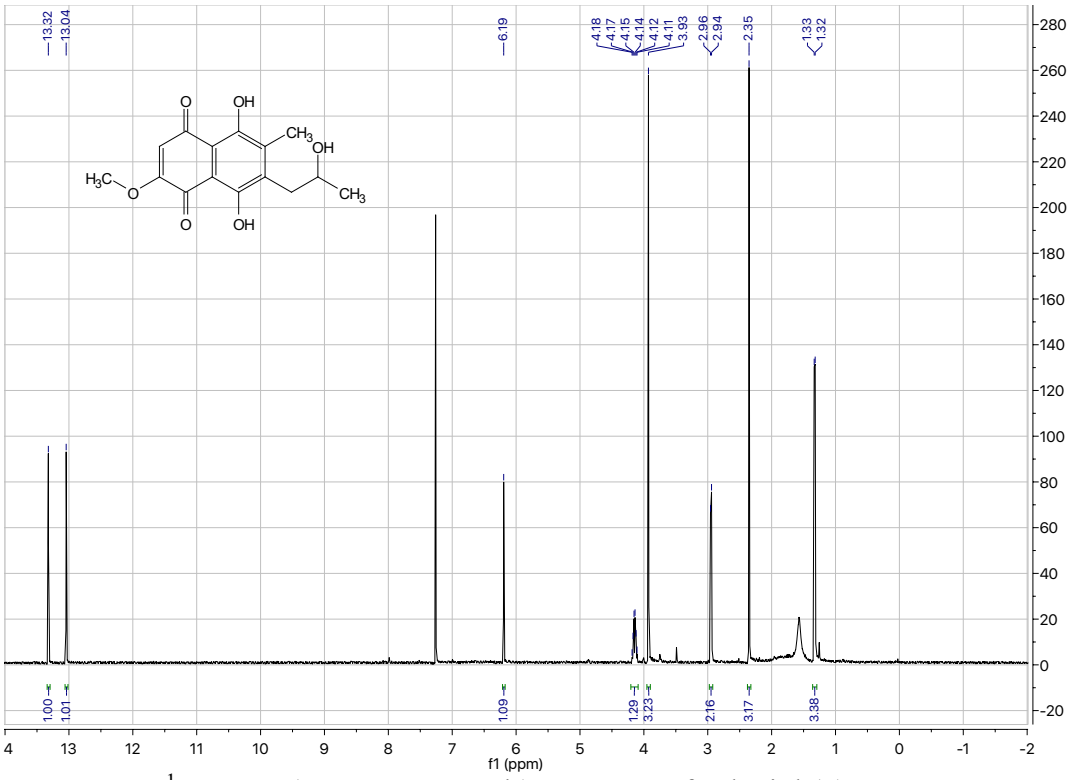

Figure A.3. ^{1}H NMR (400 MHz, $CDCl_3$) spectrum of solaniol (**3**)

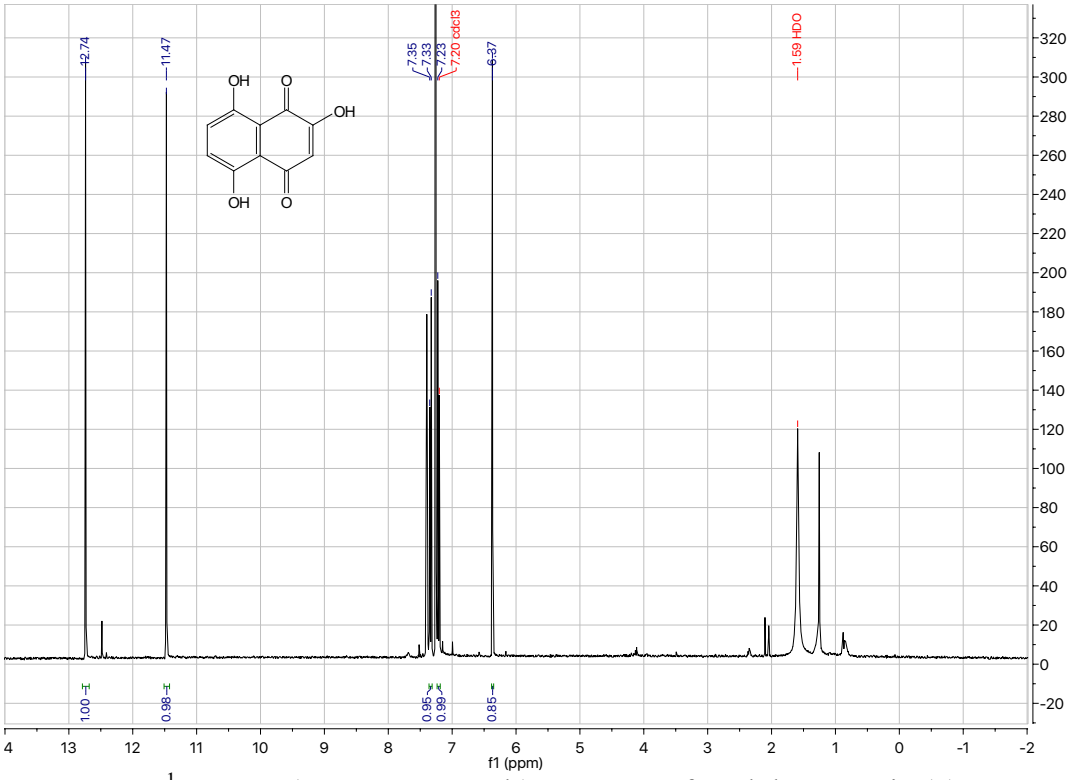

Figure A.4. ^{1}H NMR (400 MHz, $CDCl_3$) spectrum of naphthopurpurin (**4**)

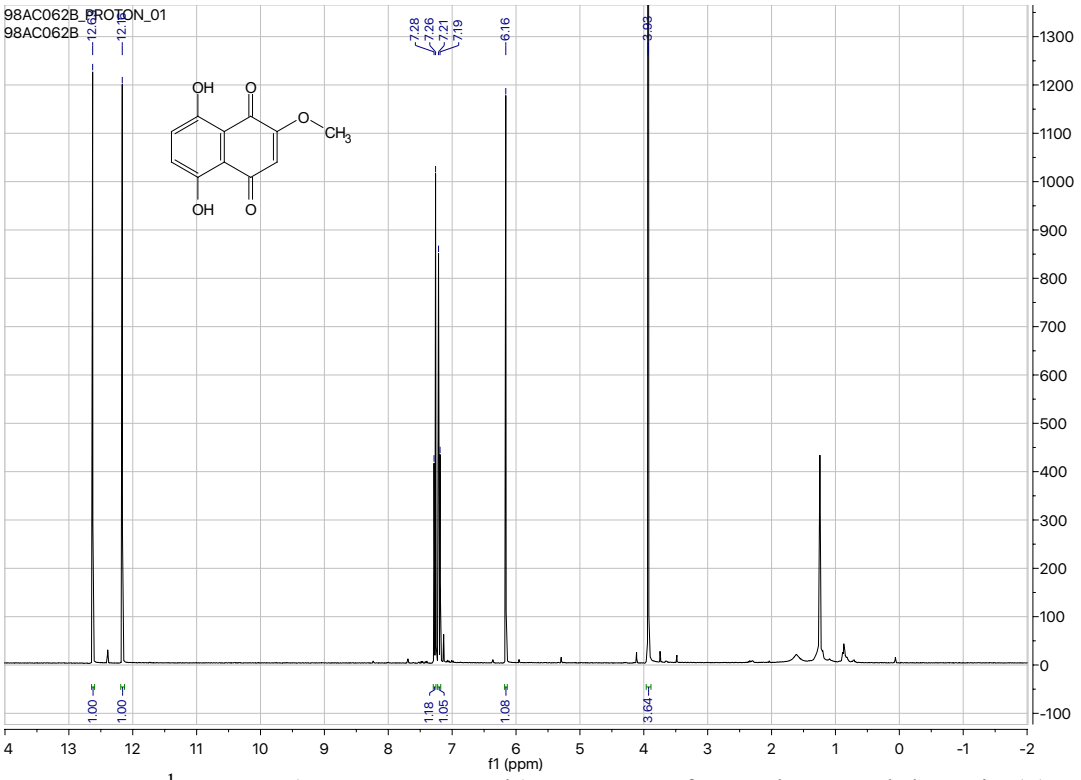

Figure A.5. ^{1}H NMR (400 MHz, $CDCl_3$) spectrum of 2-methoxynaphthazarin (**5**)

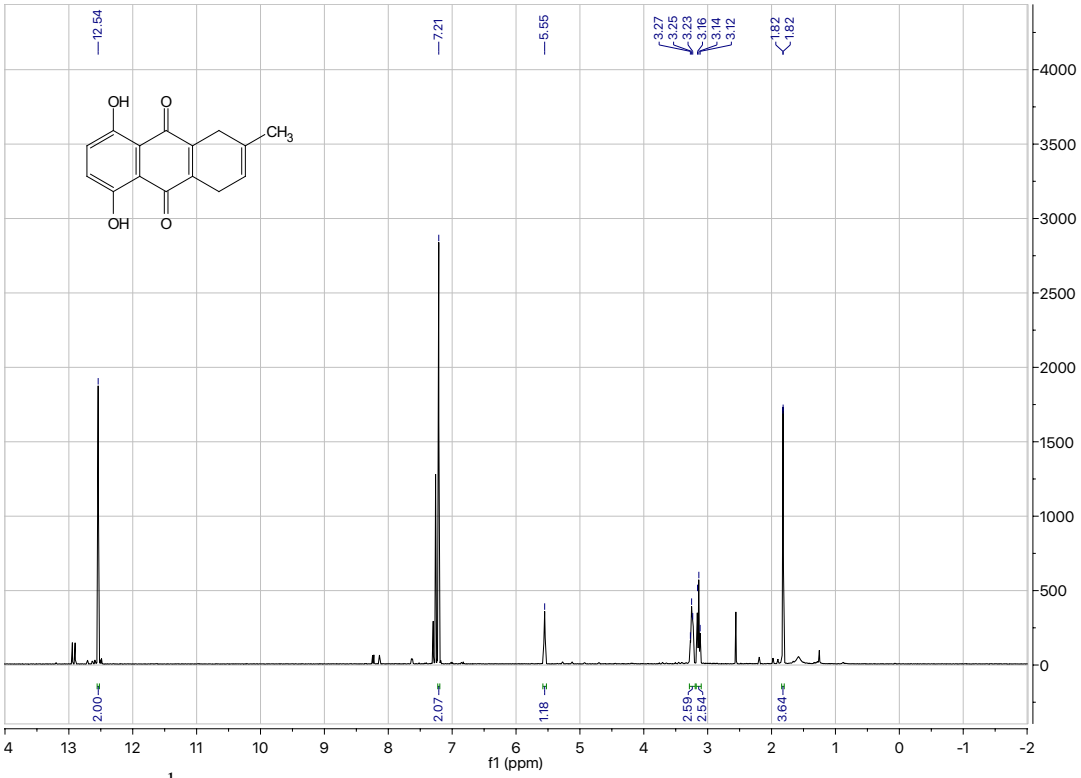

Figure A.6. ^{1}H NMR (400 MHz, $CDCl_3$) spectrum of 1,4-dihydro-5,8-dihydroxy-2-methyl-9,10-anthracenedione (**6**)

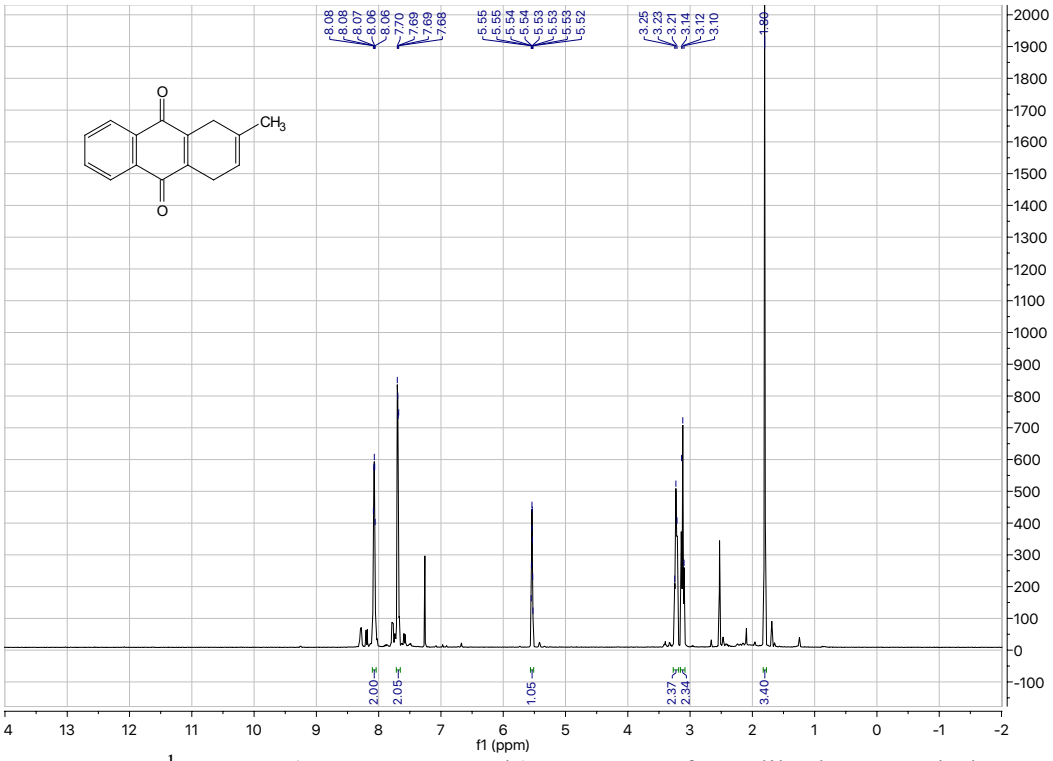

Figure A.7. ^{1}H NMR (400 MHz, $CDCl_3$) spectrum of 1,4-dihydro-2-methyl-9,10-anthracenedione (**7**)

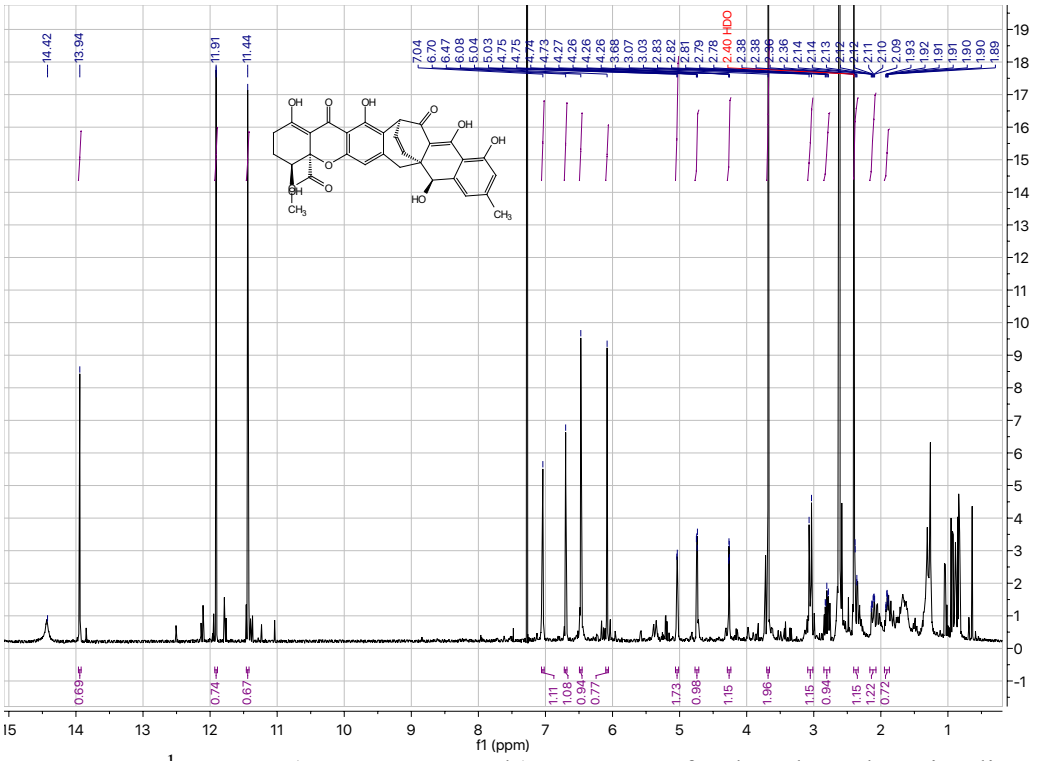

Figure A.8. ^{1}H NMR (500 MHz, $CDCl_3$) spectrum of reduced xanthoquinodin A1 (**43**)

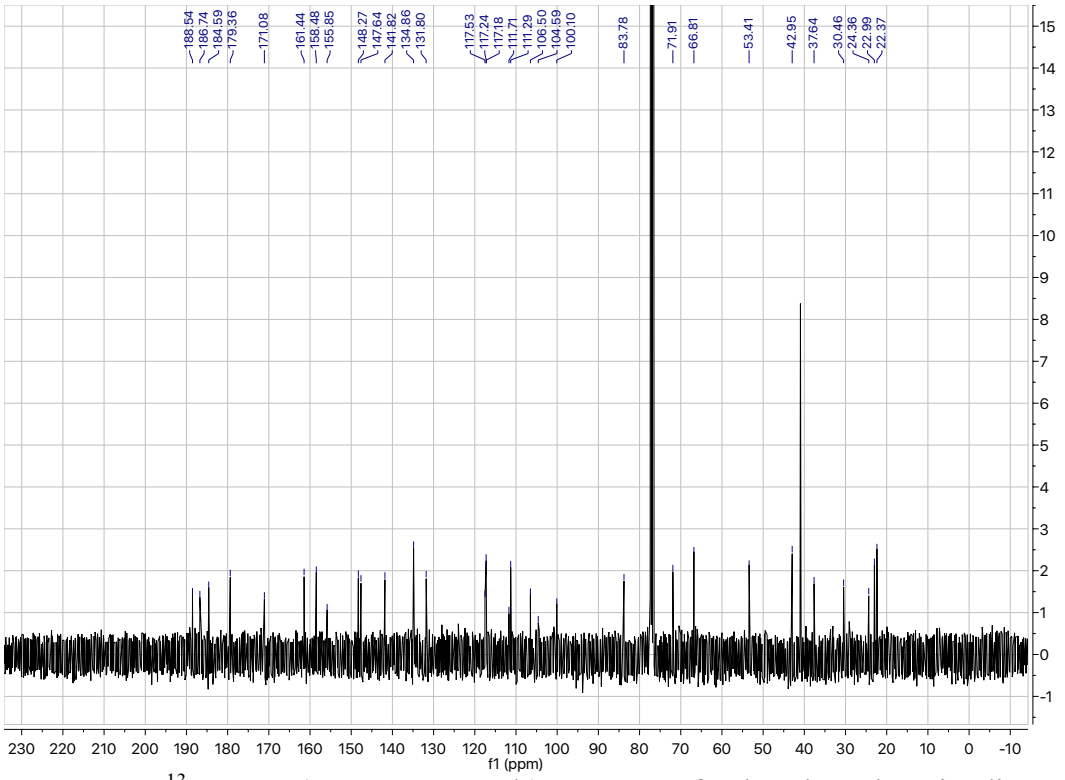

Figure A.9. ^{13}C NMR (100 MHz, $CDCl_3$) spectrum of reduced xanthoquinodin A1 (**43**)

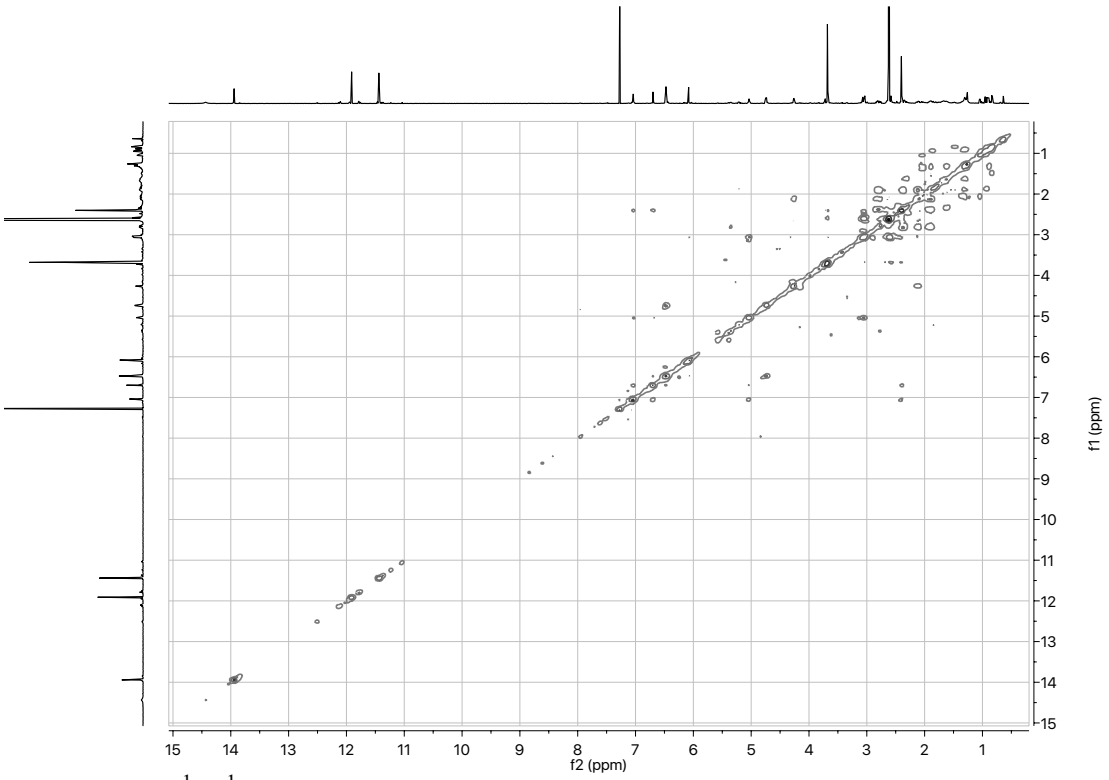

Figure A.10. ^{1}H-^{1}H COSY (500 MHz, $CDCl_3$) spectrum of reduced xanthoquinodin A1 (**43**).

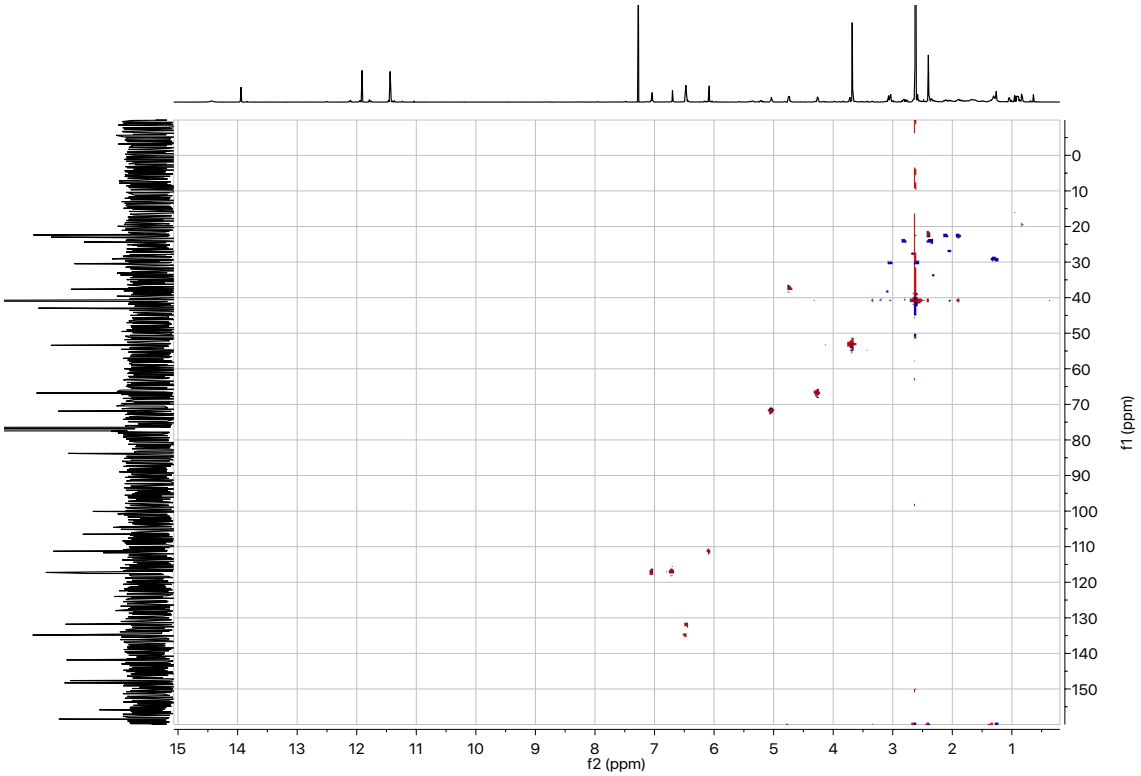

Figure A.11. HSQC (500 MHz, $CDCl_3$) spectrum of reduced xanthoquinodin A1 (**43**)

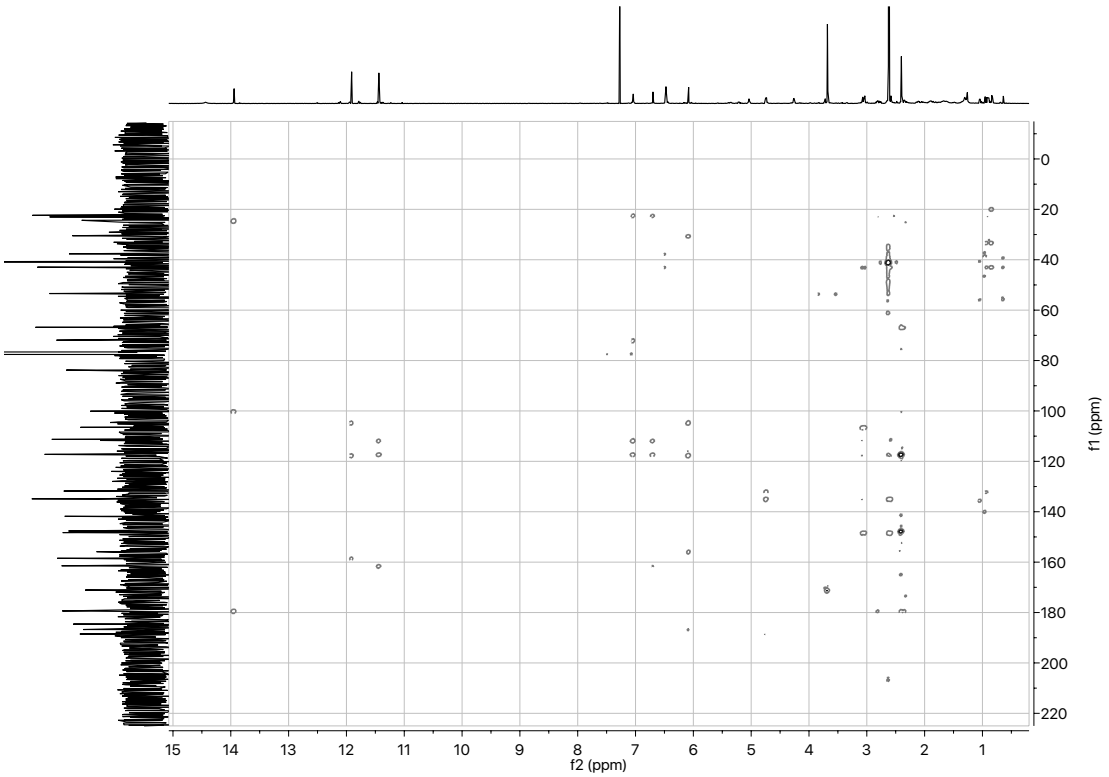

Figure A.12. HMBC (500 MHz, $CDCl_3$) spectrum of reduced xanthoquinodin A1 (**43**)

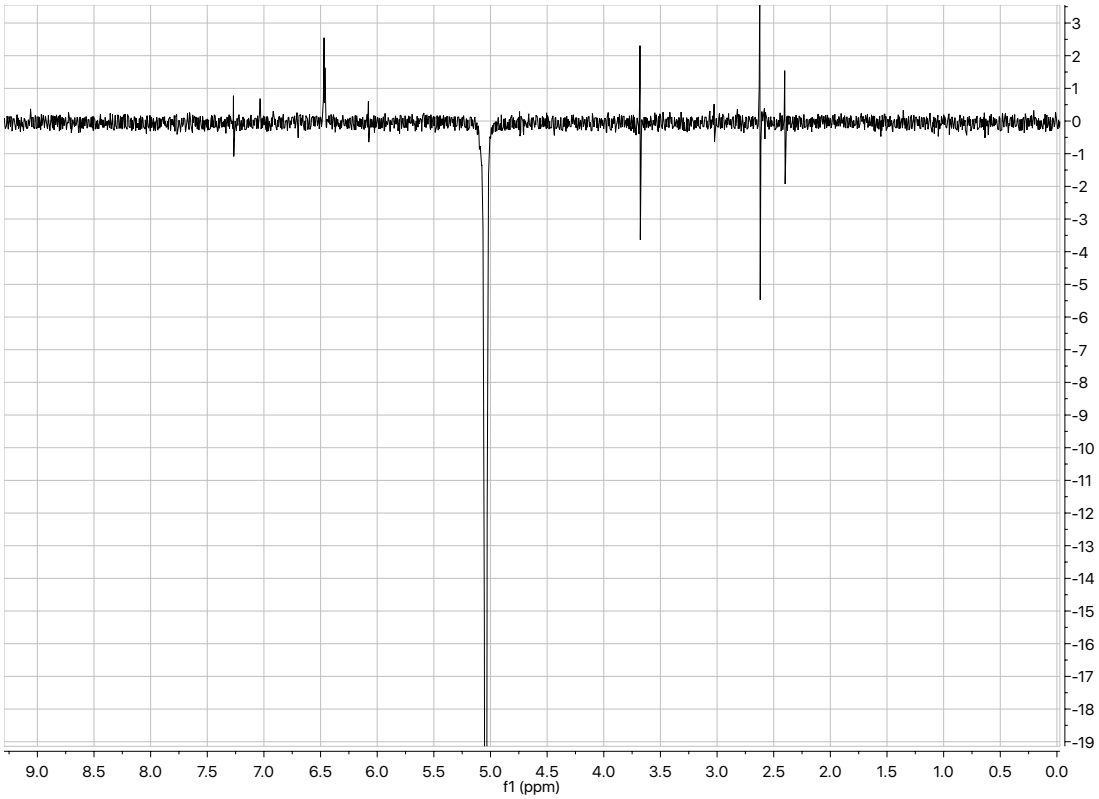

Figure A.13. 1D ROESY spectrum (500 MHz, $CDCl_3$) irradiated at 5.04 ppm for reduced xanthoquinodin A1 (**43**).

Appendix B: Supporting Data for Chapter 4

Appendix Table of Contents

Figure B.1. ^{1}H NMR spectrum of alternariol-9-methyl ether (**1**) 128

Figure B.2. ^{13}C NMR spectrum of alternariol-9-methyl ether (**1**) 128

Figure B.3. ^{1}H NMR spectrum of 4-hydroxy-3-methoxybenzophenone (**8**) 129

Figure B.4. ^{13}C NMR spectrum of 4-hydroxy-3-methoxybenzophenone (**8**) 129

Figure B.5. ^{1}H NMR spectrum of 4-hydroxy-3-methoxybenzhydrol (**9**) 130

Figure B.6. ^{13}C NMR spectrum of 4-hydroxy-3-methoxybenzhydrol (**9**) 130

Figure B.7. ^{1}H NMR spectrum of methyl 2,6-dihydroxy-4-methoxybenzoate 131

Figure B.8. ^{13}C NMR spectrum of methyl 2,6-dihydroxy-4-methoxybenzoate 131

Figure B.9. ^{1}H NMR spectrum of 1-hydroxy-3-methoxyxanthone (**10**)..... 132

Figure B.10. ^{1}H NMR spectrum of 2-hydroxy-4-methoxy-*N*-(3-pyridinylmethyl)benzamide (**12**) 132

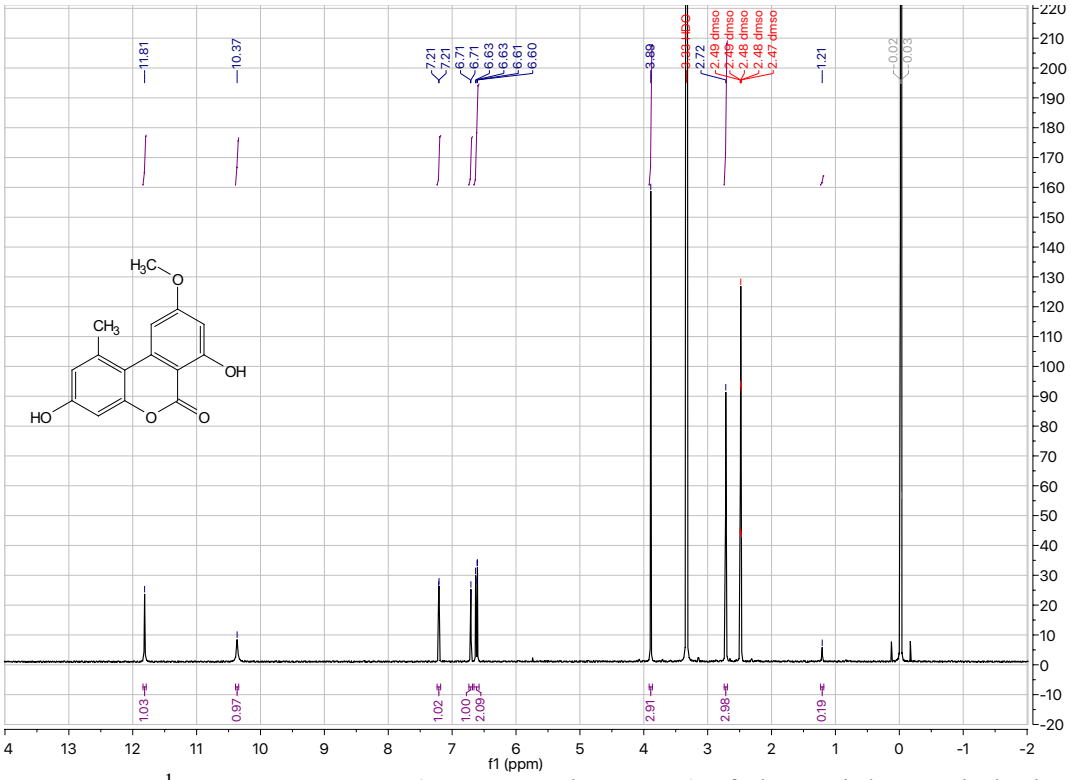

Figure B.1. ^{1}H NMR spectrum (400 MHz, d_6-DMSO) of alternariol-9-methyl ether (**1**)

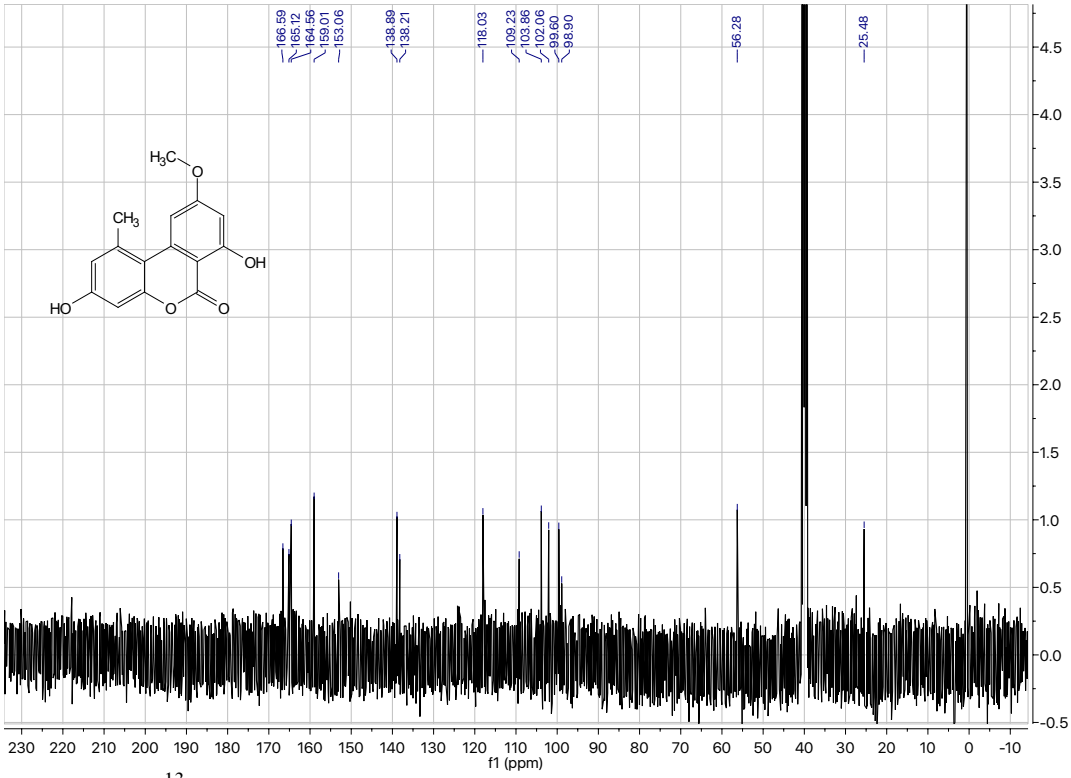

Figure B.2. ^{13}C NMR spectrum (100 MHz, d_6-DMSO) of alternariol-9-methyl ether (**1**)

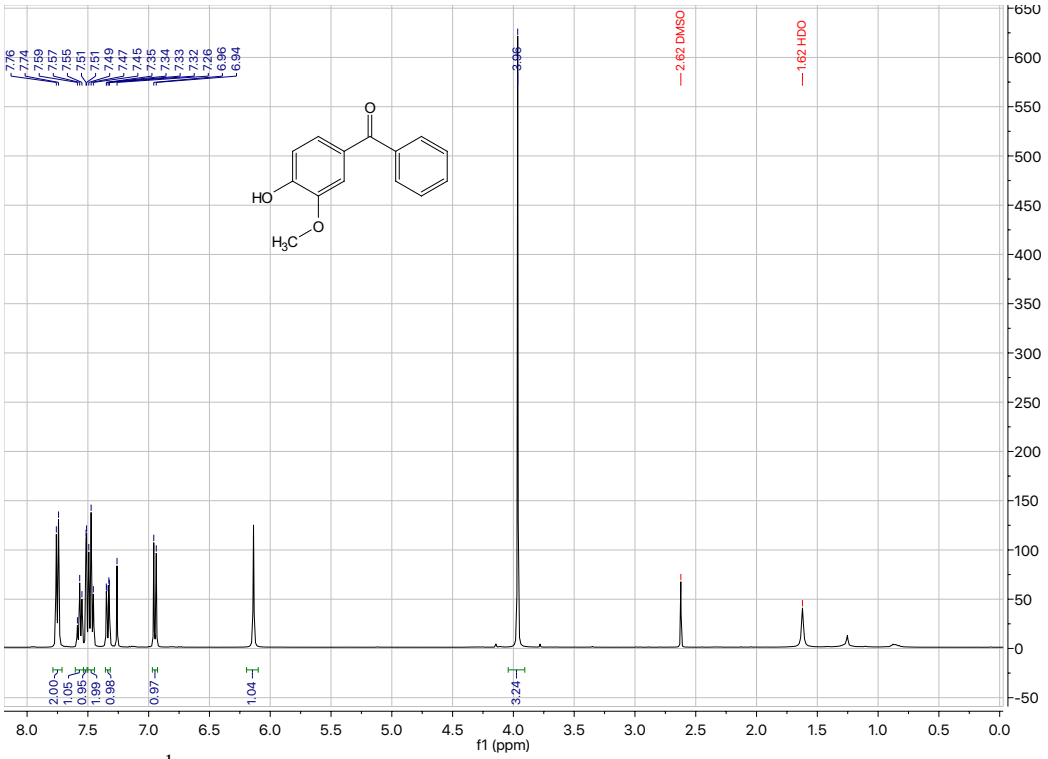

Figure B.3. ^{1}H NMR spectrum (400 MHz, $CDCl_3$) of 4-hydroxy-3-methoxybenzophenone (**8**)

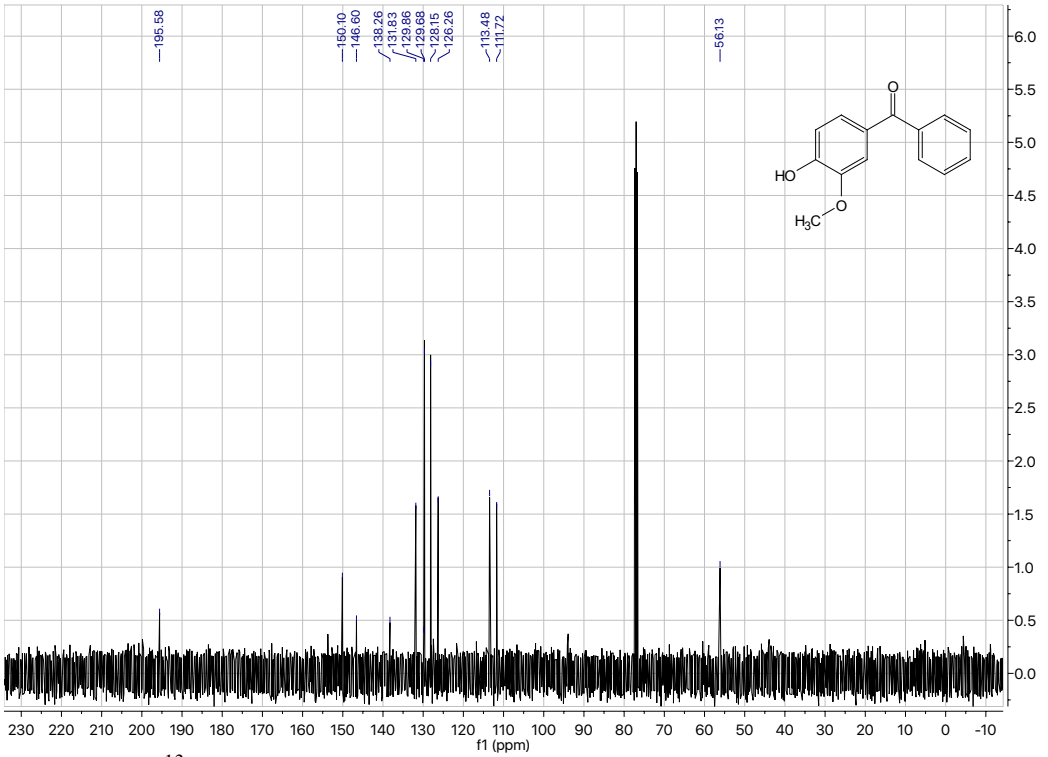

Figure B.4. ^{13}C NMR spectrum (100 MHz, $CDCl_3$) of 4-hydroxy-3-methoxybenzophenone (**8**)

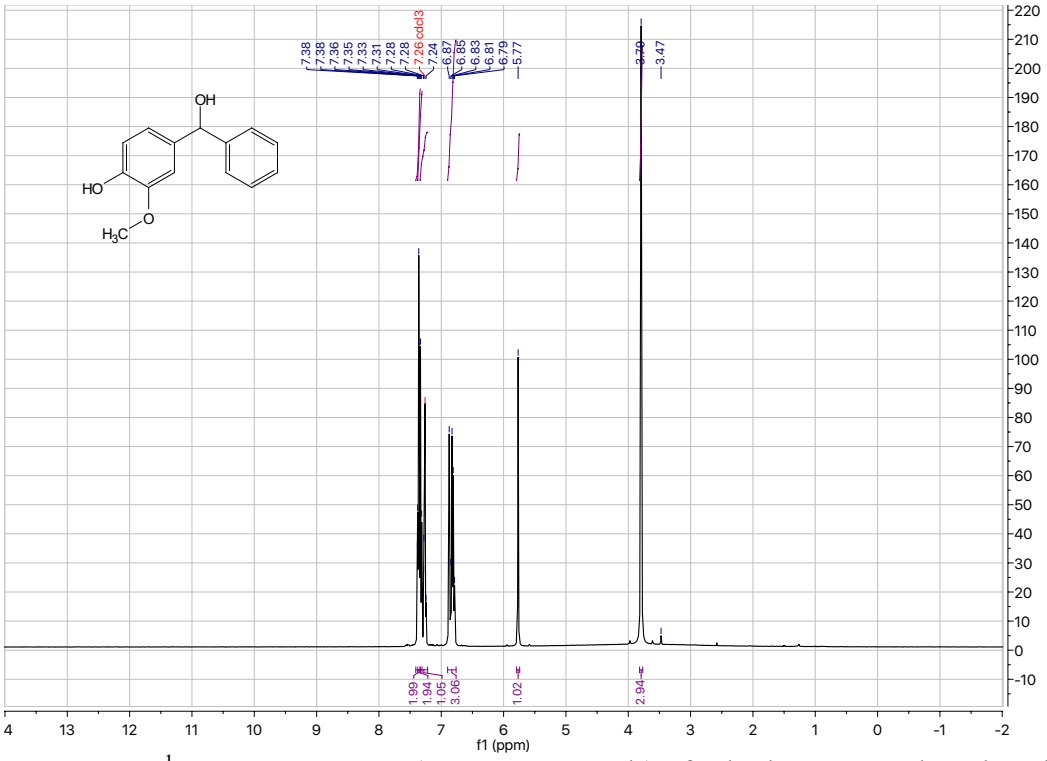

Figure B.5. ^{1}H NMR spectrum (400 MHz, $CDCl_3$) of 4-hydroxy-3-methoxybenzhydrol (**9**)

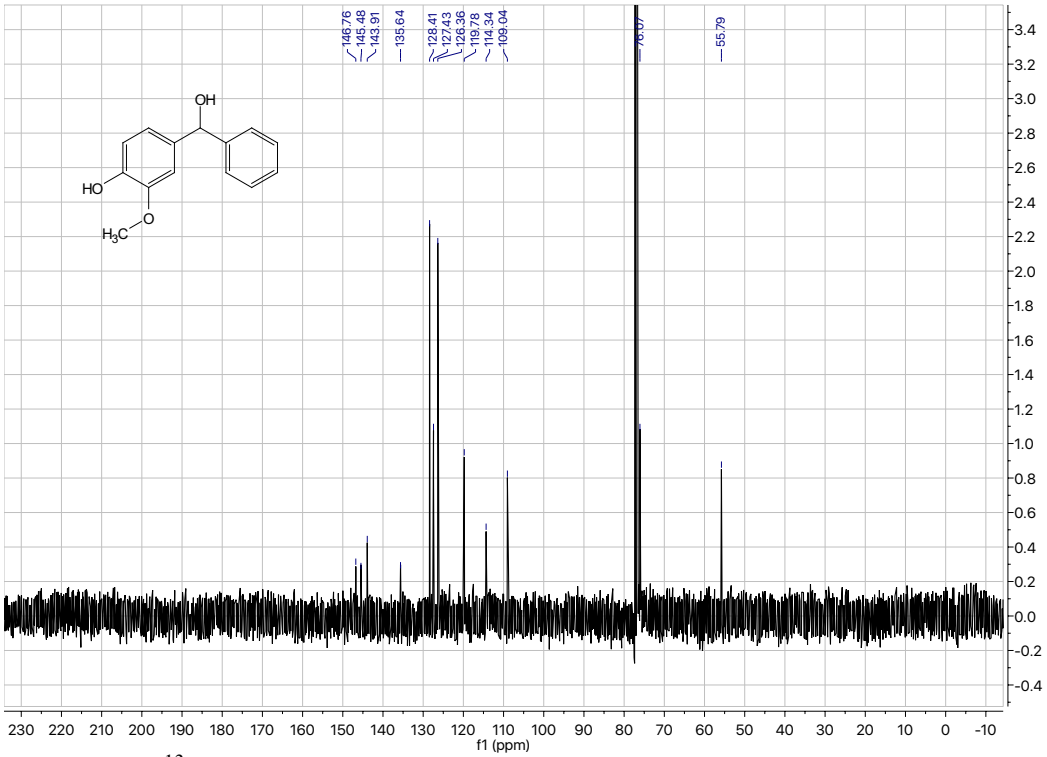

Figure B.6. ^{13}C NMR spectrum (100 MHz, $CDCl_3$) of 4-hydroxy-3-methoxybenzhydrol (**9**)

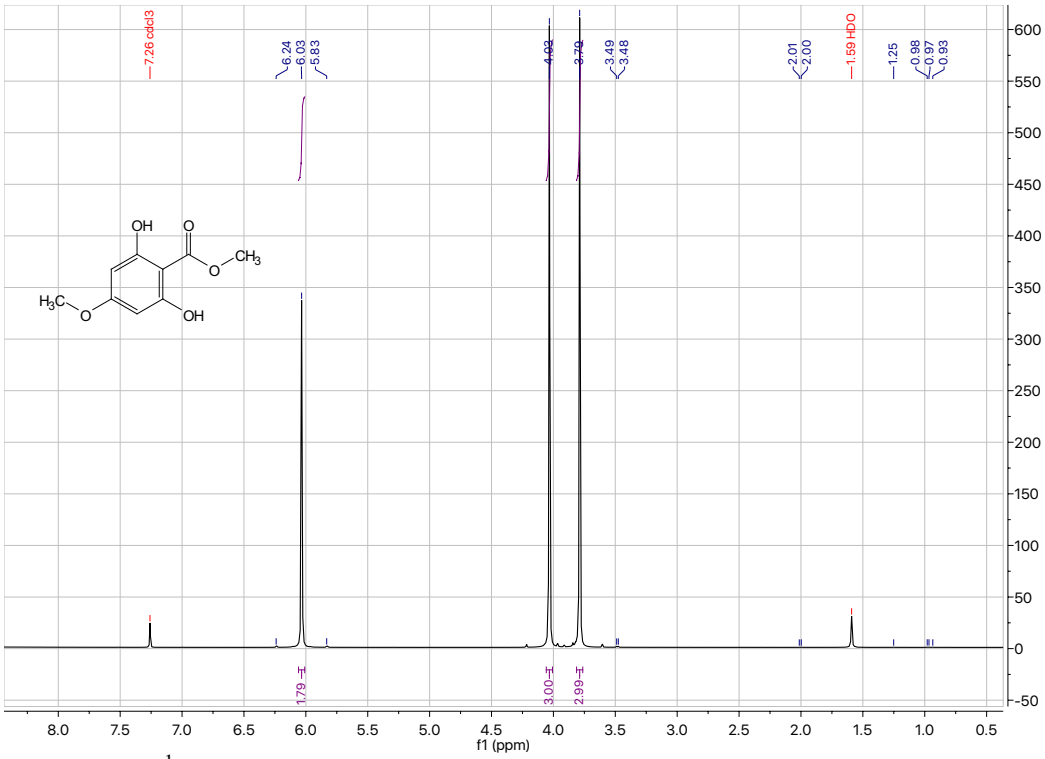

Figure B.7. ^{1}H NMR spectrum (400 MHz, $CDCl_3$) of methyl 2,6-dihydroxy-4-methoxybenzoate

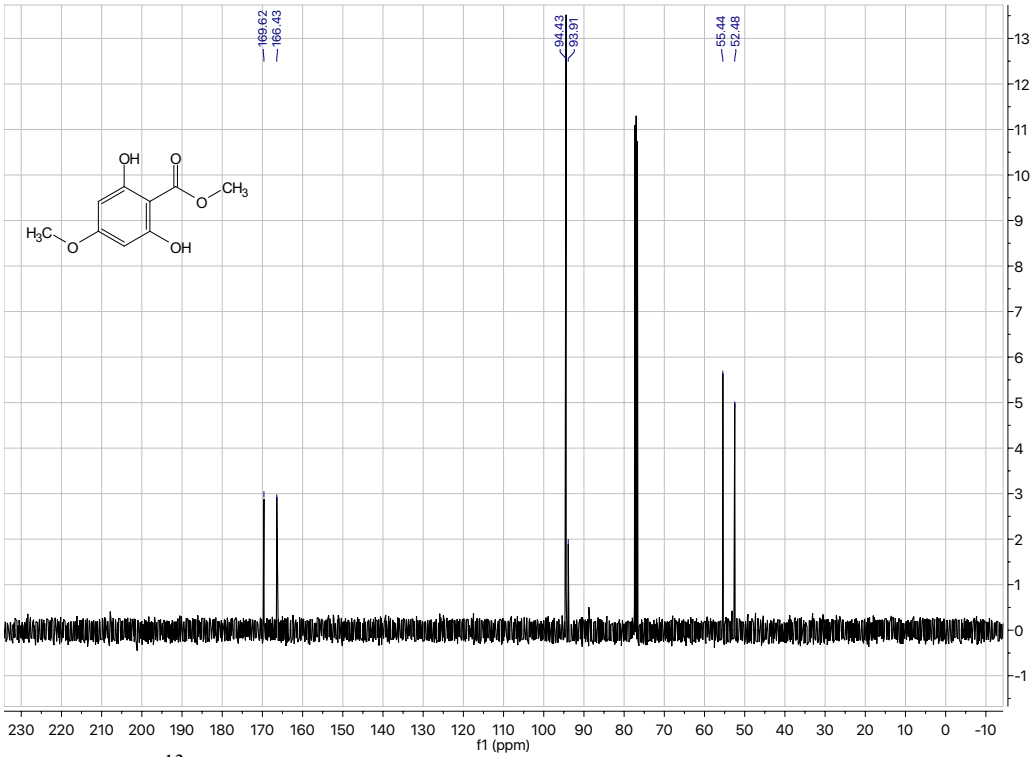

Figure B.8. ^{13}C NMR spectrum (100 MHz, $CDCl_3$) of methyl 2,6-dihydroxy-4-methoxybenzoate

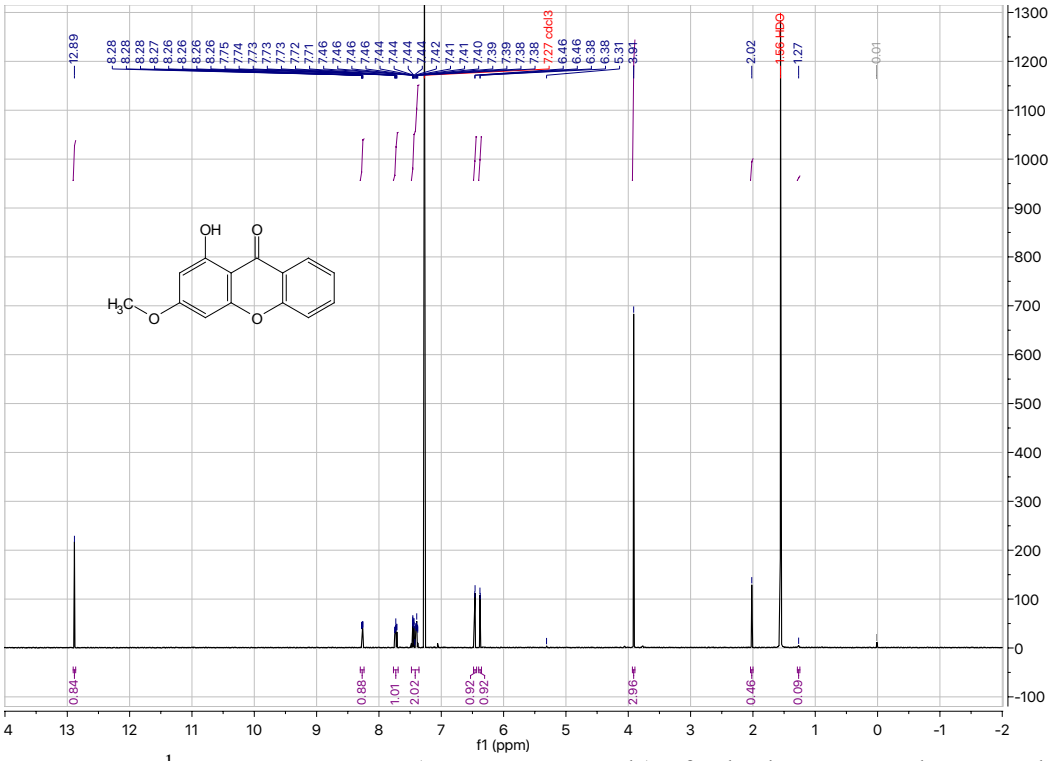

Figure B.9. ^{1}H NMR spectrum (500 MHz, $CDCl_3$) of 1-hydroxy-3-methoxyxanthone (**10**)

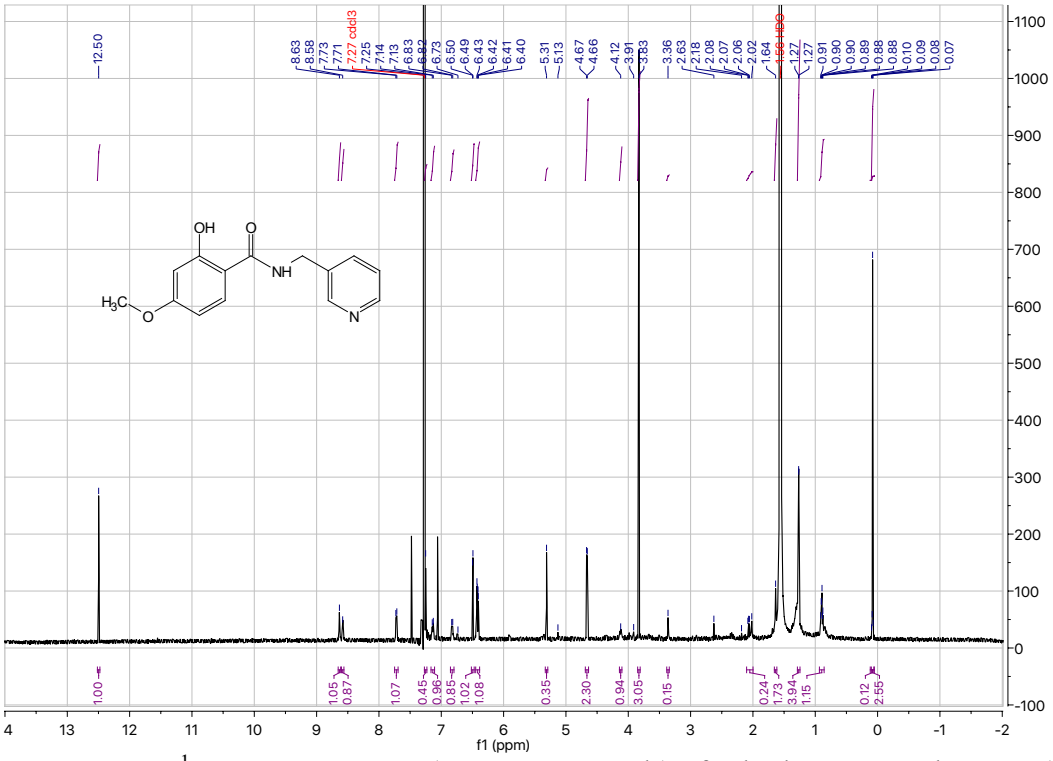

Figure B.10. ^{1}H NMR spectrum (500 MHz, $CDCl_3$) of 2-hydroxy-4-methoxy-*N*-(3-pyridinylmethyl)benzamide (**12**)

Appendix C: Supporting Data for Chapter 5

Appendix Table of Contents

Figure C.1. HRESIMS spectrum of rhizoxin K1 (**2**) 137

Figure C.2. ^{1}H NMR spectrum of compound **2** 137

Figure C.3. ^{13}C NMR spectrum of compound **2** 138

Figure C.4. COSY NMR spectrum of compound **2** 138

Figure C.5. HSQC NMR spectrum of compound **2** 139

Figure C.6. HMBC NMR spectrum of compound **2** 139

Figure C.7. ROESY NMR spectrum of compound **2** 140

Figure C.8. HRESIMS spectrum of rhizoxin T1 (**3**) 140

Figure C.9. ^{1}H NMR spectrum of compound **3** 141

Figure C.10. ^{13}C NMR spectrum of compound **3** 141

Figure C.11. COSY NMR spectrum of compound **3** 142

Figure C.12. HSQC NMR spectrum of compound **3** 142

Figure C.13. HMBC NMR spectrum of compound **3** 143

Figure C.14. ROESY NMR spectrum of compound **3** 143

Figure C.15. HRESIMS spectrum of rhizoxin T2 (**4**) 144

Figure C.16. ^{1}H NMR spectrum of compound **4** 144

Figure C.17. ^{13}C NMR spectrum of compound **4** 145

Figure C.18. COSY NMR spectrum of compound **4** 145

Figure C.19. HSQC NMR spectrum of compound **4** 146

Figure C.20. HMBC NMR spectrum of compound **4** 146

Figure C.21. ROESY NMR spectrum of compound **4** 147

Figure C.22. HRESIMS spectrum of rhizoxin M3 (**5**) 147

Figure C.23. ^{1}H NMR spectrum of compound **5** 148

Figure C.24. ^{13}C NMR spectrum of compound **5** 148

Figure C.25. COSY NMR spectrum of compound **5** 149

Figure C.26. HSQC NMR spectrum of compound **5** 149

Figure C.27. HMBC NMR spectrum of compound **5** 150

Figure C.28. ROESY NMR spectrum of compound **5** 150

Figure C.29. HRESIMS spectrum of rhizoxin T3 (**6**) 151

Figure C.30. ^{1}H NMR spectrum of compound **6** 151

Figure C.31. ^{13}C NMR spectrum of compound **6** 152

Figure C.32. COSY NMR spectrum of compound **6** 152

Figure C.33. HSQC NMR spectrum of compound **6** 153

Figure C.34. HMBC NMR spectrum of compound **6** 153

Table C.1. NMR spectral data of rhizoxin (**1**) 154

Discussion C.1. General computational information for NMR calculations 155

Figure C.35. Possible truncated diastereomers for **2** 157

Table C.2. Calculated energies and populations for **2a** 157

Table C.3. Calculated energies and populations for **2b** 157

Figure C.36. Possible truncated diastereomers for **3** and **4** 158

Table C.4. Calculated energies and populations for **3a** 158

Table C.5. Calculated energies and populations for **3b** 158

Figure C.37. Possible truncated diastereomers for **5** 159

Table C.6. Calculated energies and populations for **5a** 159

Table C.7. Calculated energies and populations for **5b** 159

Figure C.38. Possible truncated diastereomers for **6** 160

Table C.8. Calculated energies and populations for **6a** 160

Table C.9. Calculated energies and populations for **6b** 160

Figure C.39. Possible truncated diastereomers for **1** 161

Table C.10. Calculated energies and populations for **1a** 161

Table C.11. Calculated energies and populations for **1b** 161

Figure C.40. ^{13}C NMR calculation results and statistics for **1-6** 162

Table C.12. Calculated ∂H for **1a** and **1b** vs. experimental ∂H for **1** 163

Table C.13. Calculated ∂C for **1a** and **1b** vs. experimental ∂C for **1** 164

Table C.14. Calculated ∂H for **2a** and **2b** vs. experimental ∂H for **2** 165

Table C.15. Calculated ∂C for **2a** and **2b** vs. experimental ∂C for **2** 166

Table C.16. Calculated ∂H for **3a** and **3b** vs. experimental ∂H for **3** 167

Table C.17. Calculated ∂C for **3a** and **3b** vs. experimental ∂C for **3** 168

Table C.18. Calculated ∂H for **3a** and **3b** vs. experimental ∂H for **4** 169

Table C.19. Calculated ∂C for **3a** and **3b** vs. experimental ∂C for **4** 170

Table C.20. Calculated ∂H for **5a** and **5b** vs. experimental ∂H for **5** 171

Table C.21. Calculated ∂C for **5a** and **5b** vs. experimental ∂C for **5** 172

Table C.22. Calculated ∂H for **6a** and **6b** vs. experimental ∂H for **6** 173

Table C.23. Calculated ∂C for **6a** and **6b** vs. experimental ∂C for **6** 174

Discussion C.2. Liquid culture condition screening 174

Discussion C.3. General computational information for DFT calculations 175

Table C.24. Cartesian coordinates for optimized structure of **1H+** 176

Table C.25. Cartesian coordinates for optimized structure of **TS1** 177

Table C.26. Cartesian coordinates for optimized structure of **7-1** 178

Table C.27. Cartesian coordinates for optimized structure of **7-2** 179

Table C.28. Cartesian coordinates for optimized structure of **TS2** 180

Table C.29. Cartesian coordinates for optimized structure of **2H+** 181

Table C.30. DFT calculated thermodynamic data for optimized strcutures 181

Figures C.41. Potential energy scan for rotation about C11-C12 bond of **7** 182

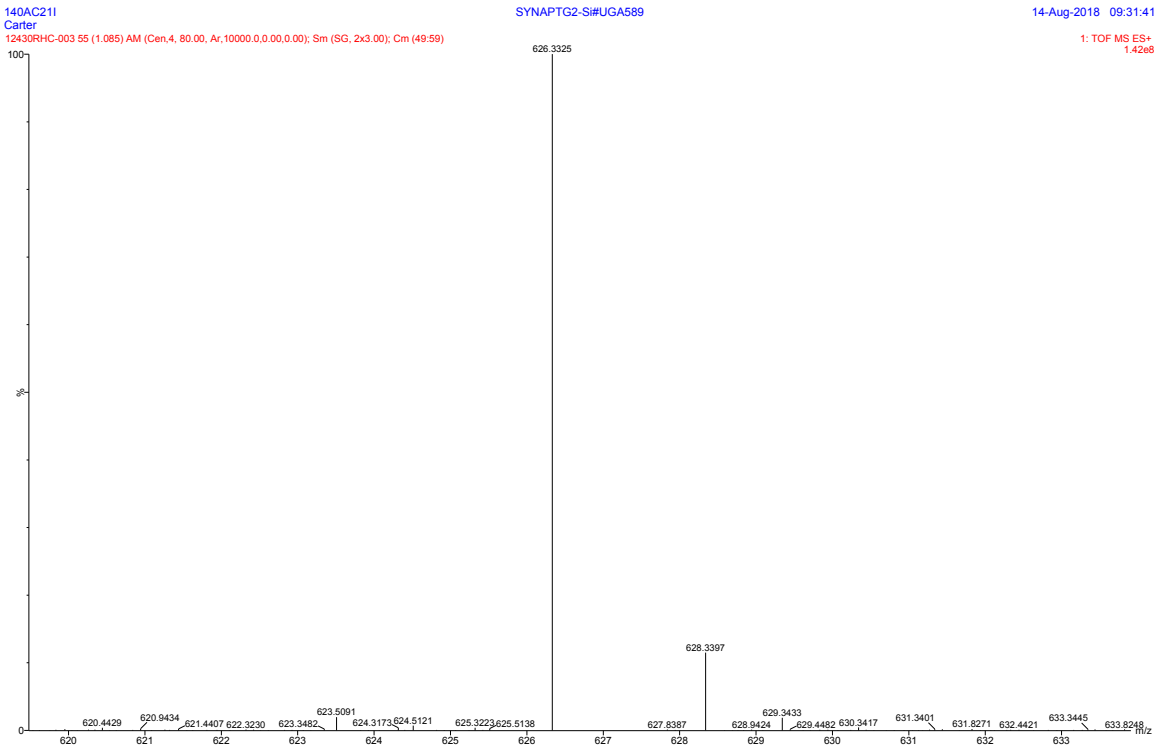

Figure C.1. HRESIMS spectrum of rhizoxin K1 (**2**)

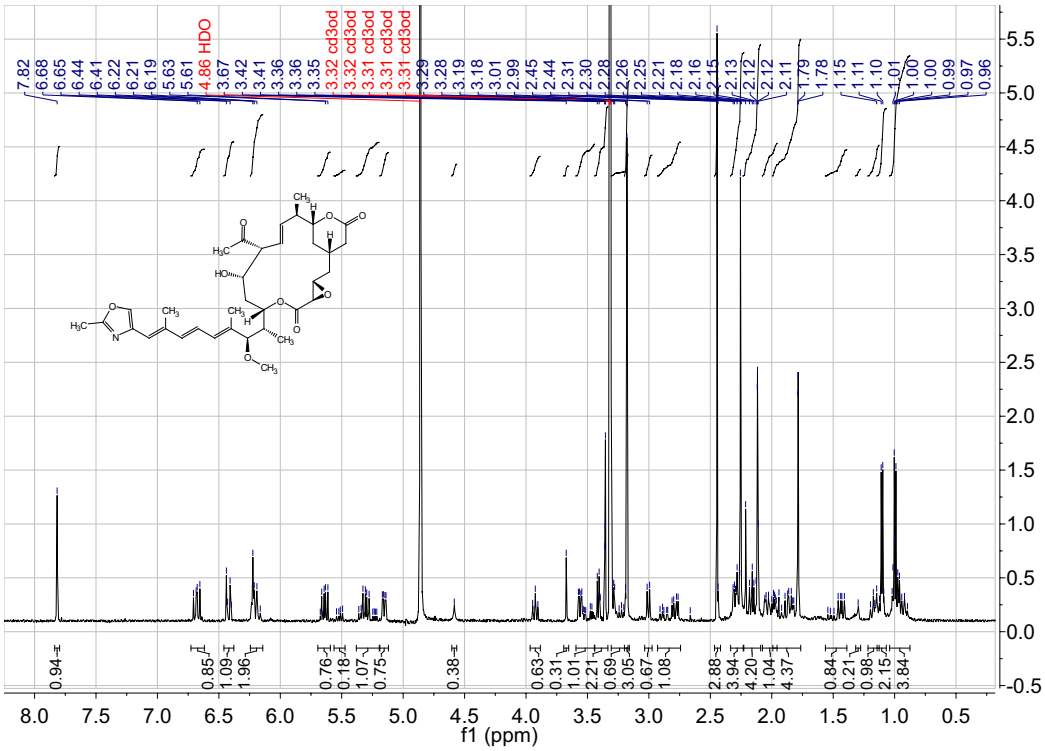

Figure C.2. ^{1}H NMR spectrum (500 MHz, d_4-methanol) of compound **2**

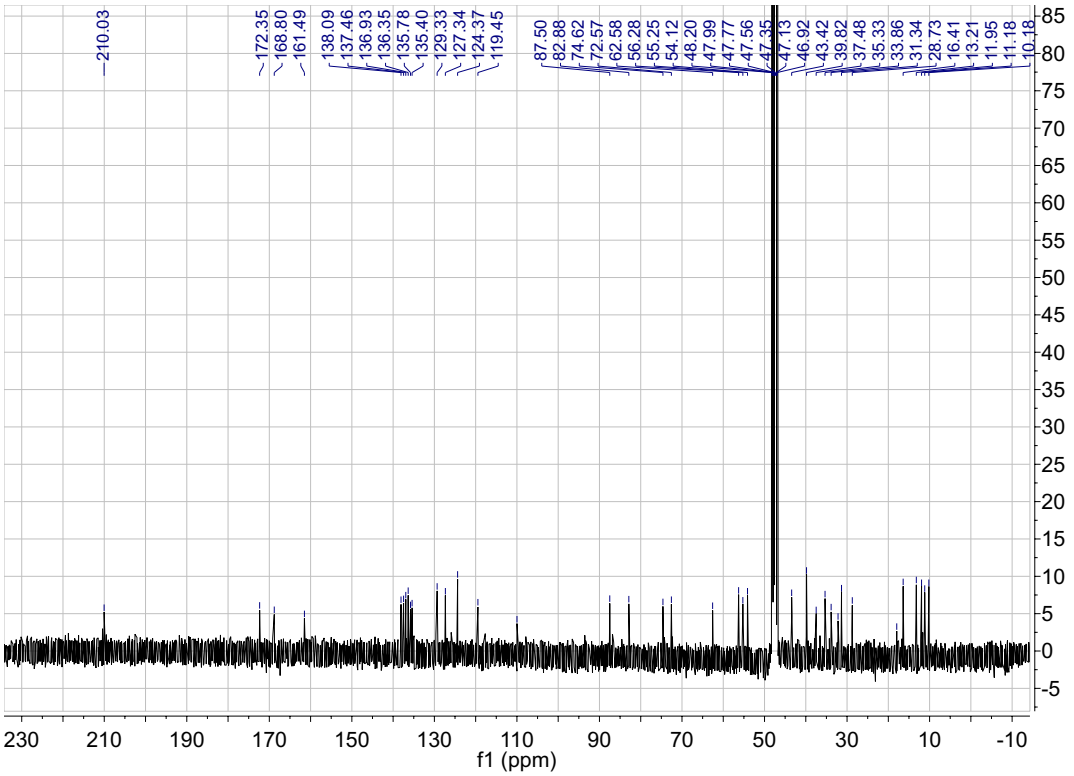

Figure C.3. ^{13}C NMR spectrum (100 MHz, d_4-methanol) of compound **2**

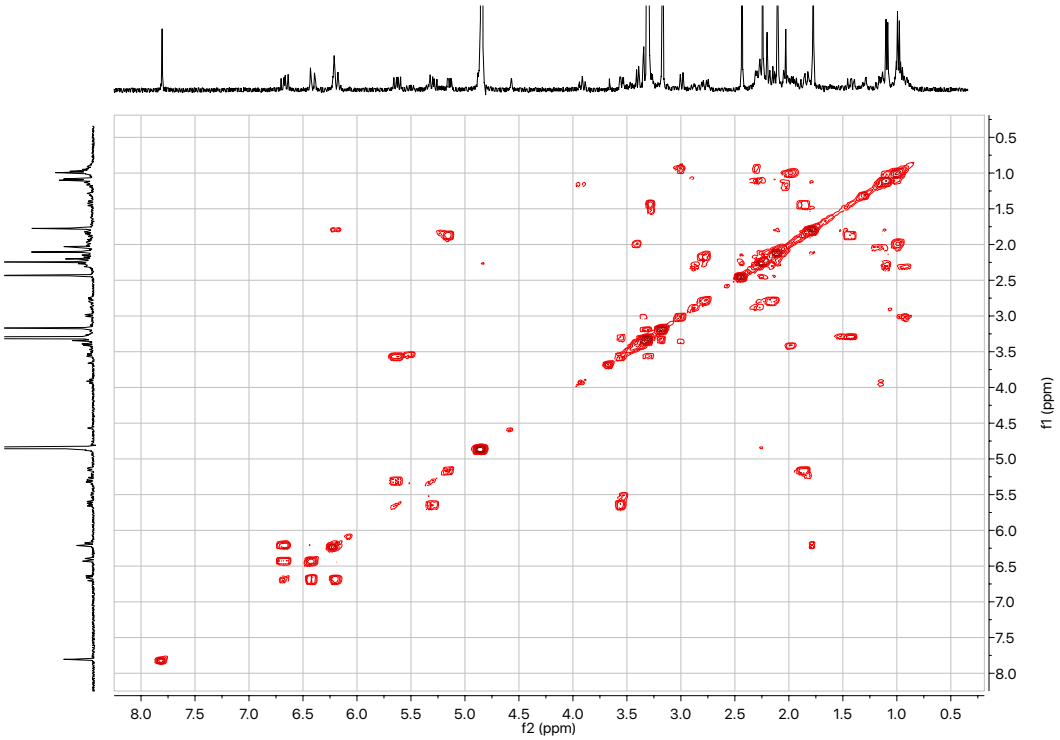

Figure C.4. COSY NMR spectrum (500 MHz, d_4-methanol) of compound **2**

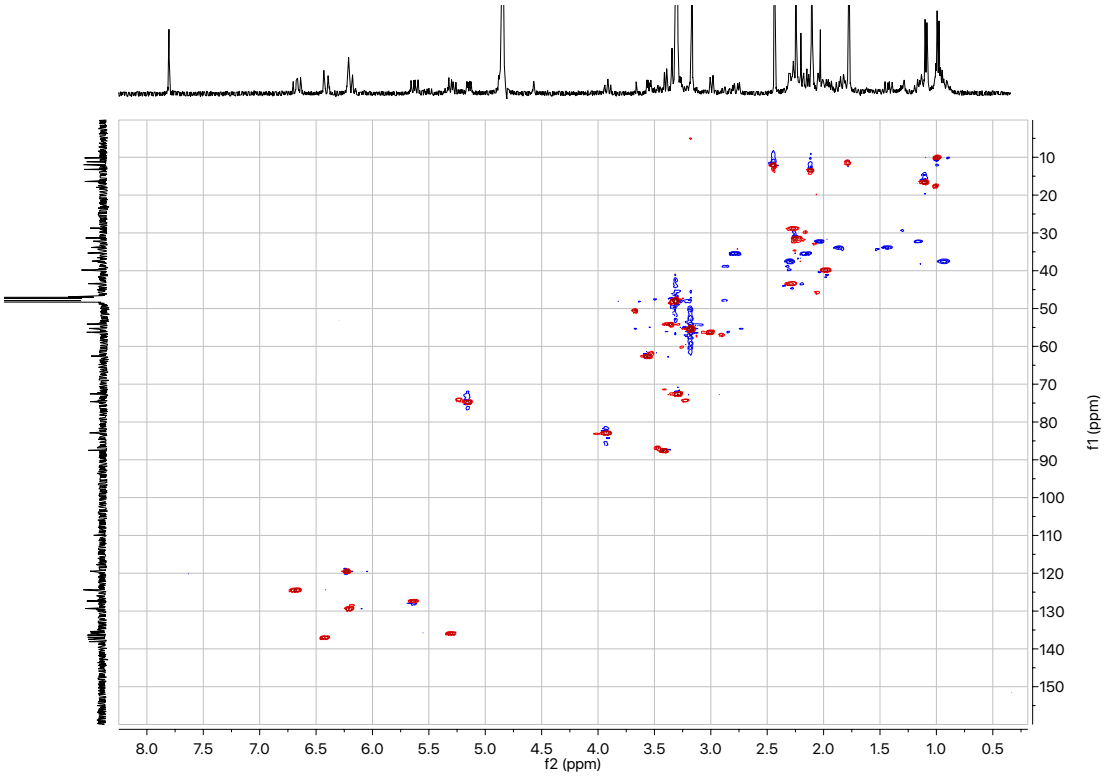

Figure C.5. HSQC NMR spectrum (500 MHz, d_4-methanol) of compound **2**

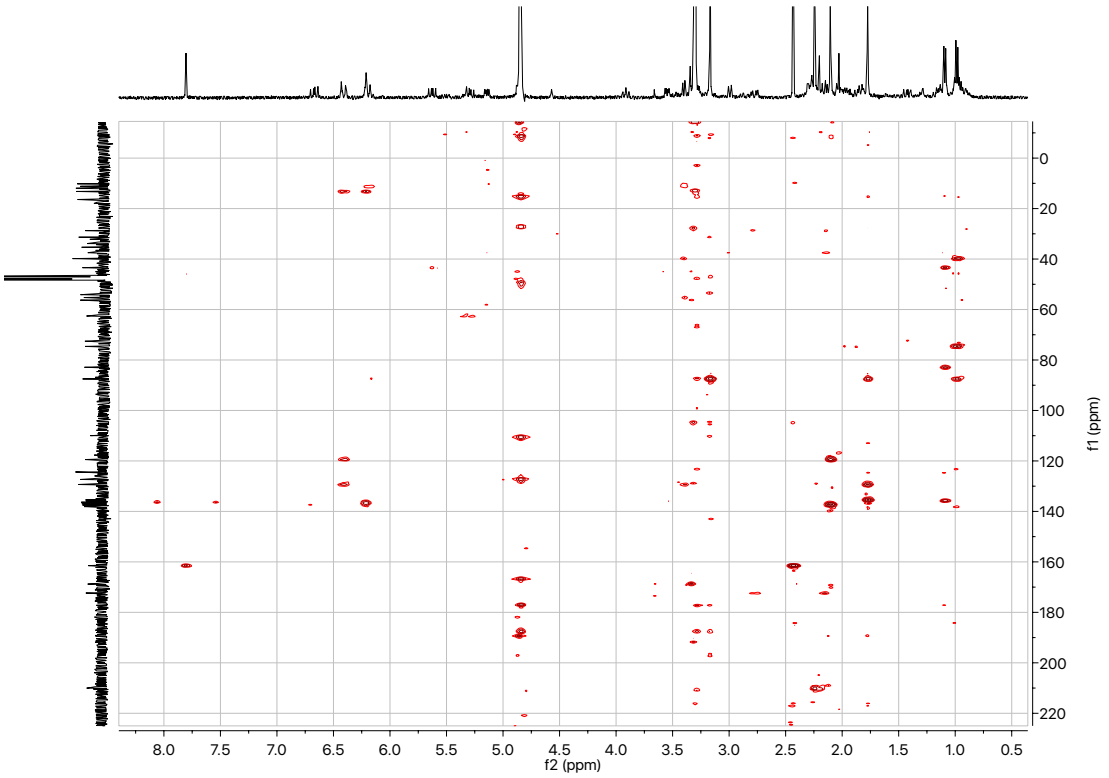

Figure C.6. HMBC NMR spectrum (500 MHz, d_4-methanol) of compound **2**

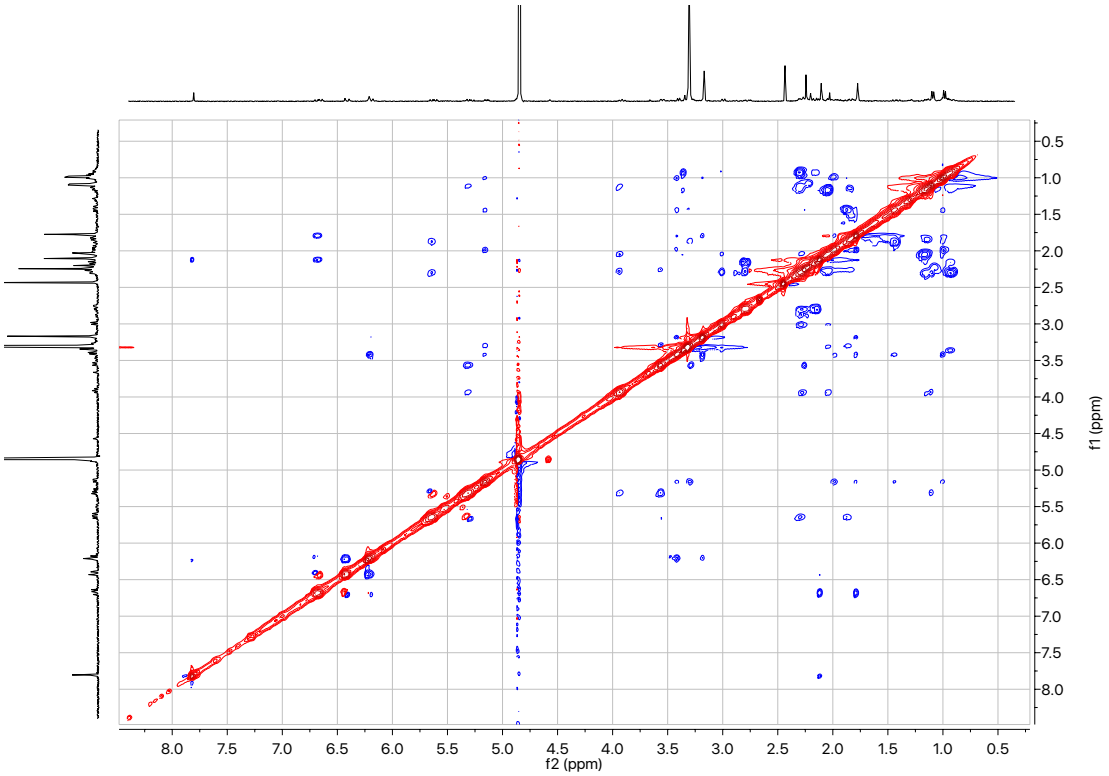

Figure C.7. ROESY NMR spectrum (500 MHz, d_4-methanol) of compound **2**

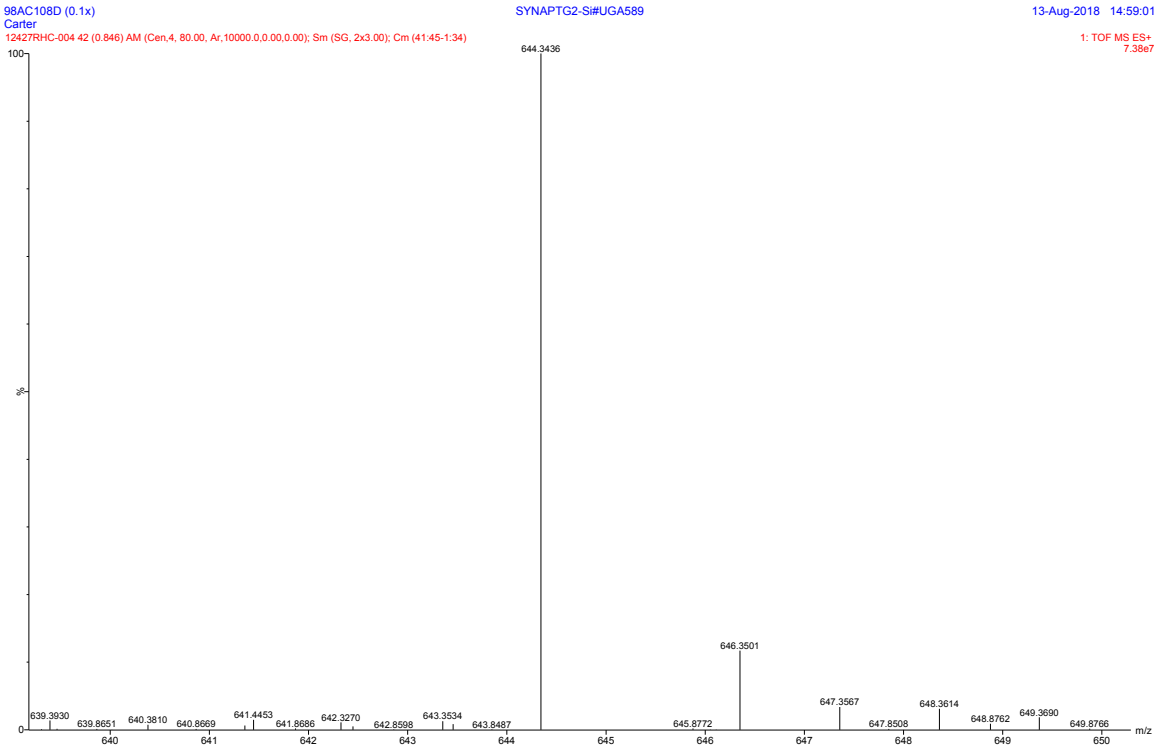

Figure C.8: HRESIMS spectrum of rhizoxin T1 (**3**).

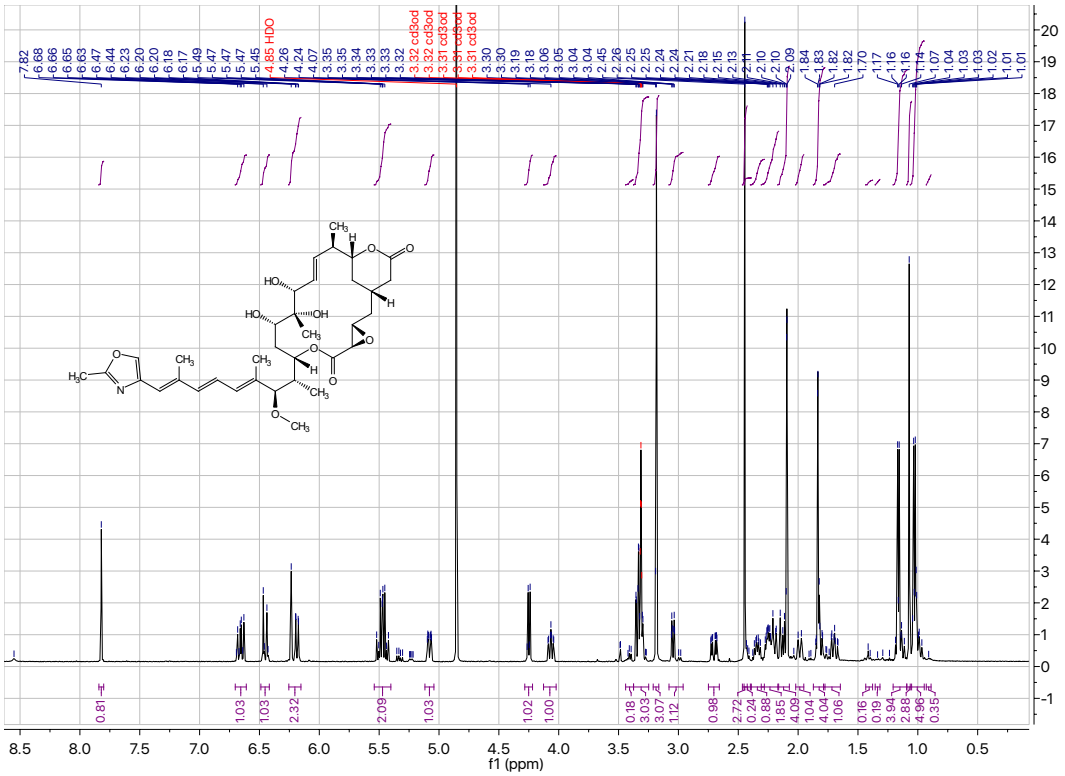

Figure C.9: ^{1}H NMR spectrum (500 MHz, d_4-methanol) of compound **3**.

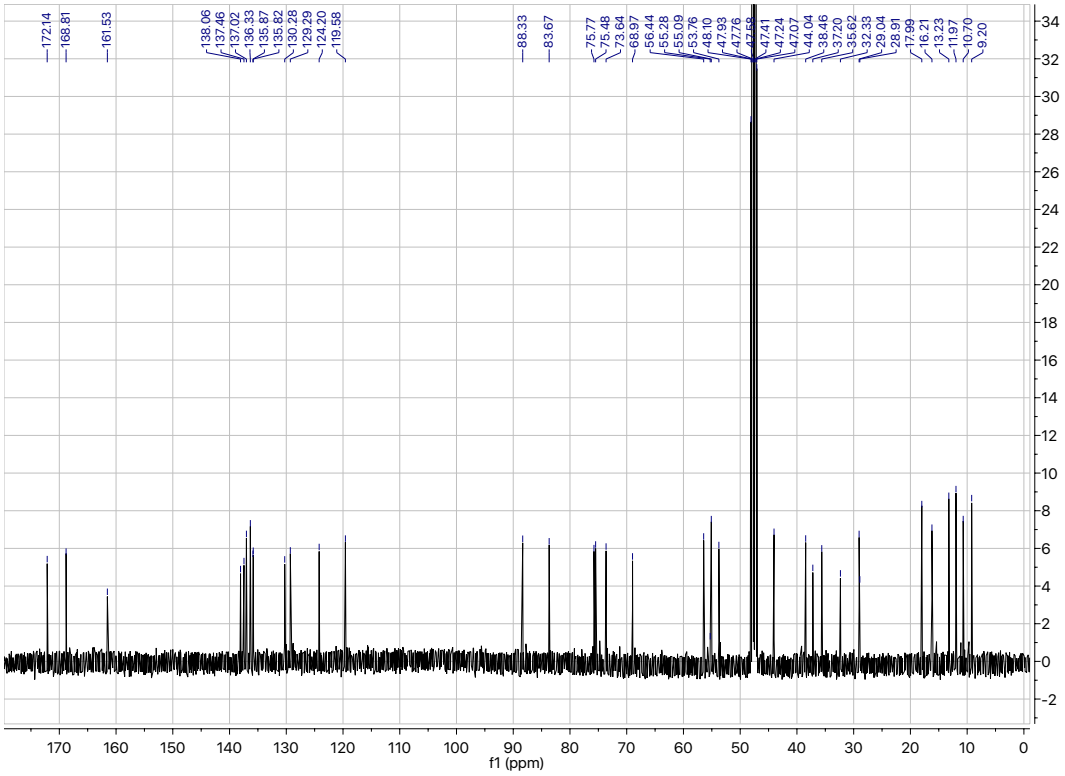

Figure C.10: ^{13}C NMR spectrum (125 MHz, d_4-methanol) of compound **3**.

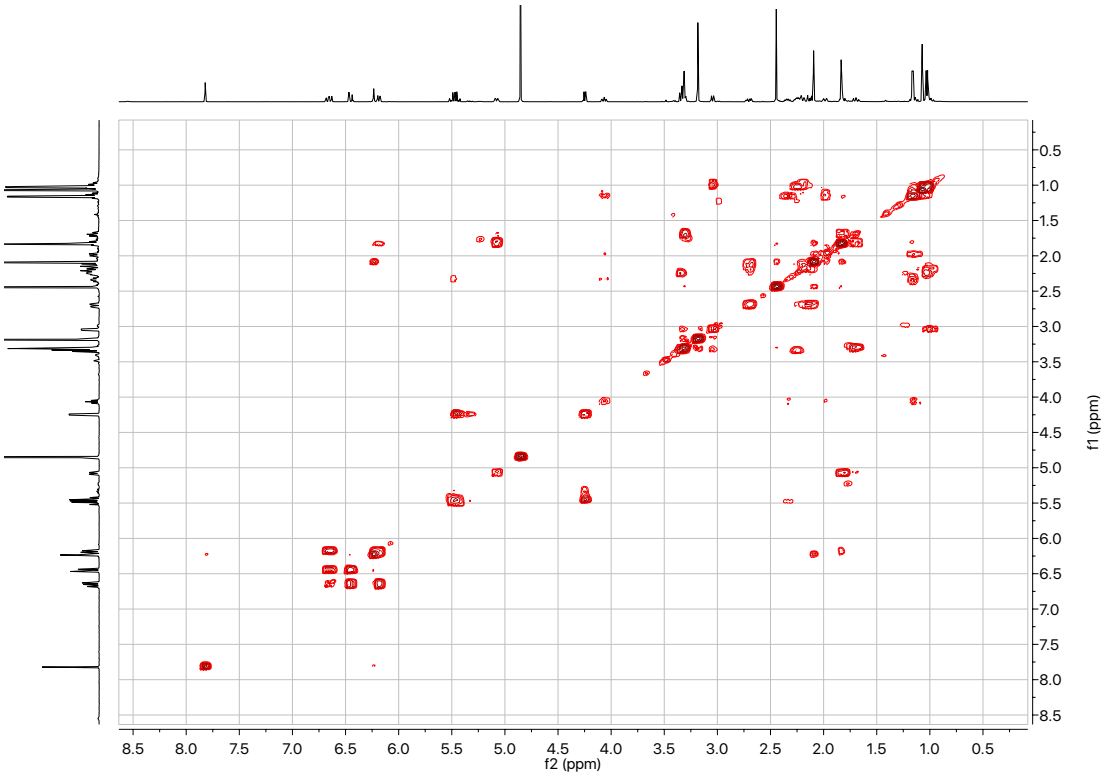

Figure C.11: COSY NMR spectrum (500 MHz, d_4-methanol) of compound **3**.

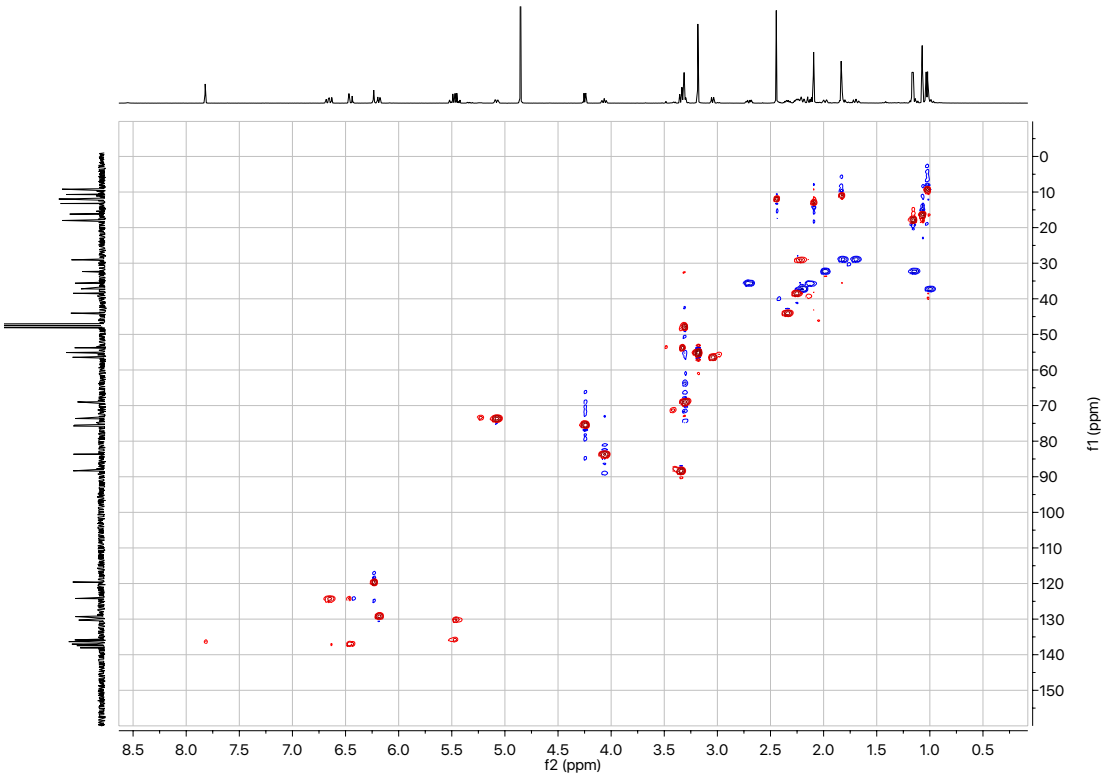

Figure C.12: HSQC NMR spectrum (500 MHz, d_4-methanol) of compound **3**.

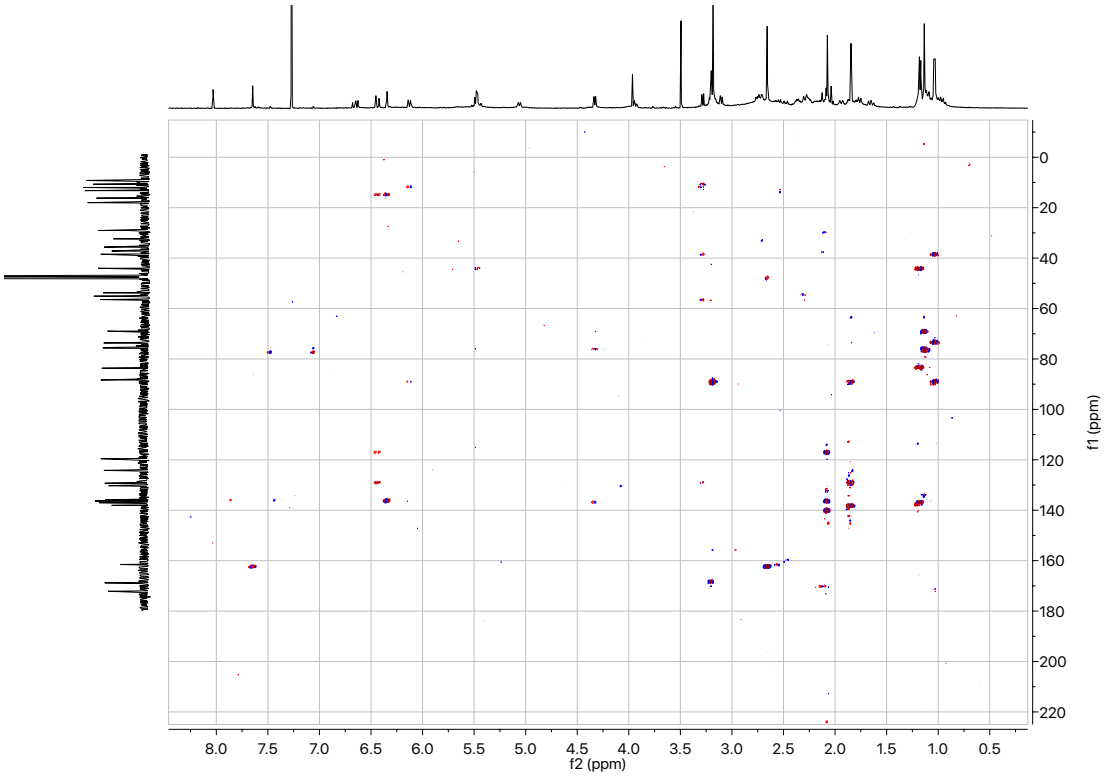

Figure C.13: HMBC NMR spectrum (500 MHz, d_4-methanol) of compound **3**.

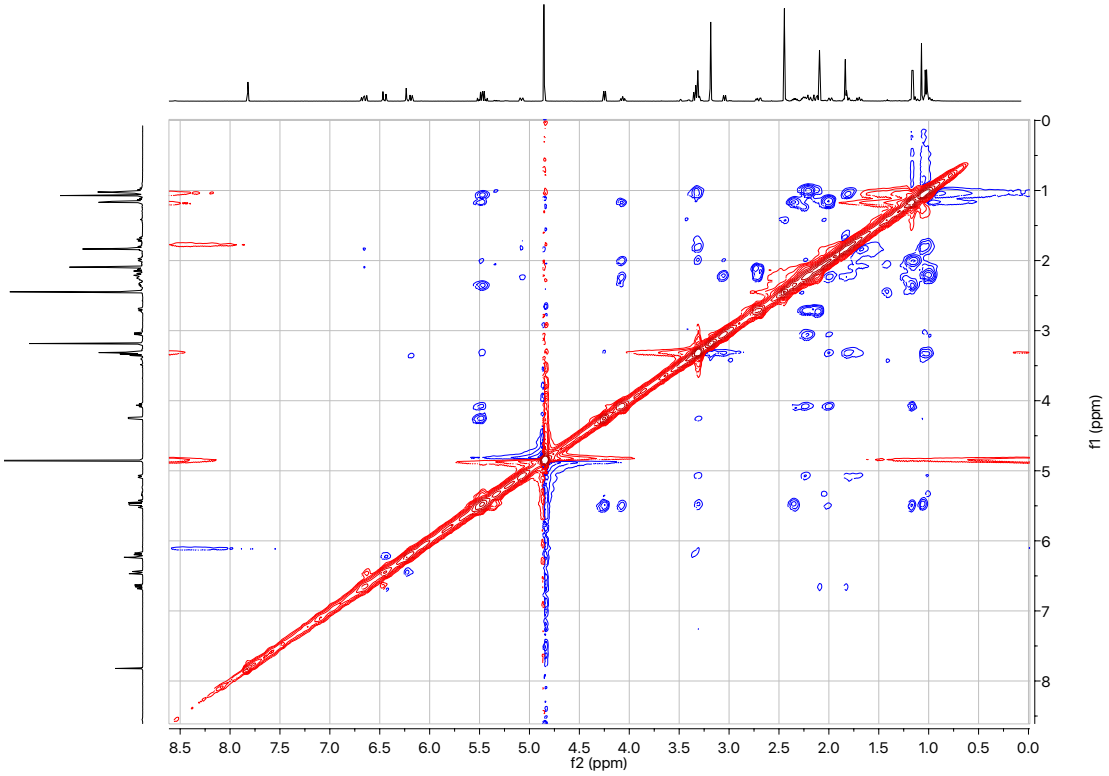

Figure C.14: ROESY NMR spectrum (500 MHz, d_4-methanol) of compound **3**.

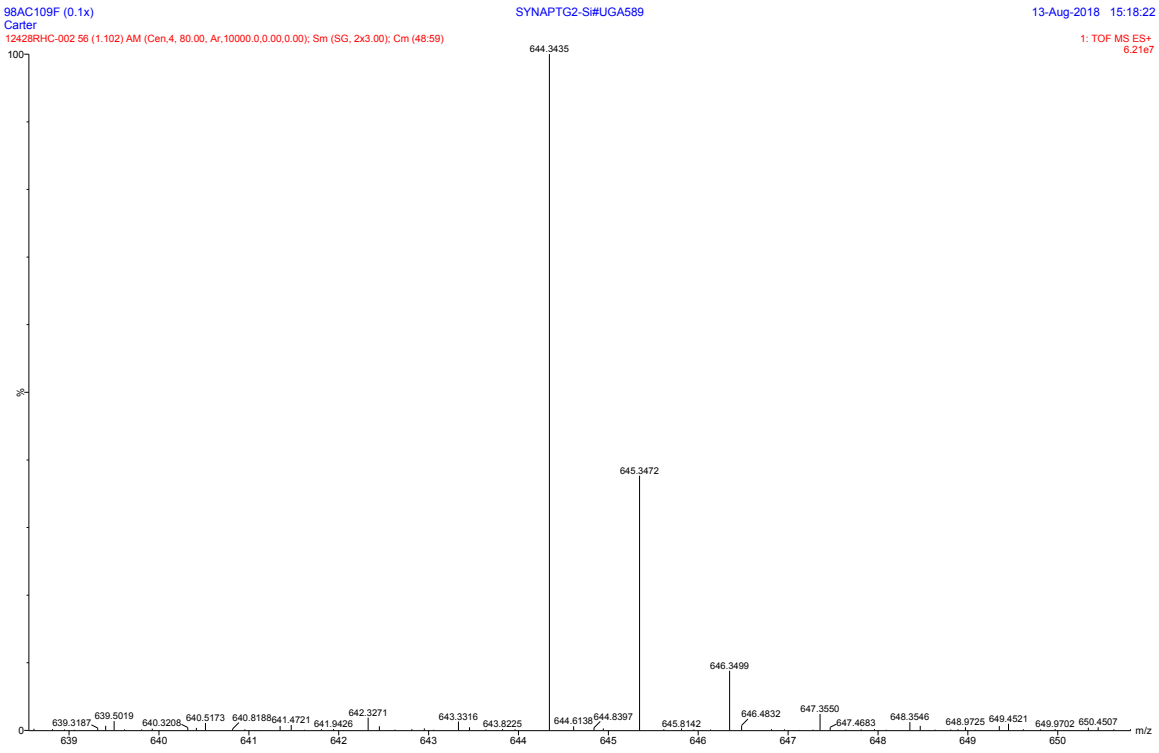

Figure C.15: HRESIMS spectrum of rhizoxin T2 (**4**).

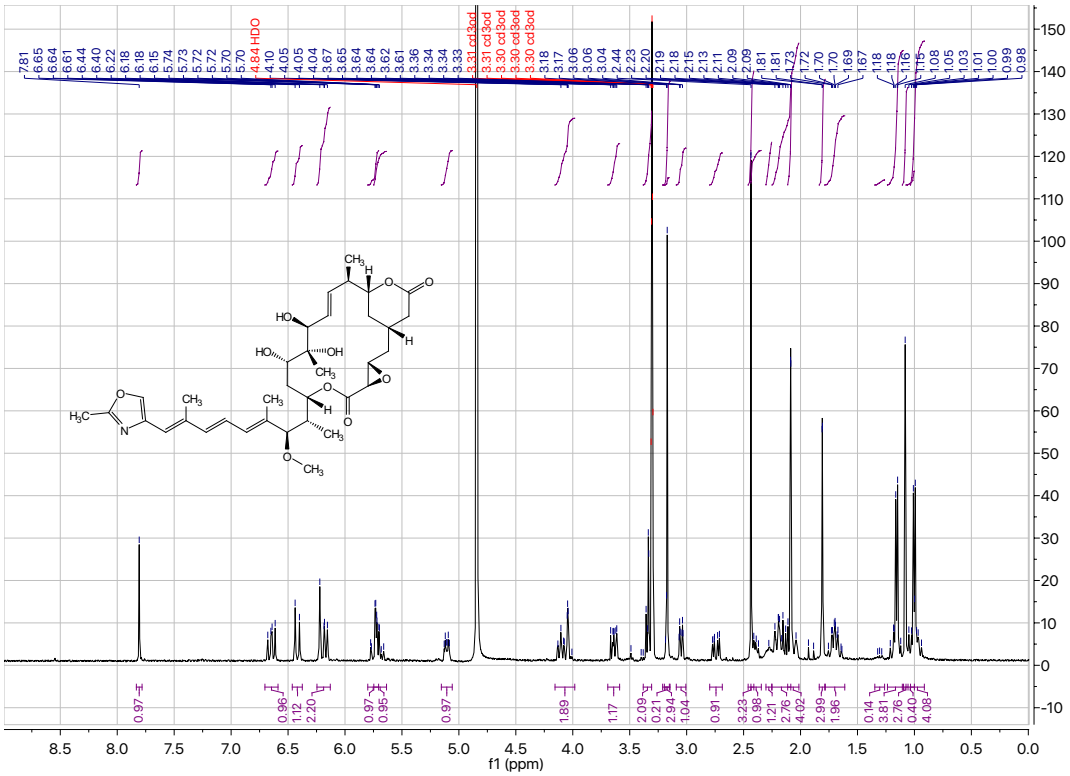

Figure C.16: ^{1}H NMR spectrum (400 MHz, d_4-methanol) of compound **4**.

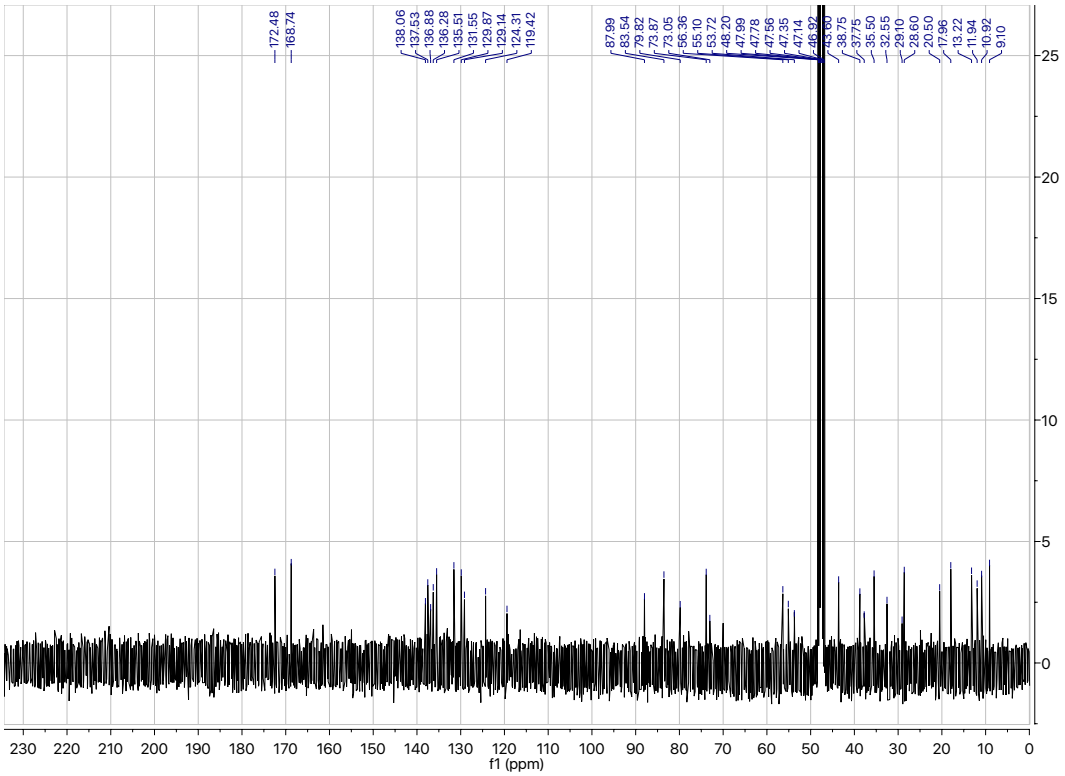

Figure C.17. ^{13}C NMR spectrum (100 MHz, d_4-methanol) of compound **4**

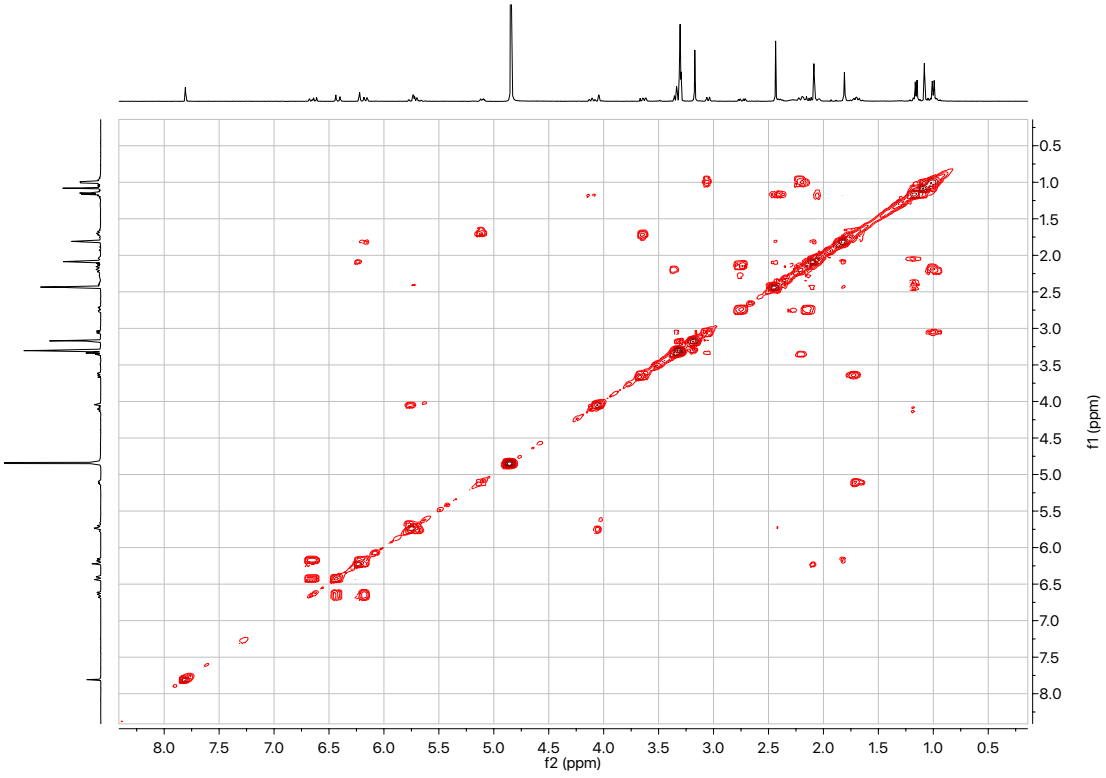

Figure C.18. COSY NMR spectrum (500 MHz, d_4-methanol) of compound **4**

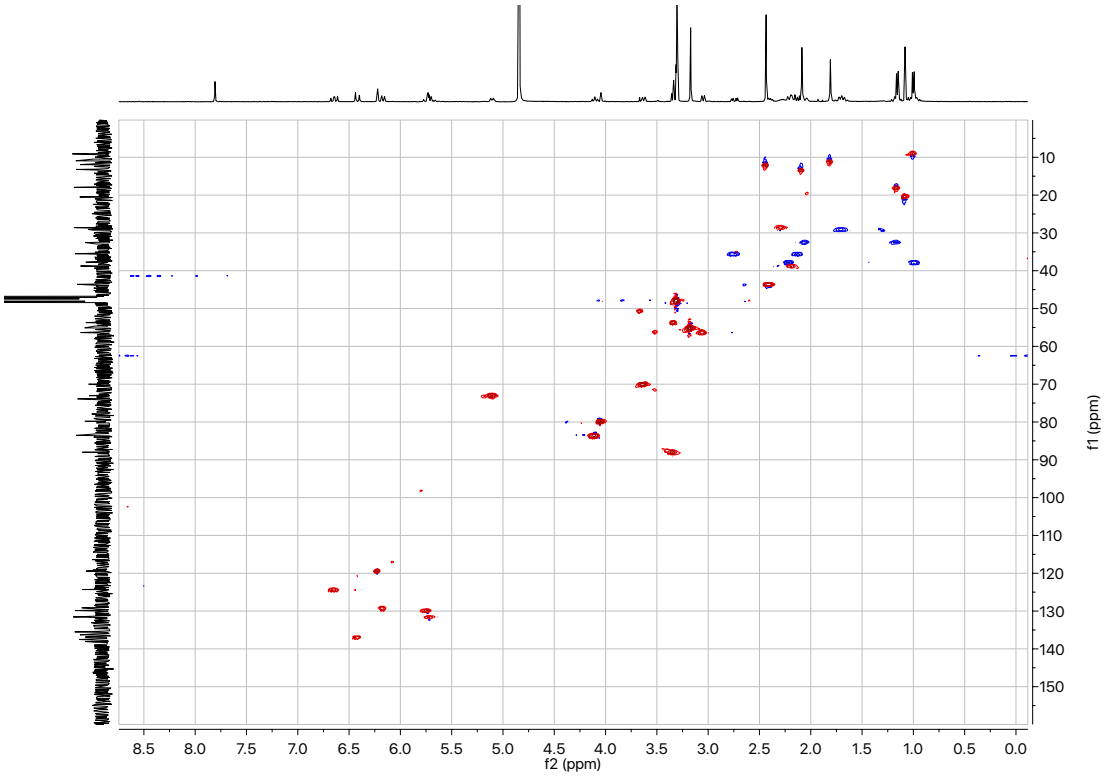

Figure C.19. HSQC NMR spectrum (500 MHz, d_4-methanol) of compound **4**

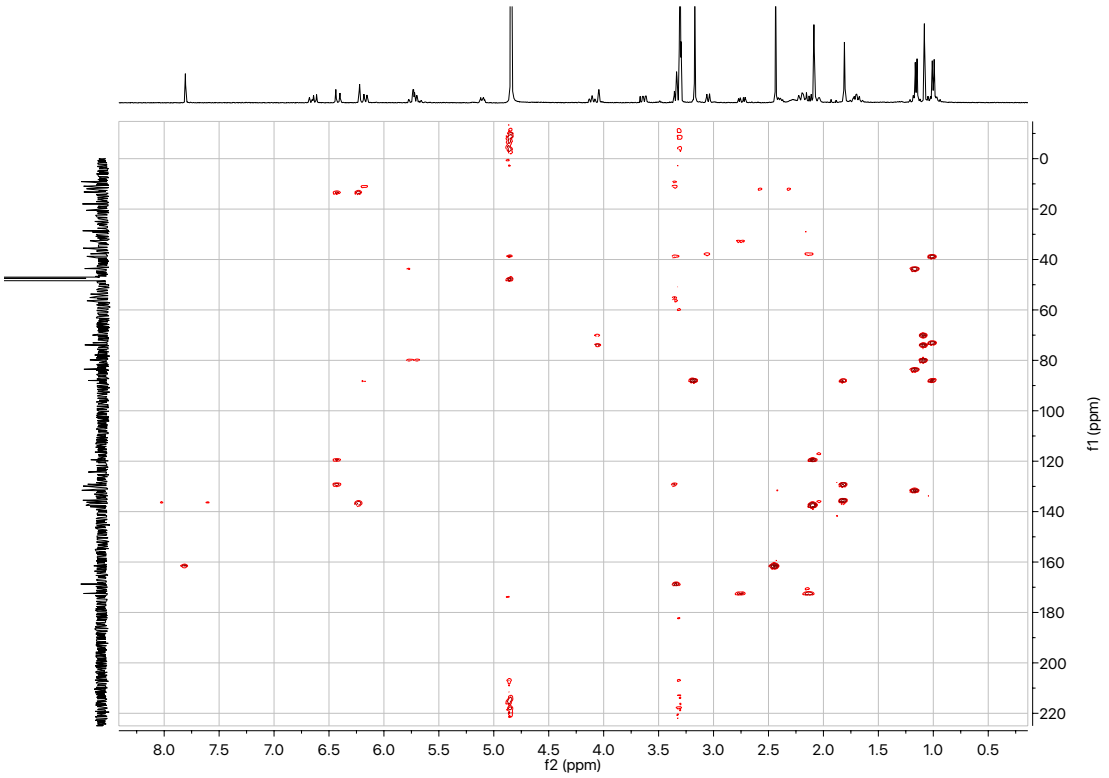

Figure C.20. HMBC NMR spectrum (500 MHz, d_4-methanol) of compound **4**

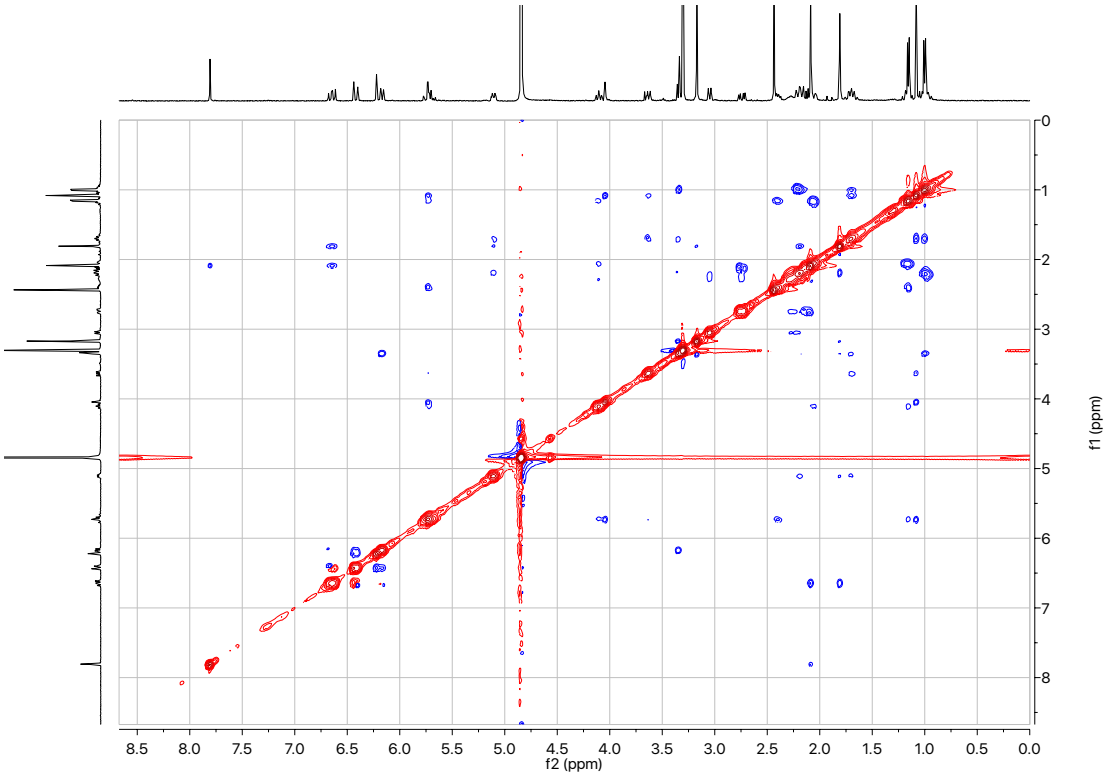

Figure C.21. ROESY NMR spectrum (500 MHz, d_4-methanol) of compound **4**

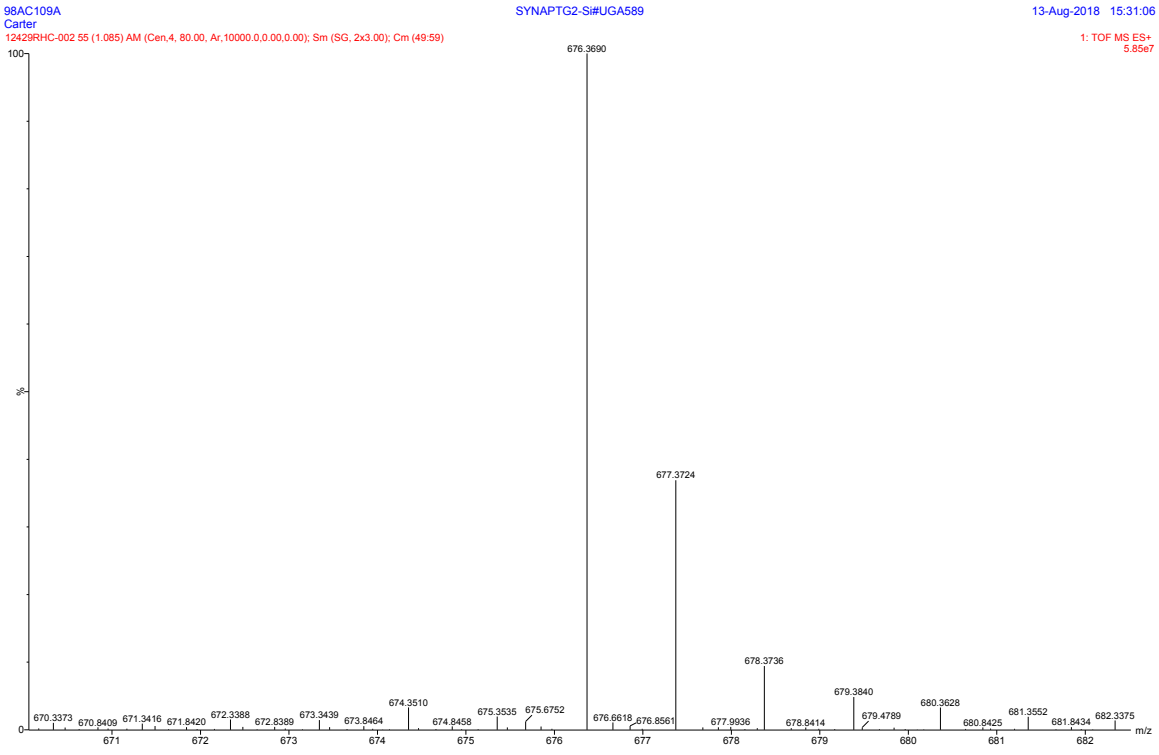

Figure C.22: HRESIMS spectrum of rhizoxin M3 (**5**).

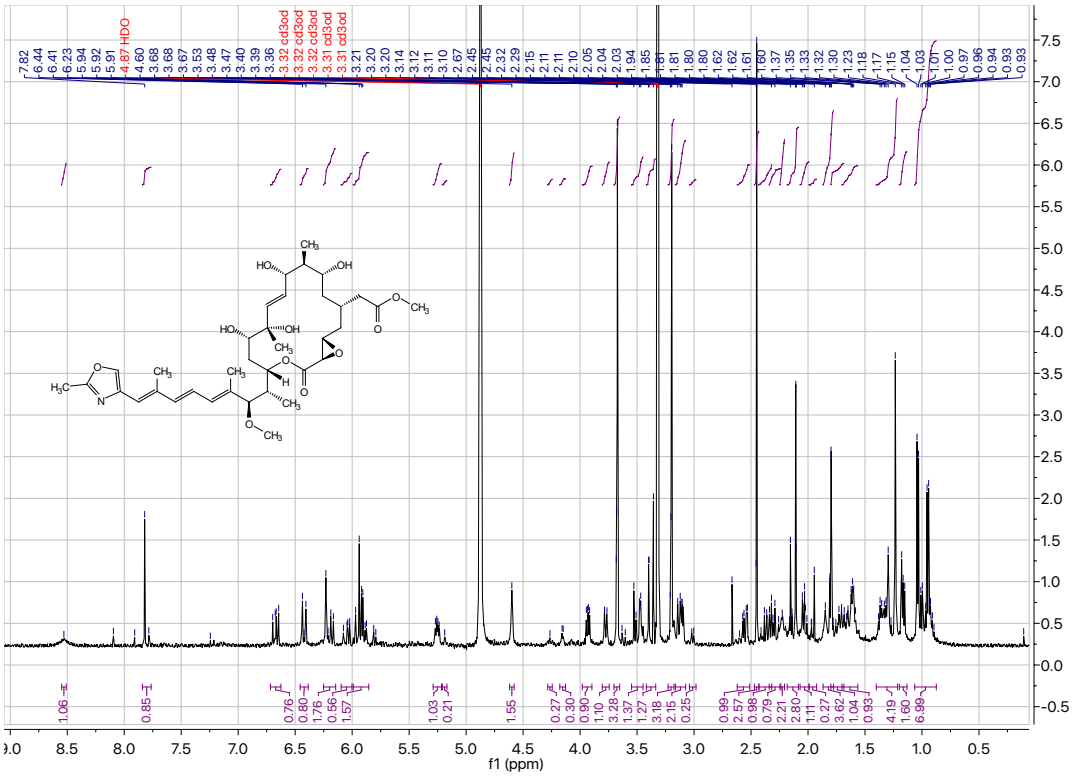

Figure C.23. ^{1}H NMR spectrum (500 MHz, d_4-methanol) of compound **5**

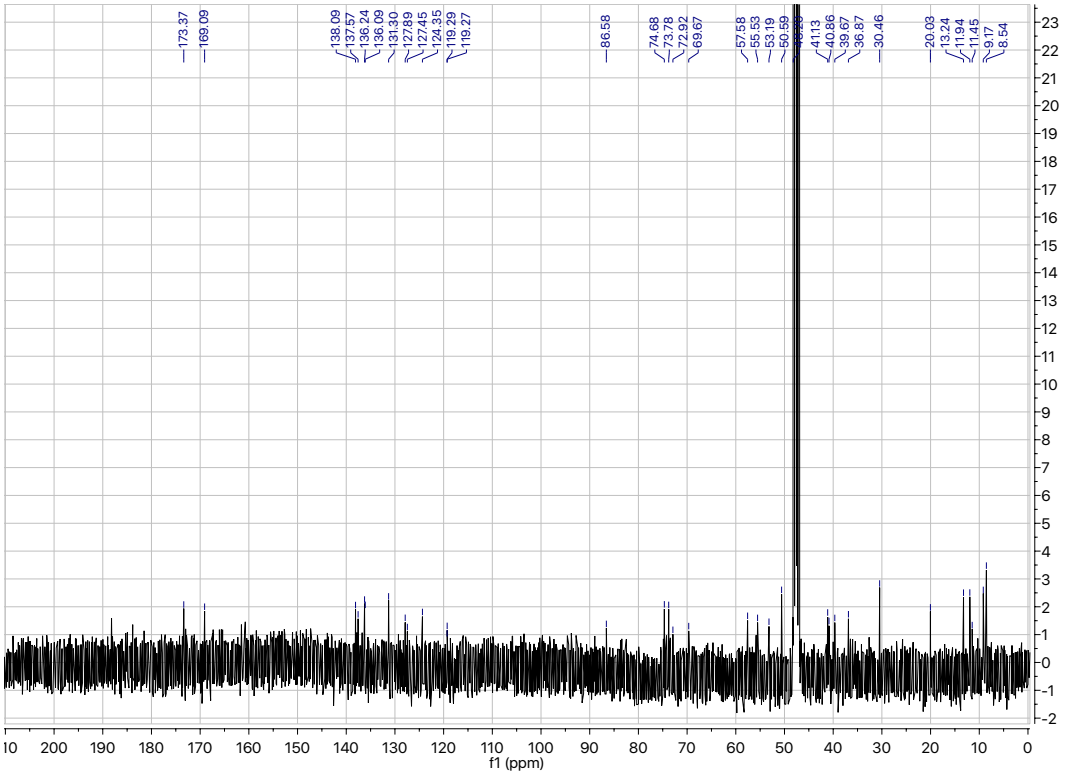

Figure C.24. ^{13}C NMR spectrum (100 MHz, d_4-methanol) of compound **5**

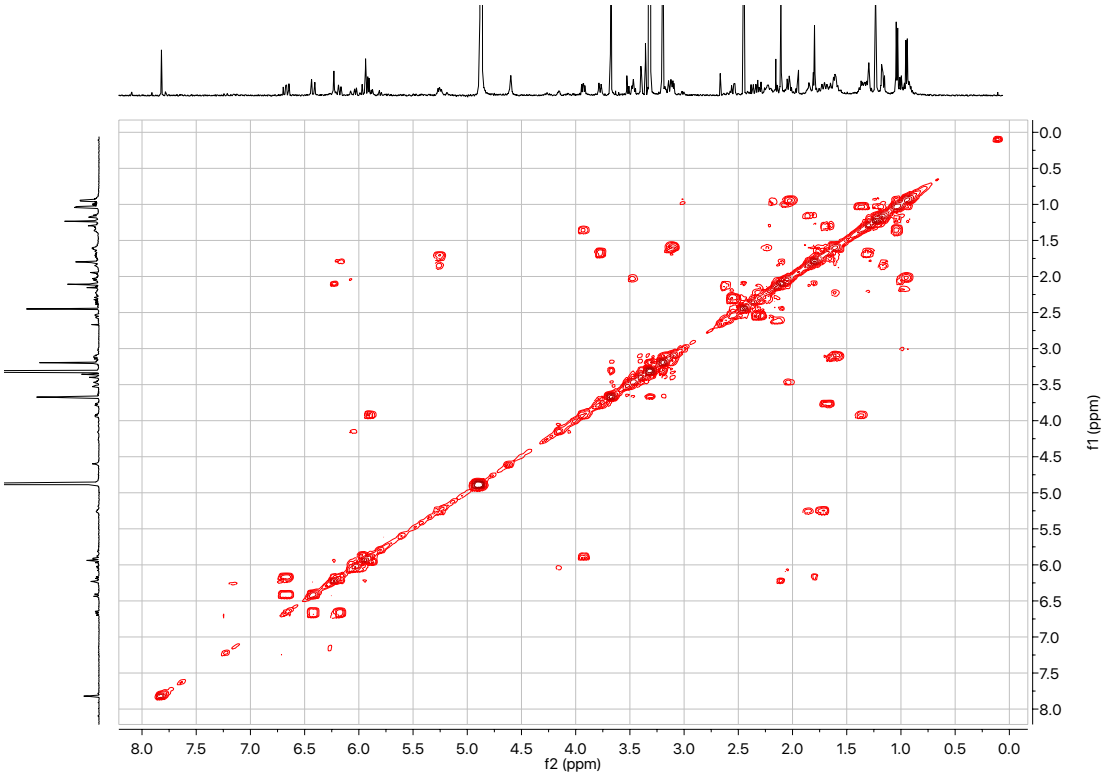

Figure C.25. COSY NMR spectrum (500 MHz, d_4-methanol) of compound **5**

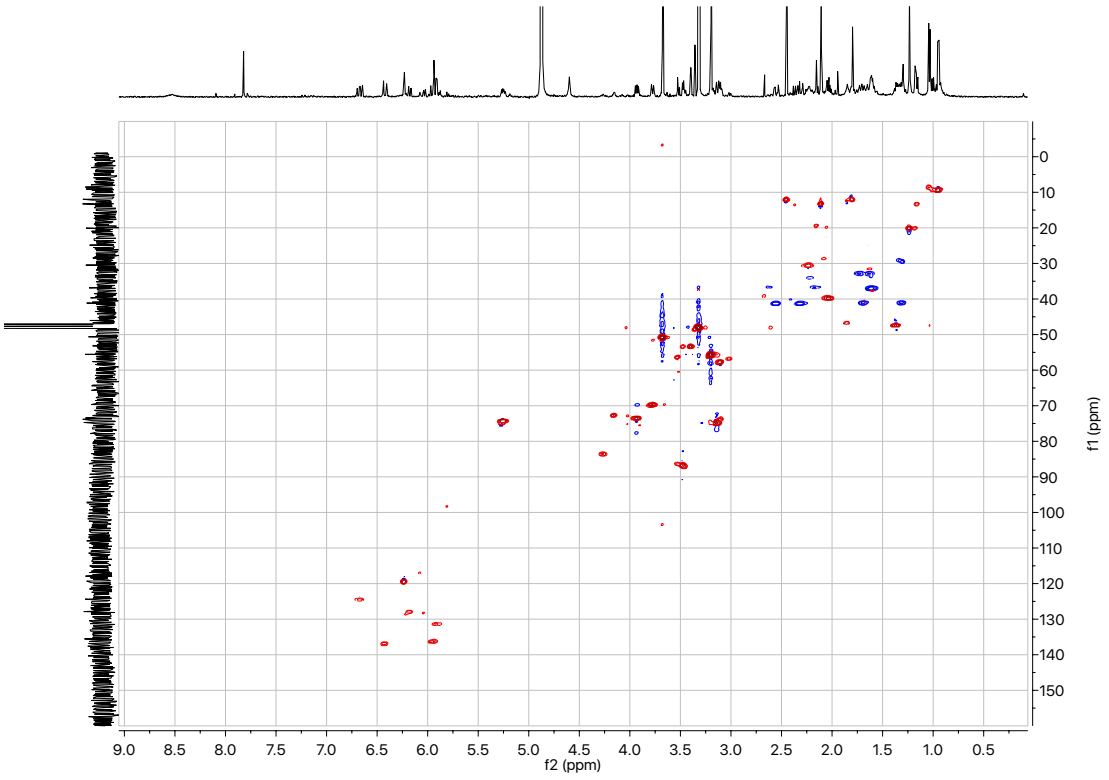

Figure C.26. HSQC NMR spectrum (500 MHz, d_4-methanol) of compound **5**

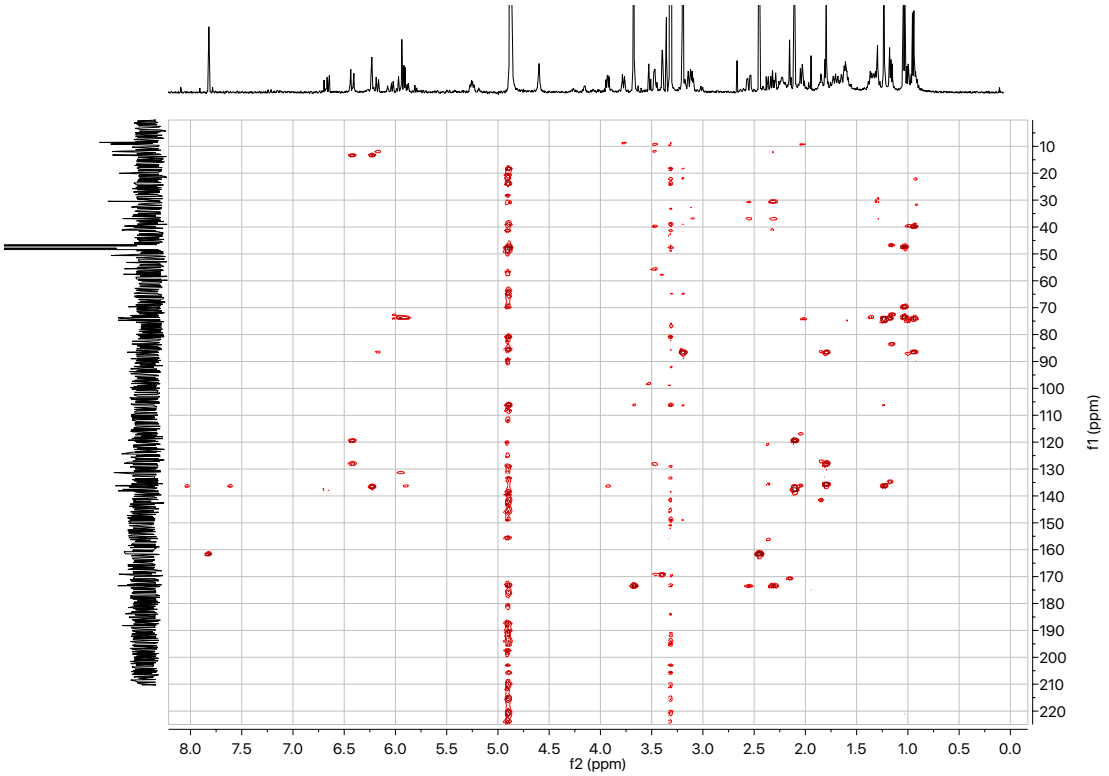

Figure C.27. HMBC NMR spectrum (500 MHz, d_4-methanol) of compound **5**

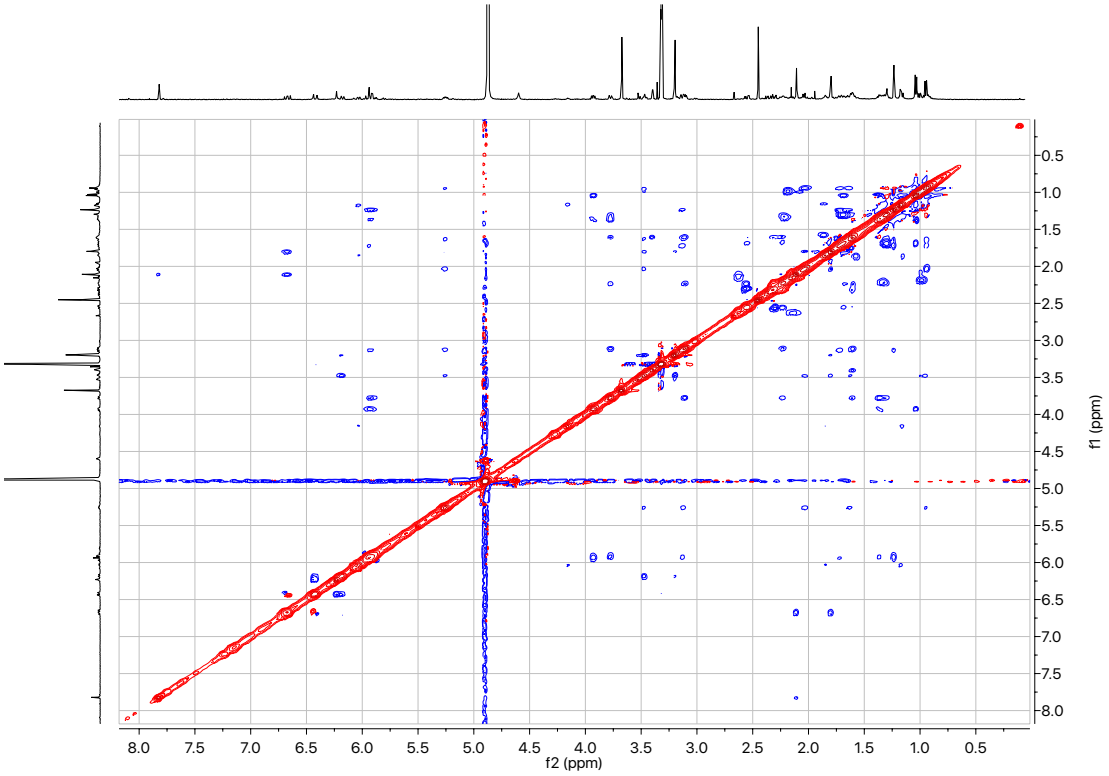

Figure C.28. ROESY NMR spectrum (500 MHz, d_4-methanol) of compound **5**

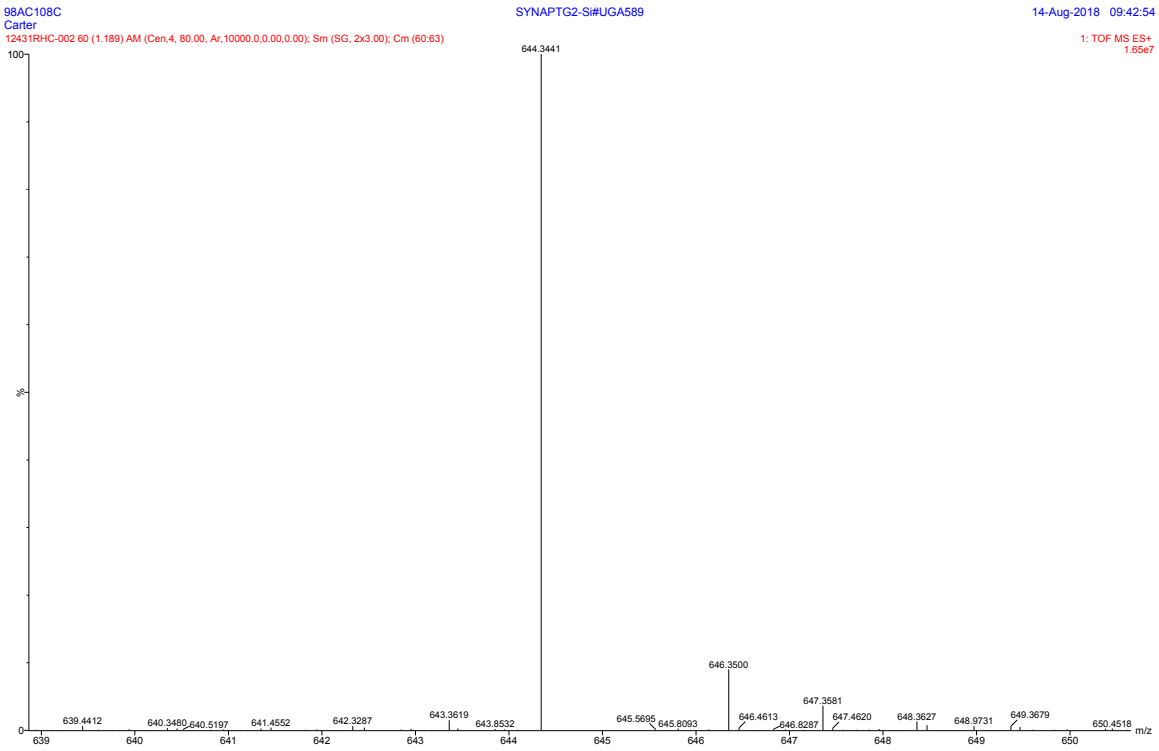

Figure C.29. HRESIMS spectrum of rhizoxin T3 (**6**)

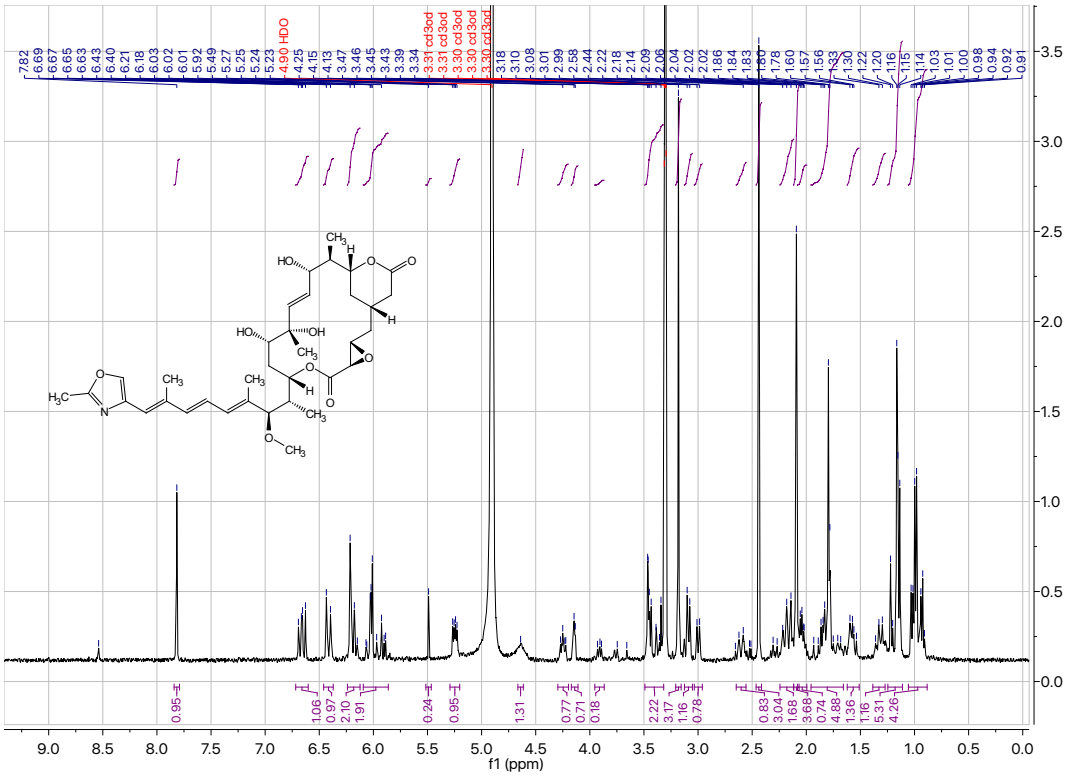

Figure C.30. ^{1}H NMR spectrum (400 MHz, d_4-methanol) of compound **6**

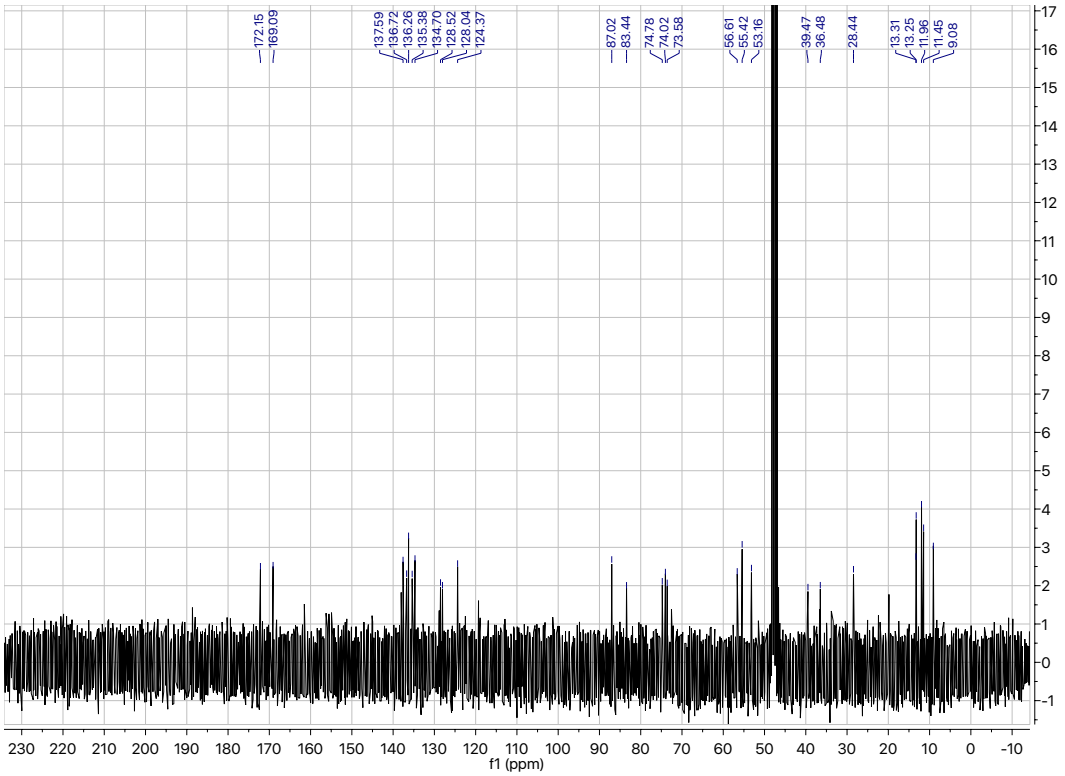

Figure C.31. ^{13}C NMR spectrum (100 MHz, d_4-methanol) of compound **6**

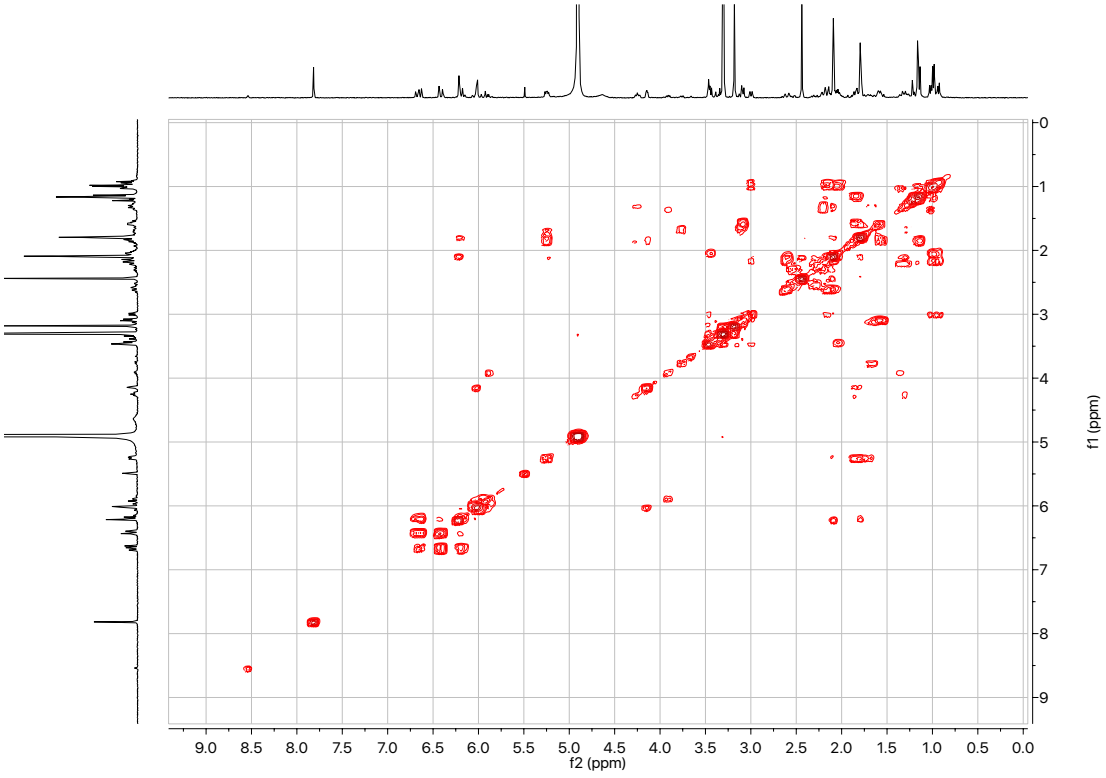

Figure C.32. COSY NMR spectrum (500 MHz, d_4-methanol) of compound **6**

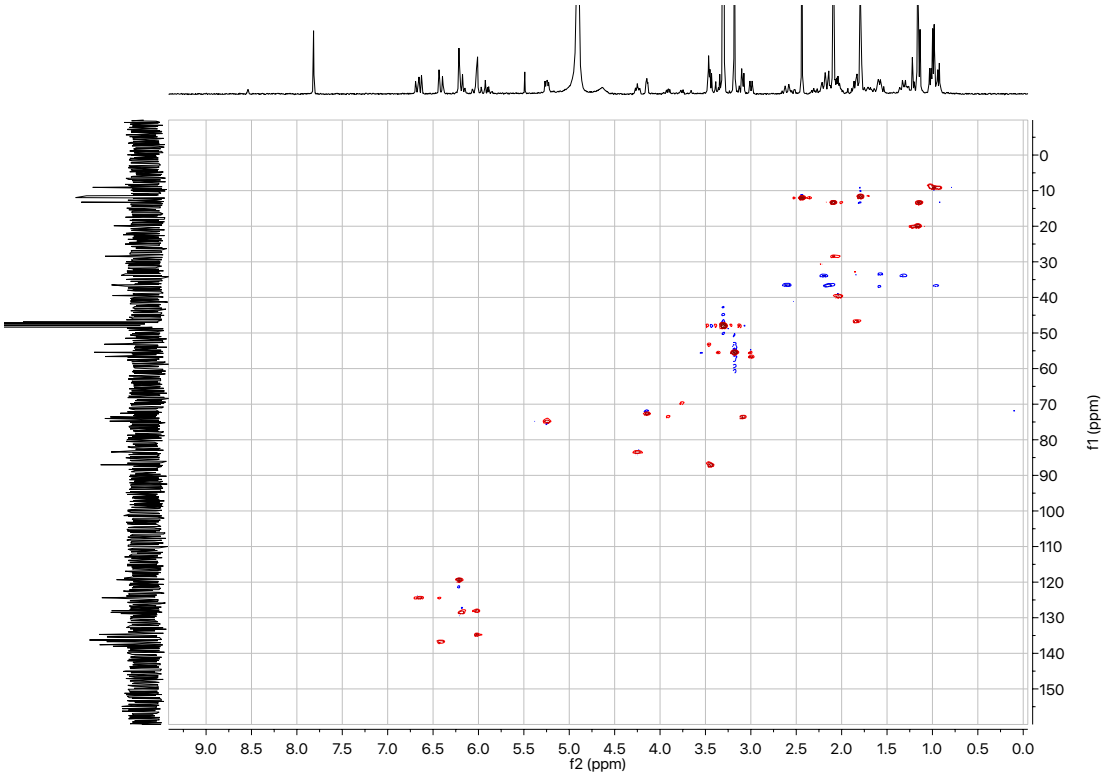

Figure C.33. HSQC NMR spectrum (500 MHz, d_4-methanol) of compound **6**

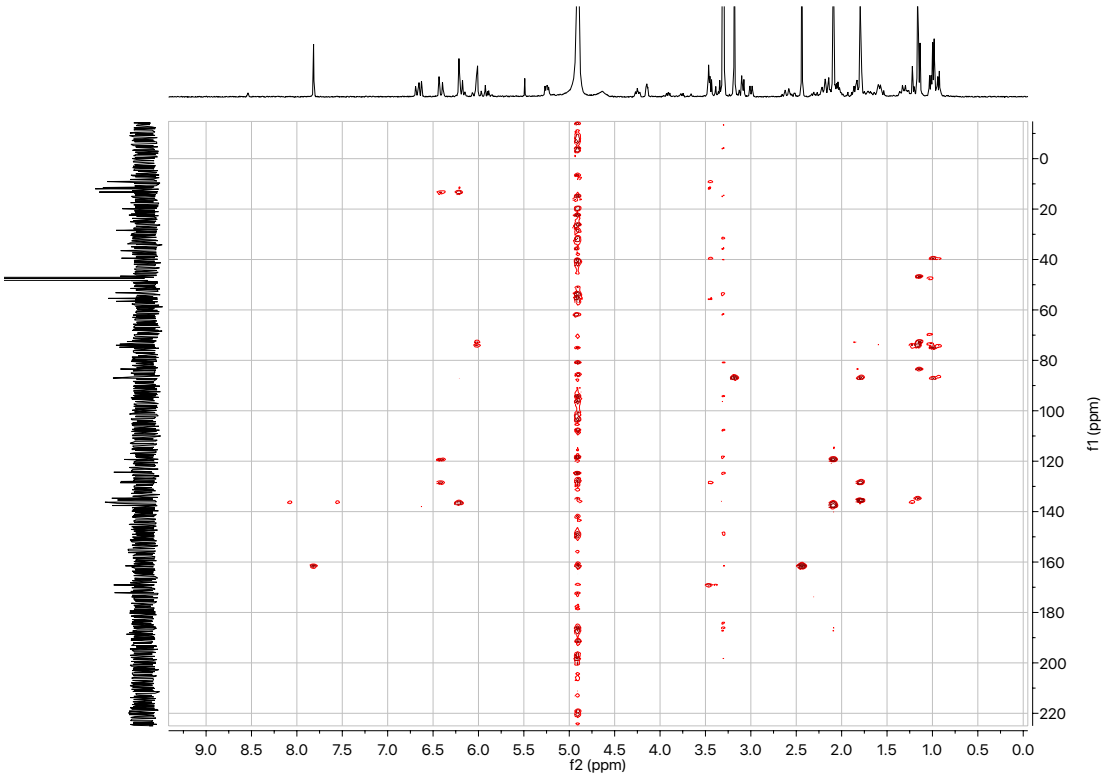

Figure C.34. HMBC NMR spectrum (500 MHz, d_4-methanol) of compound **6**

Table C.1. NMR spectroscopic data (500 MHz, d_4-methanol) of rhizoxin (**1**)

	Rhizoxin (**1**)	
No.	δ_C, type	δ_H (*J* in Hz)
1	168.4, C	
2	53.9, CH	3.15, d (2.0)
3	55.1, CH	3.26, dt (10.5, 2.0, 2.0)
4	35.1, CH_2	2.26, m
		0.86, q (11.0, 11.0, 11.0)
5	37.0, CH	2.04, m
5a	35.7, CH_2	2.99, m
		2.05, m
5b	171.7, C	
5c		
6	29.5, CH_2	1.93, m
		1.08, m
7	83.0, CH	4.02, ddd (12.0, 9.5, 3.0)
8	45.1, CH	2.34, m
8a	15.9, CH_3	1.17, d (6.5)
9	139.2, CH	5.68, dd (15.0, 10.0)
10	126.8 CH	5.45, dd (15.0, 9.0)
11	62.2, CH	3.20, d (9.0)
12	64.3, C	
12a	10.5, CH_3	1.39, s
13	77.1, CH	3.20, m
14	28.8, CH_2	2.04, m
		1.87, m
15	76.2, CH	4.54, dd (8.5, 3.5)
16	37.7, CH	2.37, m
16a	8.3, CH_3	0.99, d (6.7)
17	89.2, CH	3.33, d (9.0)
17-OMe	56.0, CH_3	3.17, s
18	137.3, C	
18a	11.9, CH_3	1.81, s
19	129.6, CH	6.15, d (11.0)
20	123.8, CH	6.65, dd (10.5, 15.0)
21	123.8, CH	6.44, d (15.0)
22	136.4, C	
22a	15.9, CH_3	2.11, s
23	120.0, CH	6.24, s
24	137.5, C	
25	136.0, CH	7.82, s
26	161.5, C	
26a	13.2, CH_3	2.44, s

Discussion C.1. General computational information for NMR calculations

Molecular mechanics calculations were performed using MacroModel[199] within the Maestro[200] software. Conformation searches were carried out using a Monte Carlo multiple minimum (MCMM) search with a Merck molecular force field (MMFFs). Structures were minimized using a truncated Newton conjugate gradients (TNCG) approach with 500 iterations and a convergence criterion of 0.05. Conformation searches were performed such that all conformers within 10.0 kJ/mol of the lowest energy conformer were found an average of at least 10 times, and all conformers within 21.0 kJ/mol of the lowest energy conformer were retained. Additionally, conformers having the same conformation of the macrolactone backbone were eliminated using a redundant conformation elimination step using a threshold of 0.5Å for displacement and 1 kJ/mol for energy.

All geometry optimizations, frequency calculations, and NMR calculations were performed using Gaussian 09.[201] All conformations retained following redundant conformer elimination were subjected to geometry optimization and subsequent frequency calculations using the mPW1PW91 functional and 6-31G(d) basis set with IEF-PCM solvation modeling setting methanol as the solvent. Gibbs free energies from these optimizations and frequency calculations were then used to perform a Boltzmann population analysis. Any conformers making up ≥1% of the total population were then subjected to GIAO NMR calculations using the mPW1PW91 functional and 6-311G(d,p) basis set with IEF-PCM solvation with methanol. Additionally, NMR coupling constants were calculated for each of these conformers using the B3LYP functional and 6-31G(d,p) basis set.

Shielding tensor constants were extracted for each conformer and a weighted average was calculated for each nucleus of interest using the Boltzmann population distribution for the conformers. The shielding tensor values for proton (31.92128) and carbon (189.5456) nuclei calculated for TMS using the same level of theory were used as a reference to determine the chemical shift values for each nucleus. Additionally, the calculated chemical shifts (y-axis) were plotted against the experimentally determined chemical shifts of each compound (x-axis) in order to obtain a best-fit line that was used to scale the calculated chemical shift values for each possible diastereomer.[194] To evaluate the computational methodology used to support the stereochemical assignments of **2**-**6**, an analysis of 13*S* and 13*R* configurations of **1** by GIAO NMR calculations was performed, correctly determining the configuration as 13*S*.

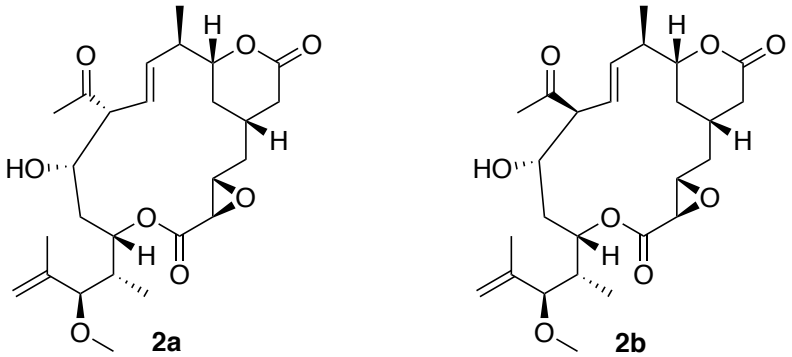

Figure C.35. Possible truncated diastereomers for **2** studied computationally.

Table C.2. Calculated energies and populations for the major conformers of **2a**. All conformers with the combined population of 98.73% were used to calculate NMR properties of **2a**.

Conformer	$\Delta E^{MMFFs, gas}$ (kJ/mol)	ΔG^{DFT} (kcal/mol)	Population %
2a-1	14.4	0.0	32.54
2a-2	9.6	0.1	29.76
2a-3	19.8	0.4	16.95
2a-4	0.0	0.5	12.95
2a-5	2.2	1.0	5.54
2a-6	20.7	2.1	0.99

Table C.3. Calculated energies and population for the major conformers of **2b**. All conformers with the combined population of 98.88% were used to calculate NMR properties of **2b**.

Conformer	$\Delta E^{MMFFs, gas}$ (kJ/mol)	ΔG^{DFT} (kcal/mol)	Population %
2b-1	16.7	0.0	28.92
2b-2	10.1	0.1	25.74
2b-3	17.7	0.5	12.01
2b-4	11.1	0.5	11.94
2b-5	9.0	1.0	5.73
2b-6	14.2	1.0	5.60
2b-7	7.2	1.0	5.08
2b-8	13.2	1.7	1.58
2b-9	15.6	1.9	1.14
2b-10	10.3	1.9	1.14

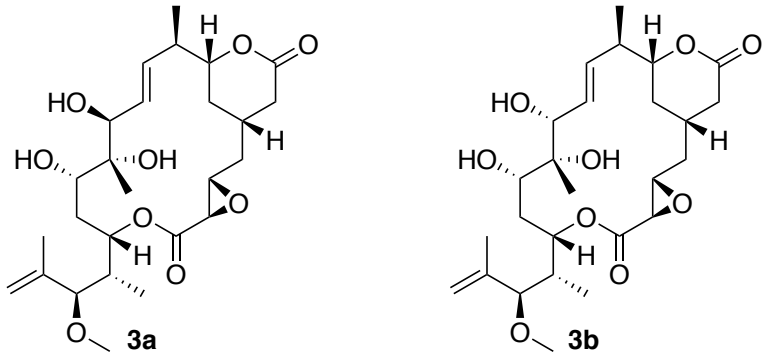

Figure C.36. Possible truncated diastereomers for **3** and **4** studied computationally.

Table C.4. Calculated energies and populations for the major conformers of **3a**. All conformers with the combined population of 99.40% were used to calculated NMR properties of **3a**.

Conformer	$\Delta E^{MMFFs, gas}$ (kJ/mol)	ΔG^{DFT} (kcal/mol)	Population %
3a-1	19.6	0.0	21.17
3a-2	16.3	0.0	19.76
3a-3	18.7	0.0	19.72
3a-4	8.4	0.3	12.74
3a-5	12.0	0.3	12.72
3a-6	12.7	0.5	9.58
3a-7	10.5	1.3	2.37
3a-8	16.5	1.6	1.34

Table C.5. Calculated energies and population for the major conformers of **3b**. All conformers with the combined population of 98.27% were used to calculate NMR properties of **3b**.

Conformer	$\Delta E^{MMFFs, gas}$ (kJ/mol)	ΔG^{DFT} (kcal/mol)	Population %
3b-1	6.5	0.0	53.26
3b-2	14.8	0.5	23.15
3b-3	11.4	1.5	4.51
3b-4	14.8	1.5	4.50
3b-5	11.0	1.6	3.79
3b-6	6.4	1.6	3.76
3b-7	3.6	1.8	2.65
3b-8	8.1	1.8	2.64

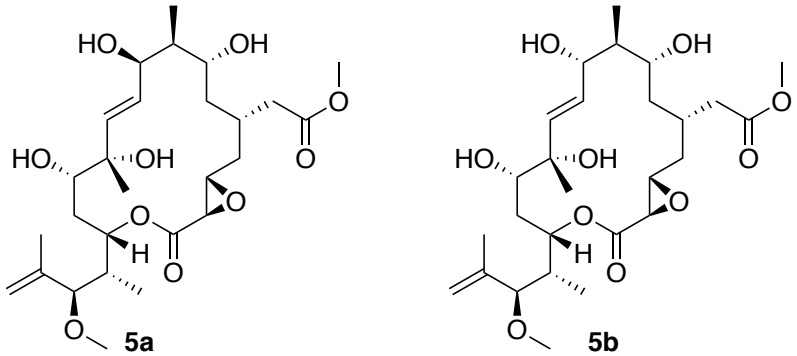

Figure C.37. Possible truncated diastereomers for **5** studied computationally.

Table C.6. Calculated energies and population for the major conformers of **5a**. All conformers with the combined population of 98.22% were used to calculate NMR properties of **5a**.

Conformer	$\Delta E^{MMFFs, gas}$ (kJ/mol)	ΔG^{DFT} (kcal/mol)	Population %
5a-1	17.6	0.0	26.02
5a-2	0.7	0.0	25.85
5a-3	13.5	0.3	16.77
5a-4	6.4	0.4	13.54
5a-5	12.0	0.7	7.78
5a-6	13.2	1.1	3.73
5a-7	18.2	1.3	2.83
5a-8	7.1	1.6	1.69

Table C.7. Calculated energies and population for the major conformers of **5b**. All conformers with the combined population of 99.15% were used to calculate NMR properties of **5b**.

Conformer	$\Delta E^{MMFFs, gas}$ (kJ/mol)	ΔG^{DFT} (kcal/mol)	Population %
5b-1	4.7	0.0	31.85
5b-2	11.0	0.1	28.59
5b-3	15.8	0.6	12.40
5b-4	17.0	0.6	12.25
5b-5	11.9	1.3	3.28
5b-6	6.2	1.4	2.81
5b-7	1.6	1.4	2.78
5b-8	12.4	1.5	2.52
5b-9	9.8	1.8	1.58
5b-10	15.5	2.0	1.08

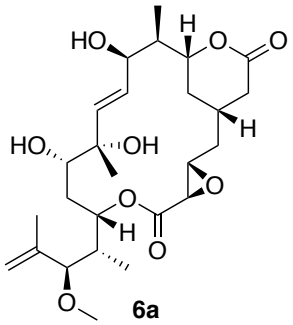

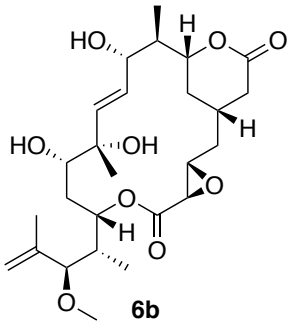

Figure C.38. Possible truncated diastereomers for **6** studied computationally.

Table C.8. Calculated energies and population for the major conformers of **6a**. All conformers with the combined population of 96.18% were used to calculate NMR properties of **6a**.

Conformer	$\Delta E^{MMFFs, gas}$ (kJ/mol)	ΔG^{DFT} (kcal/mol)	Population %
6a-1	20.3	0.0	28.48
6a-2	20.2	0.2	21.32
6a-3	18.7	0.6	10.34
6a-4	10.5	0.8	7.74
6a-5	0.0	0.9	6.67
6a-6	4.5	0.9	6.64
6a-7	18.9	1.1	4.40
6a-8	7.5	1.2	3.77
6a-9	12.5	1.4	2.50
6a-10	18.0	1.6	2.03
6a-11	2.6	1.8	1.31
6a-12	16.5	2.0	1.00

Table C.9. Calculated energies and population for the major conformers of **6b**. All conformers with the combined population of 96.23% were used to calculate NMR properties of **6b**.

Conformer	$\Delta E^{MMFFs, gas}$ (kJ/mol)	ΔG^{DFT} (kcal/mol)	Population %
6b-1	14.5	0.0	36.27
6b-2	13.9	0.3	23.06
6b-3	19.7	0.4	18.32
6b-4	17.9	1.0	6.86
6b-5	7.4	1.3	3.86
6b-6	13.7	1.5	2.77
6b-7	8.3	1.6	2.61
6b-8	11.5	2.0	1.34
6b-9	18.3	2.1	1.13

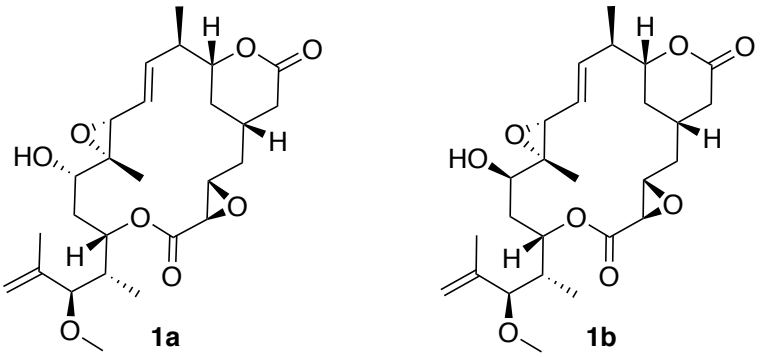

Figure C.39. Possible truncated diastereomers for **1** studied computationally.

Table C.10. Calculated energies and population for the major conformers of **1a**. All conformers with the combined population of 98.70% were used to calculate NMR properties of **1a**.

Conformer	$\Delta E^{MMFFs, gas}$ (kJ/mol)	ΔG^{DFT} (kcal/mol)	Population %
1a-1	11.3	0.0	49.48
1a-2	6.6	0.0	49.22

Table C.11. Calculated energies and population for the major conformers of **1b**. All conformers with the combined population of 97.27% were used to calculate NMR properties of **1b**.

Conformer	$\Delta E^{MMFFs, gas}$ (kJ/mol)	ΔG^{DFT} (kcal/mol)	Population %
1b-1	17.3	0.0	78.78
1b-2	6.3	1.4	7.52
1b-3	0.0	1.4	7.10
1b-4	7.1	2.1	2.19
1b-5	0.9	2.3	1.69

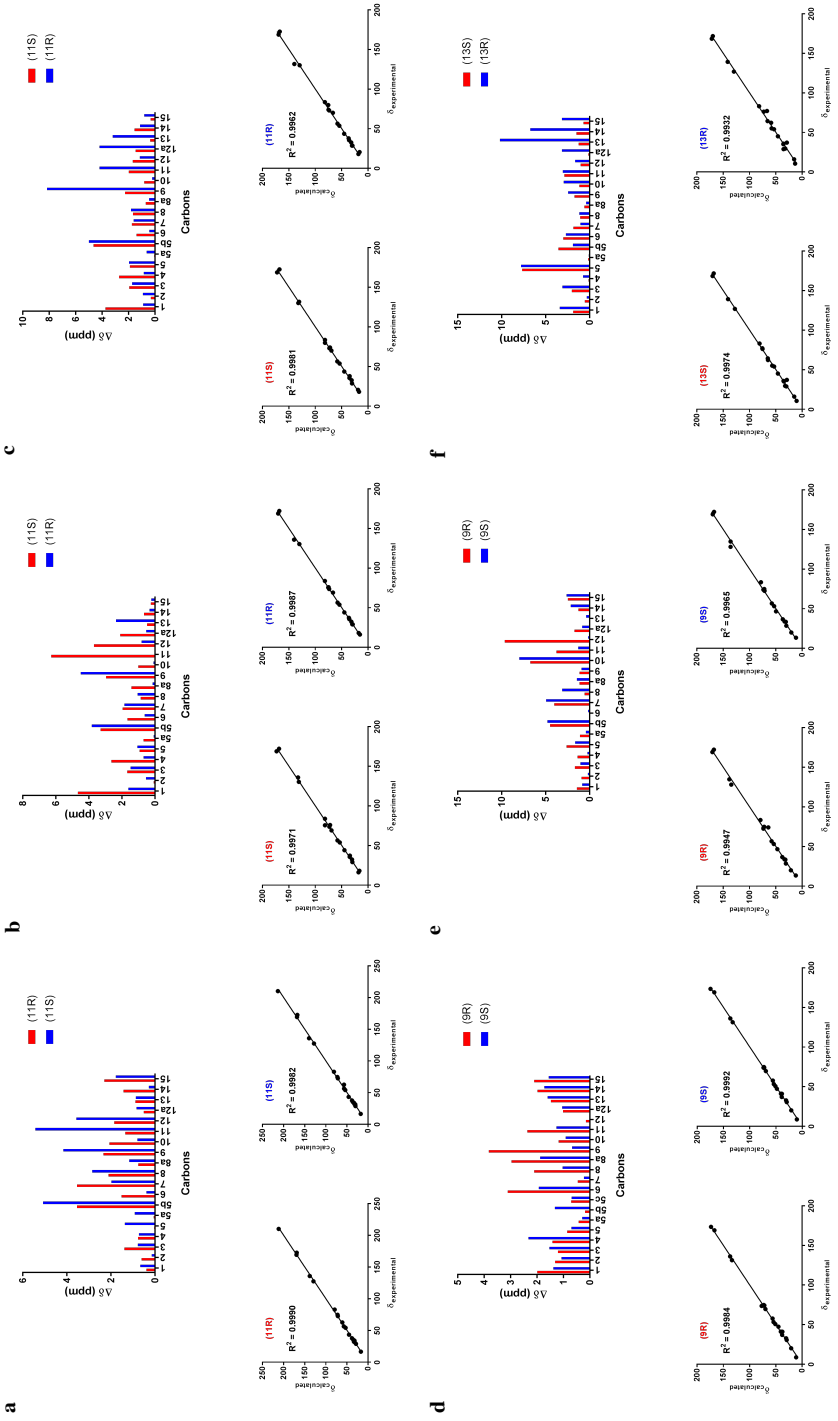

Figure C.40. ^{13}C calculation results of two plausible stereoisomers at the mPW1PW91/6-311G(d,p)-IEFPCM (methanol)//mPW1PW91/6-31G(d)-IEFPCM (methanol) level. Includes relative errors (top) and linear regressions (bottom) of calculated vs. experimental ^{13}C NMR chemical shift values for (a-e) **2-6** and (f) rhizoxin (**1**).

Table C.12. Calculated Boltzmann averaged ^{1}H chemical shifts (∂H) for **1a** and **1b** and experimental ^{1}H chemical shifts for **1** with mean absolute deviations (MAD) and standard deviations (StDev). Calculated ^{1}H chemical shifts for **1a** and **1b** were scaled using experimental ^{1}H chemical shifts of **1**.

	Exp. ∂H of 1	**Calc. 1a**	**Deviation**	**Exp. ∂H of 1**	**Calc. 1b**	**Deviation**
H2	3.15	3.04	-0.11	3.15	2.96	-0.19
H3	3.26	3.21	-0.05	3.26	3.04	-0.22
H4a	0.86	0.97	0.11	0.86	0.90	0.04
H4b	2.26	2.20	-0.06	2.26	2.09	-0.17
H5	2.04	2.05	0.01	2.04	1.97	-0.07
H5a-a	2.99	2.52	-0.47	2.99	1.95	-1.04
H5a-b	2.05	2.07	0.02	2.05	2.38	0.33
H6a	1.08	1.06	-0.02	1.08	1.80	0.72
H6b	1.93	1.82	-0.11	1.93	1.01	-0.92
H7	4.01	3.91	-0.10	4.01	3.80	-0.21
H8	2.34	2.41	0.07	2.34	2.32	-0.02
H8a	1.17	1.34	0.17	1.17	1.28	0.11
H9	5.68	5.80	0.12	5.68	5.68	0.00
H10	5.45	5.65	0.20	5.45	5.59	0.14
H11	3.20	3.27	0.07	3.20	3.26	0.06
H12a	1.40	1.55	0.15	1.40	1.61	0.21
H13	3.20	3.18	-0.02	3.20	3.83	0.63
H14a	1.87	1.78	-0.09	1.87	1.80	-0.07
H14b	2.04	2.16	0.12	2.04	2.10	0.06
H15	4.54	4.53	-0.01	4.54	5.15	0.61
		MAD	0.11		**MAD**	0.29
		StDev	0.15		**StDev**	0.44

Table C.13. Calculated Boltzmann averaged ^{13}C chemical shifts (∂C) for **1a** and **1b** and experimental ^{13}C chemical shifts for **1** with mean absolute deviations (MAD) and standard deviations (StDev). Calculated ^{13}C chemical shifts for **1a** and **1b** were scaled using experimental ^{13}C chemical shifts of **1**.

	Exp. ∂C of 1	**Calc. 1a**	**Deviation**	**Exp. ∂C of 1**	**Calc. 1b**	**Deviation**
C1	168.4	170.3	1.9	168.4	171.8	3.4
C2	53.9	53.3	-0.6	53.9	53.6	-0.3
C3	55.1	57.1	2.0	55.1	58.2	3.1
C4	35.1	35.0	-0.1	35.1	35.9	0.8
C5	37.0	29.3	-7.7	37.0	29.2	-7.8
C5a	35.7	35.5	-0.2	35.7	35.6	-0.1
C5b	171.7	168.1	-3.6	171.7	169.8	-1.9
C6	29.5	32.5	3.0	29.5	32.2	2.7
C7	83.0	81.1	-1.9	83.0	81.9	-1.1
C8	45.1	46.2	1.1	45.1	46.3	1.2
C8a	15.9	15.3	-0.6	15.9	15.5	-0.4
C9	139.2	140.9	1.7	139.2	141.7	2.5
C10	126.8	128.0	1.2	126.8	129.8	3.0
C11	62.2	65.1	2.9	62.2	59.1	-3.1
C12	64.3	65.3	1.0	64.3	66.0	1.7
C12a	10.5	10.7	0.2	10.5	13.7	3.2
C13	77.1	75.8	-1.3	77.1	66.9	-10.2
C14	28.8	30.3	1.5	28.8	35.6	6.8
C15	76.2	75.5	-0.7	76.2	73.0	-3.2
		MAD	1.7		**MAD**	3.0
		StDev	2.5		**StDev**	4.0

Table C.14. Calculated Boltzmann averaged ^{1}H chemical shifts (∂H) for **2a** and **2b** and experimental ^{1}H chemical shifts for **2** with mean absolute deviations (MAD) and standard deviations (StDev). Calculated ^{1}H chemical shifts for **2a** and **2b** were scaled using experimental ^{1}H chemical shifts of **2**.

	Exp. ∂H of 2	**Calc. 2a**	**Deviation**	**Exp. ∂H of 2**	**Calc. 2b**	**Deviation**
H2	3.35	3.13	-0.22	3.35	3.11	-0.24
H3	3.01	2.86	-0.15	3.01	2.90	-0.11
H4	0.93	1.06	0.13	0.93	1.00	0.07
H4	2.30	2.23	-0.07	2.30	2.24	-0.06
H5	2.27	2.21	-0.06	2.27	2.10	-0.17
H5a	2.16	2.07	-0.09	2.16	2.08	-0.08
H5a	2.79	2.67	-0.12	2.79	2.60	-0.19
H6	2.04	2.09	0.05	2.04	2.00	-0.04
H6	1.16	1.06	-0.10	1.16	1.10	-0.06
H7	3.92	3.80	-0.12	3.92	3.78	-0.14
H8	2.30	2.35	0.05	2.30	2.41	0.11
H8a	1.10	1.31	0.21	1.10	1.30	0.20
H9	5.30	5.48	0.18	5.30	5.41	0.11
H10	5.64	5.87	0.23	5.64	6.03	0.39
H11	3.56	3.37	-0.19	3.56	3.22	-0.34
H12a	2.25	2.40	0.15	2.25	2.35	0.10
H13	3.29	3.66	0.37	3.29	3.46	0.17
H14	1.43	1.45	0.02	1.43	1.79	0.36
H14	1.86	1.80	-0.06	1.86	1.83	-0.03
H15	5.15	4.97	-0.18	5.15	5.09	-0.06
		MAD	0.14		**MAD**	0.15
		StDev	0.16		**StDev**	0.19

Table C.15. Calculated Boltzmann averaged ^{13}C chemical shifts (∂C) for **2a** and **2b** and experimental ^{13}C chemical shifts for **2** with mean absolute deviations (MAD) and standard deviations (StDev). Calculated ^{13}C chemical shifts for **2a** and **2b** were scaled using experimental ^{13}C chemical shifts of **2**.

	Exp. ∂C of 2	**Calc. 2a**	**Deviation**	**Exp. ∂C of 2**	**Calc. 2b**	**Deviation**
C1	169.2	169.6	0.4	169.2	168.5	-0.7
C2	54.1	53.5	-0.6	54.1	54.3	0.2
C3	56.3	57.7	1.4	56.3	57.1	0.8
C4	37.5	38.3	0.8	37.5	38.2	0.7
C5	28.8	28.8	0.0	28.8	30.2	1.4
C5a	35.4	35.3	-0.1	35.4	36.3	0.9
C5b	172.6	169.1	-3.5	172.6	167.5	-5.1
C6	32.2	33.7	1.5	32.2	32.6	0.4
C7	82.9	79.4	-3.5	82.9	80.9	-2.0
C8	43.3	45.4	2.1	43.3	46.2	2.9
C8a	16.4	17.2	0.8	16.4	17.6	1.2
C9	135.8	138.1	2.3	135.8	140.0	4.2
C10	127.4	129.5	2.1	127.4	128.2	0.8
C11	62.6	61.2	-1.4	62.6	57.2	-5.4
C12	210.0	211.9	1.9	210.0	213.6	3.6
C12a	31.4	31.9	0.5	31.4	30.6	-0.8
C13	72.6	71.7	-0.9	72.6	71.7	-0.9
C14	33.9	32.5	-1.4	33.9	33.6	-0.3
C15	74.7	72.4	-2.3	74.7	72.9	-1.8
		MAD	1.5		**MAD**	1.8
		StDev	1.8		**StDev**	2.5

Table C.16. Calculated Boltzmann averaged ^{1}H chemical shifts (∂H) for **3a** and **3b** and experimental ^{1}H chemical shifts for **3** with mean absolute deviations (MAD) and standard deviations (StDev). Calculated ^{1}H chemical shifts for **3a** and **3b** were scaled using experimental ^{1}H chemical shifts of **3**.

	Exp. ∂H of 3	**Calc. 3a**	**Deviation**	**Exp. ∂H of 3**	**Calc. 3b**	**Deviation**
H2	3.05	3.09	0.04	3.30	3.13	-0.17
H3	3.30	3.10	-0.20	3.05	3.03	-0.02
H4	0.99	1.10	0.11	0.99	1.09	0.10
H4	2.19	2.12	-0.07	2.19	2.14	-0.05
H5	2.22	2.11	-0.11	2.22	2.14	-0.08
H5a	2.13	2.03	-0.10	2.13	2.05	-0.08
H5a	2.70	2.50	-0.20	2.70	2.53	-0.17
H6	1.99	1.85	-0.14	1.99	1.88	-0.11
H6	1.14	1.16	0.02	1.14	1.19	0.05
H7	4.07	3.88	-0.19	4.07	3.93	-0.14
H8	2.34	2.44	0.10	2.34	2.46	0.12
H8a	1.16	1.30	0.14	1.16	1.34	0.18
H9	5.44	5.59	0.15	5.44	5.65	0.21
H10	5.48	5.74	0.26	5.48	5.66	0.18
H11	4.25	4.04	-0.21	4.25	4.30	0.05
H12a	1.07	1.16	0.09	1.07	1.26	0.19
H13	3.31	3.57	0.26	3.31	3.18	-0.13
H14	1.82	1.98	0.16	1.70	1.65	-0.05
H14	1.70	1.65	-0.05	1.82	1.80	-0.02
H15	5.08	5.02	-0.06	5.08	5.01	-0.07
		MAD	0.13		**MAD**	0.11
		StDev	0.15		**StDev**	0.13

Table C.17. Calculated Boltzmann averaged ^{13}C chemical shifts (∂C) for **3a** and **3b** and experimental ^{13}C chemical shifts for **3** with mean absolute deviations (MAD) and standard deviations (StDev). Calculated ^{13}C chemical shifts for **3a** and **3b** were scaled using experimental ^{13}C chemical shifts of **3**.

	Exp. ∂C of 3	**Calc. 3a**	**Deviation**	**Exp. ∂C of 3**	**Calc. 3b**	**Deviation**
C1	168.8	173.5	4.7	168.8	170.4	1.6
C2	53.8	53.7	-0.1	53.8	54.3	0.5
C3	56.4	58.1	1.7	56.4	57.9	1.5
C4	37.2	34.5	-2.7	37.2	36.5	-0.7
C5	29.0	29.9	0.9	29.0	30.1	1.1
C5a	35.6	34.9	-0.7	35.6	35.7	0.1
C5b	172.1	168.8	-3.3	172.1	168.3	-3.8
C6	32.3	30.6	-1.7	32.3	31.7	-0.6
C7	83.7	81.7	-2.0	83.7	81.8	-1.9
C8	44.0	44.9	0.9	44.0	45.1	1.1
C8a	18.0	16.6	-1.4	18.0	17.8	-0.2
C9	135.8	132.8	-3.0	135.8	140.3	4.5
C10	130.3	131.3	1.0	130.3	130.2	-0.1
C11	75.5	81.8	6.3	75.5	75.5	0.0
C12	75.8	72.1	-3.7	75.8	75.0	-0.8
C12a	16.2	18.3	2.1	16.2	15.7	-0.5
C13	69.0	69.5	0.5	69.0	66.6	-2.4
C14	28.9	29.6	0.7	28.9	29.2	0.3
C15	73.6	73.3	-0.3	73.6	73.8	0.2
		MAD	2.0		**MAD**	1.2
		StDev	2.6		**StDev**	1.7

Table C.18. Calculated Boltzmann averaged ^{1}H chemical shifts (∂H) for **3a** and **3b** and experimental ^{1}H chemical shifts for **4** with mean absolute deviations (MAD) and standard deviations (StDev). Calculated ^{1}H chemical shifts for **3a** and **3b** were scaled using experimental ^{1}H chemical shifts of **4**.

	Exp. ∂H of 4	**Calc. 3a**	**Deviation**	**Exp. ∂H of 4**	**Calc. 3b**	**Deviation**
H2	3.05	3.14	0.09	3.33	3.18	-0.15
H3	3.33	3.16	-0.17	3.05	3.08	0.03
H4	0.99	1.09	0.10	0.99	1.08	0.09
H4	2.2	2.14	-0.06	2.20	2.17	-0.03
H5	2.28	2.13	-0.15	2.28	2.16	-0.12
H5a	2.13	2.05	-0.08	2.13	2.07	-0.06
H5a	2.74	2.54	-0.20	2.74	2.56	-0.18
H6	2.07	1.86	-0.21	2.07	1.89	-0.18
H6	1.17	1.15	-0.02	1.17	1.17	0.00
H7	4.1	3.96	-0.14	4.10	4.02	-0.08
H8	2.4	2.48	0.08	2.40	2.49	0.09
H8a	1.16	1.30	0.14	1.16	1.33	0.17
H9	5.7	5.73	0.03	5.70	5.81	0.11
H10	5.73	5.88	0.15	5.73	5.82	0.09
H11	4.04	4.12	0.08	4.04	4.40	0.36
H12a	1.08	1.15	0.07	1.08	1.25	0.17
H13	3.63	3.64	0.01	3.63	3.24	-0.39
H14	1.7	2.00	0.30	1.70	1.65	-0.05
H14	1.7	1.65	-0.05	1.70	1.81	0.11
H15	5.11	5.14	0.03	5.11	5.13	0.02
		MAD	0.11		**MAD**	0.12
		StDev	0.13		**StDev**	0.16

Table C.19. Calculated Boltzmann averaged ^{13}C chemical shifts (∂C) for **3a** and **3b** and experimental ^{13}C chemical shifts for **4** with mean absolute deviations (MAD) and standard deviations (StDev). Calculated ^{13}C chemical shifts for **3a** and **3b** were scaled using experimental ^{13}C chemical shifts of **4**.

	Exp. ∂C of 4	**Calc. 3a**	**Deviation**	**Exp. ∂C of 4**	**Calc. 3b**	**Deviation**
C1	168.7	172.5	3.8	168.7	169.6	0.9
C2	53.7	54.0	0.3	53.7	54.6	0.9
C3	56.4	58.4	2.0	56.4	58.1	1.7
C4	37.8	35.1	-2.7	37.8	36.9	-0.9
C5	28.6	30.5	1.9	28.6	30.6	2.0
C5a	35.5	35.4	-0.1	35.5	36.1	0.6
C5b	172.5	167.8	-4.7	172.5	167.5	-5.0
C6	32.6	31.2	-1.4	32.6	32.2	-0.4
C7	83.5	81.7	-1.8	83.5	81.9	-1.6
C8	43.6	45.3	1.7	43.6	45.4	1.8
C8a	18.0	17.3	-0.7	18.0	18.5	0.5
C9	130.0	132.3	2.3	131.6	139.8	8.2
C10	131.6	130.8	-0.8	130.0	129.8	-0.2
C11	79.8	81.8	2.0	79.8	75.6	-4.2
C12	73.9	72.2	-1.7	73.9	75.1	1.2
C12a	20.5	19.0	-1.5	20.5	16.3	-4.2
C13	70.0	69.6	-0.4	70.0	66.8	-3.2
C14	28.6	30.2	1.6	28.6	29.7	1.1
C15	73.1	73.4	0.3	73.1	73.9	0.8
		MAD	1.7		**MAD**	2.1
		StDev	2.1		**StDev**	3.0

Table C.20. Calculated Boltzmann averaged ^{1}H chemical shifts (∂H) for **5a** and **5b** and experimental ^{1}H chemical shifts for **5** with mean absolute deviations (MAD) and standard deviations (StDev). Calculated ^{1}H chemical shifts for **5a** and **5b** were scaled using experimental ^{1}H chemical shifts of **5**.

	Exp. ∂H of 5	**Calc. 5a**	**Deviation**	**Exp. ∂H of 5**	**Calc. 5b**	**Deviation**
H2	3.40	3.08	-0.32	3.10	3.07	-0.03
H3	3.10	3.18	0.08	3.40	3.15	-0.25
H4a	1.61	1.49	-0.12	1.61	1.57	-0.04
H4b	1.61	1.56	-0.05	1.61	1.55	-0.06
H5	2.23	2.13	-0.10	2.23	2.09	-0.14
H5a-a	2.32	2.49	0.17	2.55	2.45	-0.10
H5a-b	2.55	2.46	-0.09	2.32	2.43	0.11
H5c	3.68	3.68	0.00	3.68	3.63	-0.05
H6-a	1.69	1.62	-0.07	1.69	1.60	-0.09
H6-b	1.31	1.43	0.12	1.31	1.52	0.21
H7	3.77	4.17	0.40	3.77	3.78	0.01
H8	1.37	1.45	0.08	1.37	1.43	0.06
H8a	1.04	1.12	0.08	1.04	1.16	0.12
H9	3.93	4.06	0.13	3.93	4.06	0.13
H10	5.95	6.33	0.38	5.95	6.42	0.47
H11	5.91	5.72	-0.19	5.91	5.90	-0.01
H12a	1.24	1.30	0.06	1.24	1.32	0.08
H13	3.14	3.39	0.25	3.14	3.39	0.25
H14-a	1.72	1.41	-0.31	1.63	1.53	-0.10
H14-b	1.63	1.59	-0.04	1.72	1.66	-0.06
H15	5.26	4.78	-0.48	5.26	4.77	-0.49
		MAD	0.17		**MAD**	0.14
		StDev	0.22		**StDev**	0.19

Table C.21. Calculated Boltzmann averaged ^{13}C chemical shifts (∂C) for **5a** and **5b** and experimental ^{13}C chemical shifts for **5** with mean absolute deviations (MAD) and standard deviations (StDev). Calculated ^{13}C chemical shifts for **5a** and **5b** were scaled using experimental ^{13}C chemical shifts of **5**.

	Exp. ∂C of 5	**Calc. 5a**	**Deviation**	**Exp. ∂C of 5**	**Calc. 5b**	**Deviation**
C1	169.0	167.0	-2.0	169.0	167.6	-1.4
C2	53.2	54.5	1.3	53.2	54.3	1.1
C3	57.6	56.4	-1.2	57.6	56.1	-1.5
C4	36.9	38.3	1.4	36.9	39.2	2.3
C5	30.5	29.6	-0.9	30.5	29.8	-0.7
C5a	41.1	40.7	-0.4	41.1	40.8	-0.3
C5b	173.4	173.6	0.2	173.4	174.7	1.3
C5c	50.6	51.3	0.7	50.6	51.3	0.7
C6	40.9	37.8	-3.1	40.9	39.0	-1.9
C7	69.6	70.1	0.5	69.6	69.4	-0.2
C8	47.3	45.2	-2.1	47.3	48.3	1.0
C8a	8.6	11.6	3.0	8.6	10.5	1.9
C9	73.5	77.3	3.8	73.5	72.8	-0.7
C10	136.1	137.3	1.2	136.1	137.0	0.9
C11	131.3	133.7	2.4	131.3	132.6	1.3
C12	73.9	73.7	-0.2	73.9	73.9	0.0
C12a	20.1	21.1	1.0	20.1	21.2	1.1
C13	74.7	73.2	-1.5	74.7	73.1	-1.6
C14	32.6	30.6	-2.0	32.6	30.9	-1.7
C15	74.2	72.1	-2.1	74.2	72.6	-1.6
		MAD	1.5		**MAD**	1.2
		StDev	1.9		**StDev**	1.3

Table C.22. Calculated Boltzmann averaged ^{1}H chemical shifts (∂H) for **6a** and **6b** and experimental ^{1}H chemical shifts for **6** with mean absolute deviations (MAD) and standard deviations (StDev). Calculated ^{1}H chemical shifts for **6a** and **6b** were scaled using experimental ^{1}H chemical shifts of **6**.

	Exp. ∂H of 6	**Calc. 6a**	**Deviation**	**Exp. ∂H of 6**	**Calc. 6b**	**Deviation**
H2	3.47	3.23	-0.24	3.47	3.19	-0.28
H3	3.01	2.92	-0.09	3.01	2.91	-0.10
H4a	0.96	1.08	0.12	0.96	1.09	0.13
H4b	2.16	2.27	0.11	2.16	2.23	0.07
H5	2.06	2.07	0.01	2.06	2.02	-0.04
H5a-a	2.12	2.19	0.07	2.12	2.17	0.05
H5a-b	2.60	2.48	-0.12	2.60	2.46	-0.14
H6a	2.19	1.83	-0.36	2.19	1.82	-0.37
H6b	1.32	1.40	0.08	1.32	1.46	0.14
H7	4.25	4.44	0.19	4.25	4.22	-0.03
H8	1.85	1.99	0.14	1.85	1.79	-0.06
H8a	1.15	1.28	0.13	1.15	1.30	0.15
H9	4.15	4.31	0.16	4.15	4.18	0.03
H10	6.02	6.33	0.31	6.02	6.44	0.42
H11	6.02	5.93	-0.09	6.02	6.07	0.05
H12a	1.16	1.29	0.13	1.16	1.35	0.19
H13	3.09	3.00	-0.09	3.09	3.04	-0.05
H14a	1.57	1.44	-0.13	1.57	1.65	0.08
H14b	1.83	1.71	-0.12	1.83	1.77	-0.06
H15	5.25	5.05	-0.20	5.25	5.06	-0.19
		MAD	0.14		**MAD**	0.13
		StDev	0.17		**StDev**	0.17

Table C.23. Calculated Boltzmann averaged ^{13}C chemical shifts (∂C) for **6a** and **6b** and experimental ^{13}C chemical shifts for **6** with mean absolute deviations (MAD) and standard deviations (StDev). Calculated ^{13}C chemical shifts for **6a** and **6b** were scaled using experimental ^{13}C chemical shifts of **6**.

	Exp. ∂C of 6	Calc. 6a	Deviation	Exp. ∂C of 6	Calc. 6b	Deviation
C1	169.1	170.6	1.5	169.1	170.0	0.9
C2	53.2	54.1	0.9	53.2	53.4	0.2
C3	56.6	58.3	1.7	56.6	57.7	1.1
C4	36.6	38.0	1.4	36.6	36.9	0.3
C5	28.5	31.1	2.6	28.5	30.2	1.7
C5a	36.5	37.6	1.1	36.5	36.9	0.4
C5b	172.2	167.7	-4.5	172.2	167.4	-4.8
C6	33.8	33.7	-0.1	33.8	33.6	-0.2
C7	83.4	79.4	-4.0	83.4	78.4	-5.0
C8	46.6	47.2	0.6	46.6	49.7	3.1
C8a	13.4	12.2	-1.2	13.4	11.9	-1.5
C9	72.5	73.7	1.2	72.5	71.6	-0.9
C10	128.0	134.8	6.8	128.0	136.0	8.0
C11	134.7	138.5	3.8	134.7	136.0	1.3
C12	74.0	64.3	-9.7	74.0	73.8	-0.2
C12a	19.9	21.6	1.7	19.9	20.8	0.9
C13	73.6	73.5	-0.1	73.6	73.2	-0.4
C14	33.4	32.1	-1.3	33.4	31.2	-2.2
C15	74.8	72.3	-2.5	74.8	72.2	-2.6
		MAD	2.5		**MAD**	1.9
		StDev	3.5		**StDev**	2.8

Discussion C.2. Liquid Culture Condition Screening

Three media types were screened for increased production of rhizoxin analogues in *Rhizopus microsporus*.

1. Potato Dextrose Broth: 10 g/L instant mashed potatoes, 5 g/L glucose

2. Literature media recipe (substitute yeast extract for Pharmamedia):[206] 30 g/L maltose, 10 g/L peptone, 2.5 g/L KH_2PO_4, 7.5 g/L K_2HPO_4, 2.5 g/L $MgSO_4\,7H_2O$, 2.0 g/L $(NH_4)_2SO_4$, 40 g/L yeast extract

3. Literature media recipe (substitute yeast extract and glucose): 30 g/L glucose, 10 g/L peptone, 2.5 g/L KH_2PO_4, 7.5 g/L K_2HPO_4, 2.5 g/L $MgSO_4\,7H_2O$, 2.0 g/L $(NH_4)_2SO_4$, 40 g/L yeast extract

Discussion C.3. General computational information

All geometry optimizations, frequency calculations, and intrinsic reaction coordinate (IRC) calculations were performed using Gaussian 09.[201] All calculations were performed using IEF-PCM solvation modeling with water as the solvent. The lowest energy conformations for **1** and **2** were used as starting structures for protonated species **1H$^+$, 7-1** and **2H$^+$**. Geometry optimization and frequency calculations were performed using the M06-2X functional and 6-31G(d) basis set. Following geometry optimization, single point energies were calculated for each optimized structure using M06-2X/6-311++G(d,p). The difference between the single point electronic energy and the electronic energy obtained through the geometry optimization at a lower level of theory was calculated and used to adjust the Gibbs free energy.[195]

Following optimization of **1H$^+$**, **7**, and **2H$^+$**, transition states for each transformation step were determined. To determine the optimized structure of **TS1**, the Berny algorithm was used with M06-2X/6-31G(d) basis set. Frequency calculations were conducted to confirm the presence of one imaginary frequency, and IRC calculations were performed to verify the transition state. The use of the Berny algorithm to determine **TS2** ultimately failed to yield a valid transition state for the transformation of interest. However, from the obtained structure, a lower energy conformer of **7** (**7-2**) was discovered. Using **7-2**, as well as the structure of **2H$^+$**, QST2 calculations at the M06-

2X/6-31G(d) level of theory led to a valid transition state, confirmed through IRC calculations. Single point energies for **TS1** and **TS2** were obtained as previously described for $\mathbf{1H}^+$, **7-1**, and $\mathbf{2H}^+$, and corrected Gibbs free energies were determined as previously described.

Table C.24. Cartesian coordinates for the optimized structure of **1H+**

RH+	Symbol	X	Y	Z
1	C	-5.031407	0.965231	2.013465
2	C	-4.671138	-0.270375	1.663972
3	C	-4.873707	-0.763592	0.243783
4	C	-4.042303	-1.250491	2.616303
5	C	-3.55228	-1.078869	-0.480706
6	O	-5.610772	-1.974812	0.21892
7	C	-6.948454	-1.815203	0.643729
8	C	-2.505508	0.02743	-0.266122
9	C	-3.802096	-1.372449	-1.960147
10	C	-2.883816	1.328119	-0.95613
11	O	-1.234817	-0.393326	-0.830561
12	H	-2.351234	0.187694	0.806004
13	C	-0.604431	-1.395226	-0.200522
14	C	0.556816	-1.920327	-0.997722
15	O	-0.943248	-1.857092	0.862992
16	C	1.522311	-2.805527	-0.317562
17	C	2.950126	-2.921777	-0.785671
18	C	3.877261	-2.041183	0.055721
19	O	0.515121	-3.334748	-1.160776
20	C	5.316313	-2.104868	-0.444809
21	C	6.244831	-1.060714	0.141995
22	O	5.727688	0.082553	0.634868
23	C	4.325065	0.270383	0.907051
24	C	3.434471	-0.585642	0.029919
25	O	7.445966	-1.178464	0.120958
26	C	4.062745	1.775426	0.722331
27	H	3.845362	-2.394348	1.096062
28	H	4.172514	-0.000319	1.960795
29	C	2.600828	2.051034	0.916451
30	C	4.905267	2.617675	1.685112
31	C	1.753981	2.311554	-0.086901
32	C	0.333975	2.530017	0.181612
33	C	-0.70089	2.662595	-0.858103
34	C	-2.177175	2.5853	-0.465527
35	O	-0.198781	3.951413	-0.211436
36	C	-0.39177	2.511966	-2.316852
37	O	-2.840224	3.66828	-1.076959
38	H	-4.873814	1.3412	3.020856
39	H	-5.501055	1.642718	1.303465
40	H	-5.432524	0.002323	-0.320561
41	H	-4.627619	-2.17603	2.645856
42	H	-3.030901	-1.522678	2.288576
43	H	-3.981815	-0.837626	3.625865
44	H	-3.159982	-1.984313	-0.005782
45	H	-7.438318	-2.782787	0.524309
46	H	-7.006127	-1.507177	1.695524
47	H	-7.469311	-1.066195	0.031495
48	H	-2.864564	-1.583951	-2.482864
49	H	-4.455127	-2.242089	-2.055535
50	H	-4.291827	-0.52895	-2.458973
51	H	-3.945339	1.521109	-0.775362
52	H	-2.764012	1.229416	-2.040279
53	H	0.849126	-1.350863	-1.87717
54	H	1.339524	-2.985022	0.742792
55	H	3.009353	-2.632453	-1.842724
56	H	3.264018	-3.969896	-0.715375
57	H	5.77848	-3.080053	-0.274045
58	H	5.332193	-1.930939	-1.530176
59	H	3.447524	-0.207826	-1.003728
60	H	2.411098	-0.485394	0.400446
61	H	4.332468	2.014667	-0.314093
62	H	2.223377	2.00528	1.939672
63	H	4.730139	3.683512	1.519345
64	H	4.651091	2.384155	2.724625
65	H	5.966292	2.410259	1.533032
66	H	2.106494	2.345538	-1.114588
67	H	-0.005876	2.363421	1.200139
68	H	-2.252022	2.646391	0.629481
69	H	-0.417756	1.442906	-2.548282
70	H	-1.155764	3.027509	-2.901817
71	H	0.592737	2.893261	-2.59185
72	H	-2.565681	4.488484	-0.637431
73	H	0.457312	4.425722	-0.769777

Table C.25. Cartesian coordinates for the optimized structure of **TS1**

TS1	Symbol	X	Y	Z	37	O	-2.874765	3.875086	-0.93622
1	C	-4.939606	1.198661	2.07355	38	H	-4.783948	1.578446	3.079836
2	C	-4.587911	-0.041752	1.7325	39	H	-5.398605	1.876998	1.357385
3	C	-4.785264	-0.540808	0.313612	40	H	-5.341218	0.223188	-0.255938
4	C	-3.970692	-1.021361	2.692923	41	H	-4.56205	-1.942972	2.724209
5	C	-3.460831	-0.860969	-0.403677	42	H	-2.95962	-1.301635	2.370985
6	O	-5.524016	-1.75121	0.290782	43	H	-3.912148	-0.603871	3.700716
7	C	-6.863187	-1.587625	0.709125	44	H	-3.076022	-1.767759	0.074417
8	C	-2.411811	0.243445	-0.18556	45	H	-7.354141	-2.554983	0.592176
9	C	-3.704382	-1.155487	-1.884018	46	H	-6.924902	-1.274585	1.759255
10	C	-2.785903	1.541275	-0.883981	47	H	-7.380369	-0.840698	0.091235
11	O	-1.137722	-0.1866	-0.739161	48	H	-2.765388	-1.374323	-2.401165
12	H	-2.265027	0.404877	0.88757	49	H	-4.362865	-2.0208	-1.981805
13	C	-0.528014	-1.20213	-0.111033	50	H	-4.185021	-0.309289	-2.387102
14	C	0.626044	-1.745536	-0.906497	51	H	-3.85851	1.705189	-0.742771
15	O	-0.875275	-1.660794	0.951343	52	H	-2.627903	1.44513	-1.96326
16	C	1.58175	-2.637275	-0.220678	53	H	0.924637	-1.182495	-1.788003
17	C	3.011002	-2.759636	-0.682748	54	H	1.394603	-2.811066	0.839883
18	C	3.93073	-1.862421	0.150267	55	H	3.073126	-2.484627	-1.743362
19	O	0.572166	-3.159984	-1.064124	56	H	3.329229	-3.80495	-0.59592
20	C	5.367707	-1.903804	-0.359506	57	H	5.846903	-2.870012	-0.185227
21	C	6.282988	-0.841498	0.214424	58	H	5.374031	-1.736593	-1.445931
22	O	5.748611	0.299306	0.705413	59	H	3.460042	-0.046618	-0.919015
23	C	4.349044	0.462498	0.979332	60	H	2.443308	-0.330131	0.502146
24	C	3.464228	-0.414561	0.118125	61	H	4.338359	2.191649	-0.274749
25	O	7.484559	-0.935842	0.188641	62	H	2.220677	2.176431	1.964884
26	C	4.063433	1.966759	0.762301	63	H	4.69017	3.898332	1.548661
27	H	3.910138	-2.210062	1.192408	64	H	4.620312	2.607859	2.767831
28	H	4.201158	0.214371	2.038469	65	H	5.940394	2.6394	1.579709
29	C	2.606157	2.208068	0.944035	66	H	2.087202	2.463523	-1.106242
30	C	4.87745	2.83765	1.729034	67	H	0.04818	2.528259	1.252897
31	C	1.735277	2.433451	-0.079198	68	H	-2.206177	2.847264	0.732188
32	C	0.36903	2.604297	0.215424	69	H	-0.354505	1.801327	-2.480364
33	C	-0.662977	3.026884	-0.757769	70	H	-1.181737	3.349094	-2.7974
34	C	-2.136239	2.817371	-0.366727	71	H	0.571603	3.312967	-2.520059
35	O	-0.346052	4.354142	-0.228698	72	H	-2.501723	4.707943	-0.604147
36	C	-0.382736	2.865746	-2.231296	73	H	0.338723	4.777394	-0.7814

Table C.26. Cartesian coordinates for the optimized structure of **7-1**

6-1	Symbol	X	Y	Z	37	O	-3.167304	3.504367	-0.856524
1	C	-4.953627	0.919316	1.85465	38	H	-4.820295	1.333305	2.850629
2	C	-4.601594	-0.334615	1.567213	39	H	-5.386301	1.576448	1.102862
3	C	-4.760087	-0.88344	0.161685	40	H	-5.316178	-0.148328	-0.444628
4	C	-4.011023	-1.281081	2.576485	41	H	-4.605564	-2.199689	2.627384
5	C	-3.413444	-1.20296	-0.51431	42	H	-2.99396	-1.575453	2.286996
6	O	-5.477895	-2.106337	0.162688	43	H	-3.972735	-0.827676	3.569666
7	C	-6.828762	-1.951209	0.544948	44	H	-3.036208	-2.099923	-0.012269
8	C	-2.380969	-0.085496	-0.283995	45	H	-7.30089	-2.930665	0.453655
9	C	-3.613232	-1.518486	-1.996469	46	H	-6.91958	-1.600312	1.581036
10	C	-2.758946	1.207203	-0.995477	47	H	-7.344347	-1.237324	-0.112071
11	O	-1.093928	-0.508816	-0.810755	48	H	-2.664907	-1.779425	-2.475362
12	H	-2.255243	0.080247	0.790888	49	H	-4.297615	-2.36279	-2.101939
13	C	-0.489323	-1.514778	-0.165226	50	H	-4.044989	-0.665708	-2.532099
14	C	0.680397	-2.056148	-0.938846	51	H	-3.849937	1.286836	-0.991944
15	O	-0.846889	-1.966988	0.896983	52	H	-2.463377	1.153265	-2.048212
16	C	1.664145	-2.89038	-0.22027	53	H	0.964371	-1.517591	-1.840134
17	C	3.097006	-2.977359	-0.680098	54	H	1.4825	-3.030915	0.846273
18	C	3.980633	-2.010198	0.113128	55	H	3.146848	-2.743778	-1.751177
19	O	0.673177	-3.476045	-1.042919	56	H	3.457371	-4.004274	-0.550572
20	C	5.415067	-2.000658	-0.408184	57	H	5.944419	-2.932115	-0.194078
21	C	6.282802	-0.868808	0.104472	58	H	5.405573	-1.884609	-1.501074
22	O	5.697593	0.261014	0.570056	59	H	3.425601	-0.251117	-1.011421
23	C	4.300171	0.353569	0.862531	60	H	2.426902	-0.53322	0.424589
24	C	3.449598	-0.587078	0.035749	61	H	4.161533	2.051395	-0.443021
25	O	7.485883	-0.896859	0.052948	62	H	2.094402	1.817318	1.834729
26	C	3.918524	1.832118	0.602129	63	H	4.440442	3.8237	1.325201
27	H	3.983527	-2.321549	1.166664	64	H	4.442999	2.571744	2.588831
28	H	4.176843	0.131644	1.930329	65	H	5.752743	2.628621	1.387952
29	C	2.463444	1.969878	0.817949	66	H	1.880868	2.431249	-1.191778
30	C	4.683099	2.782072	1.542715	67	H	-0.067906	2.197048	1.21779
31	C	1.54893	2.268797	-0.170617	68	H	-2.37987	2.443691	0.734293
32	C	0.214838	2.386106	0.18215	69	H	-0.384758	1.973267	-2.545046
33	C	-0.851351	2.974482	-0.690609	70	H	-1.415011	3.418359	-2.699705
34	C	-2.293039	2.514002	-0.362574	71	H	0.325636	3.591306	-2.407748
35	O	-0.791702	4.286237	-0.097023	72	H	-2.850763	4.357839	-0.515891
36	C	-0.5575	2.988727	-2.177366	73	H	-0.088153	4.805137	-0.523804

Table C.27. Cartesian coordinates of the optimized structure of **7-2**

6-2	Symbol	X	Y	Z
1	C	5.281931	1.081501	-1.664733
2	C	5.280736	-0.106196	-1.058664
3	C	5.166456	-0.20466	0.451532
4	C	5.399997	-1.410512	-1.800214
5	C	3.913808	-0.965237	0.917247
6	O	6.265387	-0.910405	1.002397
7	C	7.49204	-0.224695	0.857181
8	C	2.659573	-0.441408	0.212884
9	C	3.800763	-0.948214	2.441406
10	C	2.263047	0.986886	0.573213
11	O	1.567415	-1.320709	0.595135
12	H	2.792777	-0.5246	-0.867756
13	C	0.768555	-1.785741	-0.359478
14	C	-0.341588	-2.621183	0.199018
15	O	0.881175	-1.54257	-1.545579
16	C	-1.592027	-2.709201	-0.589006
17	C	-2.930707	-2.968466	0.060951
18	C	-3.961127	-1.889454	-0.278092
19	O	-0.653907	-3.7688	-0.57258
20	C	-5.29252	-2.203366	0.39962
21	C	-6.320344	-1.095401	0.354715
22	O	-5.906649	0.17734	0.152872
23	C	-4.596669	0.511494	-0.319963
24	C	-3.538166	-0.48147	0.135317
25	O	-7.492082	-1.280307	0.564087
26	C	-4.351617	1.955522	0.198451
27	H	-4.108149	-1.891815	-1.367326
28	H	-4.642877	0.530025	-1.416853
29	C	-3.102579	2.477505	-0.389071
30	C	-5.509413	2.89188	-0.20015
31	C	-1.920925	2.637531	0.304273
32	C	-0.790556	2.997647	-0.406596
33	C	0.605076	2.896215	0.124848
34	C	0.947065	1.383689	-0.088656
35	O	1.482097	3.68464	-0.640151
36	C	0.715888	3.340646	1.581341
37	O	0.987076	1.271276	-1.499992
38	H	5.354691	1.169882	-2.745515
39	H	5.216606	2.007799	-1.098043
40	H	5.147805	0.815774	0.872683
41	H	6.19474	-2.023172	-1.361347
42	H	4.472854	-1.993824	-1.731472
43	H	5.619224	-1.246021	-2.857361
44	H	4.032958	-2.006184	0.588373
45	H	8.24865	-0.809375	1.382738
46	H	7.778652	-0.124408	-0.197271
47	H	7.435635	0.77887	1.300871
48	H	2.871172	-1.42162	2.768928
49	H	4.640878	-1.489414	2.879723
50	H	3.824998	0.075367	2.830379
51	H	3.051812	1.669155	0.237097
52	H	2.162708	1.074633	1.659198
53	H	-0.361542	-2.748734	1.278011
54	H	-1.602177	-2.166139	-1.535607
55	H	-2.813563	-3.054983	1.147925
56	H	-3.301263	-3.934828	-0.301336
57	H	-5.76491	-3.099398	-0.010266
58	H	-5.122184	-2.395809	1.468268
59	H	-3.410453	-0.425796	1.22517
60	H	-2.581546	-0.207486	-0.326083
61	H	-4.256327	1.901435	1.288245
62	H	-3.119563	2.728611	-1.45131
63	H	-5.31303	3.913362	0.131534
64	H	-5.649525	2.891387	-1.285106
65	H	-6.424485	2.535901	0.274123
66	H	-1.869757	2.379386	1.358221
67	H	-0.896649	3.299226	-1.4483
68	H	0.133083	0.777059	0.333945
69	H	0.174936	2.672183	2.255288
70	H	1.771346	3.342194	1.857909
71	H	0.325902	4.354671	1.694248
72	H	1.017014	0.329372	-1.754333
73	H	1.645292	3.201722	-1.471339

Table C.28. Cartesian coordinates of the optimized structure of **TS2**

TS2	Symbol	X	Y	Z	37	O	1.422021	1.336194	-1.763555
1	C	5.271504	0.96078	-1.396156	38	H	5.447457	1.071197	-2.462836
2	C	5.2226	-0.239132	-0.816662	39	H	5.139708	1.87635	-0.823373
3	C	4.954516	-0.370976	0.671359	40	H	4.928509	0.638781	1.116772
4	C	5.433962	-1.524977	-1.569347	41	H	6.217467	-2.120309	-1.088489
5	C	3.637109	-1.098046	0.993756	42	H	4.525591	-2.140454	-1.574924
6	O	5.96702	-1.127967	1.310657	43	H	5.719745	-1.332844	-2.605776
7	C	7.223921	-0.482543	1.308579	44	H	3.762383	-2.140437	0.672329
8	C	2.475661	-0.54319	0.163968	45	H	7.903605	-1.107637	1.889632
9	C	3.361935	-1.082639	2.497149	46	H	7.618331	-0.36502	0.29138
10	C	2.102324	0.903396	0.503011	47	H	7.155769	0.510211	1.774085
11	O	1.331813	-1.386679	0.440101	48	H	2.406186	-1.562344	2.723996
12	H	2.705205	-0.618592	-0.901382	49	H	4.154965	-1.619159	3.020621
13	C	0.540711	-1.751383	-0.567988	50	H	3.337877	-0.058985	2.886875
14	C	-0.565279	-2.638918	-0.082741	51	H	2.98015	1.541234	0.359673
15	O	0.662248	-1.390161	-1.720277	52	H	1.767221	0.963246	1.540146
16	C	-1.806706	-2.719832	-0.882174	53	H	-0.593793	-2.823115	0.987994
17	C	-3.135157	-3.016393	-0.229354	54	H	-1.829107	-2.134321	-1.802689
18	C	-4.098268	-1.833131	-0.358653	55	H	-2.978796	-3.269947	0.826066
19	O	-0.844374	-3.756874	-0.910797	56	H	-3.576368	-3.896289	-0.712184
20	C	-5.377094	-2.079883	0.437475	57	H	-5.992132	-2.87265	0.004299
21	C	-6.27435	-0.873912	0.632231	58	H	-5.115604	-2.404251	1.454449
22	O	-5.761878	0.364822	0.477652	59	H	-3.25287	-0.544502	1.176843
23	C	-4.497658	0.605792	-0.163128	60	H	-2.57683	-0.283701	-0.439613
24	C	-3.500317	-0.508	0.106468	61	H	-3.858084	1.93256	1.404206
25	O	-7.419047	-0.973932	0.999108	62	H	-2.775265	2.276241	-1.465968
26	C	-4.030565	1.9872	0.322949	63	H	-4.735271	4.044177	0.379976
27	H	-4.356011	-1.72458	-1.421583	64	H	-5.259441	3.143605	-1.057997
28	H	-4.691187	0.663566	-1.243968	65	H	-6.017043	2.821167	0.515442
29	C	-2.754562	2.319416	-0.374467	66	H	-1.544382	2.729771	1.321306
30	C	-5.077926	3.071963	0.01915	67	H	-0.579925	2.906537	-1.64256
31	C	-1.600845	2.669549	0.23864	68	H	0.087757	0.787855	-0.279672
32	C	-0.451175	2.941929	-0.560372	69	H	0.527646	2.869217	2.046197
33	C	0.865931	3.14751	-0.082547	70	H	2.168375	3.389478	1.594887
34	C	1.005745	1.352358	-0.450361	71	H	0.821957	4.536169	1.51138
35	O	1.821518	3.710909	-0.872853	72	H	0.99596	0.582662	-2.214553
36	C	1.107472	3.490968	1.364143	73	H	1.724749	3.397178	-1.790847

Table C.29. Cartesian coordinates of the optimized structure of **2H+**

1H+	Symbol	X	Y	Z	37	O	2.040614	1.907247	-1.864258
1	C	5.095909	0.519364	-1.517539	38	H	5.305572	0.480548	-2.583321
2	C	4.87229	-0.586308	-0.80797	39	H	5.068522	1.504424	-1.057003
3	C	4.55649	-0.500185	0.672524	40	H	4.628867	0.555444	0.987888
4	C	4.900458	-1.970546	-1.396999	41	H	5.544201	-2.623801	-0.798178
5	C	3.162577	-1.043591	1.02482	42	H	3.897397	-2.41673	-1.396338
6	O	5.467443	-1.270038	1.440257	43	H	5.268256	-1.955271	-2.425469
7	C	6.788694	-0.773455	1.393637	44	H	3.192562	-2.124891	0.831849
8	C	2.082673	-0.475023	0.099892	45	H	7.383675	-1.385276	2.073593
9	C	2.842945	-0.814541	2.501398	46	H	7.211836	-0.839089	0.383333
10	C	1.752316	0.998165	0.303517	47	H	6.827361	0.274937	1.72035
11	O	0.84032	-1.163986	0.369015	48	H	1.846289	-1.191316	2.74756
12	H	2.351559	-0.654434	-0.945377	49	H	3.575365	-1.330446	3.124681
13	C	0.599872	-2.305037	-0.286911	50	H	2.880192	0.251972	2.751848
14	C	-0.683961	-2.899636	0.203624	51	H	2.670081	1.577134	0.460701
15	O	1.296462	-2.773747	-1.153555	52	H	1.139781	1.097408	1.204881
16	C	-1.78619	-3.133655	-0.753466	53	H	-0.927461	-2.702212	1.245857
17	C	-3.213878	-3.133672	-0.274861	54	H	-1.603302	-2.87366	-1.797042
18	C	-3.94722	-1.809523	-0.503504	55	H	-3.216928	-3.37923	0.794758
19	O	-0.973101	-4.19451	-0.277429	56	H	-3.75408	-3.937901	-0.789514
20	C	-5.370616	-1.929528	0.044897	57	H	-6.003824	-2.559736	-0.584365
21	C	-6.12038	-0.636584	0.286965	58	H	-5.336269	-2.412349	1.032001
22	O	-5.431591	0.513991	0.385364	59	H	-3.188472	-0.756506	1.238728
23	C	-4.088344	0.644268	-0.123934	60	H	-2.25545	-0.457963	-0.236836
24	C	-3.269341	-0.606749	0.152341	61	H	-3.255243	1.725343	1.539592
25	O	-7.311075	-0.613455	0.487791	62	H	-2.39916	2.464859	-1.335684
26	C	-3.504345	1.92467	0.489565	63	H	-4.037827	4.000029	0.814898
27	H	-3.997289	-1.619141	-1.584397	64	H	-4.781228	3.287675	-0.62868
28	H	-4.177603	0.789434	-1.210712	65	H	-5.401516	2.872519	0.979473
29	C	-2.258696	2.293749	-0.265052	66	H	-0.867955	2.286956	1.316773
30	C	-4.496687	3.093607	0.411688	67	H	-0.256246	3.133237	-1.59411
31	C	-1.043022	2.454488	0.255228	68	H	0.365311	0.7853	-1.34293
32	C	0.13538	2.78819	-0.621509	69	H	0.460434	4.464236	1.789565
33	C	0.965693	3.952643	-0.166713	70	H	1.126335	5.820992	0.828036
34	C	1.020724	1.550304	-0.915407	71	H	-0.556603	5.206882	0.564805
35	O	2.122683	4.1088	-0.651216	72	H	1.67928	1.91207	-2.767451
36	C	0.479359	4.945836	0.802099	73	H	2.343341	3.330638	-1.291495

Table C.30. Thermodynamic data calculated for optimized structures. All energies are given in Hartrees.

	M06-2X/6-31G(d) - IEFPCM=water		**M06-2X/6-311++G(d,p) - IEFPCM=water// M06-2X/6-31G(d) - IEFPCM=water**
	Electronic Energy	**Free Energy**	**Electronic Energy**
1H+	-1615.10009938	-1614.529241	-1615.57991139
TS1	-1615.09599816	-1614.526229	-1615.57671100
7-1	-1615.09677424	-1614.528220	-1615.57876878
7-2	-1615.10750107	-1614.540339	-1615.58946855
TS2	-1615.09754221	-1614.529506	-1615.57884300
2H+	-1615.14824789	-1614.581254	-1615.62771307

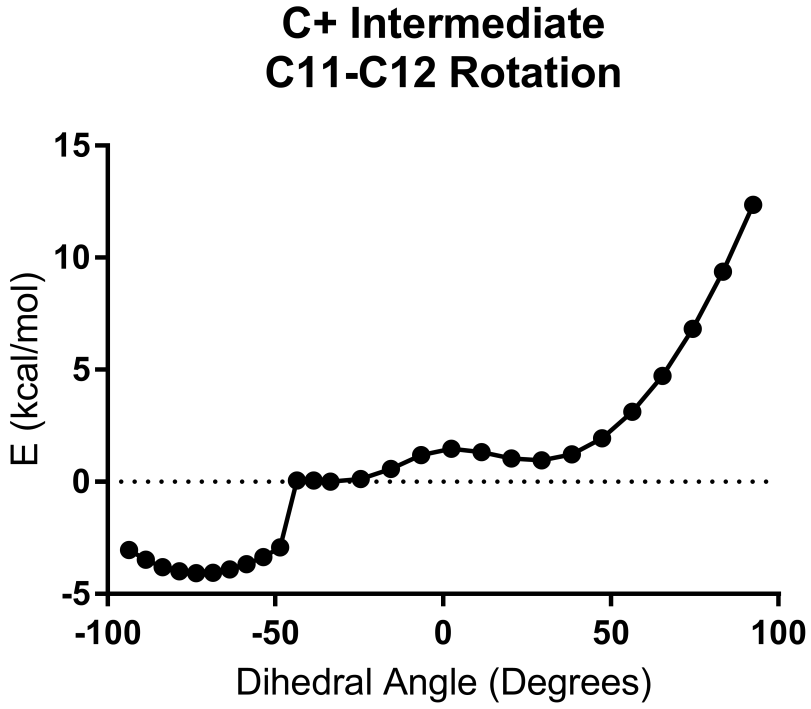

Figure C.41. Potential energy scan examining rotation about the C11-C12 bond of **7.** Dihedral angle is between C13-C11-C10-H10, with -90° being optimal for *si* face migration to yield the 11*R* product, while +90° is best aligned for *re* face migration to yield the 11*S* product. Calculation was performed at the M06-2X/6-31G(d)-IEFPCM (water) level.